Department of Environmental, Land and Infrastructure Engineering

Master of Science in Petroleum and Mining Engineering

Optimization of Peng-Robinson and Redlich-Kwong-Soave Equations of State parameters for H_2 – CH_4 mixtures

By

Marialuna Loffredo
S300892

Supervisor(s):
Prof. Dario Viberti ,Supervisor
Prof. Filippo Panini, Co-Supervisor

Politecnico di Torino
2023

Abstract

Hydrogen (H_2) is considered a clean energy fuel that can provide a sustainable energy market and overcome intermittent production issues because it can facilitate the storage of large quantities of energy to balance out long periods of poor wind power supply and seasonal fluctuations. A vast expansion of the H_2 economy requires a massive storage capacity which is available in geological storages such as deep aquifers, salt caverns and depleted hydrocarbons reservoirs. However, Underground Hydrogen Storage (UHS) is a complex procedure where containment security, pore-scale phenomena and large-scale storage capacity can be influenced by H_2 contamination due to the mixing with cushion gases and reservoir fluids. The literature lacks comprehensive investigations of existing thermodynamic models, i.e. Equations of State (EoSs), in calculating the accurate transport properties of H_2-blend mixtures essential to the efficient design of various H_2 storage processes. This study analyzes one possible route for improving the accuracy of the prediction of thermodynamic properties: the mathematical optimization of EoSs parameters to fit experimental data. Using recent experimental data from the literature for H_2 –CH_4 mixtures at different compositions, the Levenberg-Marquardt and the Trust-Region methods were used and compared for the nonlinear regression problem of the Redlich – Kwong – Soave (RKS) and Peng – Robinson (PR) cubic equations of state. The values of Ω_a, Ω_b and binary interaction parameters (BIP) were optimized using a Matlab code and the built-in function *lsqcurvefit*. It was showed that after the regression the two EoSs can predict density and compressibility factor (Z-factor) accurately, since the deviations are in both cases below 1%. The model that

better fits the experimental data is RKS one with an average deviation equal to 0.075%. In order to check the influence of the regressed parameters on the prediction of thermodynamic properties, a sensitivity analysis of the three parameters on density and Z-factor was carried out. The results showed that, for the H_2–CH_4 mixtures reported in this study and using the PR and RKS EoSs, the BIP parameter does not significantly influence the properties of interest, and density and Z-factor are mainly influenced by Ω_a and Ω_b. To further confirm this thesis, the optimization has been performed for one parameter at time first and then for both Ω_a and Ω_b with the BIP varying in the range -1 to 1. The results of this study showed that, while changing Ω_a and Ω_b highly influence the results of the optimization, varying the BIP does not affect the resulting optimal values of Ω_a and Ω_b.

Contents

List of Figures

List of Tables

Chapter 1

The Energy Dilemma

The worldwide main energy supply is achieved by fossil fuels and high-carbon emitters, such as oil and natural gas ((IEA, 2018); (IEA, 2019); (Mohanty, et al., 2021)). As a result of burning fossil fuels, increased emissions of greenhouse gases (GHG) into the atmosphere have adversely been contributing to global warming. At the same time, the dramatic growth of the worldwide population is causing an additional challenge for energy demand, which is expected to rise by about 40% by 2040 ((Ali, 2018); (Ali, et al., 2022); (Rahbari, et al., 2019)), calling for an urgent need for effective clean energy solutions.

Due to this increasing evidence of global warming in the present century, scientists at the UN Intergovernmental Panel on Climate Change have reached a consensus for reduction of greenhouse gas emissions, especially carbon dioxide (CO_2), to the atmosphere. This has also prompted steering committees of industrialized countries to assess their energy strategies based on mitigation of greenhouse gas emissions. By December 2016, 116 of the 196 parties had ratified the COP21 Paris agreement and pledged to take action to keep global warming below 2°C (United Nations, 2016). To meet this reduction target, global annual greenhouse gas emissions will need to be reduced by 85% by 2050 (IPCC, 2014) .

This reduction target is ambitious and will require nothing short of a global-energy revolution, particularly given the rapid growth of the global population (United Nations, 2016). With an anticipated 150% increase just in the electricity demand to 53.6 billion MWh (from 2010 to 2050) (World Energy Scenario, 2013), governments will be challenged to identify the best way to reduce greenhouse gas emissions while simultaneously ensuring economic competitiveness, growth and a secure energy supply.

This is also called the "Energy Dilemma": how is it possible to face a higher energy demand in order to provide energy for all but at the same time trying to follow a path of "decarbonization", reducing carbon emissions with a major transformation of the global energy system to fight climate change and pollution?

Therefore, the challenge of meeting rapidly growing energy demand while reducing harmful emissions of greenhouse gases is considerable.

Furthermore, this trend towards decarbonization, meaning a reduction in the carbon intensity of the worldwide energy use, has as direct consequence a change in the global energy mix.

The use of methane (CH_4) to generate electricity power is the step towards the reduction of CO_2 emissions that has been taken already since methane is the energy source which has the lowest CO_2 emissions per Kilowatt-Hour between the fossil fuels.

Renewable sources, such as wind power and solar energy, have emerged as promising clean alternatives (Gallo, et al., 2016) . This is because it produces only minute levels of GHG emissions and therefore they help combat the climate change caused by fossil fuel usage (Das, et al., 2001).

The contribution of such renewable energy (RE) sources to the energy mix has increased significantly in the last decade and it has become a primary source of electricity especially in Germany, Denmark, and Spain ((Wang, et al., 2012); (van der Roest, et al., 2020)).

However, their intermittency and seasonal nature depend on availability, geographic location, and atmospheric events resulting in a discrepancy between the energy supply and demand and leading to an uncontrollable energy output ((Gallo, et al., 2016); (Moustakas, et al., 2020); (Rahbari, et al., 2019); (Saidi, et al., 2020)). For example, in the spring of 2020 California curtailed up to 30000 MWh of excess renewable energy per month, but faced rolling blackouts in August because the gird was short on energy as there was no mechanism in place to store the excess energy for deployment during periods of high demand (EIA, 2021).

In order to adapt the fluctuating and non-dispatchable energy production from wind and solar resources to the actual demand, which is no longer feasible using conventional technologies, the energy industry is facing the need to store extremely large quantities of energy for long-term to seasonal periods.

The role of hydrogen (H_2) in supporting the renewable energy such as solar, wind and hydro electrical power generation is particularly interesting (Egeland-Eriksen, et al., 2021).

Since the supply of renewable energy is subject to fluctuating events (e.g., diurnal cycles, weather changes, seasonal changes in wind force), there might be an excess of energy when it is not necessary. What can we do with this extra energy? How can we store this electrical energy?

The elegant idea of storing RE in an energy carrier such as hydrogen, which is storable, transportable and utilizable can be a solution: the generation of hydrogen using excess or curtailed renewable energy can help to alleviate the drawbacks of a renewable energy system as it can be distributed directly to the end-user or stored as required for grid balancing at all scales.

1.1 Hydrogen Economy

The ‘hydrogen economy’, first coined by Prof. John Bockris during a talk he gave in 1970 at the General Motors Technical Center (Bockris, 2013), has created much excitement among scientists, economists (Rifkin, 2004), industrialists (Ball, et al., 2010), and heads of states/regions, including USA, EU ((The White House, 2003); (Borthwick, 2006); (European Commission, 2003)) and Japan (Ministry of Economy, 2016). However, the development and realization of such a hydrogen-based economy has been challenging due to the large-scale infrastructural investments needed.

While the potential of hydrogen has always been significant, the challenge in establishing a hydrogen economy has stifled progress. This is mostly because challenges had to be addressed simultaneously within all components of the hydrogen economy: production, storage, transportation and distribution, while strategic policy support had to be maintained.

Nevertheless, nowadays hydrogen economy is growing: building on important technical advances in hydrogen technologies, as well as several public– private partnerships (e.g. H2USA (H2USA, 2013), FCH Joint Undertaking in Europe (European Union) and Japan’s partnership with Toyota (Ministry of Economy, 2016)), the role of hydrogen in enabling a cost-effective transition to a low-carbon energy system is being appraised with greater coordination.

In this scenario, the concept of a Hydrogen-based Energy Storage Systems (HydESS) is gaining potential as a cost-effective solution for large-scale RE storage, transport and export; the literature reveals that HydESS are leading the way towards a 100% renewable energy economy. Therefore, there is a growing body of literature that recognizes the importance of HydESS and of utilizing hydrogen as an energy carrier to enable the shift to carbon-free energy generation and utilization. In fact, hydrogen can support this transition by replacing natural gas for domestic and industrial uses; replacing coal and natural gas for power generation; replacing fuel oil and gasoline to decarbonize transport and facilitating increased renewable energy by acting as an energy carrier to balance supply and demand.

Hydrogen is considered a clean energy fuel that can provide a sustainable energy market and overcome intermittent production issues (Mahlia, et al., 2014) since hydrogen alone can facilitate the storage of large quantities of energy to balance out long periods of poor wind power supply and seasonal fluctuations. The large scale storage of energy using as energy carrier H_2 will be the only means in the long term to provide electrical energy in quantities and at a quality level consumers are accustomed to, in parallel to the downscaling of major capacities from fossil power plants and nuclear power stations.

So, fuelled by concerns about urban air pollution, energy security, and climate change, the notion of a “hydrogen economy” is moving beyond the realm of scientists and engineers and into the lexicon of political and business leaders. In fact, among the list of proposed alternative energy sources, hydrogen appears to be the most promising large-scale fuel due to its efficient storage over time and clean combustion (Dunn, 2002).

Currently, H_2 is produced from various sources, depending on economics and feasibility (Dawood, et al., 2020). For instance, green H_2 is produced through an electrolysis process or biomass gasification. Similarly, blue H_2 (the main source of H_2 production) is produced from natural gas through steam methane reforming and coal gasification (Dawood, et al., 2020). The main types of H_2 production and expected operating conditions of the H_2-based industry are described in Figure 1.1.

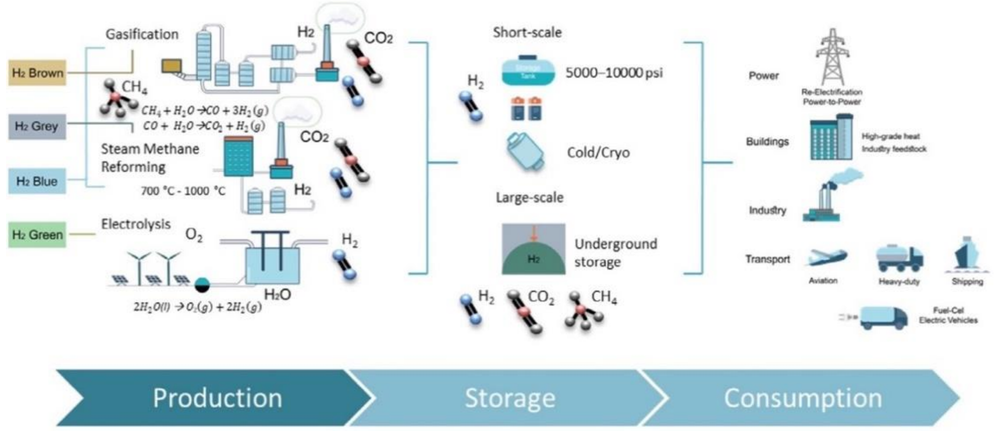

Figure 1.1: Hydrogen (H_2)-based industrial chain from various production processes of H_2 types to the consumption sectors for decarbonization. **(Alanazi, et al., 2022)**.

1.2 Hydrogen pathways in renewable energy integrated systems

Hydrogen allows for pollutant-free power generation and reduces the world's dependence on fossil fuels. Hydrogen is considered particularly important in the transport and power supply sectors, which are heavily dependent on hydrocarbons such as oil and natural gas.

The injection of hydrogen into the natural-gas grid is an extensively discussed technology for a step-by-step decarbonization of heat and power supply. The electrolytic production of hydrogen using excess electricity from renewable energy sources can contribute to a more flexible energy supply and a reduction of the demand of carbonaceous primary energy (Beckmüller, et al., 2021). This supply pathway is called "power-to-gas" (P2G) (Figure 1.2).

In this supply pathway electricity is used to generate hydrogen via electrolysis. The hydrogen generated by this process is then either injected into the gas distribution grid (mixed with natural gas or used on its own) or transformed to synthetic CH_4 in a subsequent methanation step. The methanation step combines hydrogen with captured CO_2 in a methanation reactor (either thermochemical or biological) (Götz, et al., 2016). The hydrogen gas produced can be stored in both natural gas pipelines and storage sites. This option is gaining growing interest, especially because it can be combined with biogas plants being used for synthetic CH_4 production, which enables direct use of the CO_2 from the biogas for conversion into CH_4 with hydrogen from water electrolysis (Institute of Chemical Engineering). This combination, with Carbon Capture and Storage (CCS) added, is also interesting for the concept of negative CO_2 emissions (U.S. Department of Agriculture, et al., 2014).

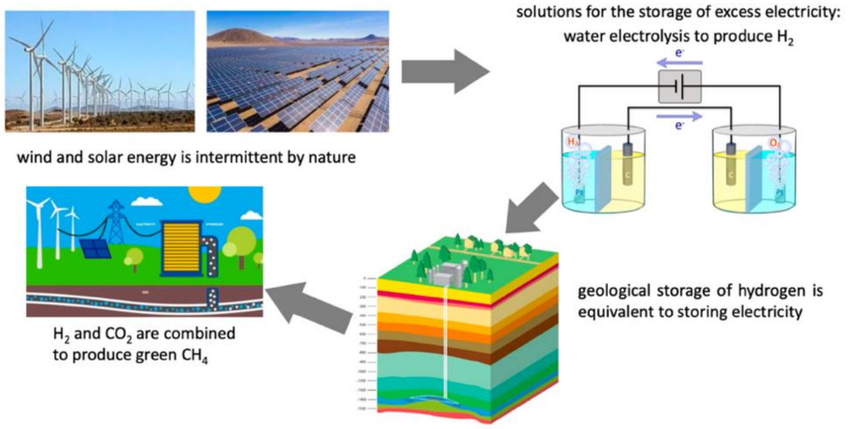

Figure 1.2: Power-to-gas supply pathway. (Verga, 2022).

Other supply pathways can be followed, as illustrated in Figure 1.3.

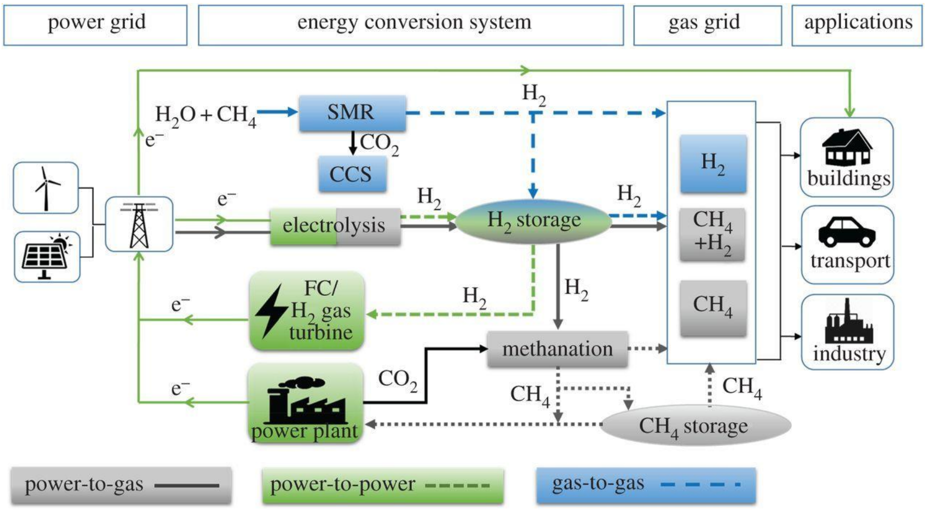

Figure 1.3: Schematic diagram showing the three main energy conversion pathways (power-to-gas, power-to-power and gas-to-gas) in a renewable energy integrated energy system. (Brandon, et al., 2017).

In the power-to-power (P2P) supply pathways, electricity is used to generate hydrogen via electrolysis. The hydrogen generated by this process is then stored in a pressurized tank (for small- scale applications) or an underground cavern (for grid-scale applications) or re-electrified when needed using a fuel cell (kW to MW scale) or a hydrogen gas turbine (multi-MW scale).

In the gas-to-gas (G2G) supply pathways, steam methane reforming (SMR) is performed: this is an established process for producing hydrogen from natural gas, and approximately 95% of hydrogen produced worldwide is produced through SMR technology. To lower the carbon footprint, CCS technology is needed to capture the CO_2 released as the by-product. This is the pathway considered by the H21 Leeds City Gate study for decarbonizing heat in the UK (Northern Gas Networks, et al., 2016).

1.3 Underground Gas storage

A vast expansion of the H_2 economy requires a massive storage capacity of Giga to Terawatt-scale compared to the limited storage and discharge capacity of the existing surface facilities (i.e., tanks and pipelines) ((Crotogino, et al., 2010); (Panfilov, 2010); (Pfeiffer, et al., 2017); (Taylor, et al., 1986)). Geological storages (known as Underground Gas Storage (UGS) Systems, in particular in case of hydrogen storage it's known as Underground Hydrogen Storage (UHS)), such as deep aquifers, depleted oil and gas reservoirs, can play a fundamental role since geological formations have storage capacities which are vast and abundant (Muhammed, et al., 2022).

The concept of underground storage is not something new since it has been investigated and now largely exploited for the storage of natural gas in order to satisfy the need for a balance between constant supply and fluctuating – seasonal and daily – energy demand.

Employing deep reservoirs as a gas storage has a long and prosperous history. We may consider Canada as a pioneer country in this field, where the first successful UGS was built in 1915 in the partially depleted gas field in Welland County, Ontario ((Foh, et al., 1979); (Lord, 2009)). About one year later, the second oldest natural gas storage (Zoar field) was built in New York (USA), which is still in operation today (IGU, 2018). These countries were the first to perceive the economic potential and feasibility of underground storage and laid the technological foundations for this industry.

The main factors in the development of gas storage activities were the growth of the gas market, the gradual discovery of new gas production fields associated with the need for transport to consumption sites and seasonal fluctuations in gas consumption (Haddenhorst, et al., 1989). An important increase in UGS number was registered in the post-World War II era, which was mainly induced by technological constrictions with piping capacity. Further progress in gas storing was recorded in Kentucky in 1946 where the aquifer was first employed as an UGS (Foh, et al., 1979). Solution-mined caverns in Michigan were first used as UGS in 1961 and the salt dome in Mississippi was first employed in 1970 as backup for hurricane disruption (Buzek, et al., 1994).

In 2018, there were 689 UGS facilities in operation worldwide (Figure 1.4).

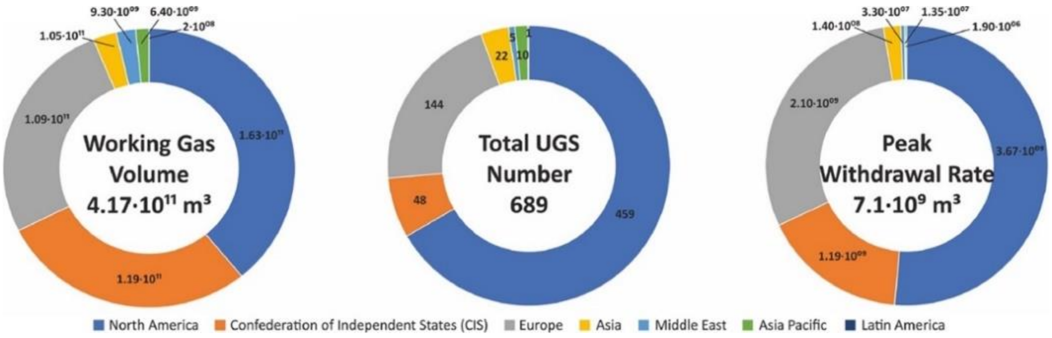

Figure 1.4: Underground Gas Storage in different regions: total number, stored volume, peak withdrawal capacity. (IGU, 2018).

1.3.1 Types of UGSs

Nowadays several types of UGSs are used ((Zivar, et al., 2021); (Lord, 2009); (Falzolgher, et al., 2005)). Underground storage of natural gas requires specific geological conditions as geological structures and hydrocarbon traps which must be sealed or separated enough from its surrounding to prevent gas leakage.

In terms of storage systems, the UGS can be divided into three types of facilities (Zivar, et al., 2021): depleted oil and natural gas reservoirs, aquifers and caverns being created in salt diapirs (Foh, et al., 1979). The first two types are storage systems in porous/fractured media.

The most common natural gas storages have been developed in depleted natural gas reservoirs (Figure 1.5) because of its economic feasibility and already available techniques and infrastructure. Aquifers are usually preferred in areas where hydrocarbon fields or reservoirs are missing; similarly, the use of caverns as storage system is based on local geological options (availability or not of depleted fields or aquifers).

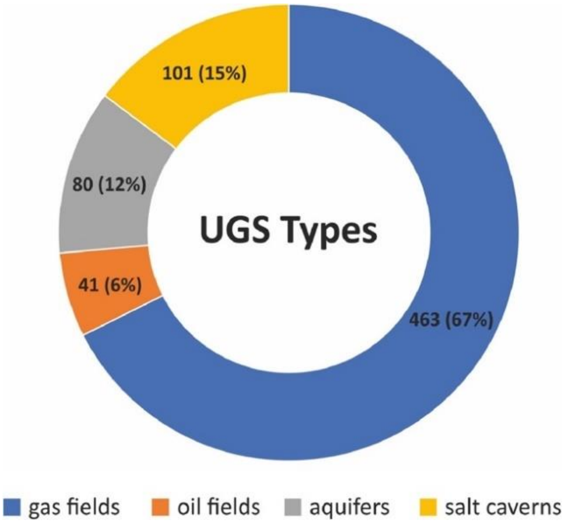

Figure 1.5: The number of underground gas storages by type and percentual proportion. (IGU, 2018).

1.3.1.1 Depleted gas or oil reservoirs/fields

Depleted fields dominate stored gas volume with a share of about 70% of total gas volume stored in UGSs. In total, 504 UGSs of this type were in use worldwide (Figure 1.5) (IGU, 2018). General considered parameters for the establishment of new reservoirs are based on geological data analyses and physical parameters of geological structures. Factors to be considered are size and shape of the geological structure, size of aquifer layer, gas-water phase (in case of depleted or partly depleted storages), properties of reservoir and surrounding rock.

Most important petrophysical parameters are:

i. porosity (the higher the better),

ii. permeability which expresses the attitude of a porous medium to be crossed by a fluid (higher permeability improves fluid transport in the reservoir),

iii. water saturation (high water saturation reduces the stored gas volume).

Another important factor is the drive mechanism which indicates how the gas moves through the reservoir. It depends on aquifer ability to move gas-water interface during filling or emptying phase. In stable depletion drive reservoir, the water-gas interface is rather stable during both injection and extraction periods. In such reservoirs the performance is high and minimal problems in production occur. The opposite case is a water driven reservoir where the performance is limited because of water production and its rising in production phase. In water driven reservoirs it is necessary to push water downward with high pressures (Falzolgher, et al., 2005).

1.3.1.2 Aquifers

Aquifers are an option to depleted reservoirs. For aquifers, a basic requirement is a porous rock layer with a proper anticlinal or adequate shape and suitable petrophysical parameters, filled with water at a depth of hundreds to a few thousand meters (Beckman, et al., 1995). The required geological properties of an aquifer are similar to depleted gas reservoirs.

Establishing UGS in an aquifer requires geological investigation and higher investment. Emphasis is mainly placed on suitable tightness of caprock vertically and a shape of the structure with a spill point position preventing gas leakage. These criteria must be precisely determined and confirmed in advance.

In 2018, there were 80 aquifer UGS facilities active worldwide (Figure 1.5) (IGU, 2018). Examples of worldwide potential storing sites are found in Germany, France, Czech Republic, Canada and Poland (Zivar, et al., 2021).

1.3.1.3 Salt Caverns

The last option is caverns leached in suitable salt formations. Salt formations occur in two forms, as domes characterized by greater depths than shallower located salt bedded deposits. New caverns are obtained through solution mining ((Lemieux, et al., 2019); (Michalski, et al., 2017)), dissolving the salt formations by injecting fresh water and extracting the formed saline water (Lord, 2009). The obtained cavern is enclosed by a salt layer, which forms an impermeable barrier and prevents gas leakage. It has special geological features as tightness and suitable mechanical properties with chemical resistivity of salt by this creating mechanical stability suitable for medium as well for short-term storage. In comparison with other types of underground storages, the cost to build such caverns are definitively lower (Zivar, et al., 2021).

UGS in salt caverns is rising and is currently responsible for about 9% of the total volume of stored underground gas. In total, 101 salt caverns were in use (Figure 1.5) worldwide in 2018 (IGU, 2018). The occurrence of this type is abundant in the US, in the region of the Great lakes where there is no other option of storing, and along the Gulf coast where there is plenty of salt domes (Lord, 2009). Some are found in Canada and in Europe, comprising the following countries: UK, USA, Romania, Germany, Poland, Turkey and Denmark (Zivar, et al., 2021).

1.3.2 Underground CO_2 storage

The underground storage has been exploited also in order to face the problem of reducing CO_2 emissions with the carbon capture and storage technique.

Carbon capture, utilization and storage (CCUS) is a mitigation measure that prevents large amounts of CO_2 from emission sources such as energy-intensive industries (such as cement, lime, steel and chemicals) and power plants, to be released into the atmosphere, supporting Europe’s pathway to achieving climate neutrality. The European Strategic Energy Technology Plan (SET-Plan), whose aim is to accelerate the deployment of low-carbon technologies, to improve new technologies and to bring down costs by coordinating national research efforts, defined ten priority areas, covering a wide range of technologies including CCUS, wind, solar, geothermal, renewable heating and cooling, and biofuels. An Implementation Working Group (CCUS SET-Plan) was established to help the progress of Research and Innovation (R&I) activities required to achieve the 2030 targets for CCS and CCU agreed by the European Commission, SET- Plan countries, and industry. In fact, CCUS can contribute around 14% of total energy-related CO_2 reductions by 2050, compared to a ‘do nothing’ approach (IEA, 2014).

As shown in Figure 1.6, there is an increase in the interest in this type of technology and there are lots of projects which has been developed in order to increase the capacity of CCS projects.

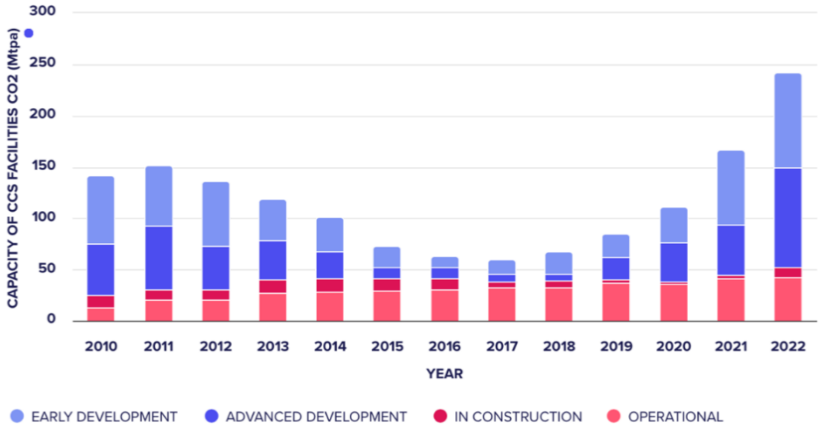

Figure 1.6: Pipeline of Commercial facilities since 2010 by capture capacity (Mtpa). (Global CSS Institute, 2022).

*2021 capacities adjusted to reflect this year's change to how capacity tonnages are interpreted, to facilitate comparison with 2022 figures.

CCUS technology involves capturing CO_2 produced by the power sector (fossil fuel, ...) and energy-intensive industries, compressing it for transportation by pipelines, by trucks and/or by ships (design pressure 100-200 bar) and:

- selling it to users such as O&G industry for Enhanced Oil Recovery or other industrial processes or

- injecting it as a supercritical fluid (CO_2 pressure > 102 bars, T>35°C), deep into a rock formation at a carefully selected and safe site, where it is permanently stored (Figure 1.7).

Permanent and safe CO_2 storage is achieved deep underground, using natural processes that trap CO_2, similar to how oil and gas is trapped for millions of years. The CO_2 is injected as a supercritical fluid (CO_2 pressure > 102 bars, T>35°C), deep into a rock formation (>700m) at a carefully selected and safe site, where it is permanently stored.

The first facility for CO_2 geological sequestration has been developed in Sleipner (Norway) in 1996; nowadays there are 26 large-scale operating facilities worldwide (2 in Europe) for carbon capture and storage (40 million ton/year) and many under way.

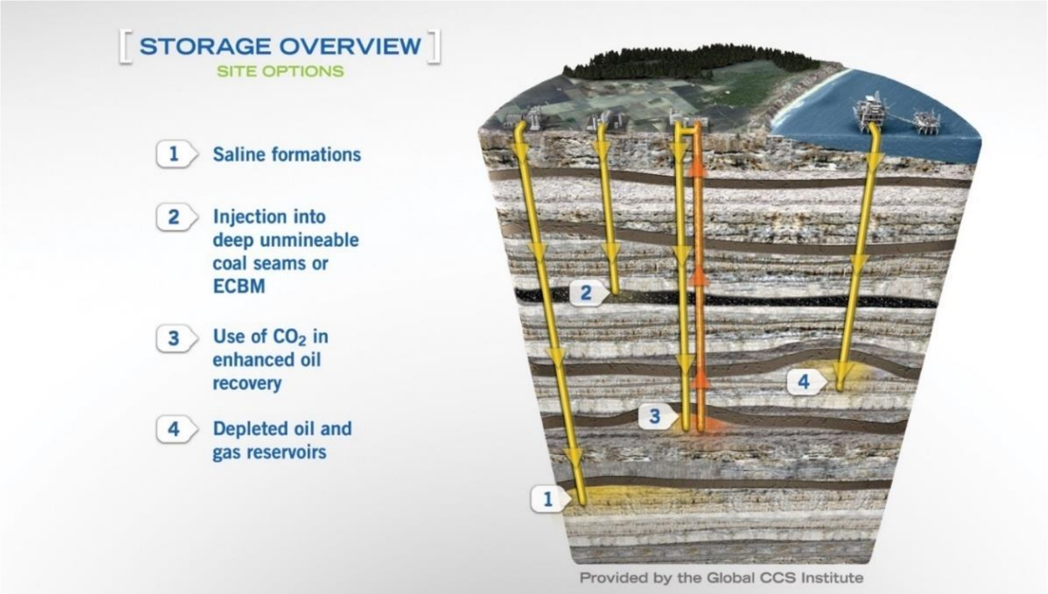

Figure 1.7: Storage Overview. (Global CSS Institute, 2022).

1.3.3 Underground H_2 storage

Despite the extensive experience in natural gas storage and other sorts of subsurface storage activities, the amount of underground hydrogen experiences is sparse, as shown in the Table 1.1.

Table 1.1: Historical record of underground hydrogen storage projects. (town gas contains hydrogen, carbon monoxide, carbon dioxide, methane, nitrogen and volatile hydrocarbons). **(Heinemann, et al., 2021)**.

Location	Storage Type	Gas Composition	Storage Volume (m^3)	Mean depth (m)	Status	Year
Teesside, UK	*Salt cavern (bedded salt)*	*95%* H_2 *3-4%* CO_2	*210.000*	*350*	*Active*	*1972*
Clemens, USA	*Salt cavern (domal salt)*	*95%* H_2	*580.000*	*1000*	*Active*	*1983*
Moss Bluff, USA	*Salt cavern (domal salt)*	H_2	*566.000*	*1200*	*Active*	*2007*
Spindletop, USA	*Salt cavern (domal salt)*	*95%* H_2	*906.000*	*1340*	*Active*	*2017*
STOPIL-H2, Etzel, France	*Salt cavern*	-	*570.00*	-	*Under development*	-
Kiel, Germany	*Salt caverns*	*Town gas*	$7.8*10^7$	*1330*	*Repurposed as natural gas storage*	-

Bad Lauchstädt, Germany	*Salt cavern & porous reservoir (depleted gas field)*	*Town gas*	$6.7*10^8$	*800*	*Repurposed as natural gas storage*	-
Underground Sun Storage, Austria	*Porous reservoir (depleted field)*	*10%* H_2	*115.000*	*1200*	*Under development*	*2017*
Yakshunovskoe Field, Russia	*Porous reservoir (depleted field)*	-	-	-	*Active*	*2010*
Hychico, Argentina	*Porous reservoir (depleted field)*	*10%* H_2	*750.000*	*815*	*Under development*	*2010-2018*
Kirchheiligen, Germany	*Porous reservoir (depleted field)*	*Town gas*	$2.4*10^8$	*900*	*Repurposed as natural gas storage*	-
Hähnlein, Germany	*Porous reservoir (aquifer)*	*Town gas*	$1.6*10^8$	*500*	*Repurposed as natural gas storage*	-
Eschenfelden, Germany	*Porous reservoir (aquifer)*	*Town gas*	$1.68*10^8$	*600*	*Repurposed as natural gas storage*	-
Engelborstel, Germany	*Porous reservoir (aquifer)*	*Town gas*	-	-	*Decommissioned*	*1955-1998*

Ketzin, Germany	*Porous reservoir (aquifer)*	*Town gas*	$1.30*10^8$	*250-400*	*Decommissioned*	*1964-2000*
Lobodice, Czech Republic	*Porous reservoir (aquifer)*	*Town gas*	$1*10^8$	*400-500*	*Repurposed as natural gas storage*	*1965-1995*
Beynes, France	*Porous reservoir (aquifer)*	*Town gas*	$3.3*10^8$	*430*	*Repurposed as natural gas storage*	*1956-1972*
HyBRIT, Sweden	*Rock cavern*	*100% hydrogen*	*100*	*30*	*Under development*	*2016*

Underground geological formations such as salt caverns, aquifers and depleted natural gas or oil reservoirs are considered as the most viable options for bulk hydrogen storage. (Amid, et al., 2016).

In particular, underground salt cavern storage has been identified as one of the most promising geological storage technologies for hydrogen, due to their technological maturity, fast cycling flexibility and large volume storage capacity (Energy Technologies Institute, 2015). Salt caverns are cavities solution mined within suitable (halite-dominated) salt formations using fresh water to dissolve the salt rock (Li, et al., 2019). The properties of the surrounding salt include low permeability and such high sealing capability, inert chemical behavior with respect to hydrogen and favorable mechanical properties that provide the ability to accommodate repeated withdrawal and extraction cycles (Evans, et al., 2021), allow for the secure storage of fluids over long periods of time (Lux, 2009).

Practical experience in hydrogen storage in salt caverns is limited to three commercial storage operations, one in the UK and three in the US, that have been providing hydrogen for the chemical industry since the 1970s and one salt cavern in Kiel Germany that stored town gas with 62% hydrogen in the 1960's and 1970's ((Crotogino, 2016); (Panfilov, 2016)). The experience from these operations in both bedded and domal salt highlights that hydrogen can be securely stored and recovered from salt caverns over many decades (Tarkowski, 2019).

Cavern storage of hydrogen has seen increased interest in the last decade, with new operations being developed in the UK (SSE thermal and Equinor, Aldbrough), US (ACES, Utah), Germany (HYPOS, Bad Lauchstadt), Netherlands (Gasunie, Veendam), and France (HyGeo, Nouvelle- Aquitane and HyPSTER/Stopil_H2, Etrez) (Le Duigou, et al., 2017). These projects are considering both new caverns and importantly the repurposing of existing caverns, indicating salt caverns offer rapid storage capacity through conversion of existing assets to hydrogen storage.

Summarizing, multiple studies have analyzed the potential of salt caverns for hydrogen storage in different areas of the world in the last decade ((Bai, et al., 2014); (Caglayan, et al., 2020); (Iordache, et al., 2014); (Lemieux, et al., 2020); (Liu, et al., 2020); (Michalski, et al., 2017); (Ozarslan, 2012); (Tarkowski, et al., 2018)) demonstrating that this established gas storage technology will be well suited to providing a large-scale storage option for hydrogen.

Geological formations such as saline aquifers and gas fields which are constituted by a combination of porous rocks overlain by impermeable mudstones or evaporites which form a sealing caprock which have been proven to securely contain gasses over millennia could be the alternative candidates to provide inter-seasonal, TWh scale hydrogen storage.

Important experience of hydrogen storage in saline aquifers was gained during aquifer storage of town gas in the 1950's through to the 1970's: aquifer storage of town gas occurred in France (Beynes), Czech Republic (Lobodice) and Germany (Engelborstel, Bad Lauchstaedt). During decades of commercial operation, there were no reports of containment failures from these town gas storage sites; however, some changes in the stored gas composition are thought to have occurred as a result of bio-geo-chemical reactions within the storage reservoirs ((Buzek, et al., 1994); (Kruck, et al., 2013); (Panfilov, 2016)). Notable is the generation of H_2S, likely due to abiotic pyrite reduction, as well as methane generation from methanogenic bacteria within the reservoir.

While hydrogen storage within porous media has recently seen growing attention, the only two pilot studies that have injected and recovered hydrogen to date are green methane projects in Austria and Argentina. These storage projects inject a mixture of natural gas with 10% hydrogen produced from renewable energy into sandstone reservoirs for green methane production by coupled CO_2/H_2 injection into reservoirs hosting methanogenic bacteria.

Two more geological options, engineered rock caverns and abandoned mine shafts, have been proposed as options of the storage of hydrogen. Engineered rock caverns involve the excavation of cavities in extremely tight and stable hard rock formations (Crotogino, 2016). In certain circumstances, abandoned mine shafts could be repurposed for the storage of energy fluids, with the inclusion of engineered barriers, such as cement or resin at the rock boundary.

These two options have raised much less interest than salt caverns or saline formations, mainly due to the technical challenges associated and the suitability requirements of the host rocks to accommodate the storage facility, however the Swedish HyBRIT project is developing a 100m^3 hard rock cavern for hydrogen to be used in the decarbonization of steel making.

In summary, salt cavern stores are considered as a mature option today. Further analysis and pilot studies are needed to demonstrate that the other potential large-scale storage options, such as depleted oil/gas fields, rock caverns and aquifers, could be practically and economically viable.

Chapter 2

Review of Equations of State

The evaluation of the properties of fluids is often a demanding task in real – life projects. Both pure fluids and mixtures behave differently than what is predicted by the traditional Equations of State (EoS), especially when the interactions between the molecules are strong or when the fluids are subjected to near-critical conditions. This justifies the need for developing estimates that can accurately predict the thermodynamic and volumetric properties of the fluids in those circumstances.

2.1 Properties of hydrogen – containing mixtures

As discussed in the Chapter 1, the subsurface storage of hydrogen provides a potential solution for load-balancing of the intermittent electricity production from renewable energy sources.

The storage of gas in the subsurface as chemical energy storage, whether as natural gas or hydrogen (the working gas), requires a cushion gas (30−70% of the total gas storage volume (Flanigan, 1995)) to prevent brine from entering the production stream and to maintain the required reservoir pressure ensuring deliverability ((Ali, et al., 2021); (Hosseini, et al., 2022); (Iglauer, et al., 2021)).

As depleted gas fields are being considered as storage sites for subsurface hydrogen storage, the in situ gas could be used as cushion gas and hence the working and cushion gasses will be of different compositions (Amid, et al., 2016). For gas storage in saline aquifers, where there is very little in situ gas present, there is a requirement to use a cushion gas that is significantly cheaper than the working gas. Considered options for aquifer storage cushion gasses are nitrogen, due to its low price, and CO_2 due to its high compressibility and potential for secure storage of this greenhouse gas ((Pfeiffer, et al., 2015); (Oldenburg, 2003); (Misra, et al., 1988)).

During the injection/production cycles, mixing of the gas components is inevitable (Figure 2.1) and is determined by parameters such as mobility ratios, density differences, molecular diffusion and mechanical dispersion (Feldmann, et al., 2016). The numerical simulation of any storage scenario must confirm that the working gas can be produced with minimal cushion gas contamination. Therefore, if the cushion gas and working gas are of different compositions, the accurate quantification of the cushion gas/working gas mixing zone is of paramount importance since, once mixing takes place, the different gaseous components will alter the properties of the gas and introduce significant uncertainty into the expected behaviour of the injected, stored and produced gas, as shown for different gas storage applications ((Ma, et al., 2019) ; (Oldenburg, et al., 2013)).

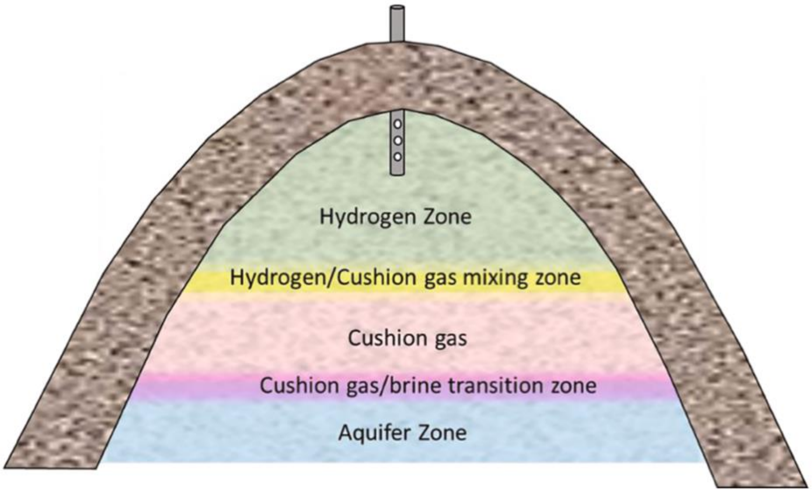

Figure 2.1: Illustration of hydrogen storage in an underground geological formation with a cushion gas and an aquifer zone. (Alanazi, et al., 2022).

For gas storage modelling, accurate thermodynamic reference data for relevant fluid mixtures, which can either be directly imported into fluid flow modelling software or can be used to confirm existing reservoir engineering software outputs, is an important tool to enhance the compliance for scenario modelling results. Furthermore, the thermodynamic data for hydrogen-containing systems can enable scientists to have a deeper understanding of reactive flow through porous media during the hydrogen storage process. Another target in a hydrogen-based economy is to establish a fundamental understanding of metering technologies and the flow measurement principles behind them. In this regard, the thermo-physical properties of hydrogen mixed gases are crucial to understand and model hydrogen transportation and flow measurement processes.

Therefore, thermo-physical properties of hydrogen-containing gas mixtures over a wide range of pressures and temperatures are pivotal to the design and optimization of hydrogen production units, transportation, and storage process. For this reason, significant effort has been made to investigate the thermodynamic properties of hydrogen-containing mixtures (see Table 2.1).

Table 2.1: Database of available experimental thermodynamic properties data in the literature for hydrogen-containing systems along with the temperature, pressure and composition range with respect to hydrogen for each binary/ternary system. (Hassanpouryouzband, et al., 2020).

No.	System: H_2 (1st Component) + X (2nd Component and beyond)	Property Type	Pressure Range (MPa)	Temperature Range (K)	x_1 range (1st component liquid mole fraction)	y_1 range (1st component gasmole fraction)
1	CH_4	VLE/Solubility/Density/Viscosity/Compressibility/Thermal Conductivity	0.22–141.40	66.89–350.00	0.002–0.859	0.034–1.000
2	C_2H_6	VLE/Compressibility	0.27–562.50	83.00–283.15	0.002–0.800	0.085–1.000
3	C_3H_8	VLE/Compressibility	0.69–55.16	93.15–366.40	0.001–0.669	0.110–0.999
4	C_4H_{10}	VLE/Solubility	2.07–53.43	144.26–394.25	0.008–0.341	0.213–0.999
5	C_5H_{12}	VLE/Solubility	0.69–27.59	273.15–463.15	0.004–0.259	0.373–0.997
6	C_6H_{14}	VLE/Solubility	1.24–68.95	277.59–506.48	0.011–0.700	0.100–0.998
7	Cyclo-C_6H_{14}	VLE/Solubility	0.10–69.04	293.15–523.15	0.000–0.367	0.549–0.997
8	N_2	VLE/Solubility/Heat Capacity/Compressibility	0.13–101.33	20.10–122.04	0.012–0.620	0.082–1.00
9	CO_2	VLE/Viscosity/Density/Thermal Conductivity	0.93–191.80	219.90–298.15	0.001–0.744	0.043–0.934
10	H_2S	Solubility	1.01–5.07	243.15–273.15	0.002–0.020	0.322–0.910
11	CO	VLE/Viscosity/Thermal Conductivity/Density	0.13–5.07	20.10–122.04	0.012–0.731	0.082–1.00
12	$CH_4 + C_2H_6$	VLE	0.27–562.50	83.00–283.15	0.002–0.800	0.085–1.000
13	$C_3H_8 + CO$	VLE	0.69–20.68	88.15–348.15	0.005–0.107	0.034–0.847
14	$CH_4 + CO_2$	VLE	6.90–27.60	227.35–258.15	0.004–0.259	0.373–0.997
15	$CH_4 + CO$	VLE	2.90–5.00	120.00–140.00	0.000–0.110	0.000–0.926
16	$C_5H_{12} + CO_2$	VLE	6.90–27.60	273.15–323.15	0.004–0.259	0.373–0.997
17	$N_2 + CO$	VLE	0.003–22.80	58.15–122.04	0.012–0.930	0.082–1.00
18	$CH_4 + N_2$	VLE	3.40–10.00	80.00–144.00	0.009–0.720	0.060–1.00

However, while the knowledge of pure H_2 thermodynamics is well established ((Michels, et al., 1941); (Seward, et al., 1981)), published properties of gas mixtures in relation to geological hydrogen storage do not cover the full range of additional gasses and often do not encompass the pressures and temperatures encountered within the hydrogen storage system (Hassanpouryouzband, et al., 2020). Therefore, reliable equations of state (EoSs) are needed to predict these properties.

This work is focused on the investigation of the properties of natural gas and hydrogen mixtures; in fact blending H_2 with natural gas (NG) for injection into depleted gas/oil reservoirs, which are already used for NG storage, is considered a good option due to the lower initial capital cost and investment needed, and potential lower operating costs.

2.2 Overview of EoSs

Equations of state (EoSs) are widely used in the oil and gas industry to predict the volumetric and phase behaviour of petroleum fluids. An EoS of a substance usually refers to an expression that describes the relationship between pressure, temperature, and volume.

An EoS is desired to represent the volumetric behaviour (along with the vapor/liquid equilibrium (VLE) and with the thermal properties) of the pure substance in the entire range of volume both in the liquid and in the gaseous state.

Numerous EoSs have been proposed to represent the phase behaviour of pure substances and mixtures in the gas and liquid states since Van der Waals introduced his expression in 1873 and these equations have been review extensively in the literature ((Economou, 2010); (Valderrama, et al., 2003); (Mangold, et al., 2019)). These equations were generally developed for pure fluids and then extended to mixtures through the use of mixing rules.

There are many examples in the literature where EoSs are compared. The findings all highlight the fact that there is currently no “all in one” EoS that will give the best prediction of all thermodynamic properties of different types of reservoir fluids. It seems that some EoSs can do better than the others only for certain reservoir fluid types and some EoSs are advantageous for particular properties.

From a theoretical base, for an ideal gas:

$$pv = RT, \tag{2.1}$$

where $v[m^3/kg]$ is the specific volume, $R[kJ/kgK]$ the specific gas constant (whose value change according to the units used), $p[Pa]$ the pressure and $T[K]$ the temperature.

When applied to real gases, the ideal gas equation (Eq. 2.1) may present large deviations. For that reason, it is common practice to introduce experimental data to improve the accuracy of the predicted results. The resulting equations are empirical and semi-empirical relationships.

2.2.1 Corresponding States Principle (CSP)

According to Van der Waals (van der Waals, 1913), in a paper published in 1873, the corresponding states principle indicates that all fluids (pure substances or mixtures), when compared at the same non-dimensional reduced temperature ($T_r = T/T_{cr}$) and non-dimensional reduced pressure ($p_r = p/p_{cr}$), present a behaviour that deviates from the ideal gas by approximately the same degree.

In a general form, the corresponding states principle can be first expressed as a 2-parameter function (Poling, et al., 2001):

$$p_r = p_r(v_r, T_r), \tag{2.2}$$

where v_r and T_r are the reduced specific volume and the reduced temperature, respectively.

Actually, this principle works only for one group of substances at a time, whose molecular constitution is relatively similar. However, to account for the situations when that is not the case, a third parameter is introduced into Eq. 2.2, the compressibility factor (z), defined as (Poling, et al., 2001):

$$z = \frac{pv}{RT}. \tag{2.3}$$

The compressibility factor may also be expressed in a non-dimensional form (Eq. 2.4):

$$z = z_C \frac{p_r v_r}{T_r}, \tag{2.4}$$

given the critical compressibility factor (Eq. 2.5) and the reduced one (Eq. 2.6):

$$z_C = \frac{p_C v_C}{RT_C}, \tag{2.5}$$

$$z_r = \frac{z}{z_C} = \frac{p_r v_r}{T_r}. \tag{2.6}$$

According to Bejan, pure substances can be described with a 2-parameter CSP and a compressibility factor (Bejan, 2006). That way, it is possible to eliminate v_r from the previous equation to obtain the following 3-parameter relationship:

$$z = z(T_r, p_r, z_c), \tag{2.7}$$

where z_c may act as the parameter related to the molecular constitution.

As a consequence, many substances can be represented in the same generalized graphic. The following graphic (Figure 2.2) was obtained experimentally by Nelson and Obert (Nelson, et al., 1954) for several substances from experimental PVT data. It can be used for most substances, but it should not be used for strongly polar fluids, helium, hydrogen, or neon unless special, modified critical constants are used (Poling, et al., 2001).

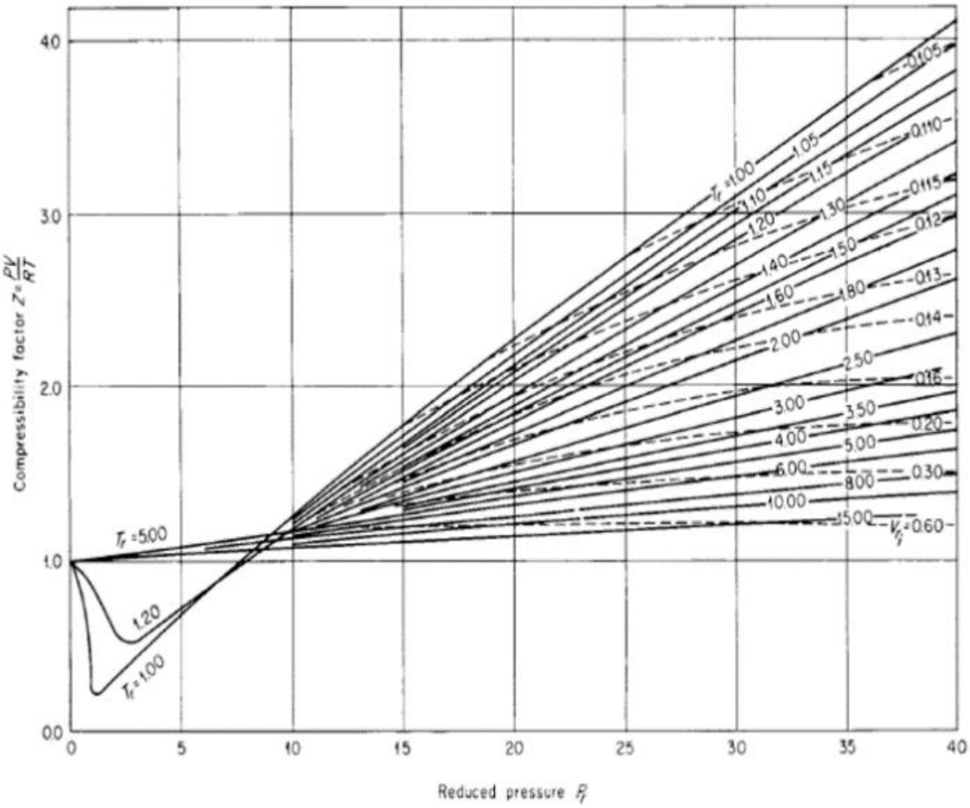

Figure 2.2: Generalized compressibility factor for all $p_r, v_r = v/(RT_c/p_c)$. (Nelson, et al., 1954).

2.2.2 Acentric Factor

An alternative for the third parameter was proposed by Pitzer et al. (Pitzer, 1955) with the introduction of the Pitzer acentric factor ω, defined as:

$$\omega = -\, log_{10}\, p_r - 1\, for\; T_r = 0{,}7 \qquad (2.8)$$

That expression assumes the value ω=0 for the "simple fluids", that were defined by Pitzer as the permanent gases with heavy molecules, such as Ar, Xe and Ne (Bejan, 2006).

The practical meaning of the Pitzer acentric factor is that each pure substance has a different value of ω that increases with the fluid polarization. Thus, highly polarized fluids, such as H_2O and NH_3, have high Pitzer acentric factors.

Finally, the 3-parameter CSP can be rewritten as:

$$z = z(T_r, p_r, \omega) \qquad (2.9)$$

2.2.3 Cubic Equations of State

Cubic Equations of State (EoSs) are a general class of equations where the specific volume has powers no higher than three. They are classified as analytical equations because they have a closed-form solution. That is important when the computational effort needs to be minimized, because iterative solutions tend to be much more time consuming. Regarding its use, the cubic EoS are accurate for predicting a fluids' characteristics far from critical conditions - for pure simple substances and non-polar mixtures. That occurs because some of the assumptions used for their development are not valid in near-critical conditions or for strong polar substances.

Daridon et al. (Daridon, et al., 1993) proposed a general formalism of the cubic EoS based on the work by Schmidt and Wenzel (Schmidt, et al., 1980), as indicated in Eq. 2.10:

$$p = \frac{RT}{v-b} - \frac{a(T)}{v^2 + ubv - wb^2}, \qquad (2.10)$$

where R is the universal gas constant, v denotes the molar volume, and u and w are parameters of the generalized EoS. In addition, a and b represent constants that depend on the component, where a represents the attraction between the molecules, whereas b defines the volume of a pure component as a function of critical temperature (T_c) and critical pressure (p_c). The assumption is that b is independent of temperature, whereas a is a function of temperature, allowing a more accurate calculation of the vapor-phase pressure of a pure component (Mathias, et al., 1991).

Several efforts have been exerted to derive mathematical formulations for the temperature dependence term ($\alpha(T)$) with a high level of consensus ((Mangold, et al., 2019); (Mathias, et al., 1983); (Twu, et al., 1991)).

The EoSs parameters are calculated according to the following equations:

$$a(T) = a_c \alpha(T), \tag{2.11}$$

where

$$a_c = \Omega_a \left(\frac{R^2 T_C^2}{p_C} \right) \tag{2.12}$$

and

$$b = \Omega_b \left(\frac{R T_C}{p_C} \right); \tag{2.13}$$

Ω_a and Ω_b are unitless constants that vary based on the developed EoS.

The purpose of introducing the α-function ($\alpha(T)$) into the equation is to achieve better matching with experimental data, especially at declined temperature and critical zone regions.

In Eq. 2.10, the first term ($\frac{RT}{v-b}$) is called repulsive term and the second one ($\frac{a(T)}{v^2+ubv-wb^2}$) the attractive term.

2.2.3.1 Van der Walls Equation of State

The simplest cubic EoS is the Van der Waals EoS (1873) (van der Waals, 1913). Van der Waals improved the ideal gas equation by introducing repulsive and attractive intermolecular interactions. This EoS is the first EoS capable of representing vapor – liquid coexistence.

The Van der Waals EOS is given by:

$$\left(p + \frac{a}{v^2} \right) (v - b) = RT. \tag{2.14}$$

To find the molar volume from pressure and temperature, this equation may be rearranged in the following form:

$$v^3 - \left(b + \frac{RT}{p} \right) v^2 + \left(\frac{a}{p} \right) v - \frac{ab}{p} = 0. \tag{2.15}$$

Eq. 2.15 is a cubic equation in terms of volume. For this reason, the Van der Waals EoS (and its modifications) is called a cubic EoS.

In the Eq. 2.14, a (known as energy parameter) and b (known as co-volume) are constants and have different values for each component.

The terms a/v^2 and b in Eq. 2.14 represent the attractive and repulsive terms, respectively. In particular the term a/v^2 corrects the value of pressure taking into account the forces of attraction between molecules, so the amount of pressure exerted by a Van der Waals gas is equal to the amount of pressure exerted by an ideal gas minus a/v^2. Concerning b, if the pressure approaches to infinite, the molar volume equals b and so b can be considered the volume of 1 mol of hard-sphere volume and is usually called co-volume. Co-volume is always less than b and so $(v - b)$ is a positive term that represents the free space between molecules.

If a and b are set to zero the upper equation reduces to an ideal gas EoS (Eq. 2.1).

The Van der Waals EOS may be rewritten in the form $p = p(v, T)$:

$$p = \frac{RT}{v - b} - \frac{a}{v^2}, \tag{2.16}$$

where the parameters a and b can be determined in terms of critical temperature and critical pressure.

In particular at the critical point of a pure component the first and second derivatives of pressure with respect to the volume at constant temperature are zero:

$$\left(\frac{\partial p}{\partial v}\right)_{p_c, v_c, T_c} = \left(\frac{\partial^2 p}{\partial v^2}\right)_{p_c, v_c, T_c} = 0. \tag{2.17}$$

It means the critical isotherm shows a horizontal inflection at the critical point.

From the Eq. 2.16 we can calculate the first and second derivative of pressure:

$$\left(\frac{\partial p}{\partial v}\right)_T = -\frac{RT}{(v - b)^2} + \frac{2a}{v^3}, \tag{2.18}$$

$$\left(\frac{\partial^2 p}{\partial v^2}\right)_T = \frac{2RT}{(v - b)^3} - \frac{6a}{v^4}. \tag{2.19}$$

At the critical point we have:

$$\left(\frac{\partial p}{\partial v}\right)_{p_c, v_c, T_c} = -\frac{RT_c}{(v_c - b)^2} + \frac{2a}{v_c^3} = 0, \tag{2.20}$$

$$\left(\frac{\partial^2 p}{\partial v^2}\right)_{p_c, v_c, T_c} = \frac{2RT_c}{(v_c - b)^3} - \frac{6a}{v_c^4} = 0. \tag{2.21}$$

From Eq. 2.20 and Eq. 2.21 we have:

$$b = \frac{v_C}{3} = 0{,}125\frac{RT_C}{p_C}, \tag{2.22}$$

$$a = \frac{9}{8}T_C v_C = 0{,}4218\frac{R^2T_C^2}{p_C}. \tag{2.23}$$

Eq. 2.15 gives three roots for molar volume at subcritical temperature, as shown in Figure 2.3.

The biggest root for volume or compressibility factor corresponds to saturated vapor, the smallest root to saturated liquid and the intermediate root has not have physical meaning because it tells that the value of $\left(\frac{\partial p}{\partial v}\right)_T$ is positive which is not physically possible for a pure component since for a pure component as the pressure increases the molar volume decreases and so $\left(\frac{\partial p}{\partial v}\right)_T$ has to be negative. In the liquid phase, at a large pressure molar volume change is very small and so $\left(\frac{\partial p}{\partial v}\right)_T$ is relatively high for a liquid phase.

At temperature higher than the critical one the Van der Waals EOS gives one real root and two complex roots which are not acceptable: if the value of the real root is near b the phase is compressed liquid whereas if it is near RT/P the phase is gas or superheated vapor. At the critical temperature all the three roots are equal to the critical volume.

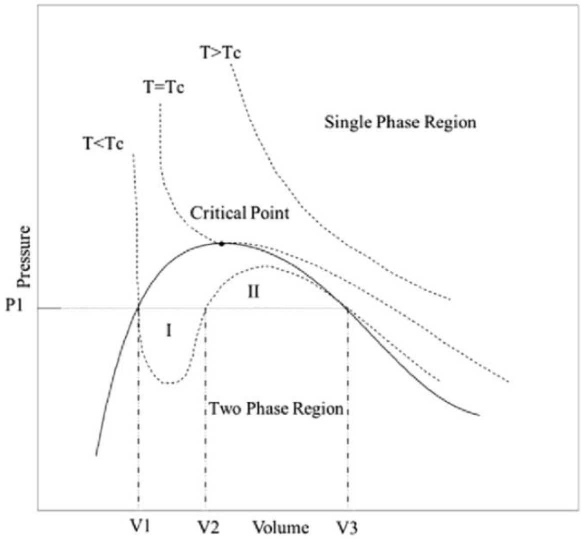

Figure 2.3: Predicted pressure-volume behaviour of a pure component at subcritical, critical and supercritical temperatures by Van der Waals-type equation of state (EoS).

The Van der Waals equation can also be written in terms of compressibility factor:

$$z^3 - \left(1 + \frac{pb}{RT}\right) z^2 + \frac{pa}{R^2T^2} z - \frac{p^2}{R^3T^3} ab = 0. \tag{2.24}$$

From Eq. 2.24 it is possible to calculate the value of z_C for which we obtain:

$$z_C = \frac{3}{8} = 0{,}375. \tag{2.25}$$

In practice, it has been verified experimentally that the critical compressibility factor of pure fluids is in the range $z_C^{(H_2O)} = 0{,}23$ to $z_C^{(H_2)} = 0{,}3$ (Poling, et al., 2001), which justifies the need for improvements.

Furthermore, this equation cannot accurately predict the behavior of dense fluids and so several modifications have been proposed to improve the capability of the equation by modifying the attractive and repulsive terms.

Therefore, to obtain higher accuracies, especially in the near-critical region, modifications to the original van der Waals EoS have been proposed. In the modified equations the boundary conditions imposed for the calculation of a and b (Eq. 2.17) are satisfied. Experimental data on pure fluids can be used in the determination of parameters of EoS and for this reason these equations are semiempirical EoSs.

2.2.3.2 Redlich and Kwong Equation of State

Redlich and Kwong (Redlich, et al., 1949) modified the attractive term of Van der Waals EOS, whereas the repulsive term in RK EOS is identical to the Van der Waals EOS.

They introduced a temperature dependency of attractive term through a coefficient α.

$$p = \frac{RT}{v - b} - \frac{\alpha(T) a_c}{v(v + b)}. \tag{2.26}$$

The parameters of the equations are calculated according to the following equations:

$$\alpha = T_r^{-0.5}\,, \tag{2.27}$$

$$a_c = 0.4247 \frac{R^2T_c^2}{p_c}, \tag{2.28}$$

$$b = 0.08664 \frac{RT_c}{p_c}, \tag{2.29}$$

where the two constants, a_c and b, are temperature independent terms.

In the Eq. 2.27 T_r is the reduced temperature and it is defined as the ratio of temperature to critical temperature.

The Redlich – Kwong equation is commonly considered one of the best of two - parameter equations of state. While it can be used to calculate with a good degree of accuracy volumetric and thermal properties of pure compounds and of mixtures, its application to multicomponent – VLE calculations often gives poor results (Soave, 1972). This fact cannot be attributed only to the inaccuracy of the mixing rules since the accuracy is not better when calculating vapor pressures of pure compounds, but it must be ascribed also to the equation's lack of accuracy in expressing the influence of temperature.

2.2.3.3 Redlich – Kwong – Soave Equation of State

Soave (Soave, 1972) proposed a more general form of temperature-dependent term in the attractive term in the RK EOS:

$$\alpha(T,m) = \left[1 + m\left(1 - \left(\frac{T}{T_C}\right)^{0.5}\right)\right]^2. \tag{2.30}$$

Soave introduced the alpha function to include the ability of accurately predict the vapor tension at a reduced temperature $T_r = 0.7$.

There have been many other expressions proposed for the alpha function. They generally present at least one of the following characteristics (Poling, et al., 2001):

1. polynomial functions of the reduced temperature,
2. exponential functions of the reduced temperature, or
3. a combination of both.

Moreover, the alpha function expressions must satisfy the following fundamental conditions (Poling, et al., 2001):

1. they must be finite and positive at each temperature,
2. they must have a value equal to one at the critical point,
3. they must tend to zero when the temperature tends to infinity,
4. they must be continuous with defined finite first and second order derivatives.

As previously presented, the Pitzer acentric factor ω takes into consideration the fact that not all substances can be approximated as having a spherical shaped molecule. Soave correlated the alpha function parameter m against the Pitzer acentric factor as:

$$m = 0.480 + 1.574\omega - 0.176\omega^2. \tag{2.31}$$

That way, we obtain the Redlich – Kwong – Soave (RKS) equation of state (Soave, 1972):

$$p = \frac{RT}{v-b} - \frac{\alpha(T)a_c}{v(v+b)}. \tag{2.32}$$

Soave compared the predicted vapor pressure from his modification and the original RK EOS for a number of substances, showing that his modification greatly improved vapor pressure predictions.

Table 2.2: Comparison of calculated vapor pressures. (Soave, 1972).

Compound		**Root mean square deviation %**	
		Original Eq. (Eq. 26)	Modified Eq. (Eq. 32)
Ethylene	0.087	20.1	2.0
Propylene	0.144	23.5	0.7
Propane	0.152	28.8	2.0
Isobutane	0.185	52.4	2.4
Cyclopentane	0.195	66.0	0.8
Toluene	0.260	129.0	0.8
n-hexane	0.301	159.0	1.9
n-octane	0.402	268.0	2.1
n-decane	0.488	402.0	1.0

While the original equation yielded vapor pressures diverging sharply from experimental values, particularly for substances having high values of the acentric factor, the proposed equation fairly fitted to the experimental data (Table 2.2).

By imposing the critical point conditions and calculating the parameters a and b, the critical compressibility factor of $z_C = 0{,}33$ is obtained. That value, even though it presents a clear improvement from the van de Waals EoS, is still higher than the experimental values obtained for pure substances. Nonetheless, the RKS EoS is considered adequate for hydrocarbons and other nonpolar compounds (Aspen Tech, 2012).

2.2.3.4 Peng and Robinson Equation of State

Another important variation of the van der Waals EoS was introduced in 1976 by Peng and Robinson (Peng, et al., 1976). In fact, although the Redlich – Kwong – Soave (RKS) has rapidly gained acceptance by the hydrocarbon processing industry because of the relative simplicity of the equation itself, RKS-EoS fails to predict liquid densities accurately, even though the calculated vapor densities are generally acceptable.

Improved liquid density prediction was the main motivation of the authors of PR-EOS which in general is superior in density predictions of reservoir fluid systems. Although this equation improves the liquid density prediction, it cannot describe volumetric behavior around the critical point.

The PR-EOS is perhaps the most popular and widely used EOS and it has the following expression:

$$p = \frac{RT}{v-b} - \frac{a_c \alpha(T)}{v(v+b) + b(v-b)}, \tag{2.33}$$

where the constants a_c and b are calculated as follow

$$a_c = 0.45724 \frac{R^2 T_c^2}{p_c}, \tag{2.34}$$

$$b = 0.07780 \frac{R T_c}{p_c}. \tag{2.35}$$

They used a similar form function for α that has been suggested by Soave (Eq. 2.30), but they correlated m against acentric factor by equating the fugacities of saturated liquid and vapor phases, at temperature ranges from normal boiling point temperature to critical temperature (differently from Soave which used only the critical point and the calculated vapor pressure at $T_r = 0.7$):

$$m = 0.37464 + 1.54226\omega - 0.26992\omega^2. \tag{2.36}$$

With those values, the critical compressibility factor can be calculated:

$$\frac{p_C}{RT_C} = \frac{z_C}{v} = \frac{1}{v-b} - \frac{\frac{\alpha(T)}{RT_C}}{v^2 + 2bv - b^2}. \tag{2.37}$$

Its value is $z_C = 0{,}3$, closer to the interval previously mentioned (0,23:0,3), showing and improvement at the critical region compared to the RKS model.

Comparison of the vapor-pressure prediction of several substances by the RKS EoS and the PR EoS with experimental data shows that the error is small for both equations, although the PR EOS performs better by a small margin (Firoozabadi, 1989).

2.2.3.5 Other Cubic Equations of State

A comparison of the predicted liquid molar volume by leading two parameter EoS with experimental data of pure compounds generally shows a systematic deviation. The deviation is almost constant over a wide pressure range away from the critical point. Hence, subtracting the predicted molar volume by a constant correction term can improve the predicted liquid density. The effect on the predicted vapor volume is generally insignificant due to its large value relative to that of liquid away from the critical point.

Peneloux et al. (Peneloux, et al., 1982)were the first who introduced the volume shift concept, i.e. shifting the volume axis, and applied it to RKS:

$$v^c = v - c. \tag{2.38}$$

In the upper equation v^c is the corrected molar volume and c is the correction term determined by matching the measured and predicted saturated liquid volumes at $T_r = 0.7$.

The Redlich – Kwong – Soave – Peneloux Equations of State expression is the following:

$$p = \frac{RT}{v + c - b} - \frac{\alpha(T, \omega)}{(v + c)(v + c + b)}. \tag{2.39}$$

The co-volume and energy parameter can be calculated with the same expressions provided for the RKS model. The parameter c is calculated with the following expression:

$$c = 0.47068(0.29441 - z_{RA})(\frac{RT_C}{p_C}). \tag{2.40}$$

Where z_{RA} is the Rackett compressibility factor.

Another improvement has been proposed by Boston and Mathias (Boston, et al., 1980) whose work attempts to improve the developed relations to cover highly polar substances, such as water, carbon dioxide and carbon monoxide, by introducing a polar parameter in the α-function (Mathias, 1983). However, at higher densities, the predictions of the pressure (p) – volume (v) – temperature (T) state are still not accurate, particularly, for H_2-blend mixtures, attributed to the quantization of translational motion and the quantum nature of H_2 (Sadus, 1992). Therefore, Schwartzentruber and Renon (Schwartzentruber, et al., 1989) introduced three additional polar parameters (i.e., p_0, p_1, p_2) to improve the calculations presented by Mathias (Mathias, 1983).

In 1980, Schmidt and Wenzel (Schmidt, et al., 1980) introduced a Van der Waals-type cubic EoS which uses three input data sets of critical temperature, critical pressure and acentric factor. This EoS yields a substance-dependent critical compressibility factor.

Schmidt – Wenzel EoS is expressed in the following form:

$$p = \frac{RT}{v-b} - \frac{a_c\alpha}{v^2 + (1+3\omega)bv - 3\omega v^2}, \tag{2.41}$$

where α is a function of temperature and a_c and b are temperature independent.

The repulsive term is similar to Van der Waals EoS and the denominator of the attraction terms is replaced with a more general second-order polynomial in terms of volume.

PR and RKS can be considered as a general form of Schmidt – Wenzel EoS: if the acentric factor is substituted by values zero and 1/3 the Schmidt – Wenzel EoS reduced to PR and RKS equations respectively.

By applying the conditions at critical point (Eq. 2.17) a_c and b are determined:

$$a_c = \Omega_{ac}\frac{R^2T_c^2}{p_c}, \tag{2.42}$$

$$b = \Omega_b\frac{RT_c}{p_c}. \tag{2.43}$$

The constants Ω_{ac} and Ω_b are calculated according to the following equations:

$$\Omega_{ac} = [1-\chi(1-q)]^3, \tag{2.44}$$

$$\Omega_b = \chi q, \tag{2.45}$$

where χ is the critical compressibility factor and it is related to the correlating parameter q by:

$$\chi = \frac{1}{3(1+q\omega)}. \tag{2.46}$$

The parameter q, defined as b/v_c, is the smallest positive root of the following equation:

$$(6\omega + 1)q^3 + 3q^2 + 3q - 1 = 0. \tag{2.47}$$

The form of α is the same as the one proposed by Soave (Eq. 2.30), however m is a function of acentric factor and reduced temperature.

The inclusion of ω in the EoS as the third parameter by Schmidt and Wenzel resulted in a variable calculated critical compressibility, according to the value of acentric factor. The predicted values are, however, about 15% higher than the true values. This was known to the authors, but it was accepted as the price for an overall optimum accuracy in predicted volumes (Danesh, 1998).

Patel and Teja (Patel, et al., 1982) presented an extension of the works of Soave, of Peng and Robinson, and of Schmidt and Wenzel. As the expression proposed by Schmidt and Wenzel, the Patel-Teja EoS also uses three input data sets of critical temperature, critical pressure and acentric factor. The equation gives a substance-dependent critical compressibility factor; in addition, this EoS can be applied for polar fluids such as alcohols, water and ammonia (Patel, et al., 1982).

The EoS presented by Patel and Teja has the following formula:

$$p = \frac{RT}{v - b} - \frac{a_c\alpha}{v(v + b) + c(v - b)}. \tag{2.48}$$

The repulsive term is identical to the repulsive term in the Van der Waals EoS. The denominator of the attraction terms is replaced by a new second-order polynomial.

The c parameter is defined as:

$$c = \Omega_c \frac{RT_c}{p_c}, \tag{2.49}$$

where

$$\Omega_c = 1 - 3\chi. \tag{2.50}$$

χ is the adjusted critical compressibility factor and is calculated by matching liquid density. It was correlated with the acentric factor for nonpolar substances by the following equation:

$$\chi = 0.329032 - 0.076788\omega + 0.0211947\omega^2. \tag{2.51}$$

The parameters a_c and b are defined similar to the Schmidt-Wenzel EoS by Eqs. 2.42 and 2.43 respectively, with different value for Ω_{ac} and Ω_b.

Ω_b is the smallest positive root of the following equation:

$$\Omega_b^3 + (2 - 3\chi)\Omega_b^2 + 3\chi^2\Omega_b - \chi^3 = 0. \qquad (2.52)$$

Ω_{ac} is determined in terms of Ω_b and χ:

$$\Omega_{ac} = 3\chi^2 + 3(1 - 2\chi)\Omega_b + \Omega_b^2 + (1 - 3\chi). \qquad (2.53)$$

The form of α in the Patel-Teja EoS is the same as proposed by Soave (Eq. 2.30).

m is correlated with the acentric factor for non polar substances as follow:

$$m = 0.452413 + 1.30982\omega - 0.295937\omega^2. \qquad (2.54)$$

If the values of 0.307 and 0.333 are substituted for χ, Patel and Teja EoS reduces to PR and RKS equations, respectively.

Using the generalized Van der Walls theory, Esmaeilzadeh and Roshanfekr used a mathematically simple cubic EoS to model attractive interactions between molecules.

The proposed equation of state in their work is as follows (Esmaeilzadeh, et al., 2006):

$$p = \frac{RT}{v - b} - \frac{a(T)}{v(v + c) + c(v - c)}, \qquad (2.55)$$

where a is a function of temperature and b and c are constant.

This EoS predicts saturated liquid density more accurately than the Patel and Teja and PR EoSs. Moreover, it is found that Esmaeilzadeh-Roshanfekr EOS is most accurate for predicting gas-condensate properties, while the original RKS and PR equations remain reliable for oil samples (Bonyadi, et al., 2007).

2.2.3.6 Extensions of cubic EoSs to mixtures

Most of the EoSs were originally developed for pure components. Each EoS has a number of parameters which are usually based on the properties of pure components such as critical properties and acentric factor. Extending the equations that had been developed for pure components for mixtures is important because most practical problems are encountered with multicomponent mixtures.

There are three approaches for extending equations to mixtures (Riazi, 2005).

I. The first approach is the determination of an input parameter such as critical temperature, critical pressure and acentric factor for mixtures (usually called pseudocritical properties). Then, the parameters of an EoS are calculated by the properties of the mixture and are substituted into the EoS that had been developed for pure components.

II. The second approach is determination of required properties for all pure components that were presented; this approach gives good results but it demands high computational time and so it is not suitable for the mixture composed by many components.

III. The third approach is based on the parameters of EoS of mixtures which are calculated using the values for pure components and the mole fraction or weight fraction of each of them and this is the most widely used.

Several mixing rules developed ((Hirschfelder, et al., 1954); (Huron, et al., 1979); (Kwak, et al., 1986); (Stryjek, et al., 1986a); (Stryjek, et al., 1986b); (Stryjek, et al., 1986c); (Economou, et al., 1997); (Prausnitz, et al., 1998)). The cubic EoS is usually extended to mixtures by the quadratic mixing rule. Peng and Robinson (Peng, et al., 1976), Redlich and Kwong (Redlich, et al., 1949) and Soave (Soave, 1972) used quadratic mixing rule in their papers.

In the work of Soave (Soave, 1972) the original generalized mixing rules were first tried:

$$a = \left(\sum_{i=1}^{N} y_i a_i^{0.5} \right)^2 , \tag{2.56}$$

$$b = \sum_{i=1}^{N} yib_i, \tag{2.57}$$

where y_i is the molar fraction of the i-th component and N is the total number of components of the mixture.

It was found that these rules can be applied with acceptable results to mixtures of nonpolar fluids, such as hydrocarbons, nitrogen, carbon monoxide, with the exclusion of carbon dioxide and hydrogen sulphide.

The equation proposed by Soave fits the experimental data well, particularly in the vapor phase, in the liquid phase also the error in the computed bubble-pressures is small. So it can be concluded that the proposed equation is able to predict the phase behavior of mixtures in the critical zone. Moreover, some binary components having largely different volatilities were investigated and so it was concluded that the mixing rules adopted were adequate.

Greater deviations, however, were found for hydrogen-containing mixtures or for systems containing carbon dioxide, although the vapor pressures of the single pure components were reproduced well; in order to fit the experimental data some empirical corrections become necessary for these systems.

In such case it is not possible to use any longer the generalized mixing rules, but one could write:

$$a = \left(\sum_{i=1}^{N} y_i \sum_{j=1}^{N} y_j \, a_{ij}^{0.5} \right)^2 , \tag{2.58}$$

$$a_{ij} = \left(1 - K_{ij}\right)\left(a_i a_j\right)^{\frac{1}{2}}, \tag{2.59}$$

where K_{ij} is an empirical correction factor called binary interaction parameter (BIP), to be determined from the experimental data, for each couple of components present in the mixture. The binary interaction parameters are found from experiment by minimization between predicted and experimental data. The binary interaction parameters that are used with a given EoS are different from the suitable binary interaction parameters for other EoSs. In other words, the binary interaction parameter is developed for particular EoSs and only should be used for those EoSs.

2.2.4 Non – Cubic Equations of State

When one needs high accuracy in the properties description, cubic analytical equations of state cannot be generally used. Though the search for better models began well before computers, the ability to rapidly calculate results or do parameter regression with complicated expressions has introduced increasing levels of complexity in the Equations of State (Poling, et al., 2001). Non-cubic equations can better describe the volumetric behavior of pure substances but may not be suitable for complex hydrocarbon mixtures (Firoozabadi, 1989). The application of non-cubic equations demands a high computational time and effort, due to their high powers in volume and large number of parameters, hence, unsuitable for reservoir fluid studies where many sequential equilibrium calculations are required. More importantly, for multi-component systems each parameter must be determined using a mixing rule, which at best is quite arbitrary (Danesh, 1998).

One of the well-known noncubic EoSs is the virial equation which is based on theories of statistical mechanics (Mason, et al., 1969). The original version of virial EoS was presented by Onnes in 1901 (Onnes, 1901) and it may be written in a power series of molar density (pressure explicit) or pressure (volume explicit) as follows:

$$z = 1 + \frac{B}{v} + \frac{C}{v^2} + \frac{D}{v^3} + \cdots, \tag{2.60}$$

$$z = 1 + B\rho_M + C\rho_M^2 + D\rho_M^3 + \cdots, \tag{2.61}$$

$$z = 1 + B'p + C'p^2 + D'p^3 + \cdots, \tag{2.62}$$

in which z is the compressibility factor, v is the molar volume, ρ_M is the molar density, p is the pressure and B, C, D, … are the second, third, fourth, and so on, virial coefficient. The coefficient B corresponds to the interaction between two molecules, coefficient C corresponds to interaction between three molecules, and so on. For a given substance, the virial coefficients depend only on the temperature.

The virial series expansion, in theory, is an infinite series, but in practice terms above the third virial coefficient are rarely used. More data is available for the second virial coefficient, but fewer data are available for the third virial coefficient.

2.2.4.1 Benedict – Webb – Rubin Equation of State

The best-known and mostly widely used noncubic EoSs are the Benedict – Webb – Rubin (BWR)-type EoSs. The BWR EOS is an empirical extension of virial EOS. The BWR EoS can be expressed as follows (Bendict, et al., 1940):

$$\begin{aligned} p = RT\rho_M + (B_0RT - A_0 - C_oT^{-2})\rho_M^2 + (bRT - a)\rho_M^3 + \alpha a\rho_M^6 \\ + cT^{-2}\rho_M^3(1 + \gamma\rho_M^2)e^{-\gamma\rho_M^2}, \end{aligned} \tag{2.63}$$

in which ρ_M is the molar density, equal to $1/v$, and $A_0, B_0, C_0, a, b, c, \alpha, \gamma$ are the eight adjustable parameters.

As an improvement from the cubic EoS, the BWR equation can treat supercritical components and is able to work in the critical area with good accuracy (Poling, et al., 2001).

2.2.4.2 Benedict – Webb – Rubin – Starling Equation of State

Many variations of BWR EoS have been proposed since the introduction of BWR EoS ((Bendict, et al., 1940); (Starling, 1966); (Starling, 1973); (Nishiumi, et al., 1975); (Nishiumi, 1980); (Nishiumi, et al., 1991); (Soave, 1995); (Wang, et al., 2001)), but the most widely used BWR-type EoS is the Benedict – Webb – Rubin – Starling (BWRS) EoS, which has been introduced by Han and Starling (Starling, 1973).

The resulting equation is an 11-parameter EoS that can be used for hydrocarbon systems that include the common light gases, such as H_2S, CO_2 and N_2.

$$\begin{aligned} p = RT\rho_M &+ (B_0RT - A_0 - C_oT^{-2} + D_0T^{-3} - E_0T^{-4})\rho_M^2 \\ &+ (bRT - adT^{-1})\rho_M^3 + (a + dT^{-1})\rho_M^6 \\ &+ cT^{-2}\rho_M^3(1 + \gamma\rho_M^2)e^{-\gamma\rho_M^2}, \end{aligned} \tag{2.64}$$

where the additional parameters are D_0, E_0 and d.

To obtain the eleven parameters, one option is to resort to relationships with the critical properties and the acentric factor:

Table 2.3: 11-Parameter EoS Relationships.

Expressions	
$\boldsymbol{\rho_{cr}B_0 = A_1 + B_1\omega}$	$\frac{\rho_{cr}a}{RT_{cr}} = A_6 + B_6\omega$
$\boldsymbol{\frac{\rho_{cr}A_0}{RT_{cr}} = A_2 + B_2\omega}$	${\rho_{cr}}^3\alpha = A_7 + B_7\omega$
$\boldsymbol{\frac{\rho_{cr}C_0}{{RT_{cr}}^3} = A_3 + B_3\omega}$	$\frac{\rho_{cr}c}{{RT_{cr}}^3} = A_8 + B_8\omega$
$\boldsymbol{{\rho_{cr}}^2\gamma = A_4 + B_4\omega}$	$\frac{\rho_{cr}D_0}{{RT_{cr}}^4} = A_9 + B_9\omega$
$\boldsymbol{{\rho_{cr}}^2 b = A_5 + B_5\omega}$	$\frac{\rho_{cr}d}{{RT_{cr}}^2} = A_{10} + B_{10}\omega$
$\boldsymbol{\frac{\rho_{cr}E_0}{{RT_{cr}}^5} = A_{11} + B_{11}\omega e^{(-3.8\omega)}}$	

Table 2.4: 11-Parameter EoS Relationships 2.

Parameter Subscript (j)	**Aj**	**Bj**
1	0.44369	0.115449
2	1.28438	-0.92073
3	0.356306	1.70871
4	0.544979	-0.2709
5	0.528629	0.349261
6	0.484011	0.75413
7	0.705233	-0.0445
8	0.504087	1.32245
9	0.030745	0.179433
10	0.073283	0.463492
11	0.00645	-0.02214

The BWRS EoS is suitable for light hydrocarbons and reservoir fluids (Riazi, 2005). The accuracy of predicted volumetric data from BWRS EoS is better than the one from cubic EoS; however, the BWRS EoS demands high computational time and is not suitable when successive equilibrium calculations are required.

2.2.4.3 Helmholtz energy – based Equations of State

Recent equations of state for mixtures are based on multi-fluid approximations and are explicit in the Helmholtz free energy. The models use equations of state in the form of fundamental equations for each mixture component along with further correlation equations to take into account the residual mixture behaviour. The models enable the accurate description of the thermodynamic properties of mixtures in the entire fluid region (i.e., in the homogeneous gas, liquid, and supercritical regions and for vapor−liquid equilibrium states) over wide ranges of temperature, pressure, and composition. The basis for the development and evaluation of such empirical equations of state for mixtures are experimental data.

In this approach, the Helmotz free energy is split into a part (a^0), which represents the properties of ideal-gas mixtures at given values for ρ, T, and **x**, and a part (a^r), which takes into account the residual mixture behavior:

$$a(\rho, T, \mathbf{x}) = a^0(\rho, T, \mathbf{x}) + a^r(\rho, T, \mathbf{x}). \qquad (2.65)$$

The use of the Helmholtz free energy in its dimensionless form $\alpha = a/RT$ results in the following equation:

$$\alpha(\delta, \tau, \mathbf{x}) = \alpha^o(\rho, T, \mathbf{x}) + \alpha^r(\delta, \tau, \mathbf{x}). \qquad (2.66)$$

δ is the reduced mixture density and τ is the inverse reduced mixture temperature:

$$\delta = \frac{\rho}{\rho_r}, \qquad (2.67)$$

$$\tau = \frac{T_r}{T}, \qquad (2.68)$$

with ρ_r and T_r being the composition-dependent reducing functions for the mixture density and temperature, as shown in Eqs. 2.69 and 2.70.

$$\rho_r = \rho_r(\mathbf{x}), \qquad (2.69)$$

$$T_r = T_r(\mathbf{x}). \qquad (2.70)$$

The dimensionless form of the Helmholtz free energy for the ideal-gas mixture α^o is given by:

$$a^o(\rho, T, \mathbf{x}) = \sum_{i=1}^{N} x_i[\alpha_{oi}^o(\rho, T) + ln x_i], \qquad (2.71)$$

where N is the number of components in the mixture, α_{oi}^o is the dimensionless form of the Helmholtz free energy in the ideal-gas state of component i, and the quantities x_i are the mole fractions of the mixture constituents. The term $x_i ln x_i$ accounts for the entropy of mixing.

In a multi-fluid approximation, the residual part of the reduced Helmholtz free energy of the mixture α^r is given by:

$$\alpha^r(\rho, T, \mathbf{x}) = \sum_{i=1}^{N} x_i \alpha_{oi}^r(\delta, \tau) + \Delta\alpha^r(\delta, \tau, \mathbf{x}), \tag{2.72}$$

where α_{oi}^r is the residual part of the reduced Helmholtz free energy of component i and $\Delta\alpha^r$ is the so-called departure function. The reduced residual Helmholtz free energy of each component depends on the reduced variables δ and τ of the mixture; the departure function additionally depends on the mixture composition **x**.

According to Eq. 2.72, the residual part of the reduced Helmholtz free energy of the mixture α^r is composed of two different parts, namely:

- the linear combination of the residual parts of all considered mixture components, and
- the departure function.

In general, the contribution of the departure function to the reduced residual Helmholtz free energy of the mixture is less than the contribution of the equations for the pure components.

Summarized, the development of mixture models based on a multi-fluid approximation requires the following three elements:

- pure substance equations of state for all considered mixture components;
- composition-dependent reducing functions $\rho_r(\mathbf{x})$ and $T_r(\mathbf{x})$ for the mixture density and temperature;
- a departure function $\Delta\alpha^r$ depending on the reduced mixture density, the inverse reduced mixture temperature, and the mixture composition.

2.2.4.3.1 GERG Equation of State

The GERG equation of state is one of the models based on the multi-fluid approximations. Developed by the Gas Research Group (GERG), this equation provides an accurate representation of the behaviour of gas mixtures under various temperature and pressure conditions. The GERG EoS has undergone several modifications.

GERG-2004 (Kunz, et al., 2007) uses accurate equations of state in the form of fundamental equations for each mixture component along with functions developed for the binary mixtures of the components to take into account the residual mixture behavior. The GERG-2004 equation of state enables the calculation of thermal and caloric properties for natural gases and other mixtures consisting of 18 components: methane, nitrogen, carbon dioxide, ethane, propane, n-butane, isobutane, n-pentane, Isopentane, n-hexane, n-heptane, n-octane, hydrogen, oxygen, carbon monoxide, water, helium, and argon.

The GERG-2008 Equation of State (Kunz, et al., 2012) is an expanded version of the GERG-2004 Equation of State (Kunz, et al., 2007): in addition to the 18 components covered by GERG-2004, the expanded version GERG-2008 also includes the three additional components n-nonane, n-decane, and hydrogen sulfide, which add up to a total of 21 components. Thus, GERG-2008 covers all of the mixtures that can be formed by the 18 pure components GERG-2004 is based on and, in addition, also all mixtures that result from the combinations of the 18 components with the three additional components given above. This is the main difference between the two mixture models. The three additional components result in 57 additional binary combinations (i.e., binary mixtures composed of the three new components and the 18 natural gas components covered by GERG-2004). With these 57 additional combinations one obtains a total of 210 binary systems covered by the expanded mixture model GERG-2008 (see also Figure 2.4).

The GERG-2008 wide-range equation of state for natural gases, similar gases, and other mixtures is based on pure substance equations of state for each considered mixture component and correlation equations developed for binary mixtures consisting of these components. This allows for a suitable predictive description of multi-component mixtures over a wide range of compositions, which means it is able to predict the properties of a variety of natural gases and other multi-component mixtures. The basis for the development of such an empirical equation of state is experimental data for several thermodynamic properties. These data are used to determine the structures, coefficients, and parameters of the correlation equations and to evaluate the behavior of the equation of state in different fluid regions (Kunz, et al., 2012).

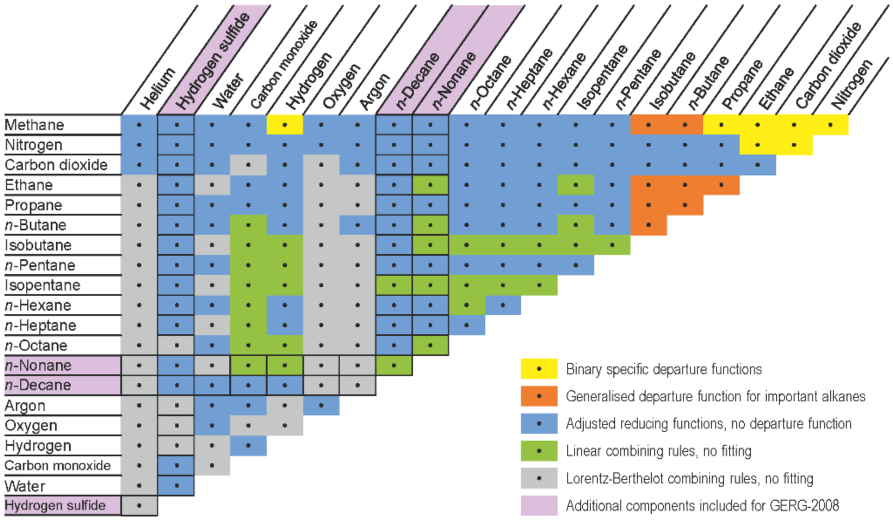

Figure 2.4: Overview of the 210 binary combinations that result from the 21 natural gas components considered for the development of the GERG-2008 equation of state. The fields corresponding to the additional 57 binary mixtures, which are formed by the combinations of the three additional components n-nonane, n-decane, and hydrogen sulfide with the "old" 18 components of GERG-2004, are framed. The diagram illustrates the different types of functions used for the description of the binary mixtures. The fields marked in yellow and orange show which of the two types of departure functions were used to fit the function to experimental data; in these cases, the parameters of the reducing functions were also fitted. The blue fields refer to binary mixtures where only the parameters of the reducing functions were fitted to experimental data. The green and gray fields indicate with which combining rule the reducing functions (without any fitting) were used. The additional components included for GERG-2008 are marked in lilac. (Kunz, et al., 2012).

The GERG- 2008 equation of state for natural gases and other mixtures of natural gas components is based on a multi-fluid approximation explicit in the reduced Helmholtz free energy (Eq. 2.66), where α^o part represents the properties of the ideal-gas mixture at a given mixture density ρ, temperature T, and molar composition **x** according to Eq. 2.71.

The residual part α^r of the reduced Helmholtz free energy of the mixture is given by:

$$\alpha^r(\delta,\tau,\mathbf{x}) = \sum_{i=1}^{N} x_i\alpha_{oi}^r(\delta,\tau) + \sum_{i=1}^{N-1}\sum_{j=i+1}^{N} x_i x_j F_{ij}\alpha_{ij}^r(\delta,\tau), \qquad (2.73)$$

where δ is the reduced mixture density and τ is the inverse reduced mixture temperature according to Eq. 2.69 and Eq. 2.70 respectively and N is the total number of components in the mixture.

Eq. 2.73 takes into account the residual behavior of the mixture at the reduced mixture variables δ and τ. The first sum in this equation is the linear contribution of the reduced residual Helmholtz free energy of the pure substance equations of state multiplied by the mole fractions x_i. The double summation in Eq. 2.73 is the departure function $\Delta\alpha^r(\delta, \tau, \mathbf{x})$, which is the summation over all binary specific and generalized departure functions $\Delta\alpha_{ij}^r(\delta, \tau, \mathbf{x})$ developed for the respective binary mixtures. All thermodynamic properties of a mixture (or pure substance) can be obtained by combining various derivatives of Eq. 2.66.

Over the entire composition range, GERG-2008 covers the gas phase, liquid phase, supercritical region, and vapor−liquid equilibrium states for mixtures of these components. The normal range of validity of GERG-2008 includes temperatures from (90 to 450) K and pressures up to 35 MPa where the most accurate experimental data of the thermal and caloric properties are represented to within their accuracy. The extended validity range reaches from (60 to 700) K and up to 70 MPa. The uncertainty of GERG-2008 in gas-phase density is 0.1 % over the temperature range from (250 to 450) K at pressures up to 35 MPa. This uncertainty estimate is valid for various types of natural gases, including natural gases rich in nitrogen, rich in carbon dioxide, rich in ethane, or rich in hydrogen (natural gas−hydrogen mixtures), natural gases containing relatively high fractions or considerable amounts of propane and heavier hydrocarbons, carbon monoxide, or oxygen, and many other mixtures (e.g., coke-oven gases) consisting of the 21 natural gas components previously listed (Kunz, et al., 2012).

2.2.4.3.2 PC – SAFT Equation of State

The perturbation theory helps describe the effects of molecular attributes, such as the size, shape, and interactions between molecules, with modifications of the expressions for dispersion forces (Nikolaidis, et al., 2021). Similar to other higher-order statistical associating fluid theory (SAFT) EoSs ((Chapman, et al., 1989); (Huang, et al., 1991)), PC – SAFT is based on statistical mechanics.

The PC – SAFT was developed by Gross and Sadowski in 2001 using the perturbation theory (Tumakaka, et al., 2005). The theoretical bases of SAFT models are founded on the first-order perturbation thermodynamic theory by Wertheim ((Wertheim, 1986); (Wertheim, 1984a); (Wertheim, 1984b)), leading to the development of EoSs, such as the one introduced by Jackson et al. (Jackson, et al., 1988) and Chapman et al. (Chapman, et al., 1989).

The perturbation-based models are often introduced to represent a simplified solution for a given molecular model. In PC – SAFT, the underlying molecular model is described as a coarse – grained representation of the molecules and their intermolecular interactions, as illustrated in Figure 2.5.

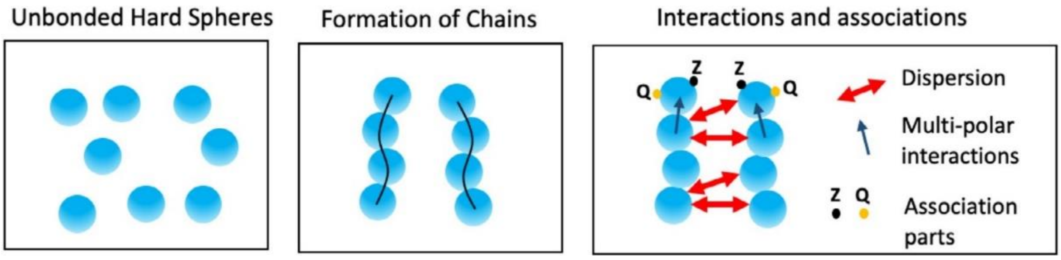

Figure 2.5: Molecular model representing the perturbed-chain system in the PC-SAFT equation of state. Schematic demonstration (i.e., dispersion, dipole–dipole, and association). (Alanazi, et al., 2022).

The principal idea of using the perturbation solutions is to split the total intermolecular forces into a reference term representing repulsive interactions and a perturbation or correction term that accounts for attractive forces. The attractive forces are further divided into different contributions. Theoretically, the first term is usually known as a function of temperature, density or pressure, and composition.

The SAFT and PC – SAFT EoSs are expressed as a summation of the reduced residual Helmholtz free energy (α^{res}) for each contributor term that represents the type of intermolecular force that occurs in the system. The residual Helmholtz free energy is the same as the Helmholtz free energy at the same temperature and volume but excluding the ideal gas Helmholtz free energy.

Thus, the molecular interaction forces for a specific number of molecules (N_i) of each component, volume (v), and density (ρ) in PC – SAFT are written in Eq. 74, as follows:

$$\frac{\alpha^{res}}{k_B T} = \frac{\alpha^{hc}}{k_B T} + \frac{\alpha^{hs}}{k_B T} + \frac{\alpha^{disp}}{k_B T} + \frac{\alpha^{assoc}}{k_B T} + \frac{\alpha^{polar}}{k_B T}, \tag{2.74}$$

where k_B is the Boltzmann constant.

The right-side expression in Eq. 2.74 represents the hard-chain reference fluid that characterizes the PC-SAFT. The superscripts in the various Helmholtz energy contributions denote the contribution from the chain formation (hc), hard-sphere repulsion (hs), dispersion (disp), association (assoc), and inter-polar (polar) interactions, respectively.

In PC – SAFT, three parameters for each pure component are required that account for the nonassociation components: the number of molecular chain segments (M), dispersion energy between segments (ε), and either the diameter (σ) or volume of the chain segment (v^{00}). For the pure components with association interactions, two more parameters are included: the association volume (κ^{AB}) and association energy between sites (the molecules, ε^{AB}).

Chapter 3

Comparison of Equations of State for H_2 mixtures: literature review

The thermodynamic modelling of vapor- liquid equilibria (VLE) for H_2-blend mixtures have been of a recent interest to many researchers ((Alanazi, et al., 2022); (Hassanpouryouzband, et al., 2020)) due to the more and more clear role of hydrogen in the ongoing energy transition.

In the work of Alanazi et al. (Alanazi, et al., 2022) cubic equations of state (EoSs), Peng – Robinson (PR) and Redlich – Kwong – Soave (SRK) and their modifications by Boston – Mathias (PR-BM) and Schwartzentruber – Renon (SR-RK), are compared in order to evaluate their accuracy in predicting the thermophysical properties of H_2-blend mixtures, including CH_4, C_2H_6, C_3H_8, H_2S, H_2O, CO_2, CO, and N_2; the Helmholtz-energy-based models (i.e., PC_SAFT and GERG2008) are analyzed, too. Binary interaction parameters are regressed to fit the experimental reference data for binary mixtures and provide optimized coefficients for each EoS.

The aim of the authors is to assess the capabilities of the thermodynamic models to provide accurate predictions for various H_2 concentrations in the mixture at high pressure and temperature conditions relevant to UHS (i.e., pressure up to 80 MPa and temperature from 313 K to 415 K) (Hassanpouryouzband, et al., 2020).

The authors used ASPEN Plus (v. 12.0) (Aspen Technology Inc., 2015), a popular application, to simulate the thermophysical behavior of the mixtures. Parameter regression was performed using the available regression methods in ASPEN properties. The most statistically reliable parameter estimates are obtained using a maximum likelihood function (MLF).

$$MLF = \sum_{n=1}^{NG} w_n \sum_{n=1}^{NP} \frac{[\left(\frac{T_{e,i} - T_{m,i}}{STD_{T,i}}\right)^2 + \left(\frac{p_{e,i} - p_{m,i}}{STD_{P,i}}\right)^2}{+ \sum_{n=1}^{NC-1} \left(\frac{x_{e,i,j} - x_{m,i,j}}{STD_{x,i,j}}\right)^2 + \sum_{n=1}^{NC-1} \left(\frac{y_{e,i,j} - y_{m,i,j}}{STD_{y,i,j}}\right)^2]} . \tag{3.1}$$

In this equation the weights (w_n) are used to weight each date group, STD is the standard deviation used to normalize all measurements within the data group, x is the liquid phase mole fraction, y is the vapor- phase mole fraction, T is the temperature and p is the pressure; NG is the number of the data group, NP denotes the number of points in each data group and NC represents the total number of components.

The collected experimental data on H_2 mixtures used in the work of Alanazi et al. (Alanazi, et al., 2022) cover a wide range of compositions, temperatures, and pressures. The focus will be on binary mixtures (H_2-CO_2, H_2-CH_4, H_2-C_2H_6, H_2-N_2, H_2-H_2S and H_2-H_2O). The composition of H_2 in the binary mixtures ranges from a mole fraction of 0.001 to 0.9 tested at temperatures and pressures that range from 63.2 K to 588.7 K and 0.01 to 138.98 MPa, respectively.

The predictions of the H_2-CO_2 mixtures are showed in Figure 3.1, presenting an example of the validation of the VLE models against the experimental data.

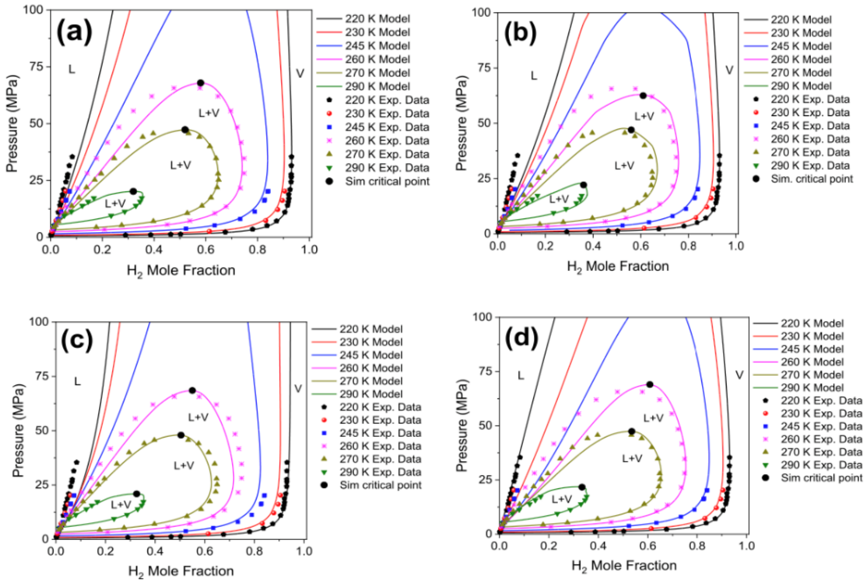

Figure 3.1: Phase equilibria diagrams of H_2-CO_2 mixtures: points represent experimental data, and solid lines represent prediction results of the developed cubic equations of state: (a) PR, (b) SRK, (c) BM-PR, and (d) SR-RK; the phase identities (L, V, and L+V), and the calculated critical point (Sim critical point) are also shown. (Alanazi, et al., 2022).

As reported by the authors, “PR, SRK, and BM-PR EoSs fail to accurately match the bubble pressure curves; since the SR-RK equation of state is the cubic equation of state that better matches the experimental data (Table 3.1), the SR-RK EoS models are used as a representative of the cubic EoSs in the comparison with noncubic EoSs (PC-SAFT and GERG2008)”.

Table 3.1: Percentage of average absolute deviation (AAD, %) between experimental data and estimates using the investigated cubic equations of state with the root mean square error (RMSE), fitted using regression over various binary interaction coefficients for H_2-CO_2 mixtures. (Alanazi, et al., 2022).

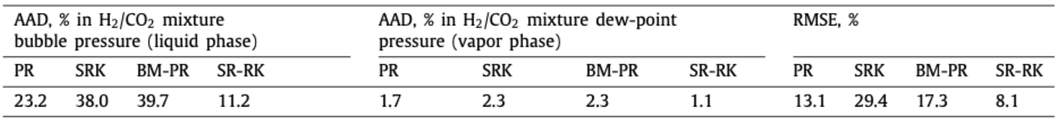

AAD, % in H_2/CO_2 mixture bubble pressure (liquid phase)				AAD, % in H_2/CO_2 mixture dew-point pressure (vapor phase)				RMSE, %			
PR	SRK	BM-PR	SR-RK	PR	SRK	BM-PR	SR-RK	PR	SRK	BM-PR	SR-RK
23.2	38.0	39.7	11.2	1.7	2.3	2.3	1.1	13.1	29.4	17.3	8.1

As an example, the results for the H_2-CH_4 are showed in figure 3.2; furthermore, the plots obtained for the mixture H_2-H_2O are reported in figure 3.3.

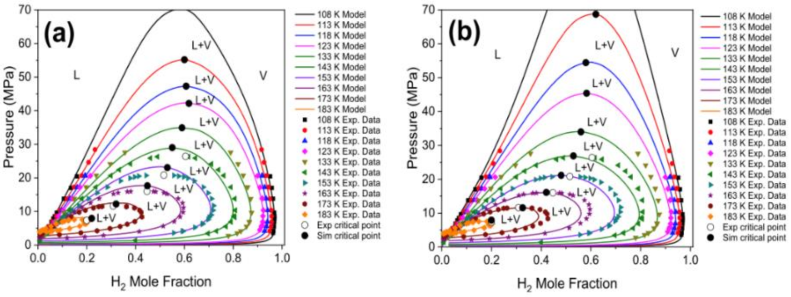

Figure 3.2: Phase equilibrium diagrams of the H_2-CH_4 mixture: (a) SR-RK and (b) PC-SAFT equations of state; the phase identities (L, V, and L+V), and the calculated critical point (Sim critical point) are also shown. (Alanazi, et al., 2022).

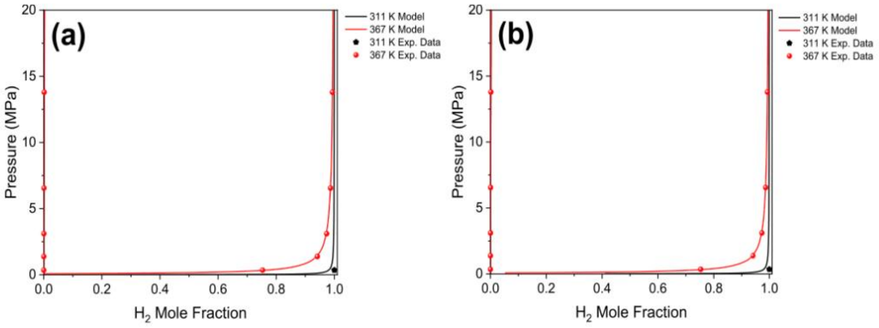

Figure 3.3: Phase equilibrium diagrams of the H_2-H_2O mixture: (a) SR-RK and (b) PC-SAFT equations of state. (Alanazi, et al., 2022).

For the H_2-CH_4 mixture (Figure 3.2), the qualitative analysis demonstrates that both the SR-RK and the PC-SAFT EoSs provide reasonably accurate results, so a quantitative analysis has been performed in order to demonstrate which EoSs is more accurate in predicting the results.

Table 3.2: Average absolute deviation (AAD) and root mean square error (RMSE) between the generated thermodynamic models using SR-RK and PC-SAFT equations of state and experimental data. (Alanazi, et al., 2022).

H_2 mixtures	AAD, % in mixture bubble pressure		AAD, % in mixture dew pressure		RMSE, %	
	SR-RK	PC-SAFT	SR-RK	PC-SAFT	SR-RK	PC-SAFT
H_2CH_4	2.82	0.68	2.25	6.70	8.32	9.89
$H_2C_2H_6$	0.86	0.63	1.57	1.34	4.30	4.62
$H_2C_3H_8$	0.63	4.34	0.45	3.34	6.22	7.89
H_2H_2O	1.84	2.53	0.18	0.24	3.97	4.91
H_2CO	3.11	0.78	1.43	1.63	1.69	9.26
H_2CO_2	32.90	26.80	1.12	1.04	8.10	8.00
H_2H_2S	17.34	16.30	1.67	5.35	9.82	12.00
H_2N_2	0.011	0.34	3.24	5.82	0.44	23.70

Regarding the density of an H_2 mixture, the results obtained by Alanazi et al. showed that “PR accuracy is not as good as the other investigated EoSs (i.e., GERG2008, PC-SAFT, and SR-RK) for the same range of pressures and temperatures”, as shown in Figure 3.4 to Figure 3.6 for the H_2-N_2 mixtures over varying H_2 mixing concentrations of 25%, 50% and 75% (Table 3.3).

Table 3.3: Maximum absolute deviation percentage (AD%) between experimental and calculated densities using VTPR, SR-RK, PC-SAFT, and GERG2008 equations of state, for 25%, 50%, and 75% H_2-N_2 mixtures. (Alanazi, et al., 2022).

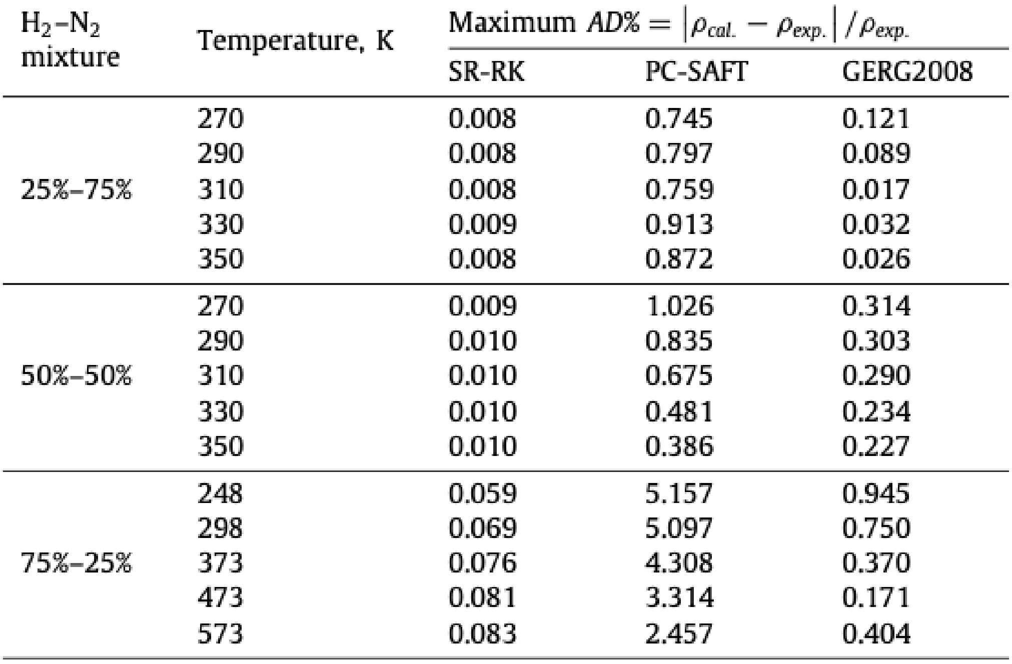

H_2–N_2 mixture	Temperature, K	Maximum $AD\% = \left|\rho_{cal.} - \rho_{exp.}\right| / \rho_{exp.}$		
		SR-RK	PC-SAFT	GERG2008
25%–75%	270	0.008	0.745	0.121
	290	0.008	0.797	0.089
	310	0.008	0.759	0.017
	330	0.009	0.913	0.032
	350	0.008	0.872	0.026
50%–50%	270	0.009	1.026	0.314
	290	0.010	0.835	0.303
	310	0.010	0.675	0.290
	330	0.010	0.481	0.234
	350	0.010	0.386	0.227
75%–25%	248	0.059	5.157	0.945
	298	0.069	5.097	0.750
	373	0.076	4.308	0.370
	473	0.081	3.314	0.171
	573	0.083	2.457	0.404

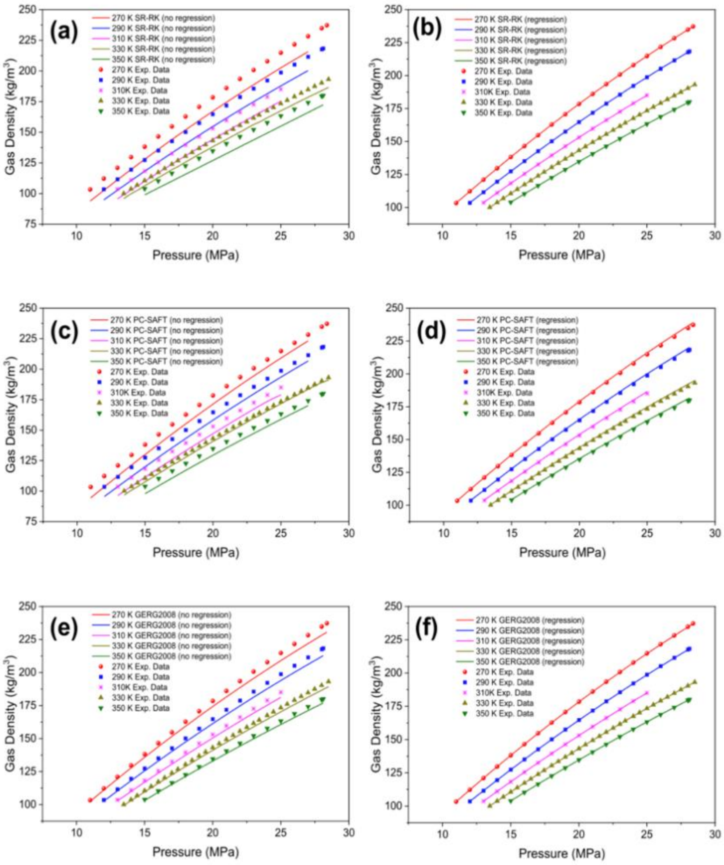

Figure 3.4: Density calculations of the 25% H_2 + 75% N_2 mixture compared to experimental data using four EoSs and regression parameters: (a) SR-RK cubic without regression, (b) SR-RK cubic with regression, (c) PC-SAFT without regression, (d) PC-SAFT with regression, (e) GERG2008 without regression, and (f) GERG2008 with regression equations of state. (Alanazi, et al., 2022).

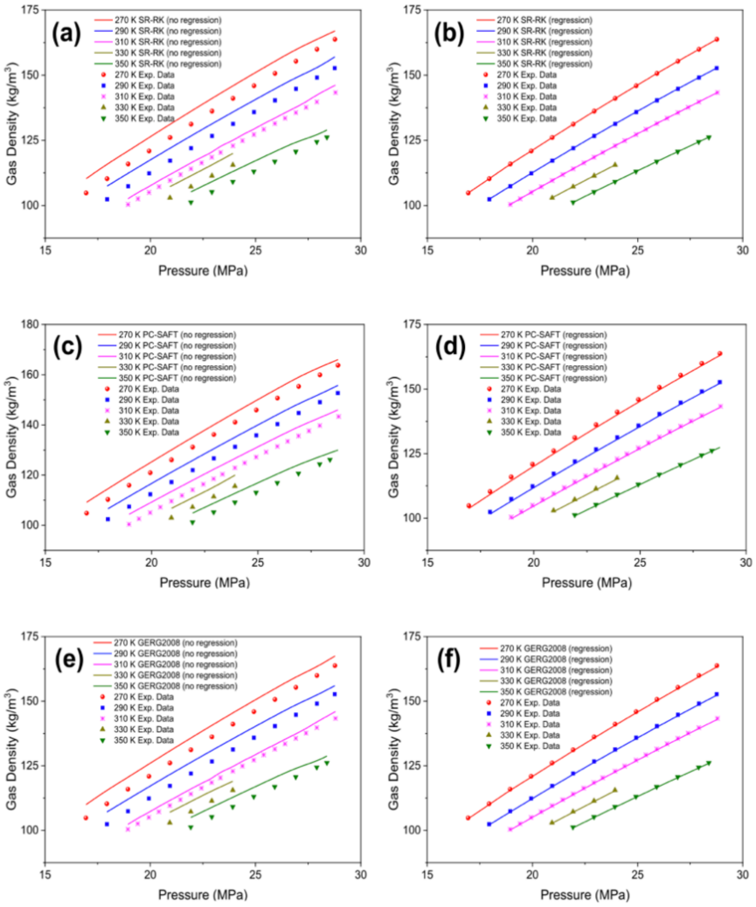

Figure 3.5: Density calculations of the 50% H_2 + 50% N_2 mixture compared to experimental data using four Eos and regression parameters: (a) SR-RK cubic without regression, (b) SR-RK cubic with regression, (c) PC-SAFT without regression, (d) PC-SAFT with regression, (e) GERG2008 without regression, and (f) GERG2008 with regression equations of state. (Alanazi, et al., 2022).

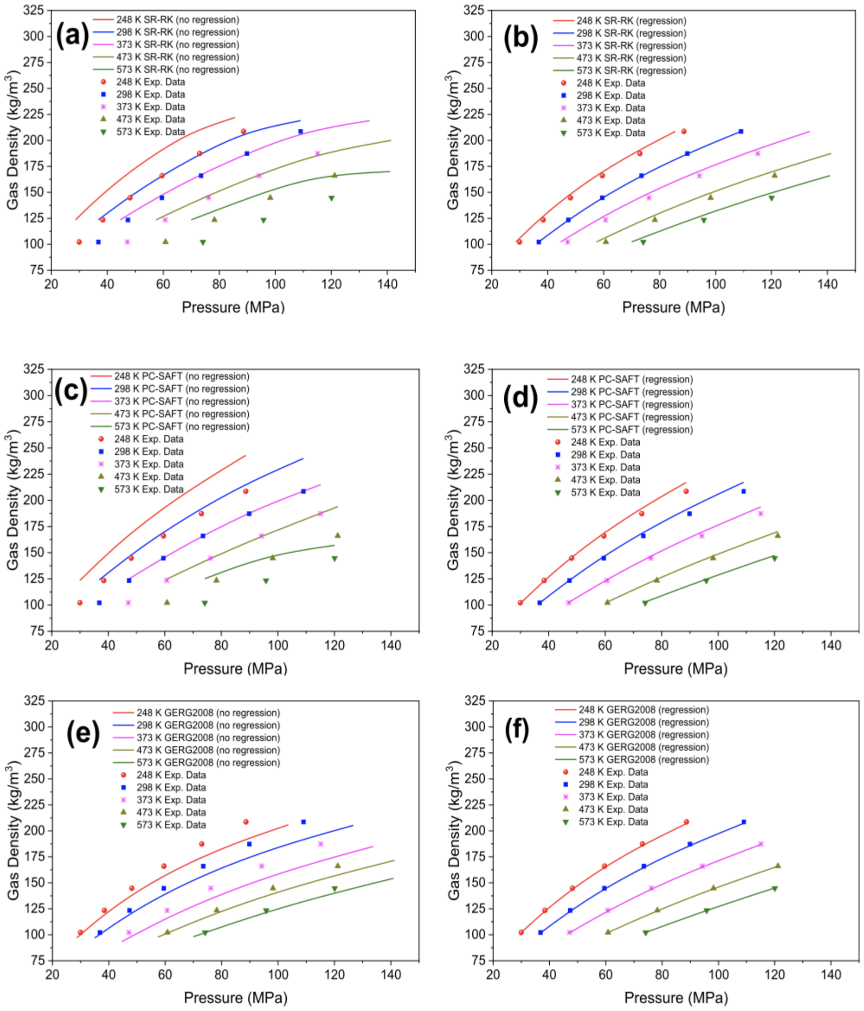

Figure 3.6: Density calculations of the 75% H_2 + 25% N_2 mixture compared to experimental data using four EoSs and regression parameters: (a) SR-RK cubic without regression, (b) SR-RK cubic with regression, (c) PC-SAFT without regression, (d) PC-SAFT with regression, (e) GERG2008 without regression, and (f) GERG2008 with regression equations of state. (Alanazi, et al., 2022).

The thermodynamic models were extended to H_2-CH_4 mixtures using three ratios of H_2 concentrations (i.e., 10%, 50%, and 90%) to calculate densities at temperature up to 450 K and pressure up to 100 MPa. The results of the calculations are displayed in Figure 3.7.

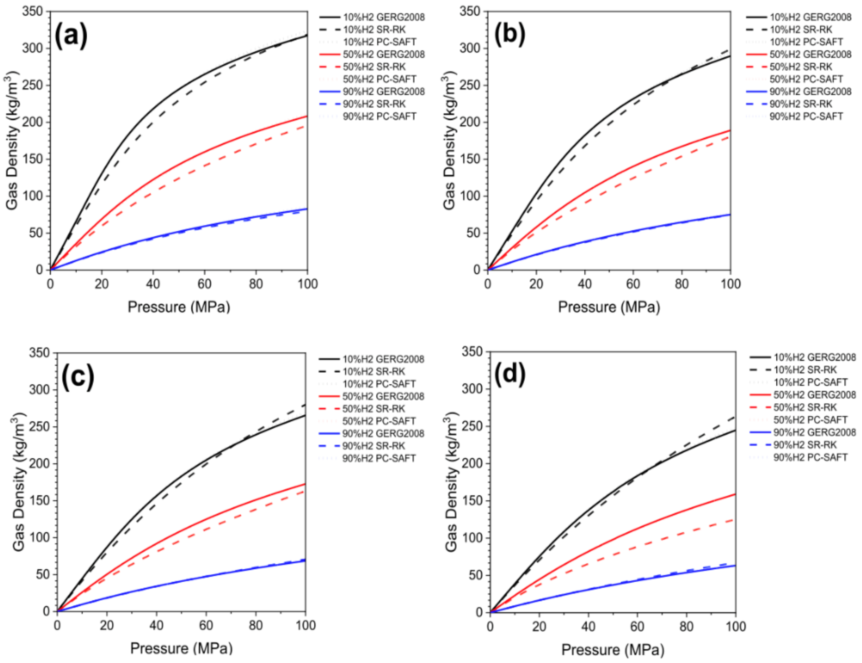

Figure 3.7: Predictions of density profiles of H_2-CH_4 mixtures with H_2 concentrations of 10%, 50%, and 90% using thermodynamic models developed using the three equations of state: GERG2008, SR-RK, and PC-SAFT for (a) 300 K, (b) 350 K, (c) 400 K, and (d) 450 K. (Alanazi, et al., 2022).

As a result it was obtained that "the PC-SAFT models have high accuracy in density predictions for binary H_2-blend mixtures and can be trusted to be used in compositional simulation models".

In the work of Hassanpouryouzband et al. (Hassanpouryouzband, et al., 2020), the GERG-2008 EoS (Kunz, et al., 2012) was used to predict phase behavior and density of gas mixtures under thermodynamic conditions which are characteristic of UHS(Figure 3.8).

Figure 3.9 presents the relative deviations of the predicted densities of GERG-2008 EoS for the hydrogen/methane mixtures whose experimental data are from Hernandez- (Hernández-Gómez, et al., 2018). The average absolute deviations (AADs) 0.044 for the 10% H_2 + 90% CH_4 mixture and 0.006 for the 50% H_2 + 50% CH_4 mixture. “The low AAD values confirm the high accuracy of GERG-2008 EoS predictions with relatively low errors”, as discussed above.

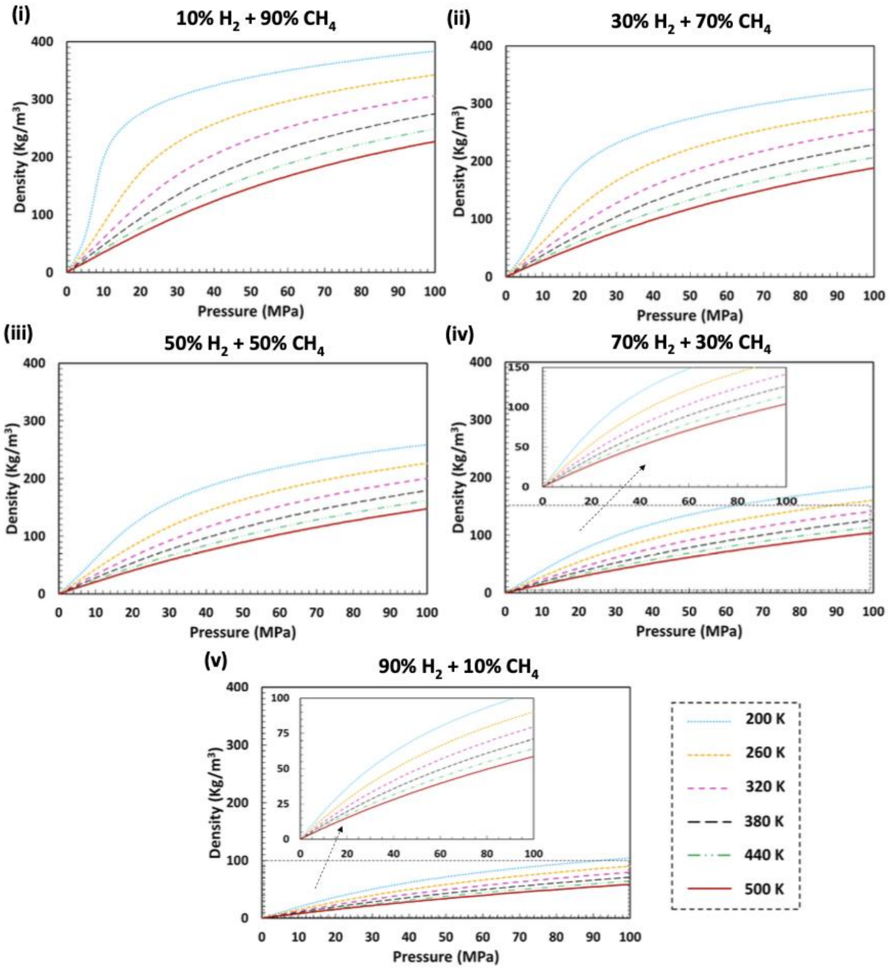

Figure 3.8: Predicted densities for different H_2 + CH_4 mixtures for various mole H_2 fractions over a wide range of pressures and temperatures using GERG-2008 EoS. Density values are greater in the presence of higher mole fractions of CH_4 in the studied systems as the density of CH_4 is considerably higher than that of H_2. The densities increase with increasing pressure (Boyle's Law) for all isotherms and reduce with increasing temperature (Charles's Law). (Hassanpouryouzband, et al., 2020).

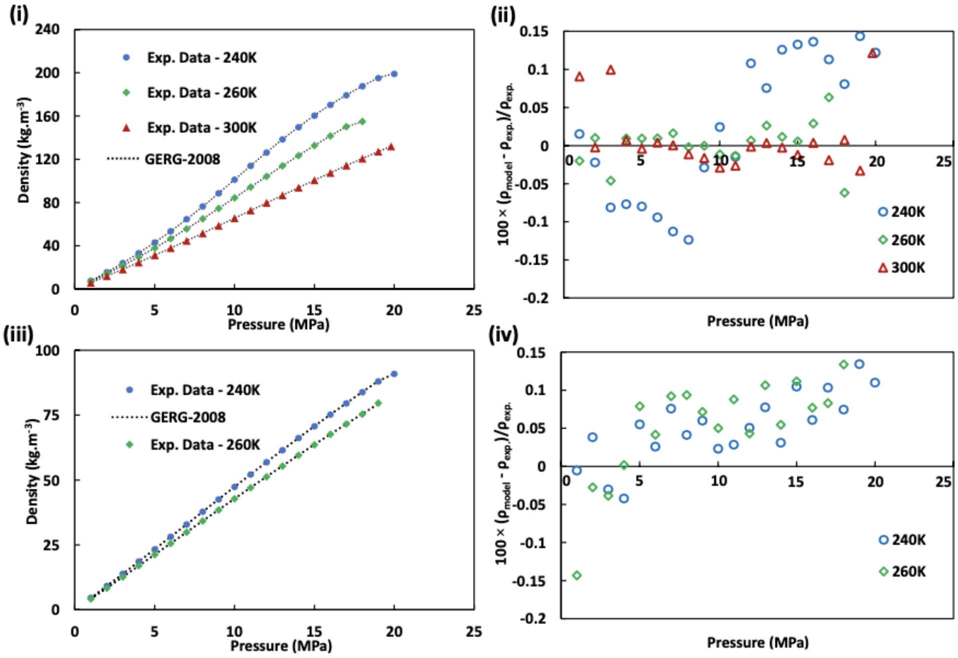

Figure 3.9: Thermodynamic modelling and experimental results of density of hydrogen/methane mixtures at a range of temperatures and pressures: (i) & (ii) are the results for a 10% H_2 + 90% CH_4 mixture and (iii) & (iv) are the results for a 50% H_2 + 50% CH_4 mixture at different pressure and temperatures. (ii) and (iv) show the relative deviations in density values predicted by GERG-2008 equation of state, ρ_{model} , from the density from the experimental (ρ_{exp}) data (Hernández-Gómez, et al., 2018), versus pressure at different temperatures. (Hassanpouryouzband, et al., 2020).

As it turned out from the literature, the equations of state that better match the experimental data for H_2-blend mixtures are the Helmholtz-energy-based ones which are the GERG 2008 and the PC – SAFT equations. Such EoSs require a huge computational time and effort, due to their high powers in volume and large number of parameters and this makes them less suitable for compositional reservoir simulations where sequential equilibrium calculations are required.

For this reason the need for a “simple” equation of state that describes the properties of H_2-blend mixtures arises. In particular, cubic equations of state, which are useful when the computational effort needs to be minimized, could be a solution.

The main issues encountered with the cubic EoS models are (Kundu, et al., 2023):

1. All EoS-based models use volume shift parameters to match the density of liquid and vapor phases and this can lead to errors in the calculation of thermodynamic properties.
2. Handling supersaturated vapor and liquid for mixtures with polar components is challenging.

Hence, an optimization process for parameters of cubic EoSs needs to be performed so that the equations can predict in a reliable and efficient way the properties of the mixture examined under given pressure and temperature conditions, in view of an increasingly frequent development of UHS.

As an example, the work of Kundu et al. (Kundu, et al., 2023) focuses on the optimization of the binary interaction parameter for H_2-blend mixtures to be used in the Redlich – Kwong – Soave Equation of State. In fact, a recent study has shown that “RKS EoS is more likely to result in reliable phase behavior and reservoir simulation (Krejbjerg, et al., 2006): considering RKS EoS mathematical formulation and simplicity, it seems to be a good choice for phase behavior calculations in UHS simulations”.

RKS EoS needs reliable Binary Interaction Parameters for its efficient and reliable application to UHS modeling.

The BIP optimization process attempts to match the available phase behavior data using RKS EoS for a well-defined mixture having N_c number of components by regression of $0.5N_C(N_C-1)$ number of $K_{i,j}$ values. These are three important parts of the optimization process: default values of the adjustable parameters (in this study the BIP), phase behavior experimental data and regression methodology which is described in Figure 3.10.

In this study, default values of BIPs are taken from Oellrich et al. (Oellrich, et al., 1981) for hydrocarbon-nonhydrocarbon mixtures. For hydrocarbon mixtures, default values of BIPs are taken from Chueh and Prausnitz (Chueh, et al., 1967) correlations.

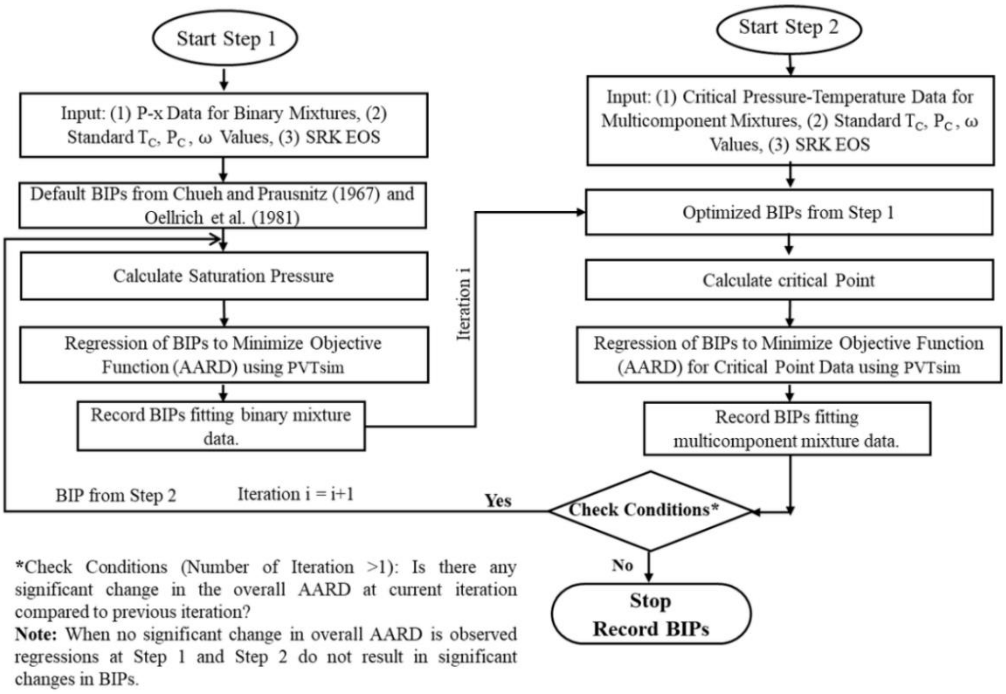

Figure 3.10: Flowchart of the regression methodology to optimize BIP for a non-hydrocarbon and hydrocarbon mixture to match the critical point data of multicomponent and P-x data of binary mixture. (Kundu, et al., 2023).

The BIP optimization process in this work is a two-step process with multiple iterations from Step 2 to Step 1 carried out using PVTSim (PVTsim Nova - Calsep, 2020).

“Step 1 process involves developing BIPs from data on binary mixtures. The BIPs are developed as a function of temperature (T) and carbon number (C_N) of n-alkane (wherever applicable) using the multiple isothermal P-x data”.

For every temperature for a binary mixture, a single value of the BIP, the one that better matches the experimental data is obtained; temperature and carbon number of the n-alkane (wherever applicable) are recorded. “Matching of multiple isothermal P- x data gives a discrete optimized value of BIPs in temperature and carbon number (CN) space which is then converted into suitable correlation”.

Step 2 of the optimization process involves the use of experimental data on critical points for multicomponent mixtures. “Discrete optimized BIP values and values from correlations are used as default values of BIPs while matching the critical point of the multicomponent mixtures. The matching of critical point requires adjustments of the default BIP values”.

Once matching is calculated for all multicomponent mixtures, Step 1 is repeated with BIP values from Step 2 as new default values. Once, new set of discrete values and correlations are obtained, Step 2 is again repeated with new default values and this iteration is continued until no significant change in the objective function is observed.

The objective function is the Average Absolute Deviation (AAD) for all data points (Eq. 3.2).

$$AAD = \frac{1}{M}\sum_{j=1}^{M}\left|\frac{prediction - data}{data}\right|_j \qquad (3.2)$$

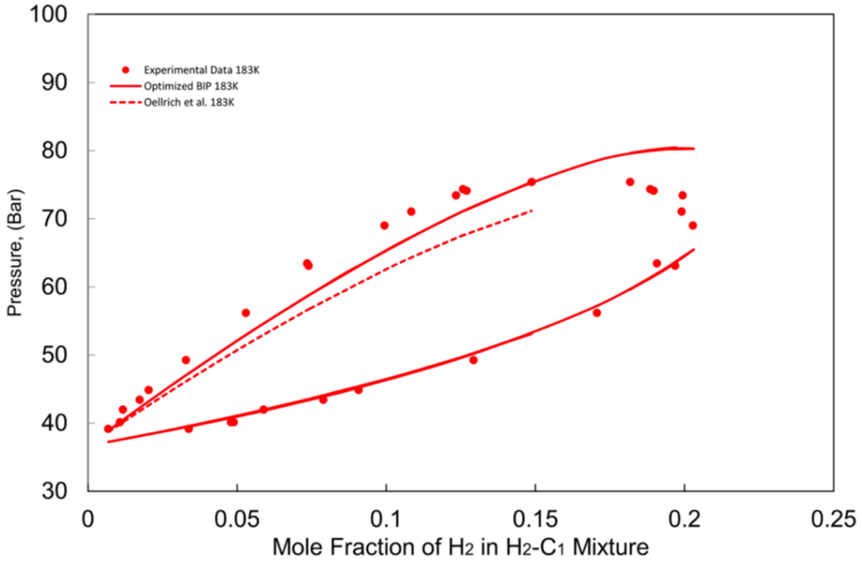

Figure 3.11: Comparison of P-x diagram from Optimized BIP with Oellrich et al. (Oellrich, et al., 1981) for SRK EOS. Dotted line: Predicted with Oellrich et al. (Oellrich, et al., 1981) default value. Solid line: Predicted with Optimized BIP. Solid Points: Experimental data for H_2-C1 mixture at 183K. (Kundu, et al., 2023).

The authors achieved the result that “RKS EOS with optimized BIP value can be safely used to model H_2 storage in depleted oil reservoir” (Kundu, et al., 2023).

A work which is worth to be mentioned is the one performed by Nielsen et al. (Nielsen, et al., 2023): the authors present “an EoS model to describe the operating envelope of a UHS operation in Austria”. They retrieved experimental data for various hydrogen/hydrocarbon mixtures to cover all the possible conditions of the depleted gas field considered; the results were used to develop a fluid model using the Peng-Robinson EoS with volume shifts. “The model was matched to (1) hydrogen-hydrocarbon gas laboratory measurements presented in this paper, (2) measured hydrogen-methane binary data (density and viscosity) taken from the literature, and (3) REFPROP (NIST) (Lemmon, 2007) calculated density and viscosity data for the hydrogen-hydrocarbon gas, hydrogen-methane binary system, and pure components”. The required tuning of the parameters in the fluid model development is discussed too.

Predictions using the proposed EoS model and NIST's GERG2008 model for the hydrogen/synthetic gas are shown in Figure 3.12. The density data measured with the proposed model are shown in Figure 3.13 and in Figure 3.14. In order to match the measured density data using the proposed PR EoS model the composition errors were identified and corrected; the normalization method used in order to correct the errors in the composition measurements is described in the paper.

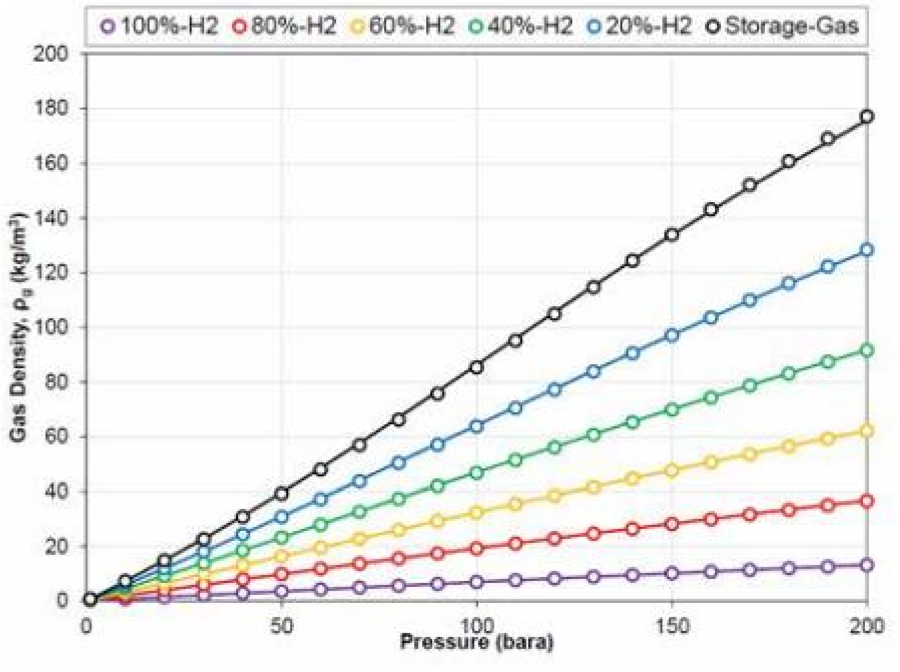

Figure 3.12: Comparison of NIST's GERG2008 model predicted densities (circles) and the proposed EoS model predicted densities (solid lined) for a hydrogen-4-component hydrocarbon gas mixture with hydrogen content ranging from 0 mole% to 100 mole% at 55°C. (Nielsen, et al., 2023).

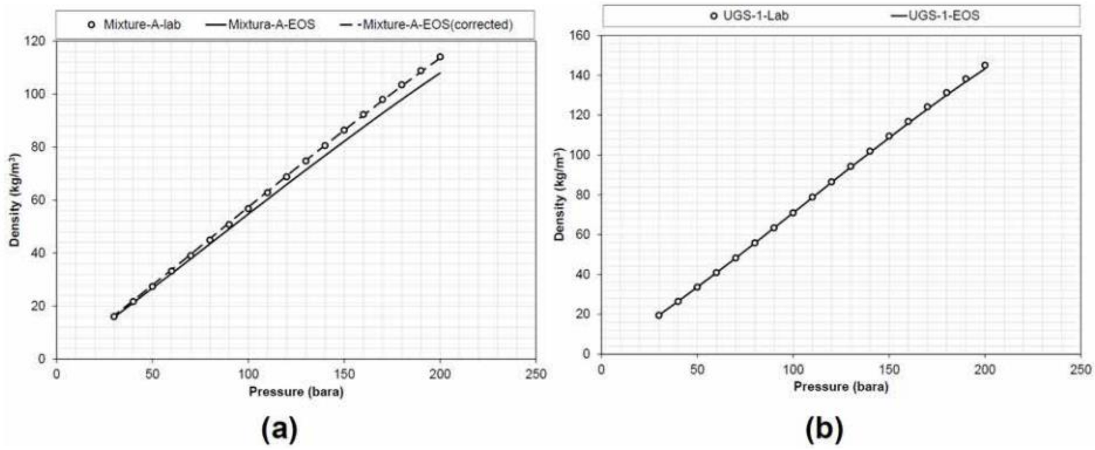

Figure 3.13: Density predictions of the proposed PR EOS model (solid line) for (a) Mixture-A and (b) UGS-1 (circle symbols). The prediction of uncorrected composition for Mixture-A is also given (dashed line). (Nielsen, et al., 2023).

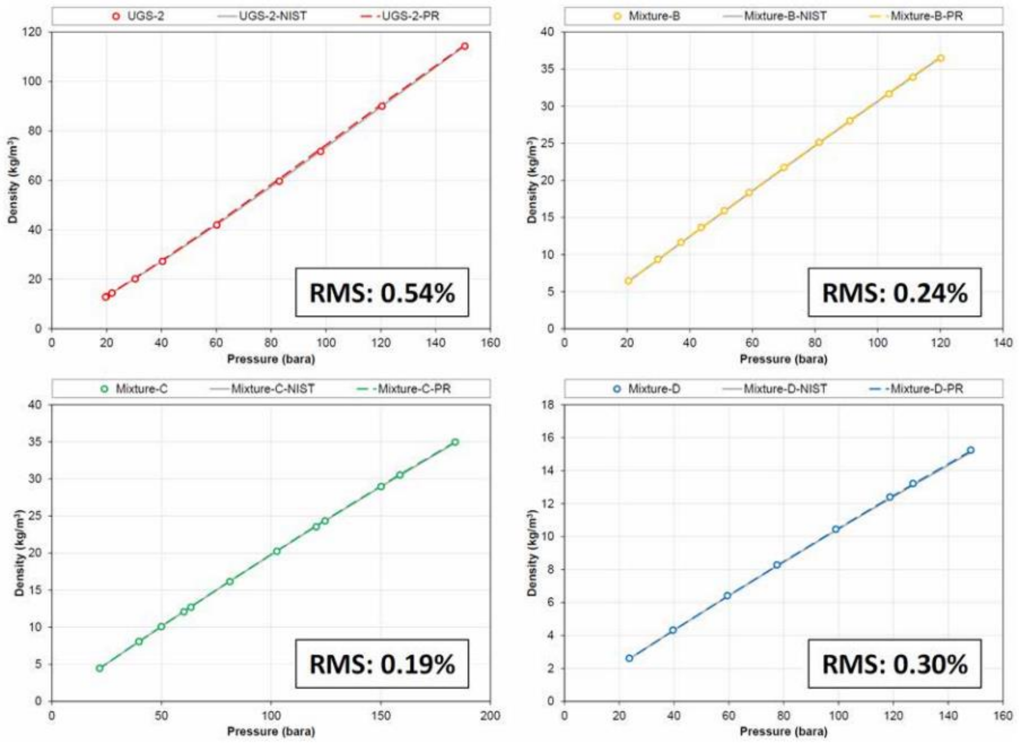

Figure 3.14: Density predictions (circles) for the storage gas (top left), Mixture-B (top right), Mixture-C (bottom left), and Mixture-D (bottom right). The predictions were made with the proposed PR EOS model (dashed line), and GERG2008 (grey solid line). (Nielsen, et al., 2023).

As a result, performing the compositional corrections needed with a tuning methodology, the PR EoS model proposed by the authors shows good accuracy in predicting the volumetric properties of H_2-blend mixtures at pressure and temperature range typical of UHS.

Since from the literature it has been observed that the PR and RKS EoSs, after the required tuning of parameters is performed, are able to predict volumetric properties of hydrogen-containing mixtures with satisfactory accuracy, the tuning of the parameters of such EoSs will be the object of the following sections.

Chapter 4

Optimization Methodology: theory

4.1 Tuning Methodology

The tuning of an EoS is the process of adjusting its parameters in order to achieve a satisfactory match between the experimental PVT data and the selected EoS model. Following the procedure, a number of parameters of the EoS can be adjusted (tuning of EoS parameters), i.e. find suitable parameter values that lead to the optimization of the match between the available experimental data and the EoS predicted thermodynamic behavior of a multicomponent mixture. This process is complicated because it requires careful inspection of the physical interpretation of the values assigned to each tuned parameter. In other words, it is of significant importance to pay particular attention to the physical soundness of the values attributed to the regression parameters apart from attempting to minimize the global error.

In this thesis, Peng – Robinson Equation of State (Eq. 2.33) and Redlich – Kwong – Soave Equation of state (Eq.2.32) are examined.

The constants of these equations, a_c and b, are calculated according to Eq. 2.12 and Eq. 2.13, respectively; Ω_a and Ω_b, which are present in these equations, are experimental values which change according to the EoSs which is used.

The α-function is calculated according to Eq. 2.30, whereas m expression changes according to the EoSs which is used (Eq. 2.36 for PR and Eq. 2.31 for RKS).

The mixing rule used in order to extent the applicability of these EoSs to multicomponent systems is the one used in the work of Soave (1972) (Eqs. 2.57 to 2.59).

In a cubic Equation of State model there are several parameters that can be adjusted. The parameters selected are referred below:

- Ω_a and Ω_b;
- K_{ij} (usually, these coefficients are derived directly from experimental equilibrium data of binary system).

4.2 What is optimization?

The EoS tuning procedure against a set of experimental data is an optimization problem during which the minimization of the global error is attempted by adjusting the values of selected regression parameters (Tassios, et al., 2002).

Optimization can be defined as the act of obtaining the best result under given circumstances. In practice, engineers need to take many technological decisions at several stages. The ultimate goal of all such decisions is either to minimize the effort and cost required or to maximize the desired benefit. Since the effort required or the benefit desired in any practical situation can be expressed as a function of certain decision variables, optimization can be described as the process of finding those variables' values that result to the maximum or minimum value of a function.

If a point x^* (Figure 4.1) corresponds to the value that minimizes the function $f(x)$, the same point also corresponds to the value that maximizes the negative of the function, $-f(x)$. Thus without loss of generality, optimization can be taken to mean minimization since the maximum of a function can be found by seeking the minimum of its negative.

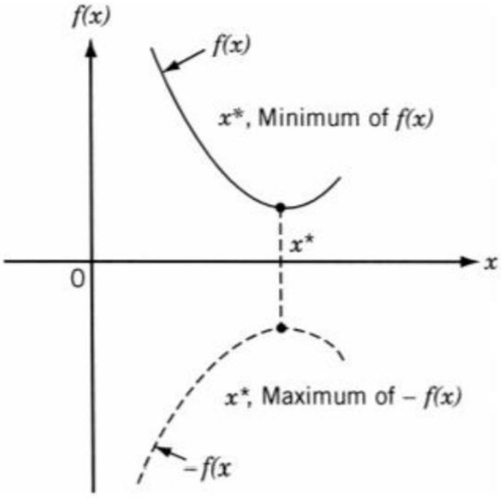

Figure 4.1: Minimum of $f(x)$ is same as maximum of $-f(x)$.

The mathematical function to be optimized is called the objective function and usually contains several variables. An objective function can be a function of a single variable for some practical problems; however, a single variable function may not be challenging from an optimization point of view.

Optimization problems may involve more than one objective function and are known as multi-objective optimization problems. Depending on the nature of the problem, the variables in the model may be real or integer (pure integer or binary integer) or a mix of both. The optimization problem could be either constrained or unconstrained.

It is important to elucidate that optimization solvers have their disadvantages, the most important of which is getting stuck at a local minimum, which is an issue that concerns non-convex problems (the majority of engineering problems are non-convex). Therefore, there is no single method for efficiently tackling all optimization problems. As a result, a number of optimization methods have been developed.

In this Thesis, the regression method that will be used for the fitting is the non-linear least squares.

4.3 The Least Square Problem

The least square problems are a widely used class of optimization problems where the objective function has the following structure:

$$f(k) = \frac{1}{2}\sum_{i=1}^{n} r_i^2(k). \tag{4.1}$$

These kinds of problems are usually the ones where the results of a model need to be compared to experimental ones (Nocedal, et al., 2006). In those cases, the difference between each measured and modeled data is called a residual (usually noted as r_i).

If one wants to fit the data in such a way that both under and over estimates are punished equally, it makes mathematical sense to minimize the sum of squares instead of minimizing the simple sum, since the squares ensure that the value to be minimized is always positive. That way, the minimization problem can be written as:

$$\min_k \frac{1}{2}\sum_{i=1}^{n} r_i^2(k). \tag{4.2}$$

In another notation, the residuals may also be expressed as a vector.

Writing $\mathbf{r}(\mathbf{k}) = \left(r_1(k) \ldots r_n(k)\right)^T$, where $r_i(k)$ are the residuals at each point, the sum of squares can be written in a more compact way by using the ℓ_2 norm:

$$\frac{1}{2}\sum_{i=1}^{n} r_i^2(k) = \frac{1}{2} \| \mathbf{r}(\mathbf{k}) \|_2^2. \tag{4.3}$$

In other terms, the least squares problem involves seeking the line (or curve) that achieves the smallest sum of the squared differences between the observed data points and the corresponding points predicted by the line (or curve).

This method is called "least squares" because it focuses on minimizing the sum of the squares of the residuals.

To illustrate this, let us consider an example.

Suppose we have a set of data points $(x_{\mathrm{i}}, y_{\mathrm{i}})$ and we want to find a line of the form $y = mx + c$ that best represents the relationship between x and y. The least squares method finds the values of m and c that minimize the sum of the squared differences between the observed y_{i} values and the predicted values $(mx_{\mathrm{i}} + c)$.

Mathematically, the least squares problem can be formulated as follows:

$$minimize\ \Sigma(y_{\mathrm{i}} - (mx_{\mathrm{i}} + c))^2$$

To find the optimal values of m and c, we differentiate this expression with respect to m and c, set the derivatives to zero, and solve the resulting system of equations. The solution gives you the values of m and c that minimize the sum of the squared differences.

In this particular study, our objective is to estimate the density value and the compressibility factor while optimizing the values of Ω_a, Ω_b and bip in such a way that a specific model aligns well with the experimental data for the H_2 mixtures.

Therefore, the residual is defined as:

$$\mathbf{r}_1(\mathbf{k}) = \boldsymbol{\rho}_{calc}\left(\mathbf{k}, \mathbf{p}_{exp}\right) - \boldsymbol{\rho}_{exp}, \tag{4.4}$$

$$\mathbf{r}_2(\mathbf{k}) = \mathbf{z}_{calc}\left(\mathbf{k}, \mathbf{p}_{exp}\right) - \mathbf{z}_{exp}, \tag{4.5}$$

where k is the vector of the values we want to optimize (Ω_a, Ω_b and bip), ($\boldsymbol{\rho}_{calc}(\mathbf{k}, \mathbf{p}_{exp})$) and ($\mathbf{z}_{calc}(\mathbf{k}, \mathbf{p}_{exp})$) are the sets of calculated densities and compressibility factor respectively (using a model, i.e.PR, RKS) and ($\boldsymbol{\rho}_{exp}$) and ($\mathbf{z}_{exp}$) are the sets of experimental densities and compressibility factors.

Least squares problems fall into two categories: linear or ordinary least squares and nonlinear least squares, depending on whether or not the residuals are linear in all unknowns.

4.3.1 Linear Least Square Problem

The linear least squares problem is a specific formulation of the least squares problem where the relationship between the variables is assumed to be linear. It is commonly used in linear regression analysis to find the best-fit line that represents the relationship between the independent variable(s) and the dependent variable.

In a linear least square problem, we seek the solution of the following problem:

$$\min_{k} f(k) = \frac{1}{2} \| \mathbf{r}(\mathbf{k}) \|_2^2, \tag{4.6}$$

where the residual is linear in k.

The first step in the minimization problem is to determine the stationary points.

To find a minimum of the objective function (local or global minimum), a first-order necessary condition is (Nocedal, et al., 2006):

If k^* is a local minimizer and f is continuously differentiable in an open neighborhood of k^*,

$$\nabla \mathbf{f}(\mathbf{k}^*) = 0. \tag{4.7}$$

Writing that explicitly, for any k, we obtain:

$$\nabla \mathbf{f}(\mathbf{k}) = \sum_{i=1}^{n} r_i(k) \nabla r(k)_i. \tag{4.8}$$

Since the Jacobian is defined as

$$\mathbf{J}(\mathbf{k}) = \begin{bmatrix} \nabla r_1 \\ \cdots \\ \nabla r_n \end{bmatrix}, \tag{4.9}$$

we can write

$$\boldsymbol{\nabla} \mathbf{f}(\mathbf{k}) = \mathbf{J}(\mathbf{k})^T \mathbf{r}(\mathbf{k}), \tag{4.10}$$

and also

$$\boldsymbol{\nabla}^2 \mathbf{f}(\mathbf{k}) = \mathbf{J}(\mathbf{k})^T \mathbf{J}(\mathbf{k}) + \sum_{\mathbf{i}=\mathbf{1}}^{\mathbf{n}} \mathbf{r}(\mathbf{k})_i \boldsymbol{\nabla}^2 \mathbf{r}_i(\mathbf{k}) = \mathbf{J}(\mathbf{k})^T \mathbf{J}(\mathbf{k}). \tag{4.11}$$

The residual has a linear dependence on k, therefore, its second derivative is zero.

According to Nocedal & Wright (Nocedal, et al., 2006), it is possible to define a matrix $\mathbf{J}$, independent of k, such that:

$$\mathbf{r}_1(\mathbf{k}) = \mathbf{Jk} - \boldsymbol{\rho}_{exp}, \tag{4.12}$$

$$\mathbf{r}_2(\mathbf{k}) = \mathbf{Jk} - \mathbf{z}_{exp}. \tag{4.13}$$

Therefore the gradient and Hessian of the objective function become

$$\nabla \mathbf{f}_1(\mathbf{k}) = \mathbf{J}^T(\mathbf{J}\mathbf{k} - \boldsymbol{\rho}_{exp}), \tag{4.14}$$

$$\nabla^2 \mathbf{f}_1(\mathbf{k}) = \mathbf{J}^T\mathbf{J}; \tag{4.15}$$

$$\nabla \mathbf{f}_2(\mathbf{k}) = \mathbf{J}^T(\mathbf{J}\mathbf{k} - \mathbf{z}_{exp}), \tag{4.16}$$

$$\nabla^2 \mathbf{f}_2(\mathbf{k}) = \mathbf{J}^T\mathbf{J}. \tag{4.17}$$

It is clear from Eq. 4.6 that f(k) is convex. As a consequence, the following theorem holds (Nocedal, et al., 2006):

If $k^* \in \mathbb{R}$ *is a local minimizer, i.e.* $\overline{\nabla f(k^*)} = 0$*, then* k^* *is a global minimizer.*

That is a powerful result in case of a linear objective function, and it permits us to write the following system of equations:

$$\mathbf{J}^T\mathbf{J}\mathbf{k}^* = \mathbf{J}\boldsymbol{\rho}_{exp}, \tag{4.18}$$

$$\mathbf{J}^T\mathbf{J}\mathbf{k}^* = \mathbf{J}\mathbf{z}_{exp}, \tag{4.19}$$

that are known as the normal equations (Nocedal, et al., 2006), and the solution is the minimizer of the linear objective function, that differs mainly on how this equation is solved (Cholesky factorization, QR factorization and so on).

4.3.2 Non-Linear Least Square Problem

The non-linear least squares problem is an extension of the least squares problem that allows for nonlinear relationships between variables. Unlike the linear least squares problem, which assumes a linear relationship between the variables, the nonlinear least squares problem considers models with nonlinear equations.

When the residual function is non-linear, the fitting problem described above needs a more detailed solution, mainly because the structure of the Hessian is more complex. In non-linear problems, we can no longer say that the objective function is always convex and, therefore, the stationary points will be local minima (or maxima), depending on the result of the Hessian calculation.

From the expression of the Hessian

$$\nabla^2 \mathbf{f}(\mathbf{k}) = \mathbf{J}(\mathbf{k})^T \mathbf{J}(\mathbf{k}) + \sum_{\mathbf{i=1}}^{\mathbf{n}} \mathbf{r}(\mathbf{k})_i \nabla^2 \mathbf{r}_i(\mathbf{k})), \tag{4.20}$$

we now need to evaluate the Hessian of the residuals ($\nabla^2 r_i\ (k)$) which is defined as in Eq. 4.21:

$$\mathbf{H}(\mathbf{k}) = \begin{bmatrix} \nabla^2 r_1 \\ \cdots \\ \nabla^2 r_n \end{bmatrix}. \tag{4.21}$$

That requires considerable additional computational effort because an iterative optimization algorithm is typically used.

The algorithm starts with an initial guess of the parameters and it iteratively updates the values based on the observed data. The objective function, which represents the sum of the squared differences, is minimized by adjusting the parameter values in each iteration.

The specific optimization algorithm used depends on the nature of the nonlinear model and the available computational resources. Some common algorithms include the Gauss-Newton method, the Levenberg-Marquardt algorithm, and the trust region method.

Solving the nonlinear least squares problem can be computationally expensive and it may require careful initialization of the parameter values. It is also important to consider the convergence criteria and the possibility of multiple local minima in the optimization process.

4.3.2.1 Gauss Newton Method

This method is used with a line search algorithm, where a descendent search direction $p_j\ s.t. f(k_i + p_j) < f(k_i)$ is chosen. The most important search direction is the Newton direction, derived from the second-order Taylor expansion

$$f(k_i + p_j) \approx \mathbf{f}_J + \mathbf{p}^T \nabla \mathbf{f}_J + \frac{1}{2} \mathbf{p}^T \nabla^2 \mathbf{f}_J, \tag{4.22}$$

where the search direction is the solution obtained by minimizing the above function.

By setting the first derivative to zero

$$p_j^{GN} = -\left(\nabla^2 \mathbf{f}_J\right)^{-1} \nabla \mathbf{f}_J, \tag{4.23}$$

the interest in simplifying the Hessian calculation becomes clear.

The Gauss-Newton method is the simplest method for minimizing the non-linear least square problem and it is based on the principle that the Hessian calculation can be approximated to:

$$\nabla^2 \mathbf{f}_J \approx \mathbf{J}(\mathbf{k})^T \mathbf{J}(\mathbf{k}). \tag{4.24}$$

This simplification holds well (Nocedal, et al., 2006) since there are many situation in which the term $\mathbf{J}(\mathbf{k})^T \mathbf{J}(\mathbf{k})$ is much higher compared to the second one $(\sum_{i=1}^{n} r(k)_i \nabla^2 \mathrm{r_i}(k))$, at least close to the solution, and the convergence rate of Gauss–Newton is similar to that of Newton's method. That will occur when $\|r(k)_i \nabla^2 \mathrm{r_i}(k)\|$ is significantly smaller than the eigenvalues of $\mathbf{J}(\mathbf{k})^T \mathbf{J}(\mathbf{k})$.

This behavior is usually seen when either the residuals $r(k)_i$ are small or when they are nearly affine (so that the $\|\nabla^2 \mathrm{r_i}(k)\|$ are small). Therefore, if the least square solution presents relatively large residuals or the initial guess is too far from the solution, the approximation may no longer be adequate.

4.3.2.2 Levenberg – Marquardt Method

The Levenberg-Marquardt method is an iterative optimization algorithm commonly used to solve nonlinear least squares problems. It is named after the mathematicians Kenneth Levenberg and Donald Marquardt, who independently developed the method ((Levenberg, 1944); (Marquardt, 1963)).

The Levenberg-Marquardt method combines the strengths of two other optimization algorithms: the Gauss-Newton method and the method of gradient descent. It provides a balance between the efficient convergence of the Gauss-Newton method and the robustness of gradient descent which is an optimization technique which iteratively updates the model parameters based on the gradient of the objective function with respect to those parameters. Specifically, the algorithm starts with initializing the parameters, calculates the objective function, computes the gradient, updates the parameters by descending along the gradient direction with a fixed learning rate, and repeats this process until a termination condition is met. The goal is to converge to a local or global minimum of the objective function, achieving the best possible optimization point.

The Levenberg-Marquardt method iteratively updates the parameter values in each step to gradually approach the optimal solution (Fletcher, 1971).

The algorithm begins with an initial estimate of the parameters. At each iteration, it calculates the Jacobian matrix which provides information about the local slope of the model function.

The Levenberg-Marquardt method then adjusts the parameter values by solving a system of equations that combines the information from the Jacobian matrix and a damping factor. The damping factor is introduced to control the step size in each iteration and ensure stable convergence (Press, et al., 2007). If the damping factor is large, the algorithm behaves similarly to gradient descent, taking larger steps to converge quickly. If the damping factor is small, the algorithm behaves more like the Gauss-Newton method, focusing on local improvements.

The Levenberg-Marquardt method dynamically adjusts the damping factor during the optimization process. It starts with a larger damping factor and gradually reduces it as the algorithm gets closer to the optimal solution. This allows for efficient convergence while avoiding overshooting and oscillations.

The convergence of the Levenberg-Marquardt method is determined by the change in the sum of squared differences between iterations. The algorithm continues iterating until the convergence criteria are met, such as reaching a specified tolerance or the number of iterations exceeding a limit.

In the following the description of the algorithm in mathematical terms is reported.

Reminding that we are interested in solving the least square problem posed by Eq. 4.8, we need to define, at each iteration I, a region with radius Δ_i, where the function f will be evaluated using a Taylor-series approximation:

$$\mathbf{f}(\mathbf{k}_i + \mathbf{p}) = \mathbf{f}(\mathbf{k}_i) + \nabla\mathbf{f}(\mathbf{k}_i)^T\mathbf{p} + \frac{1}{2}\mathbf{p}^T\nabla^2\mathbf{f}(\mathbf{k}_i + \mathrm{t}\mathbf{p})\mathbf{p}, \tag{4.25}$$

where $t \in (0,1)$.

The Levenberg–Marquardt method can be obtained by using the same Hessian approximation as in the Gauss-Newton method, but replacing the line search with a trust-region strategy. One motivation to use a trust region strategy is avoid one of the deficiencies of Gauss–Newton method - when the Jacobian is rank-deficient, or nearly so.

Since the same Hessian approximations are used both for Gauss-Newton and Levenberg-Marquardt, the local convergence properties of the two methods are similar (Nocedal, et al., 2006).

Recalling the approximation for the Hessian (Eq. 4.24; Eq. 4.25), the previous equation can be written as (Nocedal, et al., 2006):

$$\mathbf{m}_i(\mathbf{p}) = \frac{1}{2}\|\mathbf{r}(\mathbf{k}_i)\|_2^2 + \mathbf{p}^T\mathbf{J}_i(\mathbf{k})\mathbf{r}(\mathbf{k}_i) + \frac{1}{2}\mathbf{p}^T\mathbf{J}_i(\mathbf{k})^T\mathbf{J}_i(\mathbf{k})\mathbf{p}, \qquad (4.26)$$

where $\mathbf{m_i}(\mathbf{p})$ is the model function of the objective function f at each iteration i, that is supposed to be a good approximation of the function in a region of radius p, sufficiently small.

At each iteration the following sub problem needs to be solved:

$$\min_{\mathrm{p}}\|\mathbf{J}_i\mathbf{p} + \mathbf{r}(\mathbf{k}_i)\| \ \textit{subject to}\ \|\mathbf{p}\| \le \Delta_i. \qquad (4.27)$$

The solution of the minimization algorithm can be classified in the following way:

1. If a solution of the Gauss-Newton step lies inside the trust region, i.e. $p_j^{GN} < \Delta_j$, then it will also be a solution to Eq. 4.26,
2. Otherwise, there is a $\lambda > 0$ such that the solution $p_j^{LM} = \|\Delta_\mathrm{j}\|$ and $(\mathbf{J}_i^T\mathbf{J}_i + \lambda I)p = -\mathbf{J}_i^T r_j$.

To find a λ that satisfies the conditions above, a root finding algorithm based on the Cholesky or QR factorization may be used (Alfriend, et al., 2010).

4.3.2.3 Trust region reflective algorithm

The trust region algorithm is an iterative optimization method commonly used to solve unconstrained and constrained nonlinear optimization problems. It aims to find the optimal solution within a region around the current iterate, called the trust region (Nocedal, et al., 2006).

In the trust region algorithm, the optimization problem is typically defined as minimizing an objective function $f(x)$ subject to some constraints. The algorithm starts with an initial estimate of the solution, denoted as x_0.

At each iteration, the trust region algorithm approximates the objective function using a local model, such as a quadratic or cubic model, that represents the behavior of the function within the trust region. This local model is based on the current iterate and is used to guide the search for the optimal solution.

The trust region algorithm defines a trust region radius, which determines the size of the region around the current iterate where the local model is considered accurate. Initially, the trust region is large, allowing for a more exploratory search. As the algorithm progresses, the trust region typically shrinks to focus the search around the most promising areas. In each iteration, the trust region algorithm solves a subproblem within the trust region. This subproblem involves minimizing the local model subject to the trust region constraint. The solution to this subproblem provides a new candidate iterate for the next iteration.

The trust region algorithm evaluates the quality of the candidate iterate by comparing the actual reduction in the objective function with the predicted reduction based on the local model. If the candidate iterate provides a sufficient reduction and satisfies additional criteria, such as satisfying constraints, it is accepted as the new iterate. Otherwise, the trust region is adjusted, and a new candidate iterate is generated.

The process continues iteratively until a termination condition is met, such as reaching a specified tolerance, exceeding a maximum number of iterations, or satisfying convergence criteria.

In this work, the trust region reflective algorithm was used as implemented in Matlab ((Branch, et al., 1999); (Coleman, et al., 1994)).

Chapter 5

Optimization of PR and RKS EoSs parameters

For the purpose of optimizing the binary interaction parameter (BIP), Ω_a and Ω_b, the non-linear least square problem was solved using a Matlab optimization code. To this end, the function *lsqcurvefit*, which part of the Optimiztion Toolbox, was used (https://it.mathworks.com/help/optim/ug/lsqcurvefit.html).

lsqcurvefit finds the coefficient x that solve the problem

$$\min_{x} \| F(x, xdata) - ydata \|_2^2 = \min_{x} \sum_{i} (F(x, xdata_i - ydata_i)^2, \qquad (5.1)$$

given input data $xdata$, and the observed output $ydata$, where $xdata$ and $ydata$ are matrices or vectors, and $F\ (x, xdata)$ is a matrix-valued or vector-valued function of the same size as $ydata$.

In this thesis the focus is on the optimization of Ω_a, $\Omega_b$and BIP parameters so the data calculated with a given EoS model (i.e., PR or RKS) fit the experimental data for the H_2-CH_4 mixtures.

In order to find the compressibility factor (z – factor) and the density, the equations of state have been rearranged to obtain an expression explicit respectively in the compressibility factor and in the density.

PR equation of state has been rearranged in order to obtain an expression explicit in z (Eq. 5.2), where A and B are given by Eq. 5.3 and Eq. 5.5 respectively, and an expression explicit in v (Eq. 5.6), where v is the molar volume ($kmol/m^3$) and from which the density can be obtained by Eq. 5.7, where MM is the molar mass of the mixture considered:

$$z^3 + z^2(B-1) + z(A - 3B^2 - 2B) + B^3 + B^2 - AB = 0, \tag{5.2}$$

$$A = \frac{ap}{R^2T^2}, \tag{5.3}$$

$$a = a_c\alpha(T), \tag{5.4}$$

$$B = \frac{bp}{RT}, \tag{5.5}$$

$$pv^3 + v^2(pb - RT) + v(a - 3b^2p - 2RTb) + pb^3 + RTb^2 - ab = 0\,, \tag{5.6}$$

$$\rho = v^{-1} \cdot MM. \tag{5.7}$$

The constants a_c and b are given by Eq. 2.12 and Eq. 2.13, respectively; the α-function is calculated by Eq. 2.30 and m by Eq. 2.36.

RKS equation of state has been rearranged in order to obtain an expression explicit in z (Eq. 5.8), where A and B are given by Eq. 5.3 and Eq. 5.5 respectively, and an expression explicit in v (Eq. 5.9), where v is the molar volume ($kmol/m^3$) and from which the density can be obtained by Eq. 5.7:

$$z^3 - z^2 + z(A - B^2 - B) - AB = 0, \tag{5.8}$$

$$pv^3 - RTv^2 + v(a - b^2p - RTb) - ab = 0. \tag{5.9}$$

The constants a_c and b are given by Eq. 2.12 and Eq. 2.13, respectively; the α-function is calculated by Eq. 2.30 and m by Eq. 2.31.

Since we are dealing with mixtures, a mixing rule has to be adopted: as said previoulsy, the mixing rule used is the one that Soave used in his work (Eq. 2.57 to Eq. 2.59).

Since we are dealing with binary mixtures, the mixing rule reduces to:

$$a_{mix} = y_1^2a_1 + y_2^2a_2 + \left(1 - K_{i,j}\right)2y_1y_2(a_1a_2)^{0.5}, \tag{5.10}$$

$$b_{mix} = b_1y_1 + b_2y_2, \tag{5.11}$$

where a_{mix} and b_{mix} are the parameters of the mixture, whereas with 1 we indicate the 1st component and with 2 we indicate the 2nd component.

The equations 5.2, 5.6, 5.8 and 5.9 are all cubic equations which have one real root and two complex roots because we are dealing with mixtures at thermodynamic conditions far from the critical point and therefore they are always found in the vapour phase and phase change never occurs (dry gas).

The equations have been solved in Matlab as shown in the following figures.

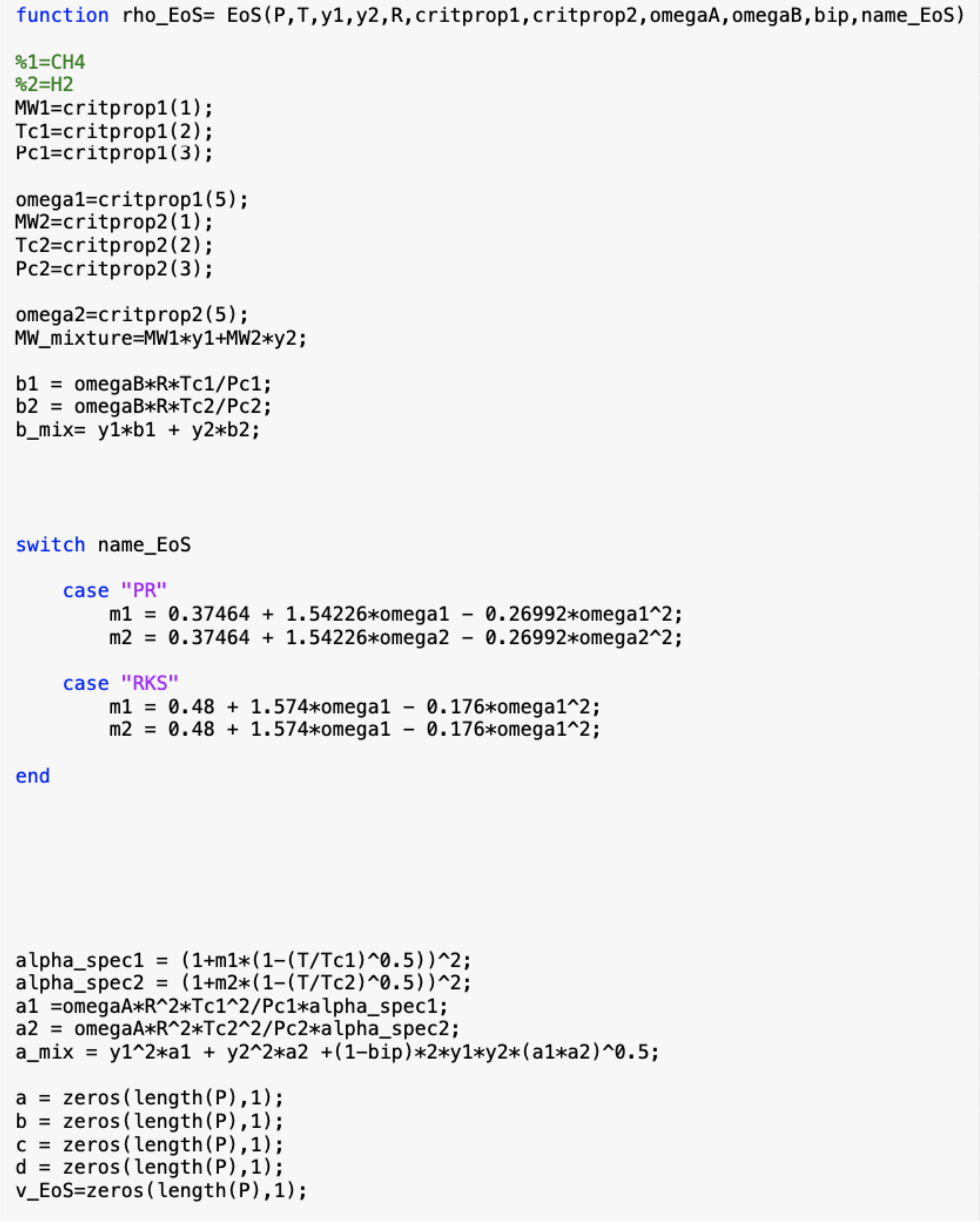

```
function rho_EoS= EoS(P,T,y1,y2,R,critprop1,critprop2,omegaA,omegaB,bip,name_EoS)

%1=CH4
%2=H2
MW1=critprop1(1);
Tc1=critprop1(2);
Pc1=critprop1(3);

omega1=critprop1(5);
MW2=critprop2(1);
Tc2=critprop2(2);
Pc2=critprop2(3);

omega2=critprop2(5);
MW_mixture=MW1*y1+MW2*y2;

b1 = omegaB*R*Tc1/Pc1;
b2 = omegaB*R*Tc2/Pc2;
b_mix= y1*b1 + y2*b2;



switch name_EoS

    case "PR"
        m1 = 0.37464 + 1.54226*omega1 - 0.26992*omega1^2;
        m2 = 0.37464 + 1.54226*omega2 - 0.26992*omega2^2;

    case "RKS"
        m1 = 0.48 + 1.574*omega1 - 0.176*omega1^2;
        m2 = 0.48 + 1.574*omega1 - 0.176*omega1^2;

end





alpha_spec1 = (1+m1*(1-(T/Tc1)^0.5))^2;
alpha_spec2 = (1+m2*(1-(T/Tc2)^0.5))^2;
a1 =omegaA*R^2*Tc1^2/Pc1*alpha_spec1;
a2 = omegaA*R^2*Tc2^2/Pc2*alpha_spec2;
a_mix = y1^2*a1 + y2^2*a2 +(1-bip)*2*y1*y2*(a1*a2)^0.5;

a = zeros(length(P),1);
b = zeros(length(P),1);
c = zeros(length(P),1);
d = zeros(length(P),1);
v_EoS=zeros(length(P),1);
```

```
switch name_EoS

   case "PR"

for jj=1:length(P)
    a(jj,1) = P(jj);
    b(jj,1) = P(jj)*b_mix - R*T;
    c(jj,1) = a_mix - 2*b_mix*R*T - 3*b_mix^2*P(jj);
    d(jj,1) = -a_mix*b_mix + b_mix^2*R*T...
                + P(jj)*b_mix^3;
    r = [a(jj) b(jj) c(jj) d(jj)];
    v = sort(roots(r));
            for ii=1:3
                   if  imag(v(ii))==0
                       v_EoS(jj)=v(ii);
                   end
            end
end

    case "RKS"

for jj=1:length(P)
    a(jj) = P(jj);
    b(jj) = - R*T;
    c(jj) = a_mix - b_mix*R*T-P(jj)*(b_mix^2);
    d(jj) = -a_mix*b_mix;
    r = [a(jj) b(jj) c(jj) d(jj)];
    v = sort(roots(r));
             v = sort(roots(r));
            for ii=1:3
                   if  imag(v(ii))==0
                       v_EoS(jj)=v(ii);
                   end
            end
end

end

rho_EoS = MW_mixture./v_EoS;

end
```

Figure 5.1: Matlab function to solve EoSs explicit in v (Eq. 5.6 and Eq.5.9).

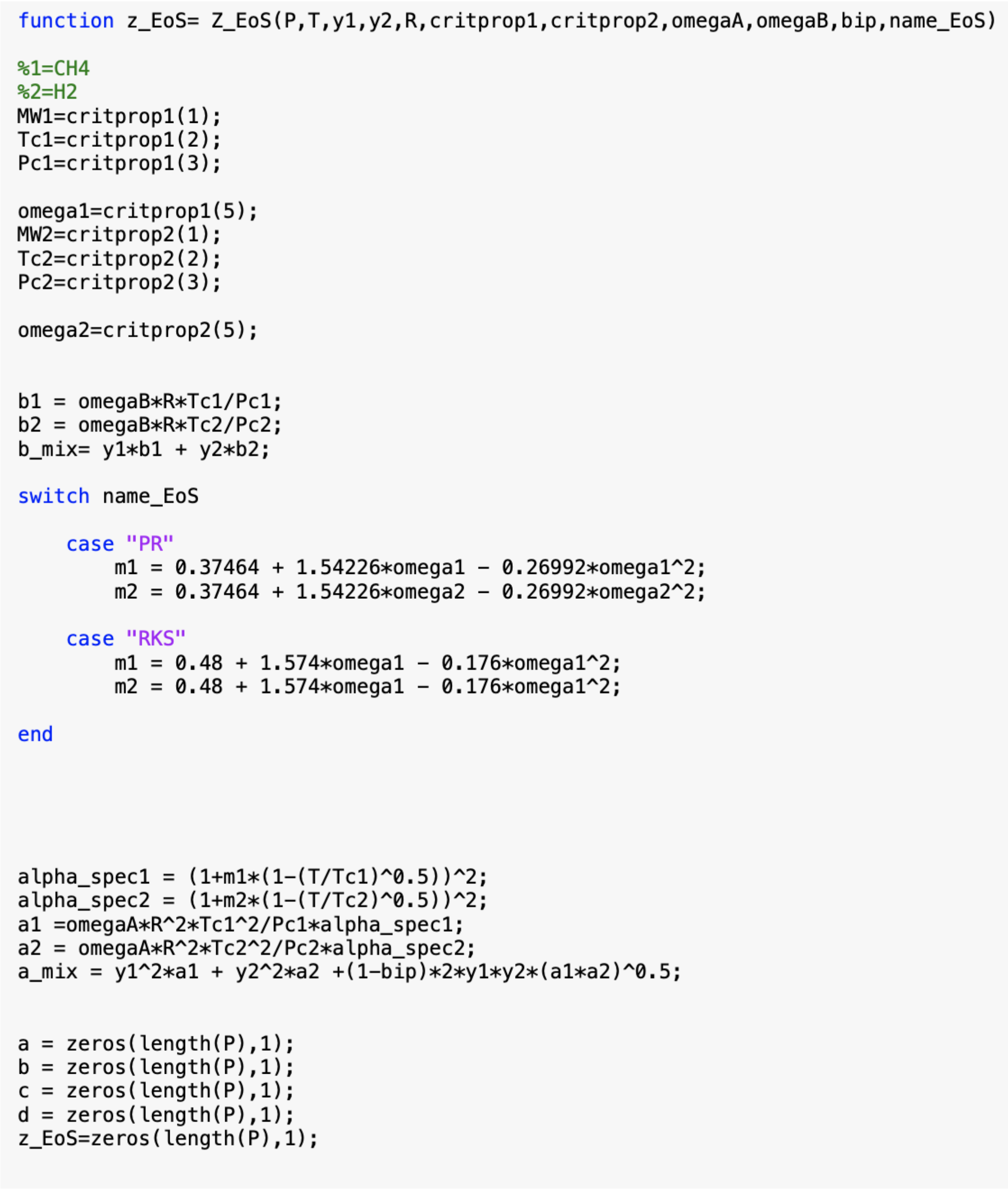

```
function z_EoS= Z_EoS(P,T,y1,y2,R,critprop1,critprop2,omegaA,omegaB,bip,name_EoS)

%1=CH4
%2=H2
MW1=critprop1(1);
Tc1=critprop1(2);
Pc1=critprop1(3);

omega1=critprop1(5);
MW2=critprop2(1);
Tc2=critprop2(2);
Pc2=critprop2(3);

omega2=critprop2(5);


b1 = omegaB*R*Tc1/Pc1;
b2 = omegaB*R*Tc2/Pc2;
b_mix= y1*b1 + y2*b2;

switch name_EoS

    case "PR"
        m1 = 0.37464 + 1.54226*omega1 - 0.26992*omega1^2;
        m2 = 0.37464 + 1.54226*omega2 - 0.26992*omega2^2;

    case "RKS"
        m1 = 0.48 + 1.574*omega1 - 0.176*omega1^2;
        m2 = 0.48 + 1.574*omega1 - 0.176*omega1^2;

end





alpha_spec1 = (1+m1*(1-(T/Tc1)^0.5))^2;
alpha_spec2 = (1+m2*(1-(T/Tc2)^0.5))^2;
a1 =omegaA*R^2*Tc1^2/Pc1*alpha_spec1;
a2 = omegaA*R^2*Tc2^2/Pc2*alpha_spec2;
a_mix = y1^2*a1 + y2^2*a2 +(1-bip)*2*y1*y2*(a1*a2)^0.5;


a = zeros(length(P),1);
b = zeros(length(P),1);
c = zeros(length(P),1);
d = zeros(length(P),1);
z_EoS=zeros(length(P),1);
```

```
switch name_EoS

    case "PR"

for jj=1:length(P)
    B= b_mix*P(jj)/(R*T);
    A= a_mix*P(jj)/(R^2*T^2);
    a(jj,1) = 1;
    b(jj,1) = B - 1;
    c(jj,1) = -3*B^2-2*B+A;
    d(jj,1) = B^3+B^2-A*B;
    r = [a(jj) b(jj) c(jj) d(jj)];
    z = sort(roots(r));
           for ii=1:3
                if imag(z(ii))==0
                     z_EoS(jj)=z(ii);
                 else
                     continue
                 end
            end

end

    case "RKS"

    for jj=1:length(P)
    a(jj) = 1;
    b(jj) = - 1;
    c(jj) = -((b_mix*P(jj))^2)/(R*T)^2-(b_mix*P(jj))/(R*T)+(a_mix*P(jj))/(R*T)^2;
    d(jj) = -((P(jj)^2)/(R*T)^3)*a_mix*b_mix;
    r = [a(jj) b(jj) c(jj) d(jj)];
   z = sort(roots(r));
           for ii=1:3
                if imag(z(ii))==0
                     z_EoS(jj)=z(ii);
                 else
                     continue
                 end
            end
     end
end
end
```

Figure 5.2: Matlab function to solve EoSs explicit in *z* (Eq. 5.2 and Eq.5.8).

5.1 Optimization procedure

As said previously, the parameters to be optimized are referred below:

- Ω_a and Ω_b;
- K_{ij} which is the binary interaction parameter.

To use *lsqcurvefit* you need to provide some key information: the nonlinear regression model which is the mathematical function that specifies the functional form of the relationship between the independent variables and the dependent variable (in our case Z_EoS and EoS), the experimental data, and an initial guess of the model parameters.

Here is an overview of the general steps to use *lsqcurvefit*:

1. Define the model.
   Before using *lsqcurvefit*, we need to define the mathematical model function that we want to fit to the experimental data. The model function should take a parameter vector as input and return a vector of predicted values.
2. Prepare the data.
   Organize the experimental data into input vectors or matrices x and the corresponding output values y. Make sure the data is properly arranged for the model fitting.
3. Define initial parameters.
   Specify an initial starting point for the parameter vector. These initial values provide a starting estimate for the optimization process.
4. Call *lsqcurvefit*.
   Run *lsqcurvefit* by using the model function, initial parameter values, input data x, and output data y as arguments. It is also possible to provide additional options or constraints.
5. Obtain the fitted parameters and residuals.
   After the fitting process is complete, *lsqcurvefit* returns the optimized parameter values that best fit the model to the data.
6. Analyze and evaluate the fit.
   Once we have obtained the fitted parameters, we can analyze the results, such as assessing the goodness of the fit, plotting the fitted curve against the data.

The *lsqcurvefit* function uses iterative optimization algorithms to minimize the sum of the squared differences between the observed data and the predicted values based on the model. It adjusts the parameter values iteratively until convergence is achieved, aiming to find the best-fit solution.

The default optimization algorithm used by *lsqcurvefit* is the Levenberg-Marquardt algorithm.

Beside the Levenberg-Marquardt algorithm, other algorithms can be used by *lsqcurvefit*, such as the trust region method.

The choice between using the trust region method or the Levenberg-Marquardt algorithm depends on the specific problem and data characteristics. The trust region option can be useful for constrained optimization problems or when you need to balance exploration and the use of local information.

In MATLAB, the trust region option can be specified using the *'Algorithm'* option in the *lsqcurvefit* function. The Levenberg-Marquardt algorithm is the default setting and can be used without specifying any additional options.

The function programmed in Matlab for performing the optimization process is showed in the following figure.

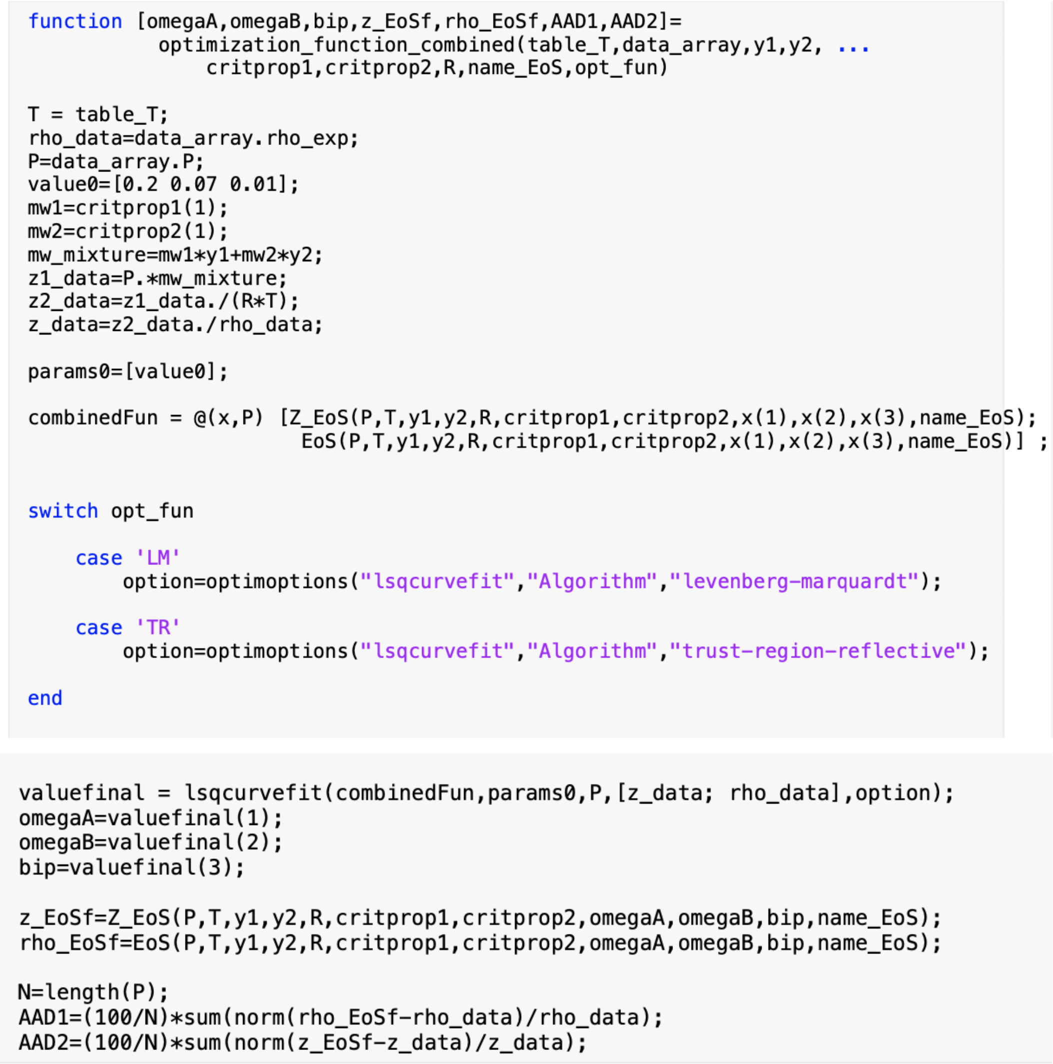

```
function [omegaA,omegaB,bip,z_EoSf,rho_EoSf,AAD1,AAD2]=
           optimization_function_combined(table_T,data_array,y1,y2, ...
               critprop1,critprop2,R,name_EoS,opt_fun)

T = table_T;
rho_data=data_array.rho_exp;
P=data_array.P;
value0=[0.2 0.07 0.01];
mw1=critprop1(1);
mw2=critprop2(1);
mw_mixture=mw1*y1+mw2*y2;
z1_data=P.*mw_mixture;
z2_data=z1_data./(R*T);
z_data=z2_data./rho_data;

params0=[value0];

combinedFun = @(x,P) [Z_EoS(P,T,y1,y2,R,critprop1,critprop2,x(1),x(2),x(3),name_EoS);
                       EoS(P,T,y1,y2,R,critprop1,critprop2,x(1),x(2),x(3),name_EoS)] ;


switch opt_fun

    case 'LM'
        option=optimoptions("lsqcurvefit","Algorithm","levenberg-marquardt");

    case 'TR'
        option=optimoptions("lsqcurvefit","Algorithm","trust-region-reflective");

end
```

```
valuefinal = lsqcurvefit(combinedFun,params0,P,[z_data; rho_data],option);
omegaA=valuefinal(1);
omegaB=valuefinal(2);
bip=valuefinal(3);

z_EoSf=Z_EoS(P,T,y1,y2,R,critprop1,critprop2,omegaA,omegaB,bip,name_EoS);
rho_EoSf=EoS(P,T,y1,y2,R,critprop1,critprop2,omegaA,omegaB,bip,name_EoS);

N=length(P);
AAD1=(100/N)*sum(norm(rho_EoSf-rho_data)/rho_data);
AAD2=(100/N)*sum(norm(z_EoSf-z_data)/z_data);
```

Figure 5.3: Matlab function to solve the optimization problem.

The *lsqcurvefit* has been implemented as follow:

```
valuefinal = lsqcurvefit(combinedFun,params0,P,[z_data; rho_data],option)
```

Where combinedFun includes the density and the compressibility factor calculated from the EoS called (‘name_EoS’), i.e. PR or RKS, P and z_data and rho_data are the experimental data to be fitted.

It should be noted that the optimization is based both on the z_data and on the rho_data, so the algorithm is used for the fitting of the two functions (Z_EoS and EoS) to two sets of data ((z_data, P); (rho_data, P)).

The algorithm implemented is the following:

1- Define the functions that need to be implemented simultaneously.
   The functions are:
   - Z_EoS(P,T,y1,y2,R,critprop1,critprop2,x(1),x(2),x(3),name_EoS)
   - EoS(P,T,y1,y2,R,critprop1,critprop2,x(1),x(2),x(3),name_EoS).

   These functions receive the experimental values (P, T, y1, y2), the data of each species needed for calculating the two properties (R, critprop1, critprop2), the parameters that need to be optimized which are indicated as x(1), x(2), x(3) and are respectively Ω_a, Ω_b and the binary interaction parameter.
2- Create a function “combinedFun” which is a handle to a function that combines “Z_EoS” and “EoS” together.
3- Call that function using an anonymous function, defining P and x (which is a vector that includes Ω_a, Ω_b and the binary interaction parameter) as the variables.

   ```
   combinedFun=@(x,P)
   [Z_EoS(P,T,y1,y2,R,critprop1,critprop2,x(1),x(2),x(3),name_EoS);
   EoS(P,T,y1,y2,R,critprop1,critprop2,x(1),x(2),x(3),name_EoS)].
   ```

4- Define an initial guess for the parameters that need to be optimized, which are Ω_a, Ω_b and the binary interaction parameter; the initial guesses are included in the vector “value0”.
5- Call the optimization function.

   ```
   valuefinal=lsqcurvefit(combinedFun,params0,P,[z_data; rho_data],option)
   ```

   where “valuefinal” is the vector that includes the value of Ω_a, Ω_b and the binary interaction parameter optimized and “params0” is the vector “value0”.

The “option” changes according to the type of optimization algorithm one wants to implement. In fact when one calls the function, also the “opt_fun” needs to be defined and one can choose between the Levenberg-Marquardt algorithm and the trust region method, as shown in the following piece of code:

```
Switch opt_fun

  case ‘LM’
    option=optimoptions(“lsqcurvefit”,”Algorithm”,”92evenberg-marquardt”);

  case ‘TR’
    option=optimoptions(“lsqcurvefit”,”Algorithm”,”trust-region-reflective”);

end
```

6- Calculate the average absolute deviation (AAD%) as shown in the following equations.

$$AAD\%(\rho) = \frac{100}{N}\sum_{i=1}^{N}\frac{\left|\rho_{EoS} - \rho_{exp}\right|}{\rho_{exp}}, \tag{5.12}$$

$$AAD\%(z) = \frac{100}{N}\sum_{i=1}^{N}\frac{\left|z_{EoS} - z_{exp}\right|}{z_{exp}}, \tag{5.13}$$

where N is the number of experimental data.

5.2 Experimental Data

The EoS tuning procedure is applied using the experimental data from Hernández-Gómez et al. (Hernández-Gómez, et al., 2018), who measured the density of the mixtures tested at different pressure and temperature.

Three (CH_4 + H_2) binary mixtures were prepared by the Federal Institute for Materials Research and Testing (Bundesanstalt für Materialforschung und -prüfung, BAM) in Berlin, Germany, according to the ISO 6142-1 ((Hernández-Gómez, et al., 2018); (ISO 6142-1, 2015)).

The preparation of the mixtures was carried out as follows. In the first step, the equimolar mixture of (0.50 CH_4 + 0.50 H_2) was prepared by introducing pure hydrogen followed by pure methane into an evacuated recipient cylinder.

The other two binary mixtures were subsequently prepared by diluting a predefined amount of the (0.50 CH_4 + 0.50 H_2) parent mixture with a known amount of methane.

Experimental (p, ρ, and T) data for the three (CH_4 + H_2) binary mixtures were obtained at temperatures of 240, 250, 260, 275, 300, 325, and 350 K and pressures up to 20 MPa. During the measurements, the pressure was reduced in 1 MPa steps from 20 to 1 MPa for each isotherm.

The experimental data obtained are reported in the paper of Hernández-Gómez (Hernández-Gómez, et al., 2018); an example of how the data are reported in the paper is shown in Table 5.1.

Table 5.1: Experimental data - Mixture 50% CH_4 + 50% H_2. (Hernández-Gómez, et al., 2018).

T (K)	p (Mpa)	ρ (kg/m^3)
240,069	19,008	88,009
240,071	18,016	83,857
240,07	17,008	79,535
240,069	16,013	75,179
240,068	15,002	70,674
240,069	14,011	66,173
240,069	13,003	61,522
240,069	12,005	56,857
240,069	11,006	52,137
240,069	10,006	47,368
240,069	9,002	42,553
240,069	8,003	37,747
240,069	7	32,918
240,07	6,003	28,124
240,07	5	23,326
240,07	4,003	18,584
240,073	3,002	13,857
240,071	2	9,174
240,069	1	4,558

The data have been subdivided according to the temperature values and average values of T have been considered for every range: six values of temperature have been identified for the mixture 50% CH_4 + 50% H_2 and seven for the other two mixtures.

Table 5.2: Average Temperatures - Mixture 50% CH_4 + 50% H_2. (Hernández-Gómez, et al., 2018).

T (K)
240.06945
250.0365
260.0314
275.0048
324.9593
349.9473

Table 5.3: Average Temperatures - Mixture 90% CH_4 + 10% H_2. (Hernández-Gómez, et al., 2018).

T (K)
240.0758
250.0455
260.0449
275.0120
299.9567
324.9635
349.9505

Table 5.4: Average Temperatures - Mixture 95% CH_4 + 05% H_2. (Hernández-Gómez, et al., 2018).

T (K)
240.0758
250.0456
260.0403
275.0140
299.9581
324.9654
349.9494

The critical properties, molar masses and acentric factors of H_2 and CH_4 are listed in Table 5.5.

Table 5.5: Critical properties, molar masses and acentric factors.

	MW (kg/kmol)	**T_c (K)**	**P_c (bar)**	**v_c (m^3/kmol)**	**ω (-)**
H2	2.01588	33.19	12.9999975	0.065	-0.218
CH4	16.04246	190.564	46.04208	0.098	0.013

5.3 Sensitivity analysis of EoS parameters on z-factor and density

Before performing the tuning of the EoSs parameters according to the optimization procedure described previously, a sensitivity analysis on how Ω_a, Ω_b and BIP influence the density and the compressibility factor is presented. The sensitivity analysis is performed both for RKS and PR models and for the range of temperature and pressure reported in the data presented in the Section 5.2. The variations of z – factor and density are tested first against the variation of Ω_a, then against the variation of Ω_b and finally against the variation of the BIP, while the parameters which are not changed are kept constant and equal to default values.

5.3.1 Sensitivity analysis: RKS EoS Results

When performing the sensitivity analysis using the RKS model, the default values of Ω_a, Ω_b and BIP are reported in the following table.

Table 5.6: Default values of Ω_a, Ω_b and BIP for RKS EoS.

Ω_a	Ω_b	**BIP**
0.427447	0.08664	-0.15

First, the variations of z – factor and density are tested varying Ω_a. Ω_a values are changed in the range 0.1 to 1, because that is the range of values usually found for that parameter. Figures 5.3, 5.4 and 5.5 show the calculated density for each value of Ω_a tested for the three mixtures of H_2-CH_4 and the figures 5.6, 5.7 and 5.8 show the calculate z-factor for each value of Ω_a tested for the three mixtures of H_2-CH_4.

$\boldsymbol{\Omega_a} \uparrow \boldsymbol{\rho} \uparrow$

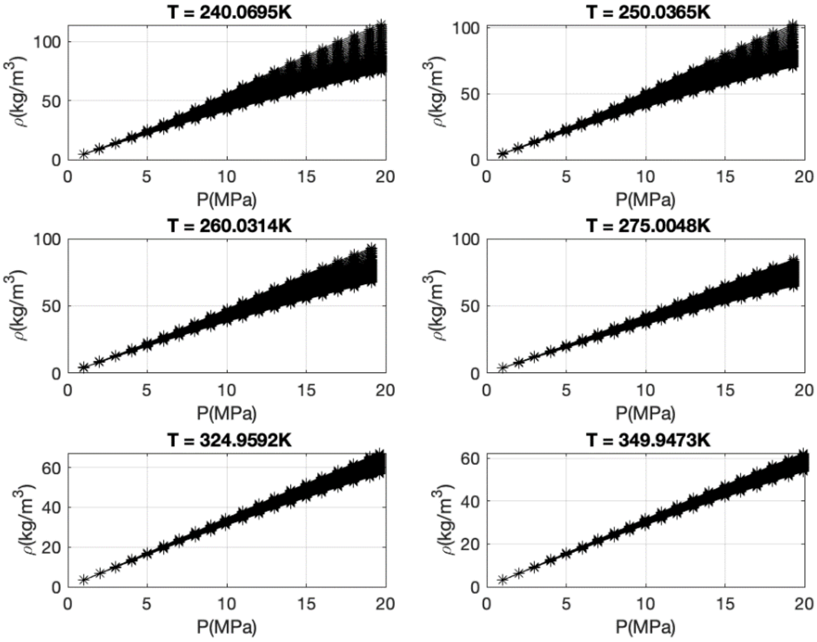

Figure 5.4: Variation of Ω_a – density – 50% CH_4 + 50% H_2, RKS.

$\boldsymbol{\Omega_a} \uparrow \boldsymbol{\rho} \uparrow$

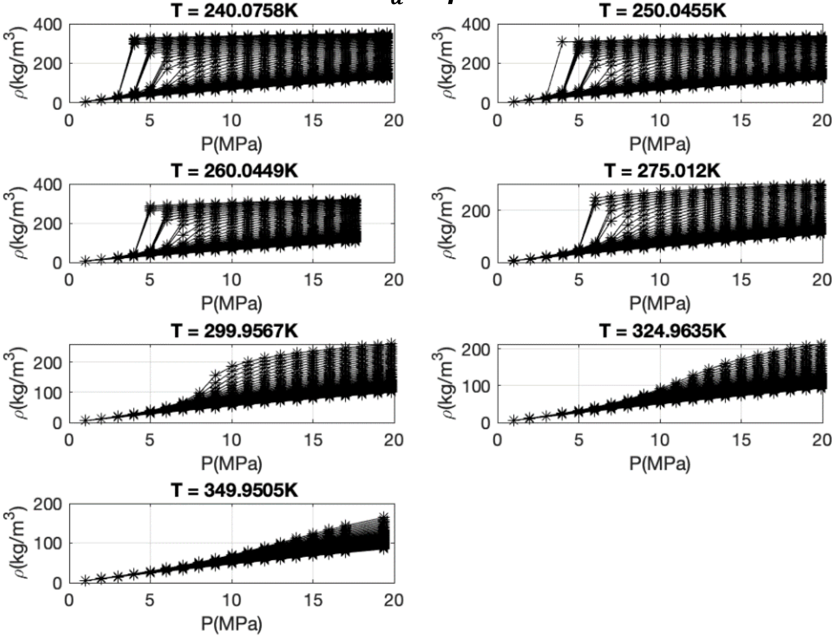

Figure 5.5: Variation of Ω_a – density – 90% CH_4 + 10% H_2, RKS.

$\boldsymbol{\Omega_a} \uparrow \boldsymbol{\rho} \uparrow$

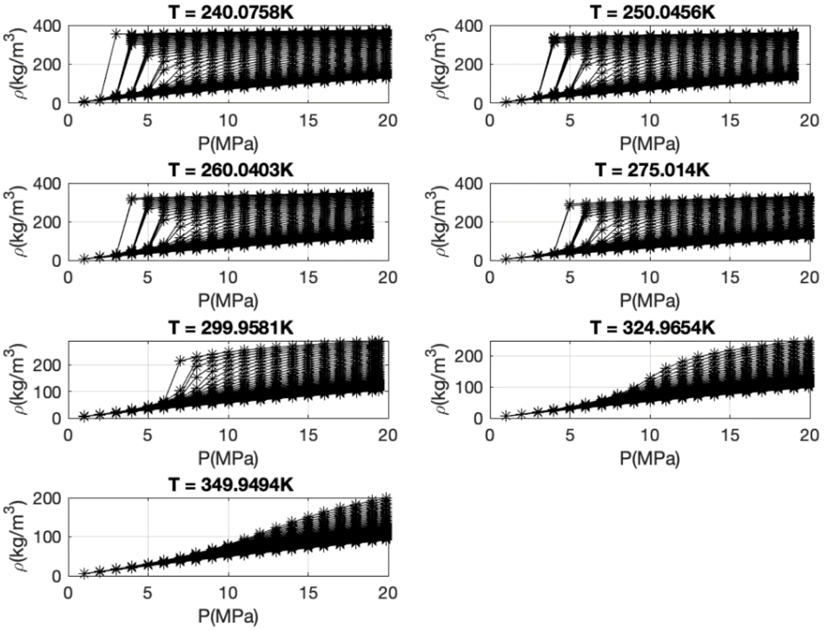

Figure 5.6: Variation of Ω_a – density – 95% CH_4 + 05% H_2, RKS.

$\boldsymbol{\Omega_a} \uparrow \boldsymbol{z} \downarrow$

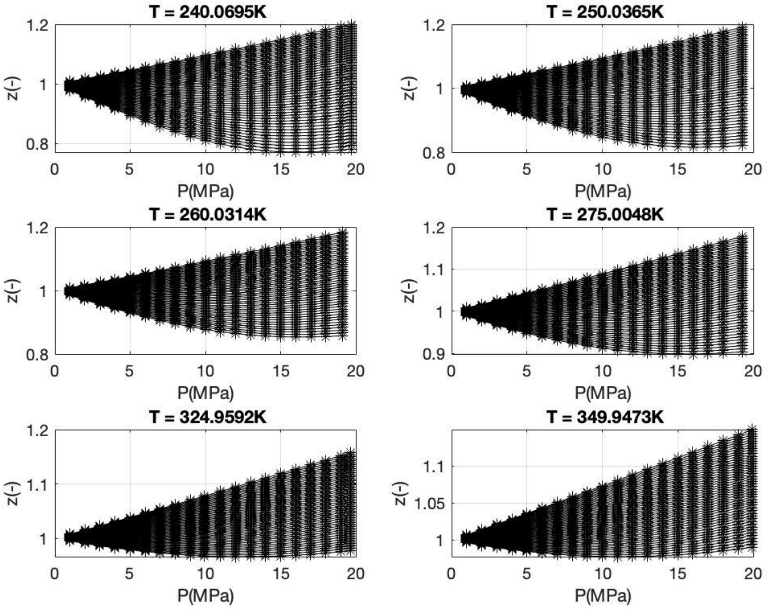

Figure 5.7: Variation of Ω_a – z-factor – 50% CH_4 + 50% H_2, RKS.

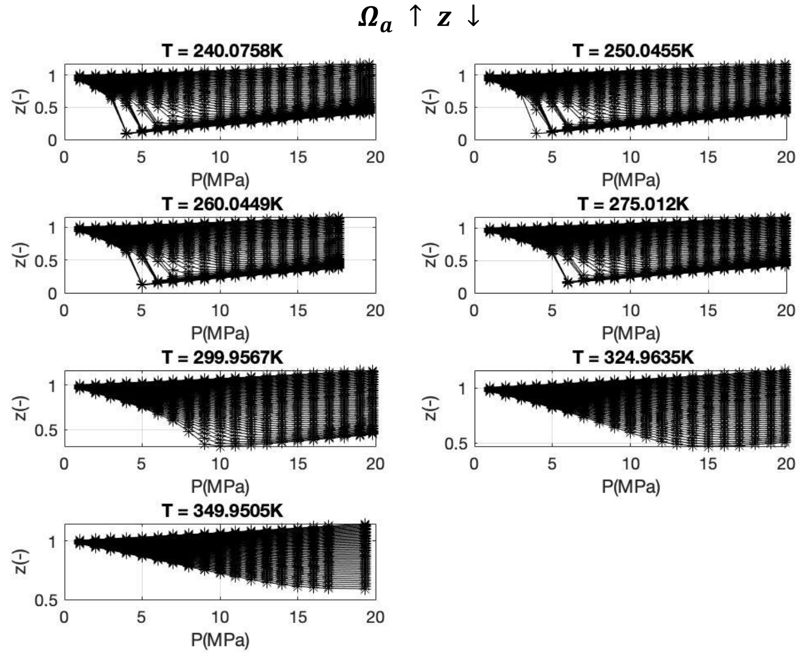

Figure 5.8: Variation of Ω_a – z-factor – 90% CH_4 + 10% H_2, RKS.

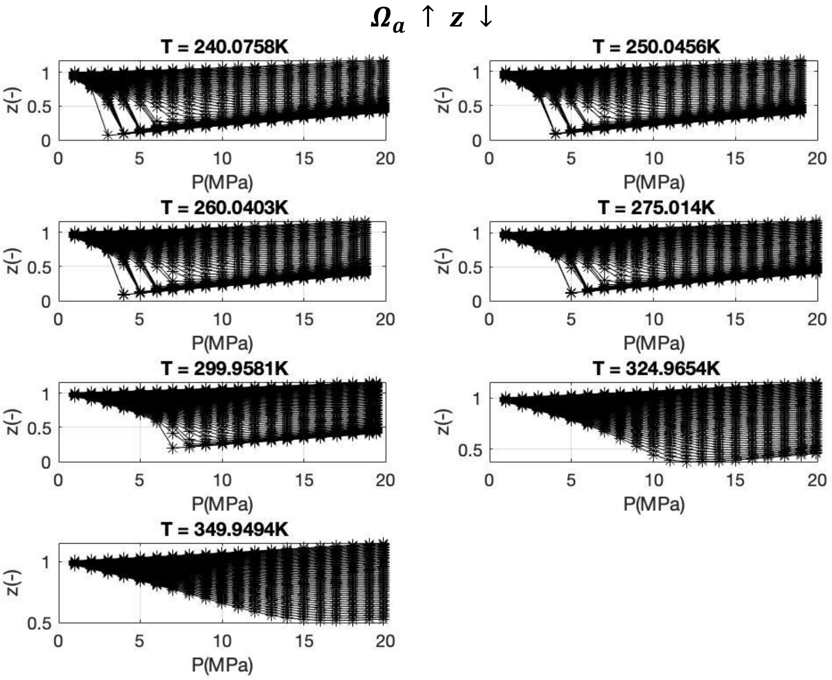

Figure 5.9: Variation of Ω_a – z-factor – 95% CH_4 + 05% H_2, RKS.

Then, the variations of z – factor and density are tested varying Ω_b. Ω_b values are changed in the range 0.01 to 0.1, because that is the range of values usually found for that parameter. Figures 5.10, 5.11 and 5.12 show the calculated density for each value of Ω_b tested for the three mixtures of H_2-CH_4 and the figures 5.13, 5.14 and 5.15 show the calculate z-factor for each value of Ω_b tested for the three mixtures of H_2 - CH_4.

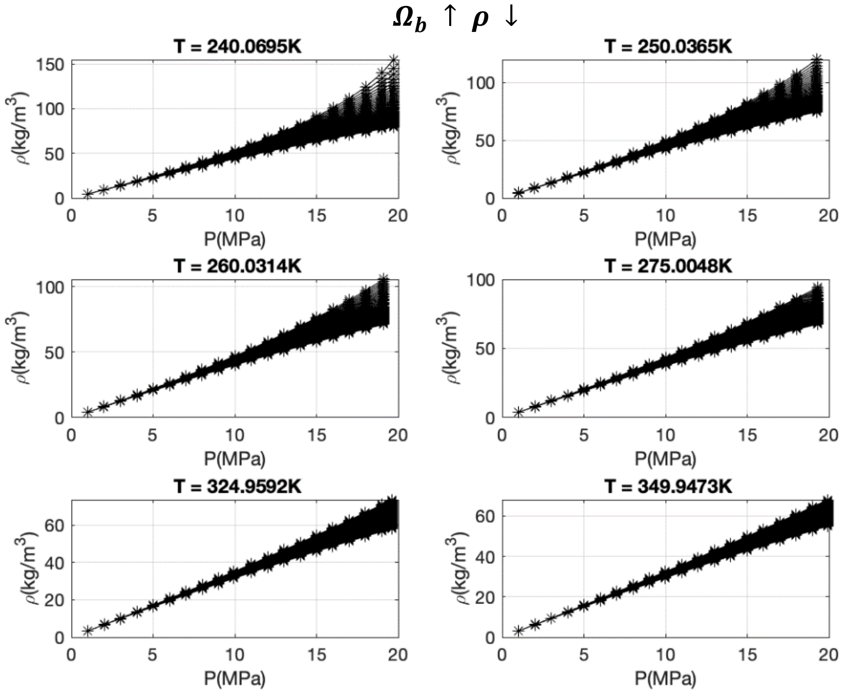

Figure 5.10: Variation of Ω_b – density – 50% CH_4 + 50% H_2, RKS.

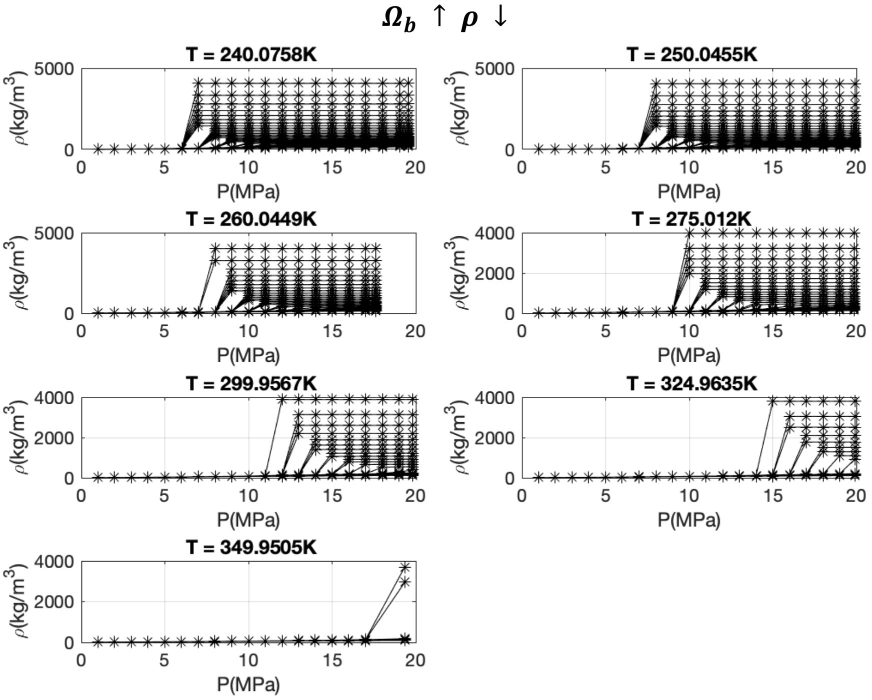

Figure 5.11: Variation of Ω_b – density – 90% CH4 + 10% H2, RKS.

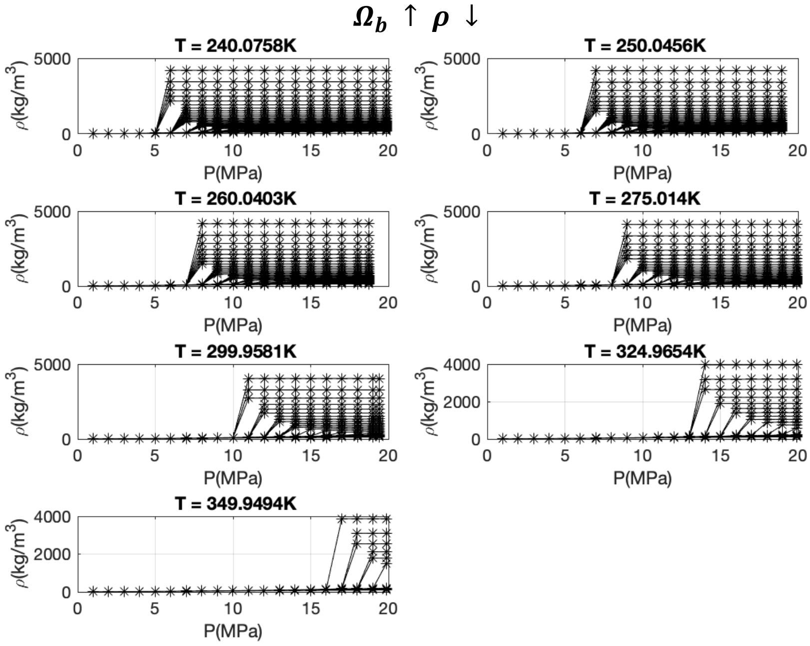

Figure 5.12: Variation of Ω_b – density – 95% CH4 + 05% H2, RKS.

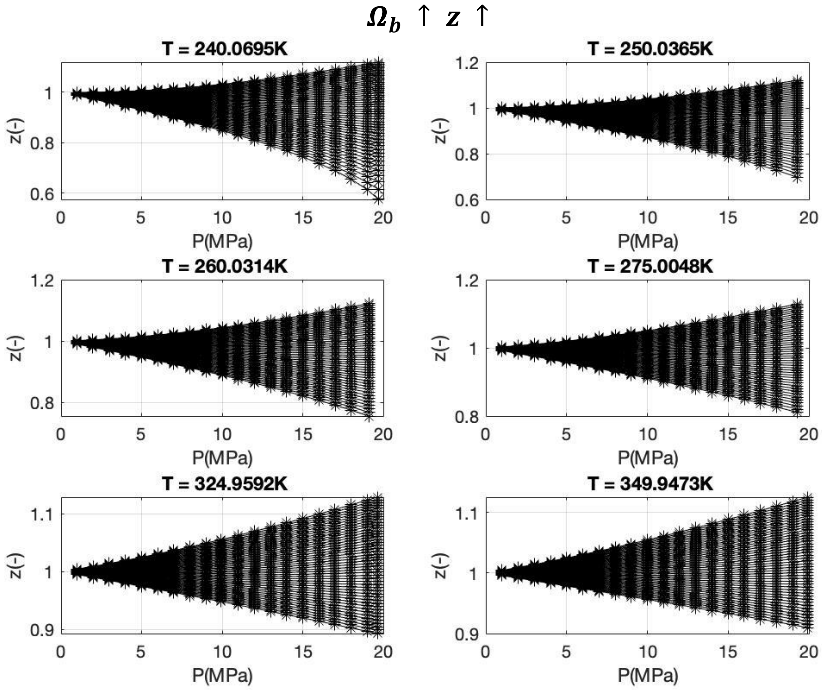

Figure 5.13: Variation of Ω_b – z-factor – 50% CH_4 + 50% H_2, RKS.

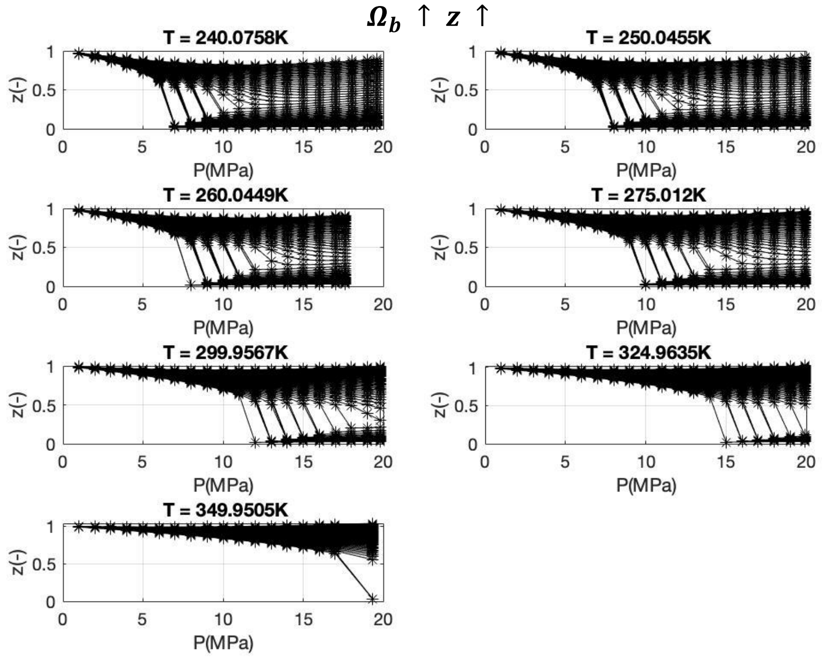

Figure 5.14: Variation of Ω_b – z-factor – 90% CH_4 + 10% H_2, RKS.

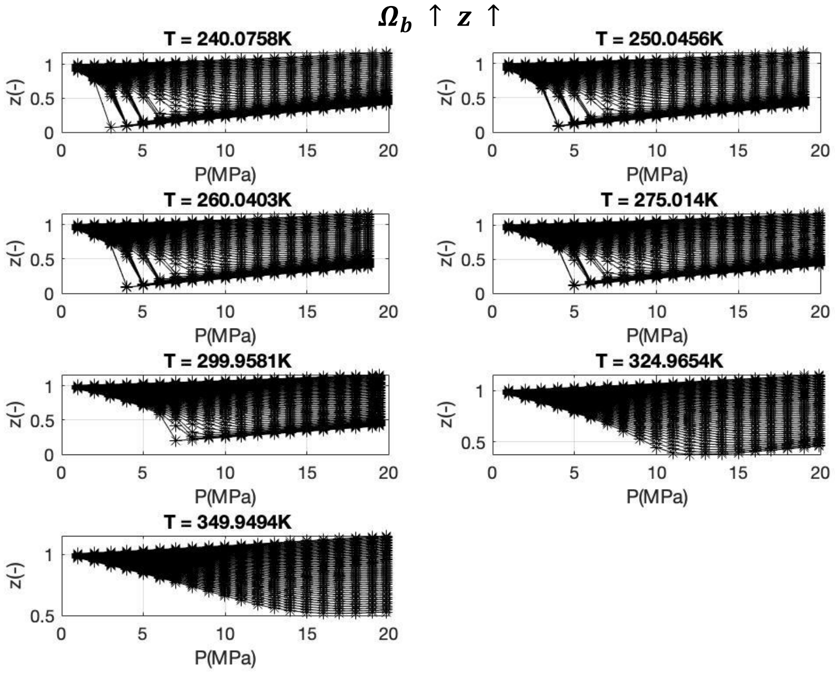

Figure 5.15: Variation of Ω_b – z-factor – 95% CH_4 + 05% H_2, RKS.

From the overall plots, the first tendency that can be noted is that the values of Ω_a and Ω_b highly influence the density and the z – factor of the mixtures tested. This means that the calculated properties are strongly dependent on the values of such parameters. Furthermore, the influence of these parameters on the calculated properties increases as the pressure increases: while at low pressure the curves almost overlap, when the pressure increases the lines start to differ one from the other. Also, it is evident from the plots that the dependency on the values of Ω_a and Ω_b decreases as the temperature increases.

In addition, comparing the plots for the three different mixtures, it can be noted that the mixtures with higher quantities of CH_4 are more sensitive to the variation of Ω_a and Ω_b (see figures 5.5, 5.6, 5.8, 5.9, 5.11, 5.12, 5.14, 5.15) in comparison with the ones where those quantities are lower (see figures 5.4, 5.7, 5.10, 5.13).

Finally, the variations of z – factor and density are tested varying BIP. BIP values are changed in the range -1 to 1, because that is the range of values usually found for that parameter. Figures 5.16, 5.17 and 5.18 show the calculated density for each value of BIP tested for the three mixtures of H_2-CH_4 and the figures 5.19, 5.20 and 5.21 show the calculate z-factor for each value of BIP tested for the three mixtures of H_2-CH_4.

$$\boldsymbol{BIP \uparrow \rho \downarrow}$$

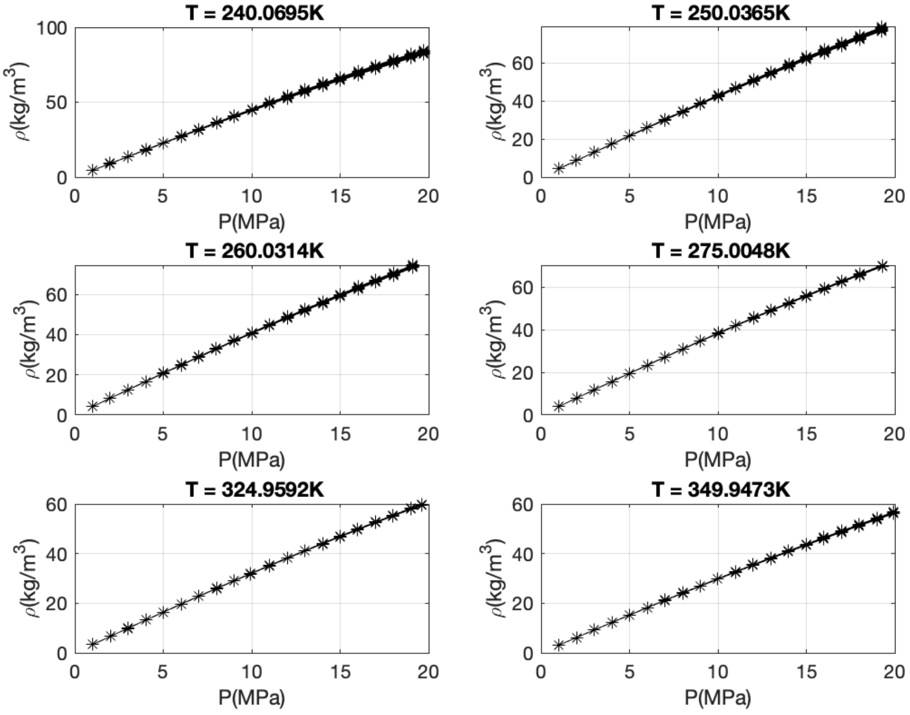

Figure 5.16: Variation of BIP – density – 50% CH_4 + 50% H_2, RKS.

$BIP \uparrow \rho \downarrow$

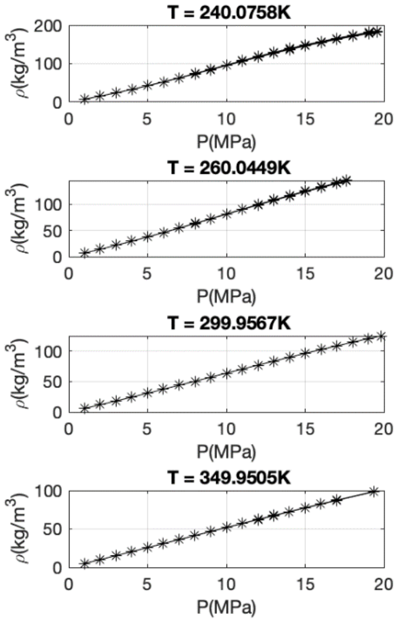

Figure 5.17: Variation of BIP – density – 90% CH_4 + 10% H_2, RKS.

$BIP \uparrow \rho \downarrow$

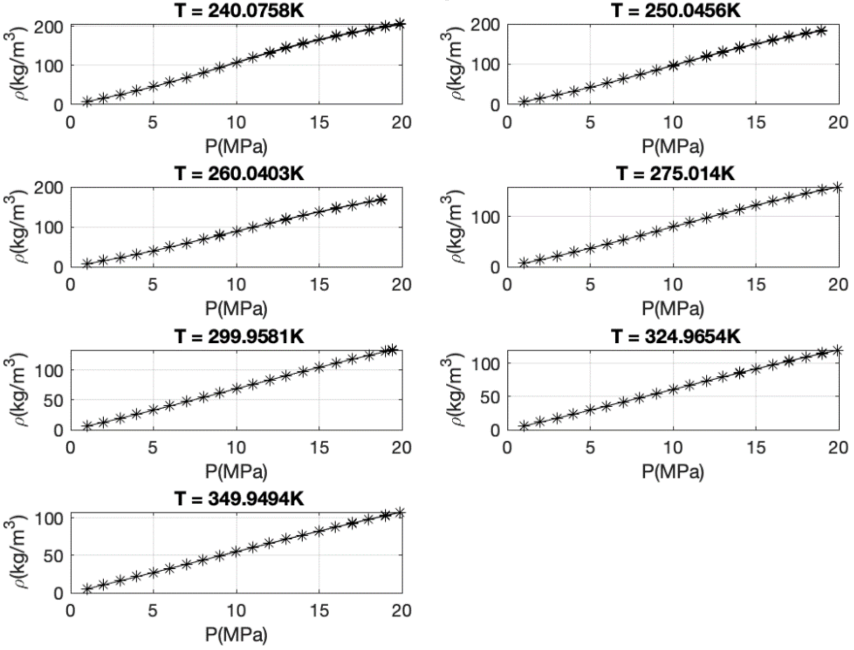

Figure 5.18: Variation of BIP – density – 95% CH_4 + 05% H_2, RKS.

$\boldsymbol{BIP \uparrow \rho \downarrow}$

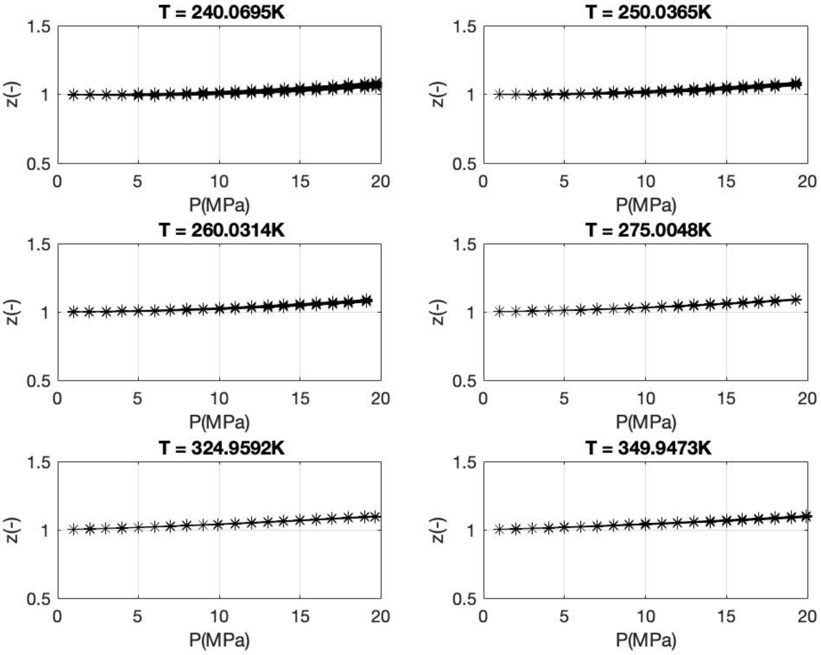

Figure 5.19: Variation of BIP – z-factor – 50% CH_4 + 50% H_2, RKS.

$\boldsymbol{BIP \uparrow z \uparrow}$

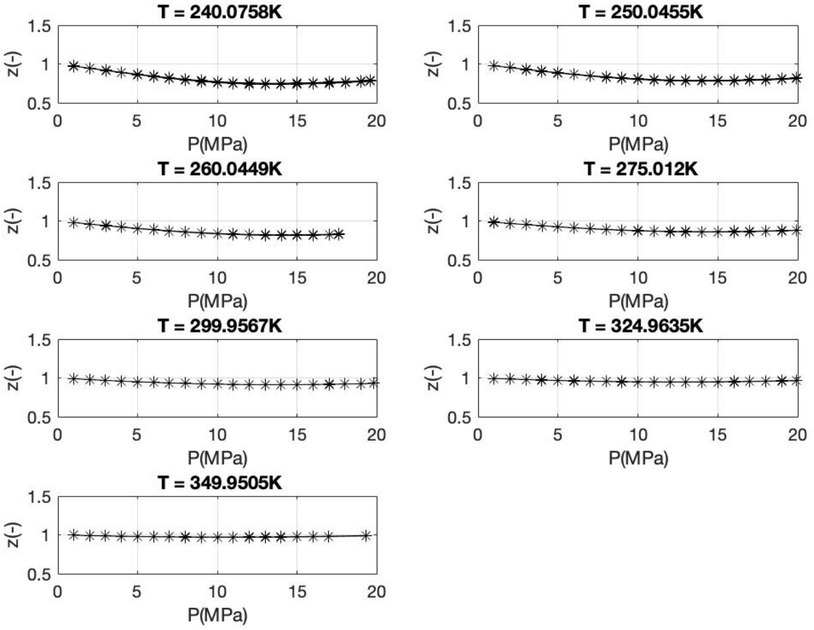

Figure 5.20: Variation of BIP – z-factor – 90% CH_4 + 10% H_2, RKS.

$BIP \uparrow z \uparrow$

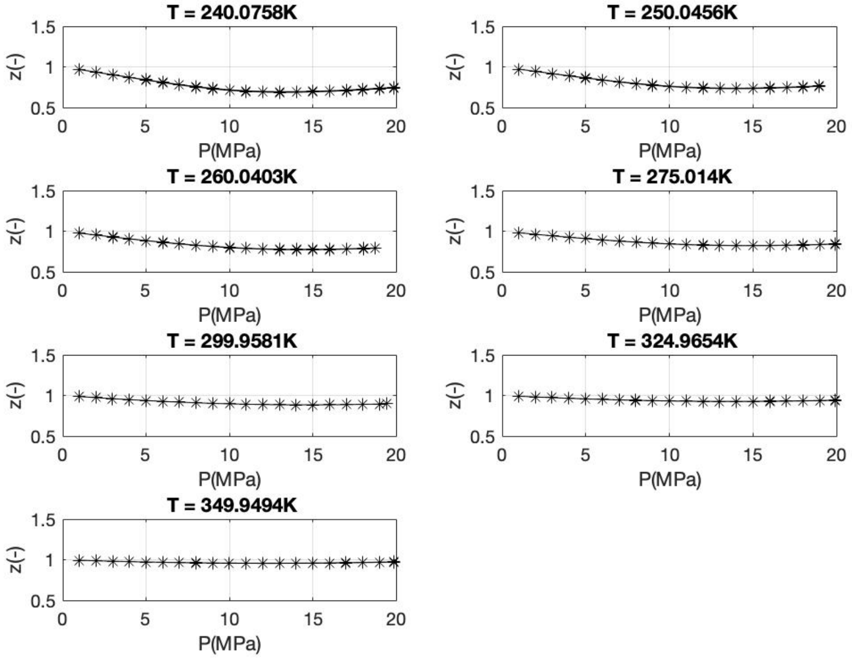

Figure 5.21: Variation of BIP – z-factor – 95% CH_4 + 05% H_2, RKS.

From the overall plots it can be noted that the value of BIP does not significantly influence the density and the z – factor of the mixtures tested.

In summary, from the results of the sensitivity analysis performed it is clear that the density and the z – factor are not strongly dependent on the BIP, while they are highly sensitive to the values of Ω_a and Ω_b and this dependency is increasingly evident when the pressure increases and when quantities of CH_4 in the mixture are higher, while it slightly decreases when the temperature increases.

5.3.2 Sensitivity analysis: PR EoS Results

When performing the sensitivity analysis using the PR model, the default values of Ω_a, Ω_b and BIP are reported in the following table.

Table 5.7: Default values of Ω_a, Ω_b and BIP for PR EoS.

Ω_a	Ω_b	BIP
0.45724	0.0778	-0.15

First, the variations of z – factor and density are tested first against the variation of Ω_a. Ω_a values are changed in the range 0.1 to 1, because that is the range of values usually found for that parameter. The following plots were obtained where the figures 5.22, 5.23 and 5.24 show the calculated density for each value of Ω_a tested for the three mixtures of H_2-CH_4 and the figures 5.25, 5.26 and 5.27 show the calculate z-factor for each value of Ω_a tested for the three mixtures of H_2-CH_4.

$\boldsymbol{\Omega_a \uparrow \rho \uparrow}$

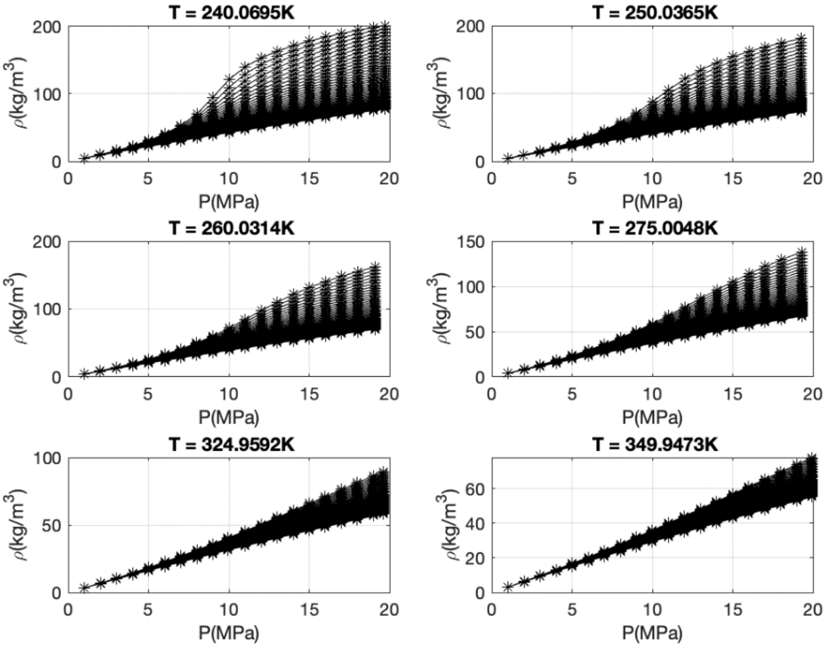

Figure 5.22: Variation of Ω_a – density – 50% CH_4 + 50% H_2, PR.

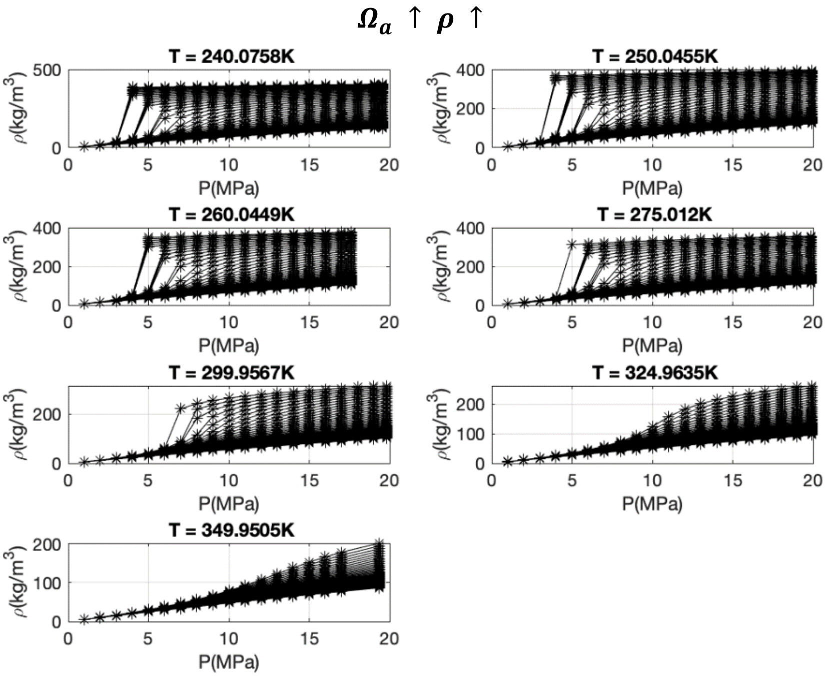

Figure 5.23: Variation of Ω_a – density – 90% CH_4 + 10% H_2, PR.

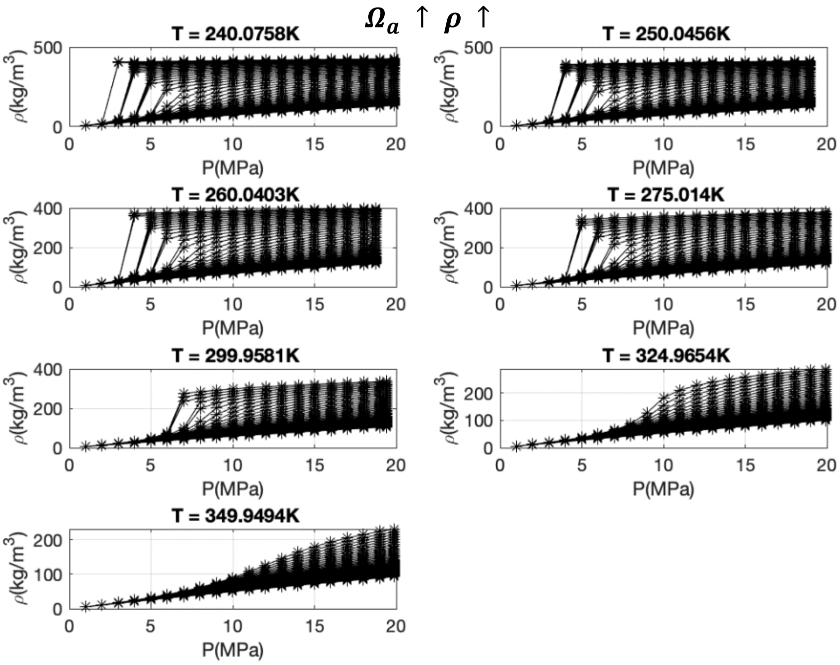

Figure 5.24: Variation of Ω_a – density – 95% CH_4 + 05% H_2, PR.

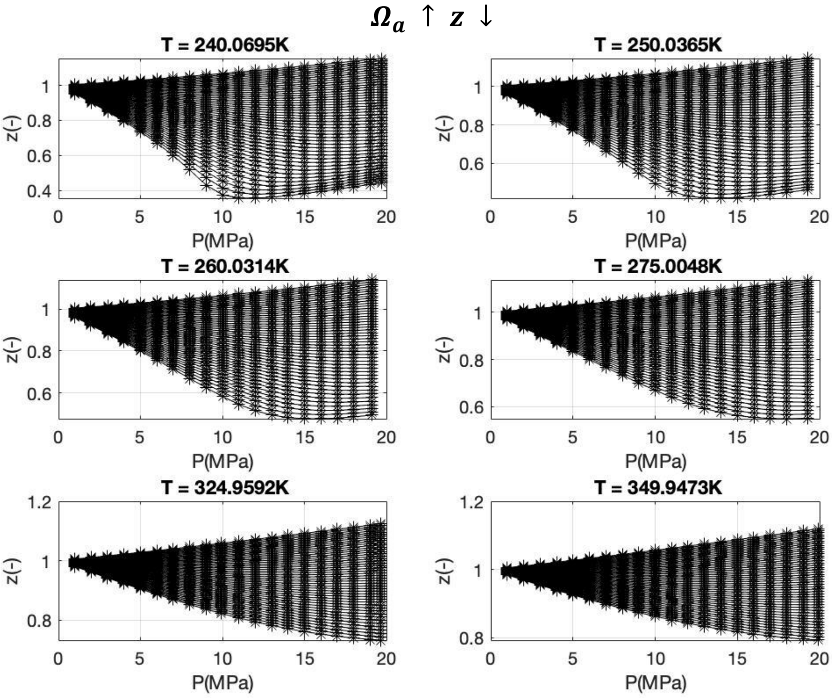

Figure **5.25**: Variation of Ω_a – z-factor – 50% CH_4 + 50% H_2, PR.

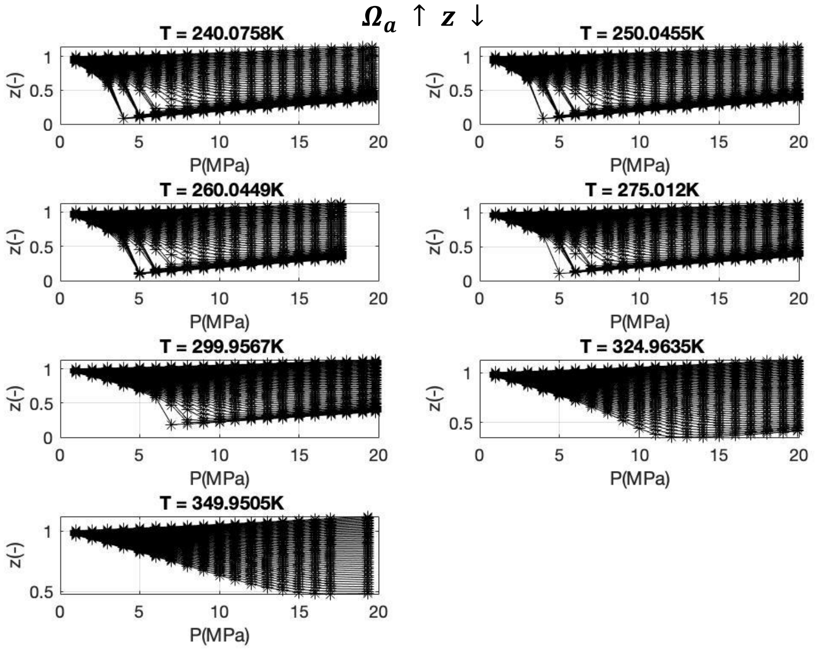

Figure **5.26**: Variation of Ω_a – z-factor – 90% CH_4 + 10% H_2, PR.

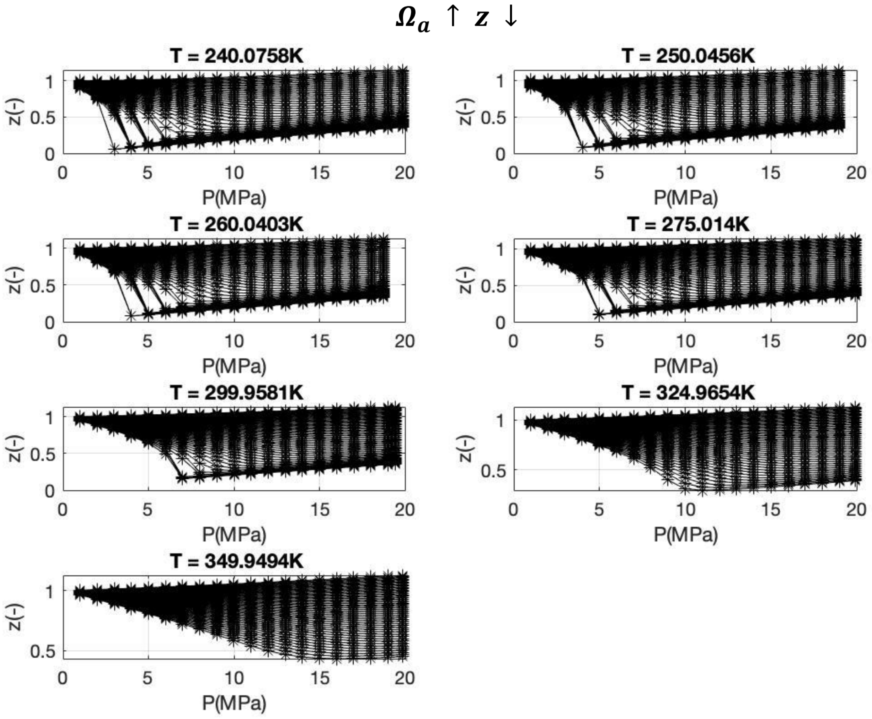

Figure 5.27: Variation of Ω_a – z-factor – 95% CH_4 + 05% H_2, PR.

Then, the variations of z – factor and density are tested first against the variation of Ω_b. Ω_b values are changed in the range 0.01 to 0.1, because that is the range of values usually found for that parameter. The following plots were obtained where the figures 5.28, 5.29 and 5.30 show the calculated density for each value of Ω_b tested for the three mixtures of H_2-CH_4 and the figures 5.31, 5.32 and 5.33 show the calculate z-factor for each value of Ω_b tested for the three mixtures of H_2-CH_4.

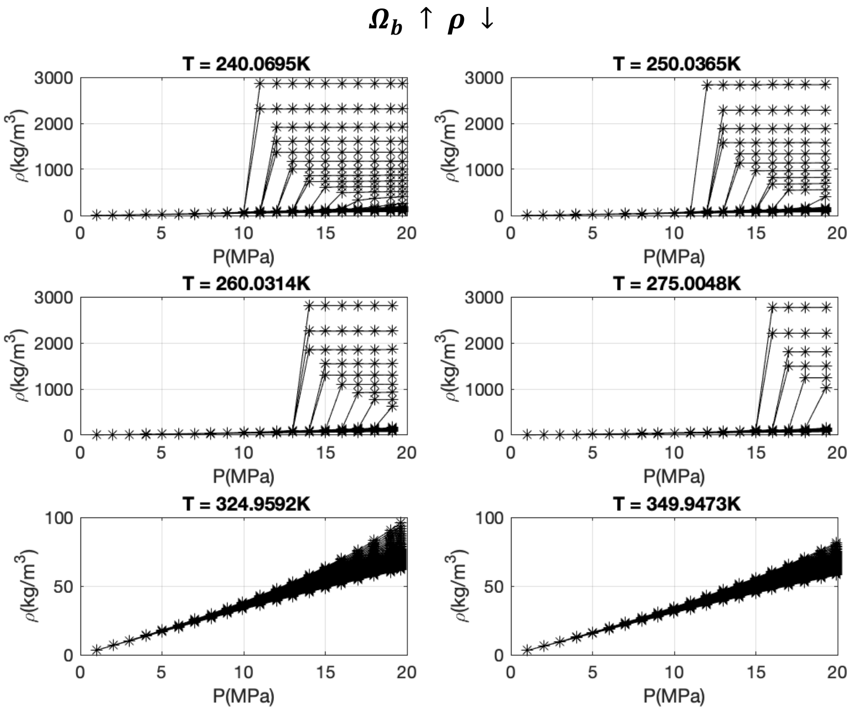

Figure 5.28: Variation of Ω_b – density – 50% CH4 + 50% H2, PR.

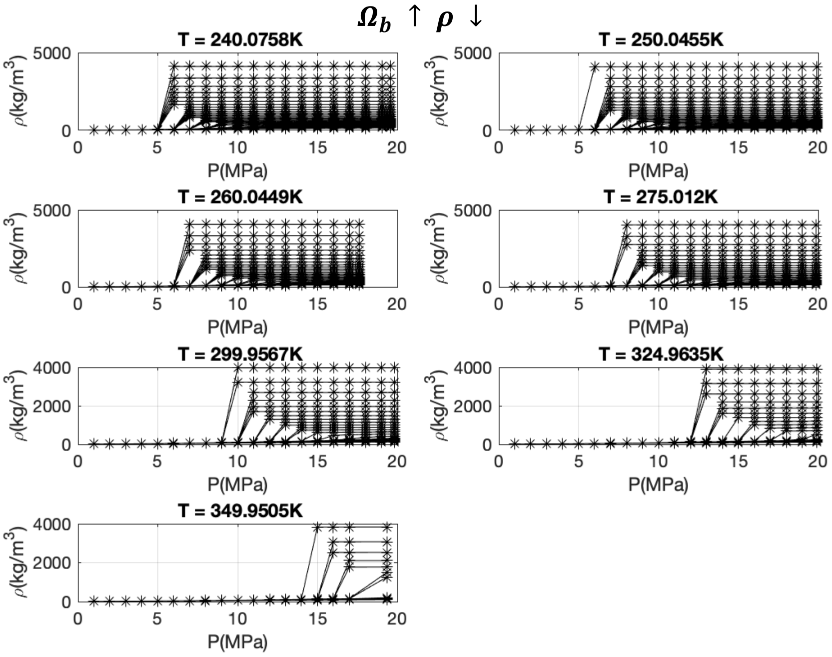

Figure 5.29: Variation of Ω_b – density – 90% CH4 + 10% H2, PR.

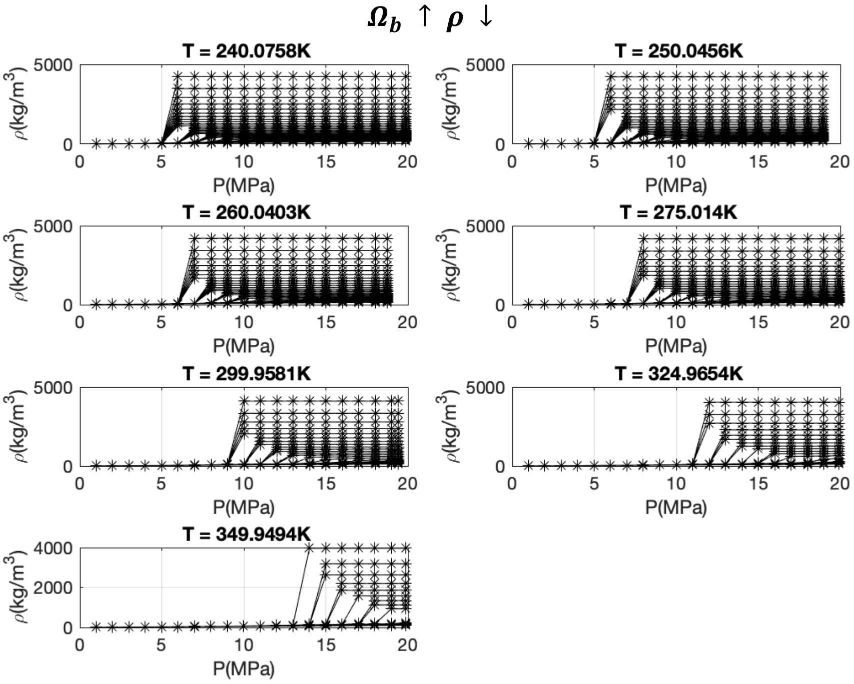

Figure 5.30: Variation of Ω_b – density – 95% CH_4 + 05% H_2, PR.

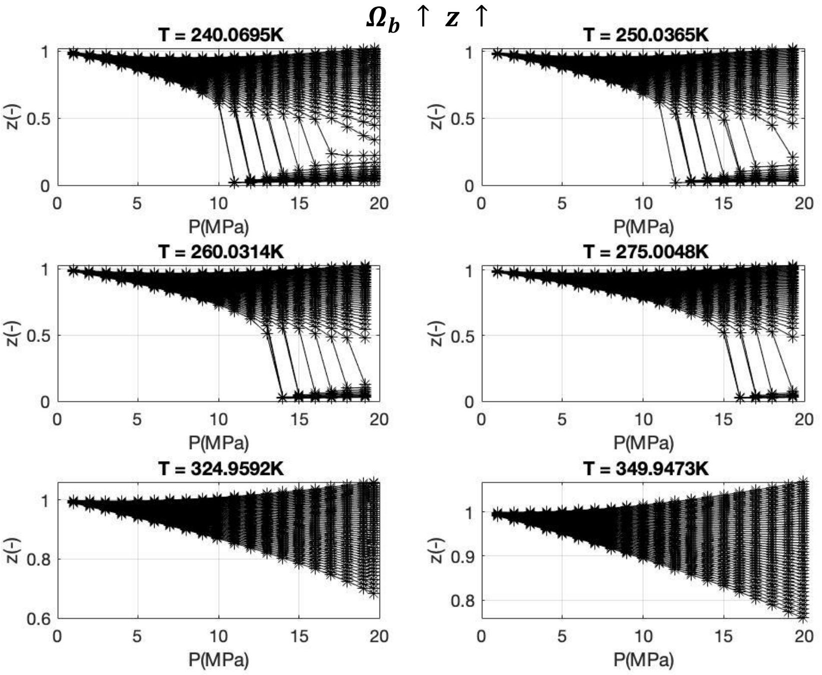

Figure 5.31: Variation of Ω_b – z-factor – 50% CH_4 + 50% H_2, PR.

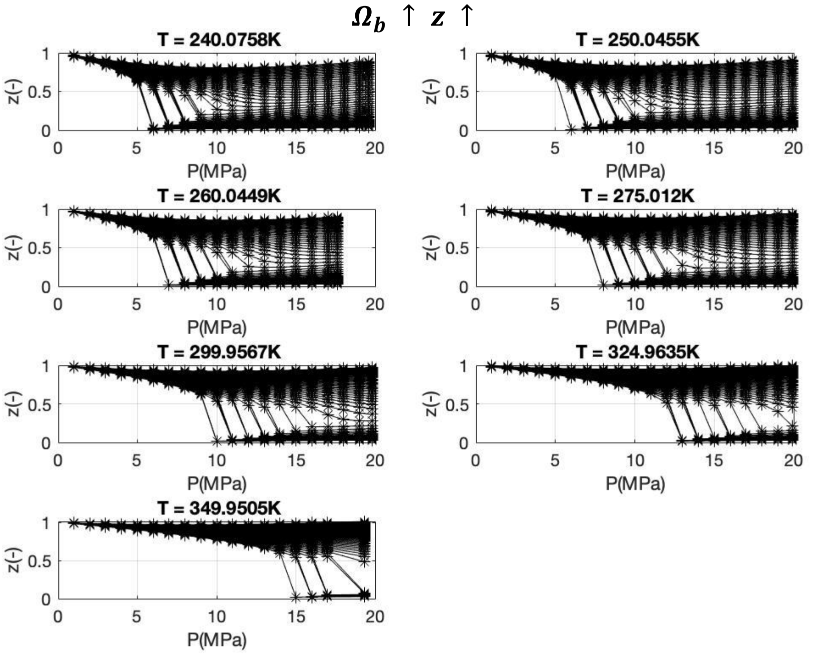

Figure 5.32: Variation of Ω_b – z-factor – 90% CH_4 + 10% H_2, PR.

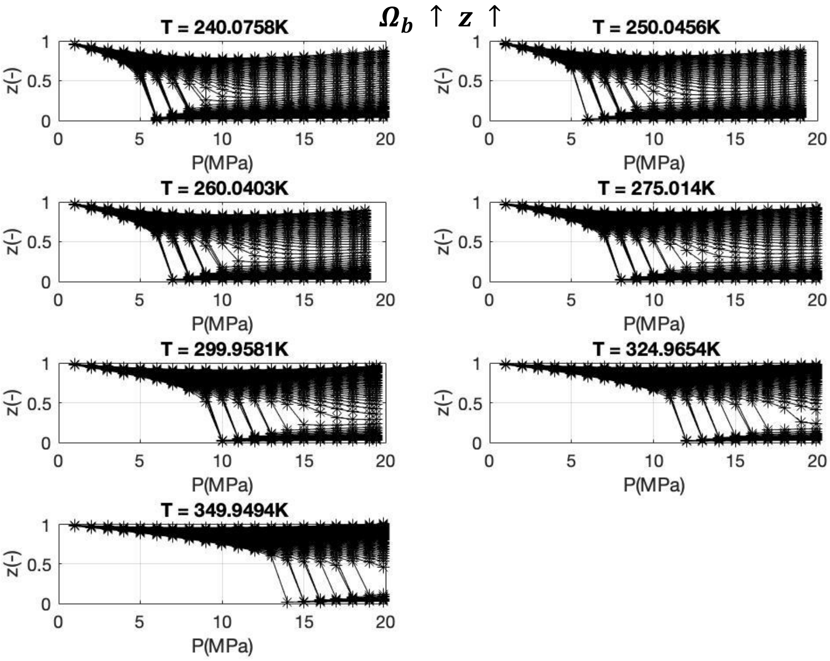

Figure 5.33: Variation of Ω_b – z-factor – 95% CH_4 + 05% H_2, PR.

From the overall plots, in the PR EoS the values of Ω_a and Ω_b highly influence the density and the z – factor of the mixtures tested. Furthermore, also in this case the influence of these parameters on the calculated properties increases as the pressure and the quantity of CH_4 in the mixture increases, whereas it slightly decreases when the temperature increases, although it is still high.

Finally, the variations of z – factor and density are tested first against the variation of BIP. BIP values are changed in the range -1 to 1, because that is the range of values usually found for that parameter. The following plots were obtained where the figures 5.34, 5.35 and 5.36 show the calculated density for each value of BIP tested for the three mixtures of H_2-CH_4 and the figures 5.37, 5.38 and 5.39 show the calculate z-factor for each value of BIP tested for the three mixtures of H_2-CH_4.

$\boldsymbol{BIP} \uparrow \boldsymbol{\rho} \downarrow$

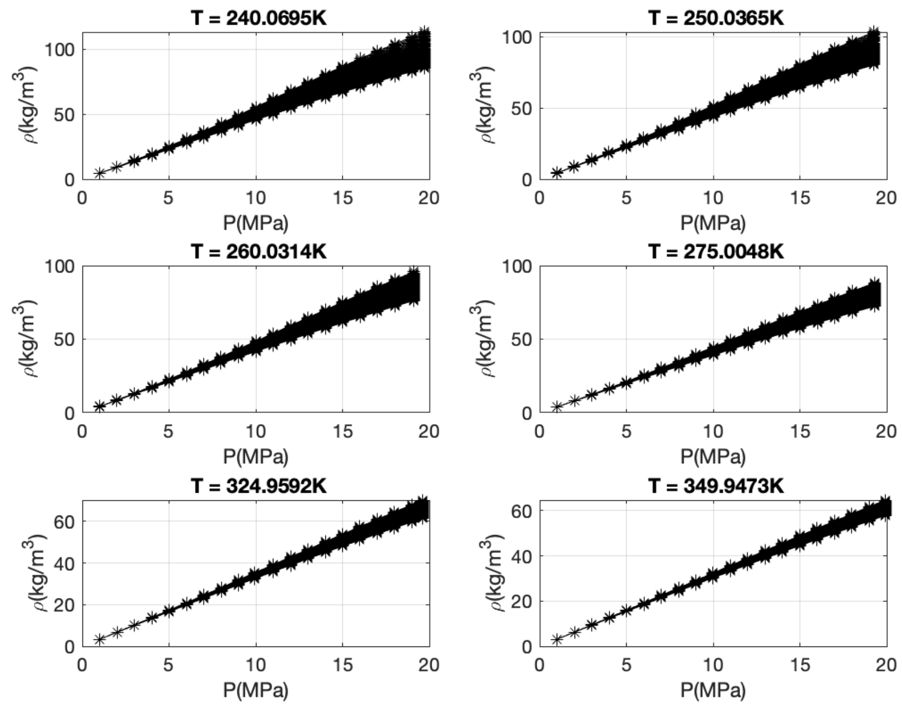

Figure 5.34: Variation of BIP – density – 50% CH_4 + 50% H_2, PR.

$\boldsymbol{BIP} \uparrow \boldsymbol{\rho} \downarrow$

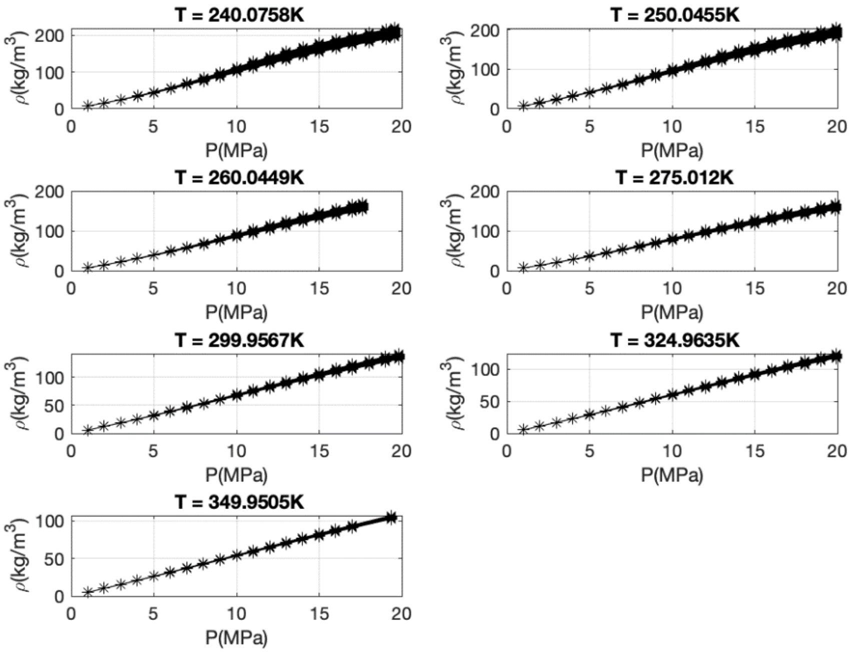

Figure 5.35: Variation of BIP – density – 90% CH_4 + 10% H_2, PR.

$\boldsymbol{BIP} \uparrow \boldsymbol{\rho} \downarrow$

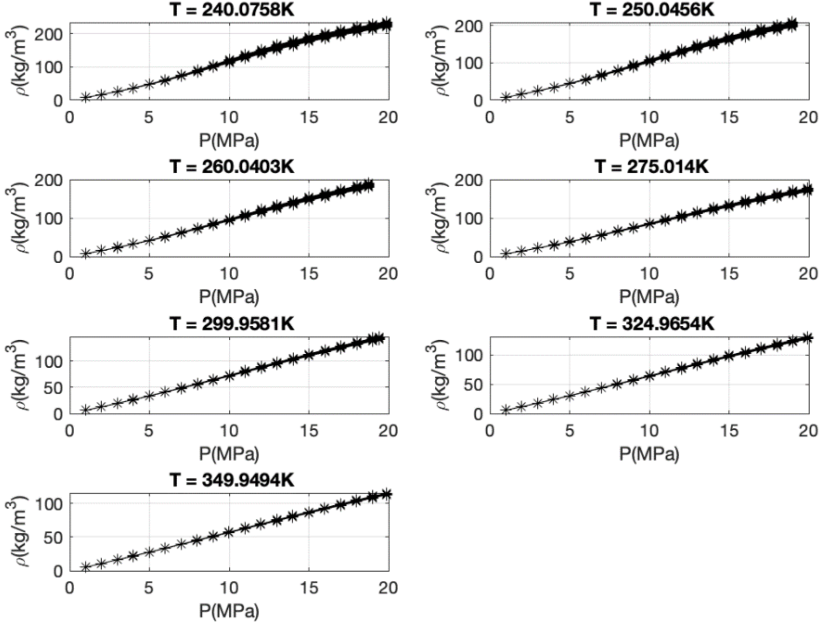

Figure 5.36: Variation of BIP – density – 95% CH_4 + 05% H_2, PR.

BIP ↑ z ↑

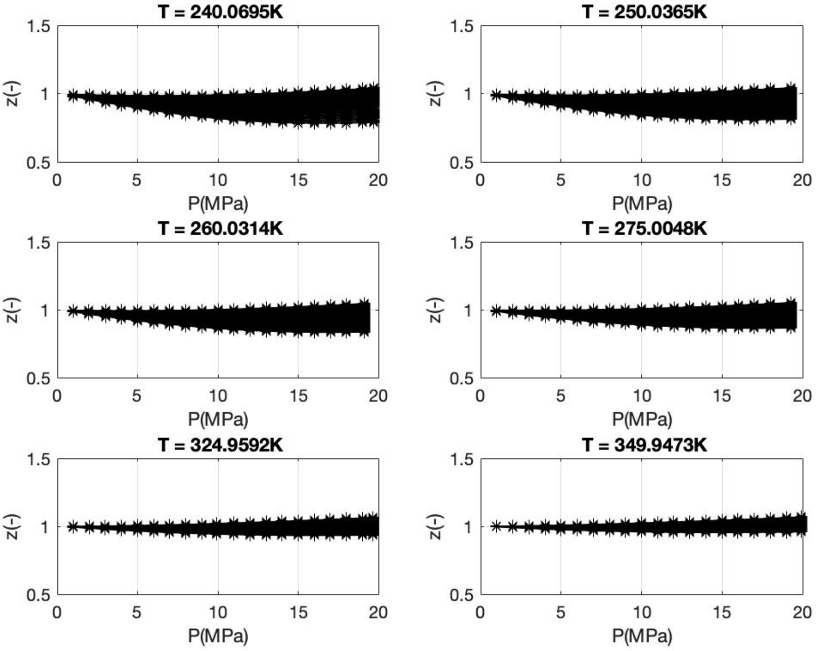

Figure 5.37: Variation of BIP – z-factor – 50% CH_4 + 50% H_2, PR.

BIP ↑ z ↑

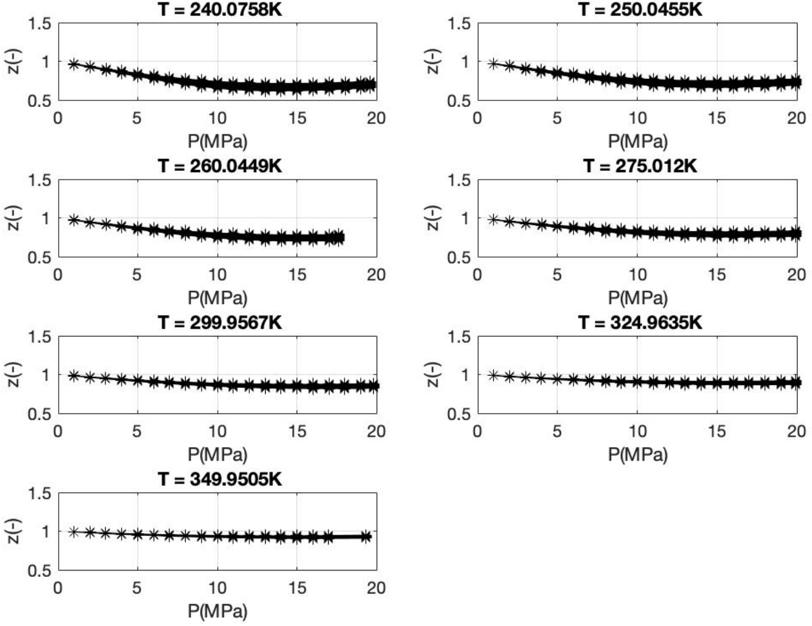

Figure 5.38: Variation of BIP – z-factor – 90% CH_4 + 10% H_2, PR.

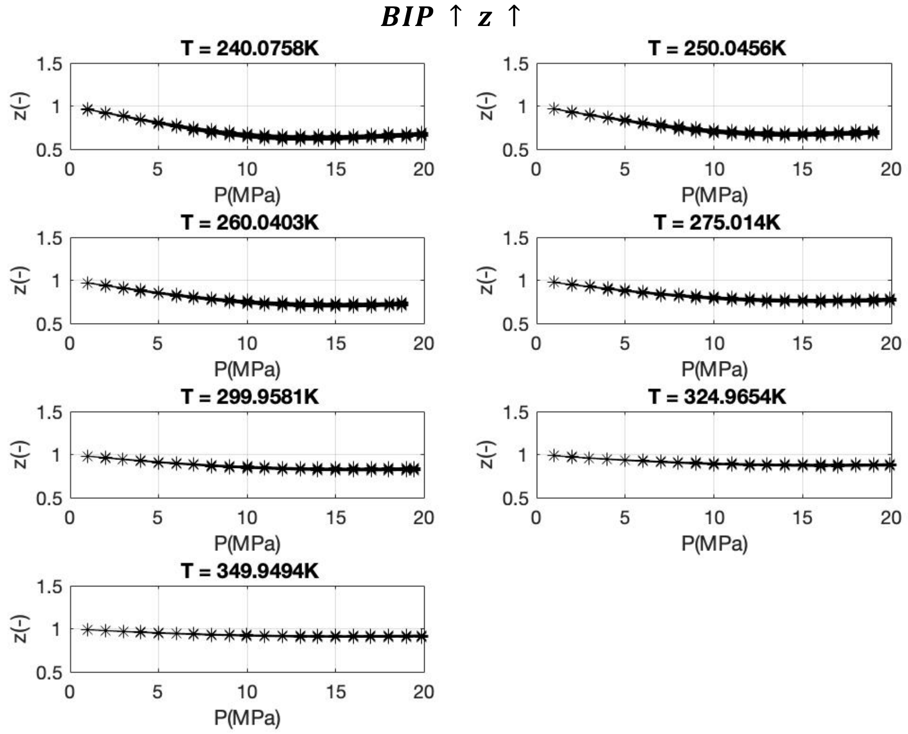

Figure 5.39: Variation of BIP – z-factor – 95% CH_4 + 05% H_2, PR.

From the overall plots it can be noted that the density and the z – factor are slightly influenced by the value of BIP and this dependency is higher for the mixtures with higher quantities of H_2 are higher (figures 5.34 and 5.37) in comparison with the ones where those quantities are lower (figure 5.35, 5.36, 5.38, 5.39) and it is more clear when the temperature is lower.

In summary, from the results of the sensitivity analysis performed it is clear that the density and the z – factor are not strongly dependent on the BIP, especially in case of high quantities of H_2. On the contrary the sensitivity of the values of Ω_a and Ω_b is prominent and this dependency is increasingly evident when the quantities of CH_4 in the mixture increases, while it slightly decreases when the temperature increases.

Chapter 6

Results

In this Section the results of for the Ω_a, Ω_b and BIP estimation are presented.

First of all a comprehensive presentation and analysis of the results for the three parameters optimization are presented, once using the RKS EoS and once using the PR EoS, with a comparison of the results obtained from the two equations. Then, the robustness analysis of the optimization method, by changing its tolerance and algorithms, is also presented. Furthermore, since from the sensitivity analysis it turned out that the BIP does not influence significantly the accuracy of the EoSs in predicting the density and the z-factor, the optimization of the parameters have been performed for one parameter at time in order to further confirm this statement. In particular, first the optimization of Ω_a is performed, then only Ω_b, after that Ω_a and Ω_b are optimized simultaneously and finally the optimization is performed only for BIP. Conclusions on the effectiveness of the method employed, suggested improvements and/or points to be reviewed to improve the validation of the discrepancies between experimental and calculated data are presented at the end.

Before performing the optimization of the three parameters, in order to verify if it is needed or not, the density and the z – factor are calculated using first RKS EoS and then PR EoS using the default values of Ω_a, Ω_b and BIP (which are reported in table 5.6 for RKS and in table 5.7 for PR) and the results are plotted together with the experimental data to verify if the models are able to predict accurately the properties without optimizing the values of the model parameters.

The results are showed in the following figures.

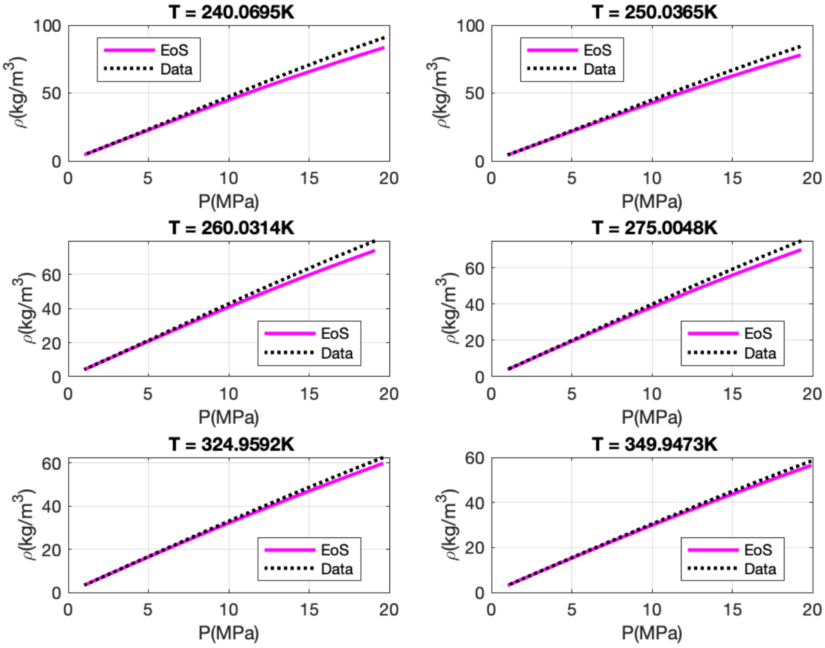

Figure 6.1: density – 50% CH_4 + 50% H_2, RKS.

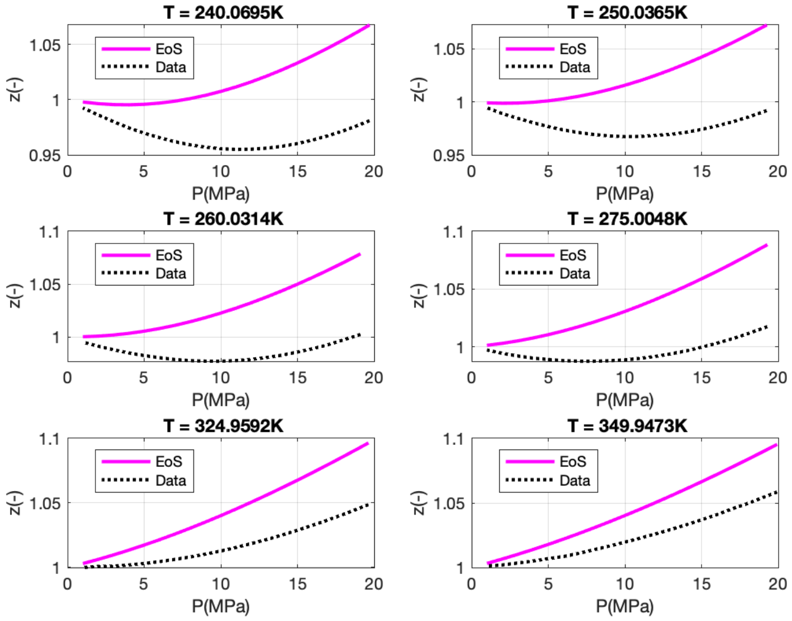

Figure 6.2: z-factor – 50% CH_4 + 50% H_2, RKS.

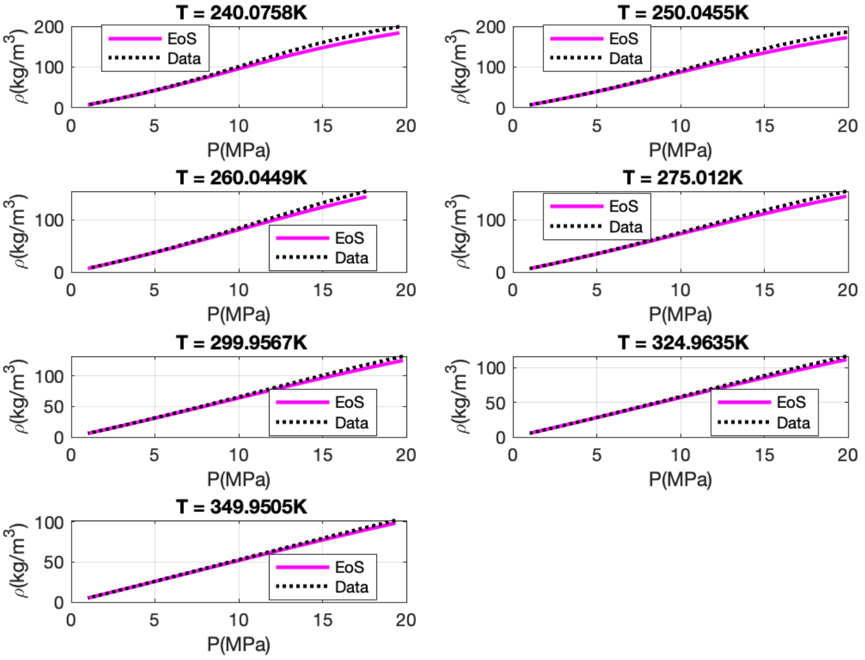

Figure 6.3: density – 90% CH_4 + 10% H_2, RKS.

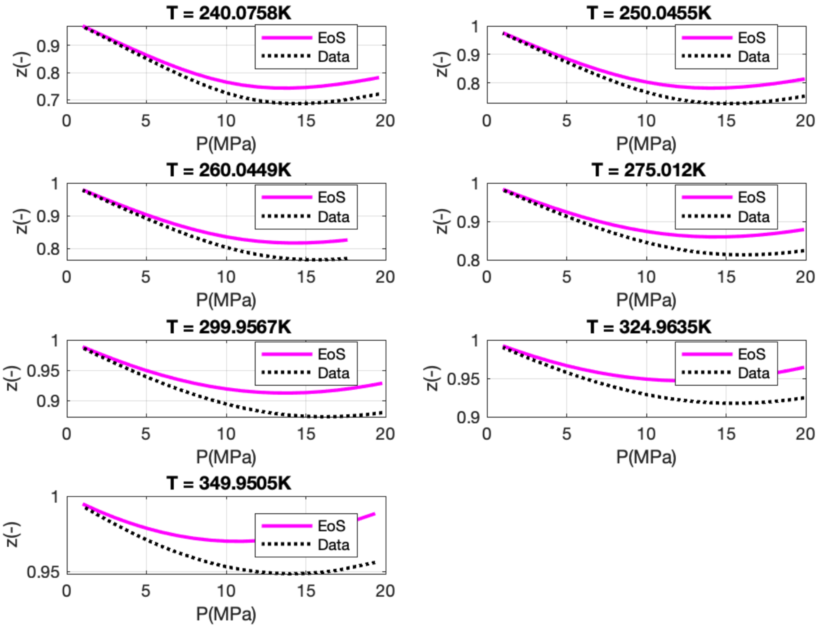

Figure 6.4: z-factor – 90% CH_4 + 10% H_2, RKS.

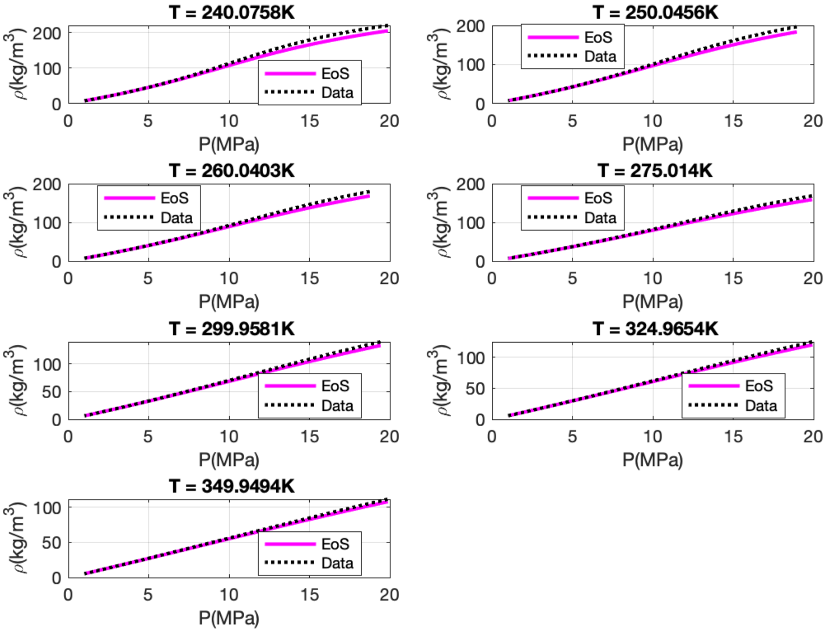

Figure 6.5: density – 95% CH_4 + 05% H_2, RKS.

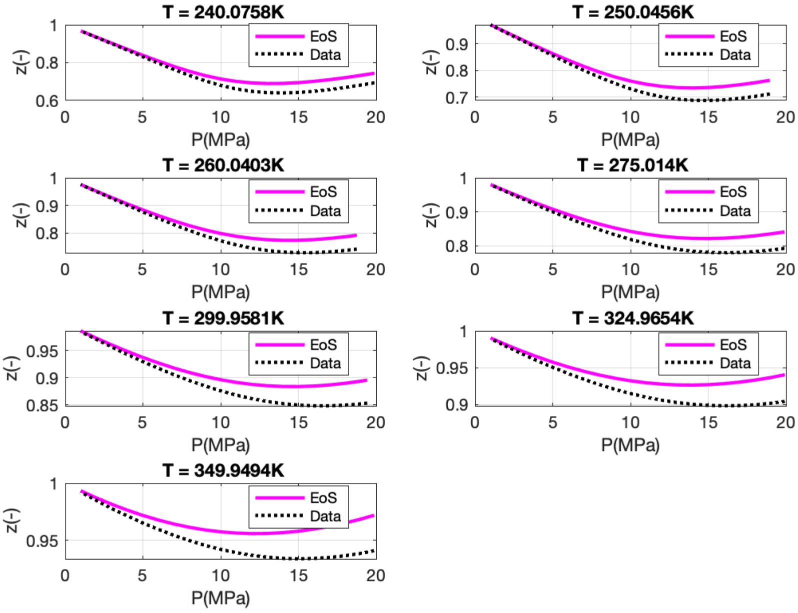

Figure 6.6: z-factor – 95% CH_4 + 05% H_2, RKS.

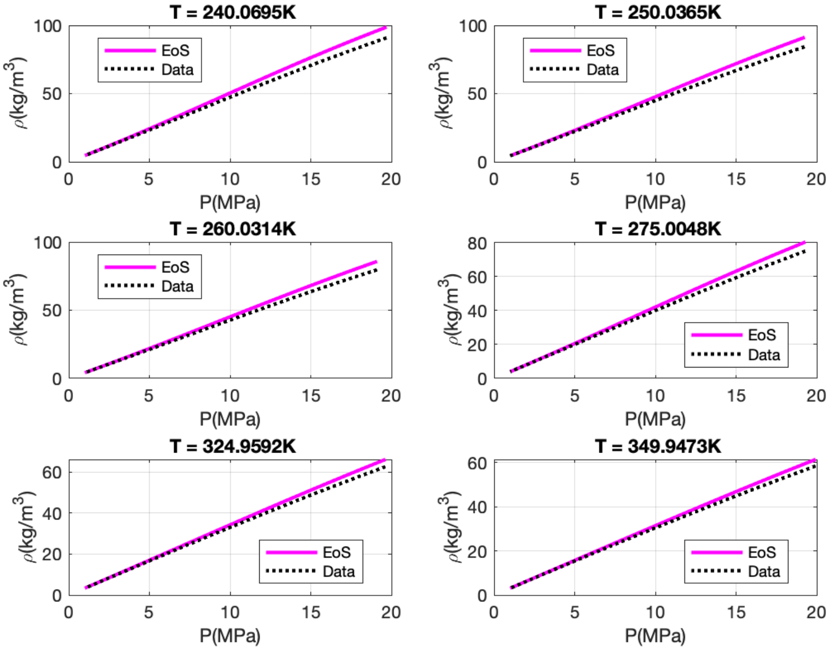

Figure 6.7: density – 50% CH_4 + 50% H_2, PR.

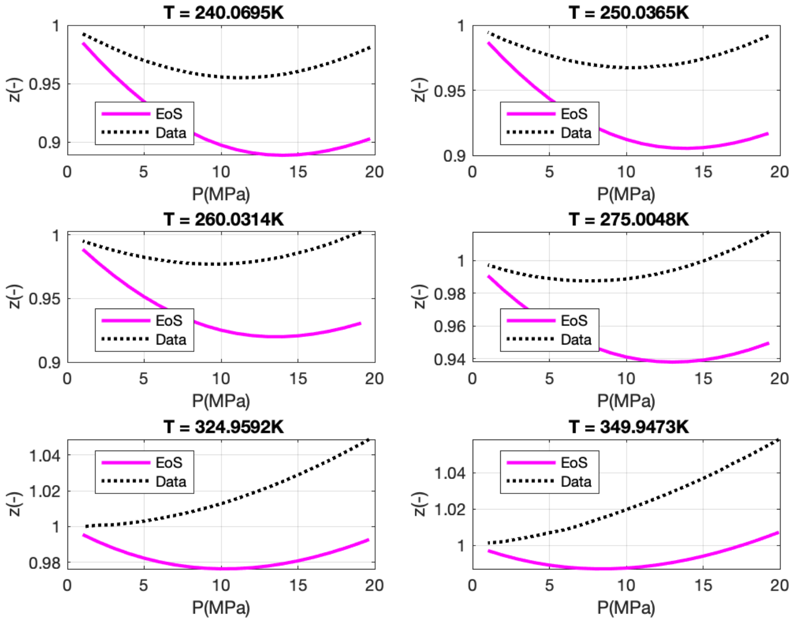

Figure 6.8: z-factor – 50% CH_4 + 50% H_2, PR.

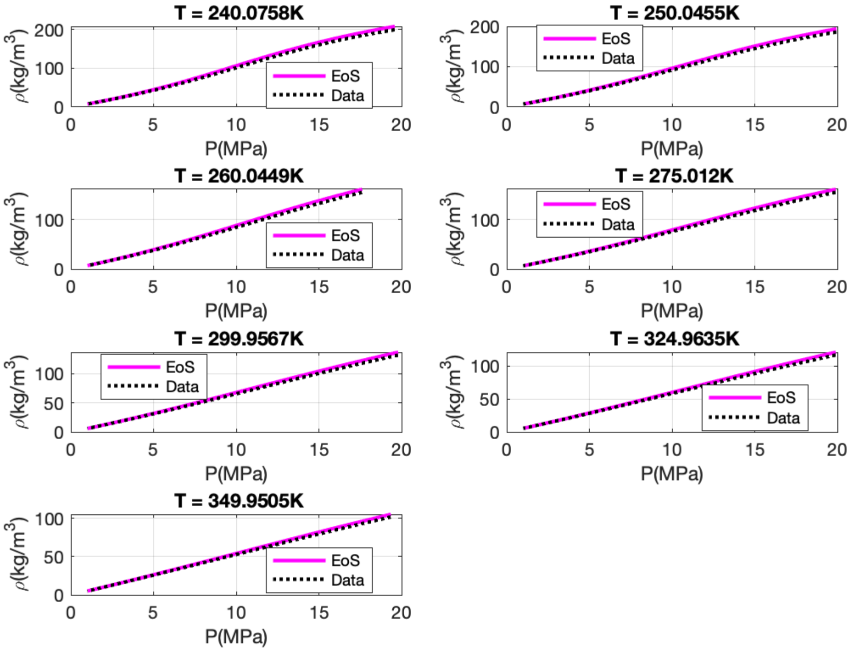

Figure 6.9: density – 90% CH_4 + 10% H_2, PR.

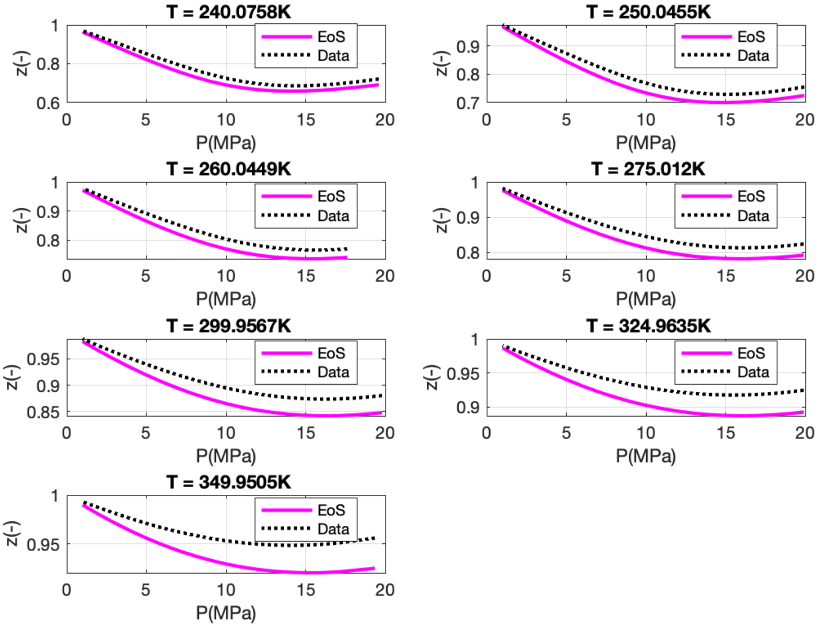

Figure 6.10: z-factor – 90% CH_4 + 10% H_2, PR.

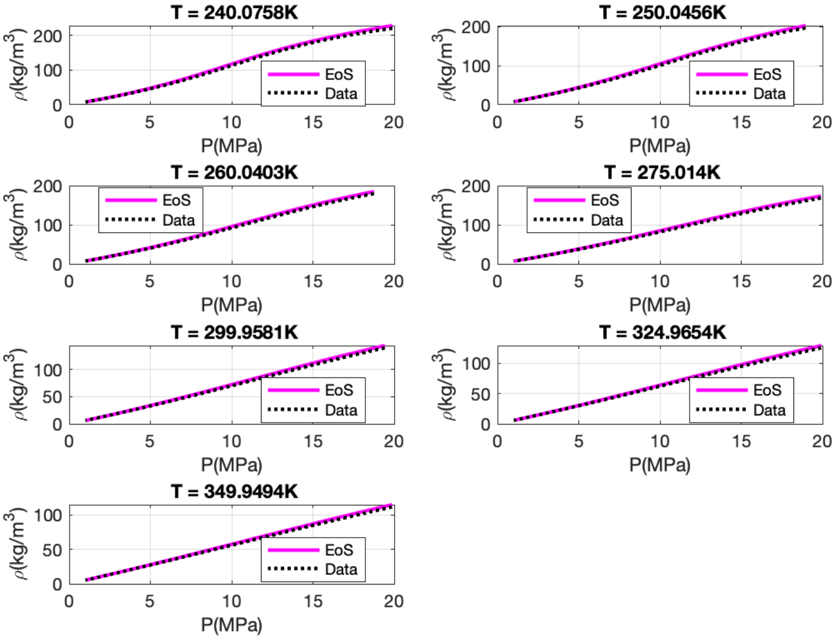

Figure 6.11: density – 95% CH_4 + 05% H_2, PR.

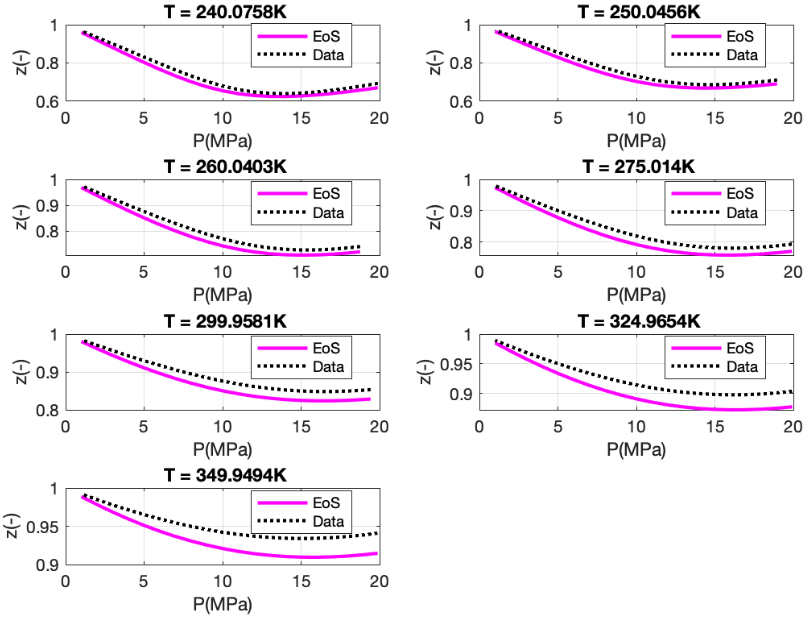

Figure 6.12: z-factor – 95% CH_4 + 05% H_2, RKS.

From the overall plots it can been seen that the density and the z – factor calculated with the EoSs diverges from the one retrieved using the experimental data. So the need for the optimization of the models parameters arises.

6.1 Optimization of Ω_a, Ω_b and BIP for each isotherm

The optimization of Ω_a, Ω_b and the binary interaction parameter have been performed using the algorithm previously described (Figure 5.3). The optimization has been performed first using the Redlich – Kwong – Soave equation of state and then using the Peng – Robinson equation of state.

6.1.1 RKS EoS Results

When using the RKS EoS, the initial guesses for the parameters to be optimized are reported in table 6.1.

Table 6.1: Initial guesses for optimization when using RKS EoS.

Ω_a	Ω_b	BIP
0.427447	0.08664	-0.15

The results for the mixture 50% CH_4 + 50% H_2 are shown in the Figures 6.13 to 6.18; the results for the mixture 90% CH_4 + 10% H_2 are shown in the Figures 6.19 to 6.25; the results for the mixture 95% CH_4 + 05% H_2 are shown in the Figures 6.26 to 6.32. the fitting of the density is reported in the first plot (the one on the left) and the fitting of the compressibility factor is reported in the second plot (the one on the right).

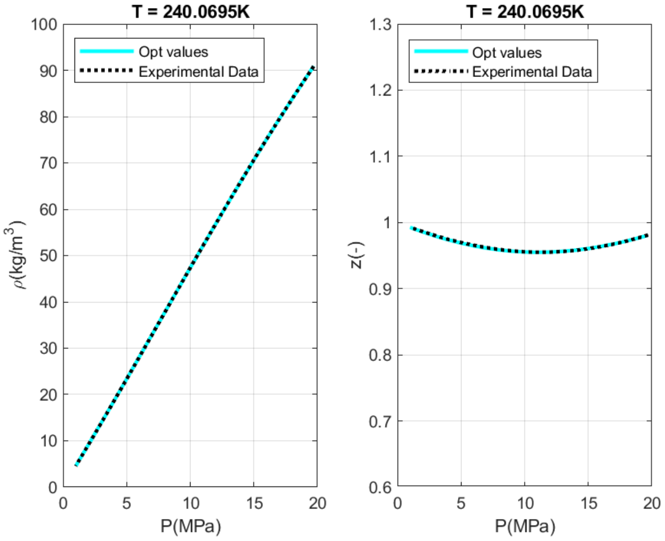

Figure 6.13: optimization results T1 – 50% CH_4 + 50% H_2, RKS.

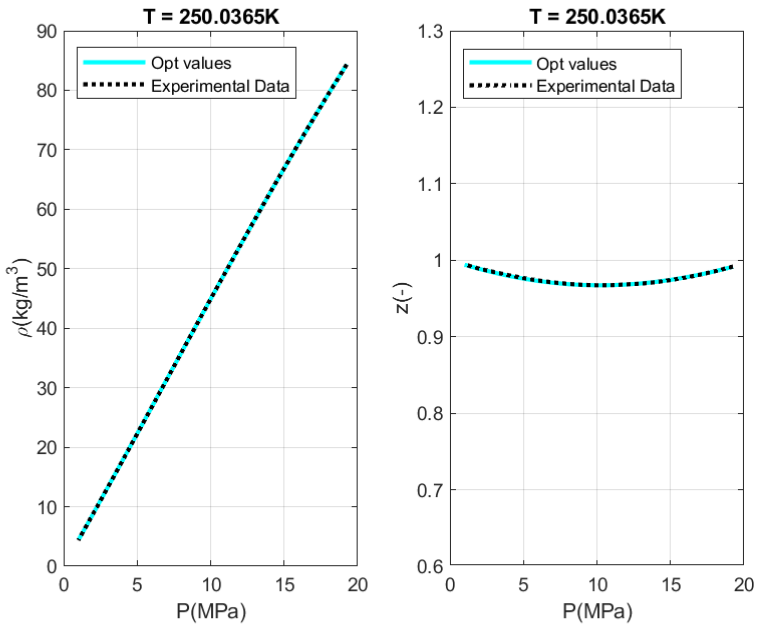

Figure 6.14: optimization results T2 – 50% CH_4 + 50% H_2, RKS.

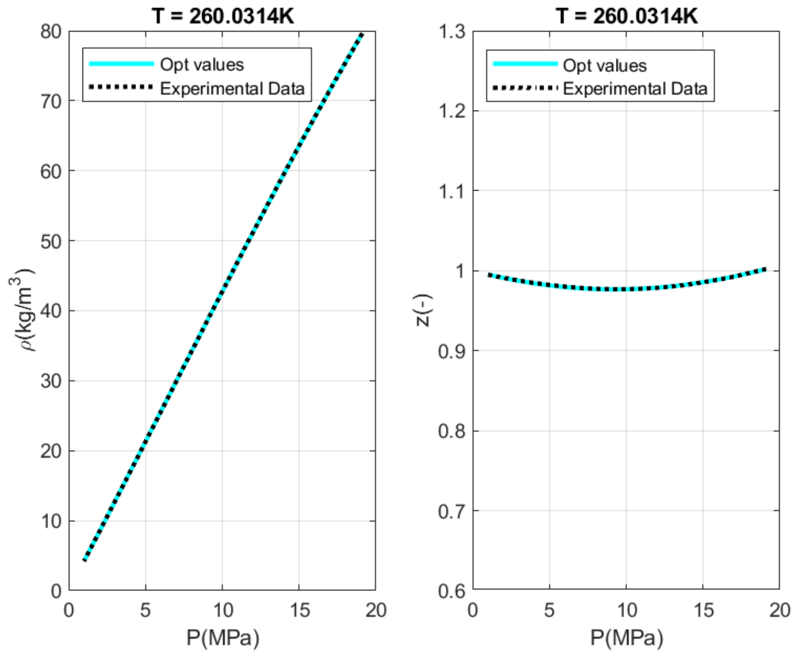

Figure 6.15: optimization results T3 – 50% CH_4 + 50% H_2, RKS.

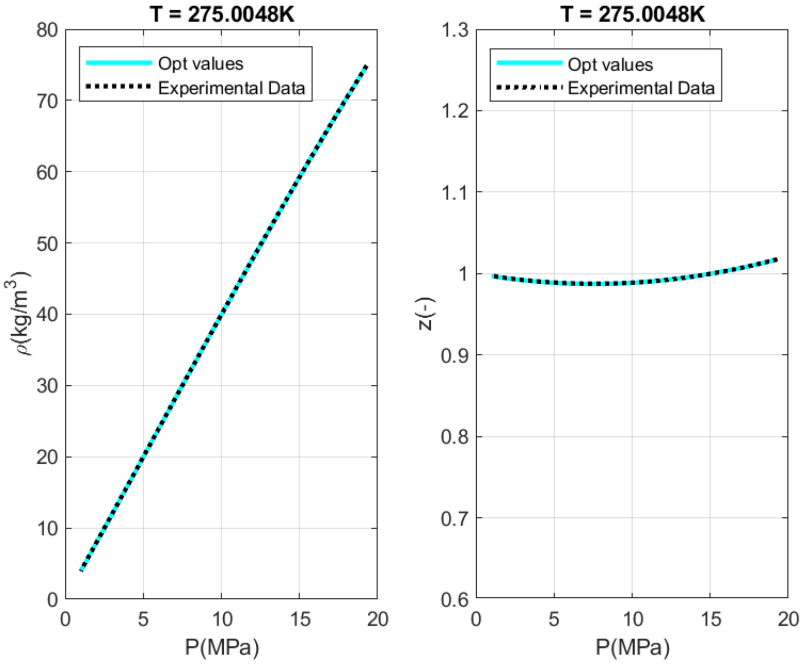

Figure 6.16: optimization results T4 – 50% CH_4 + 50% H_2, RKS.

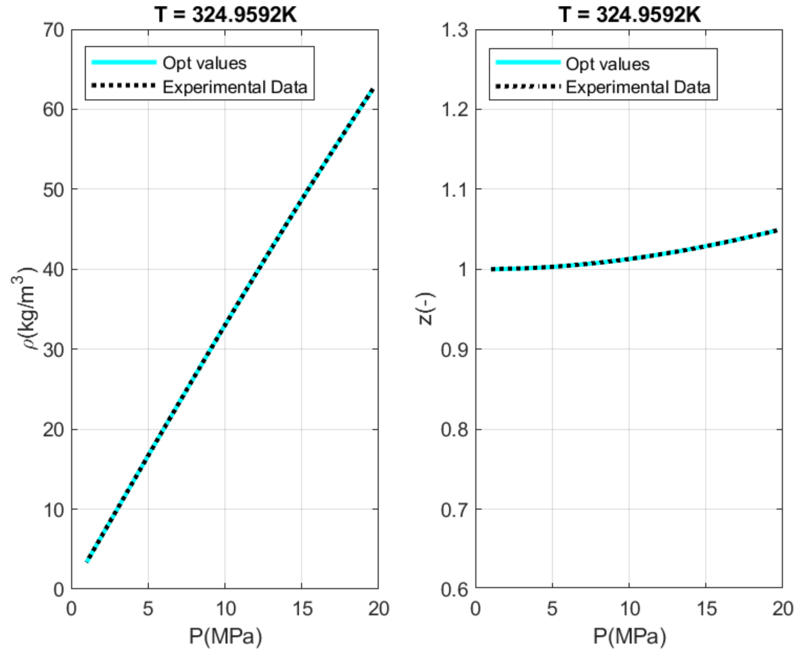

Figure 6.17: optimization results T5 – 50% CH_4 + 50% H_2, RKS.

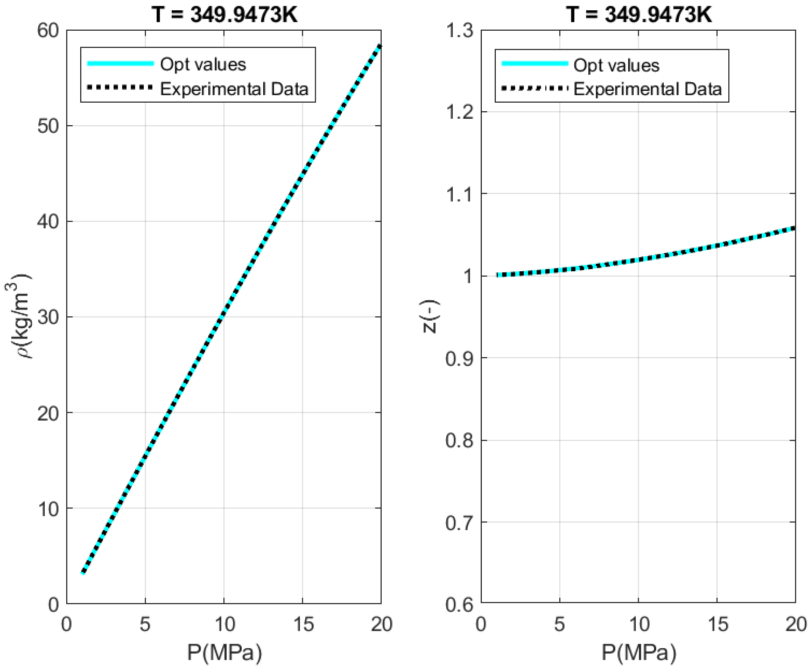

Figure 6.18: optimization results T6 – 50% CH_4 + 50% H_2, RKS.

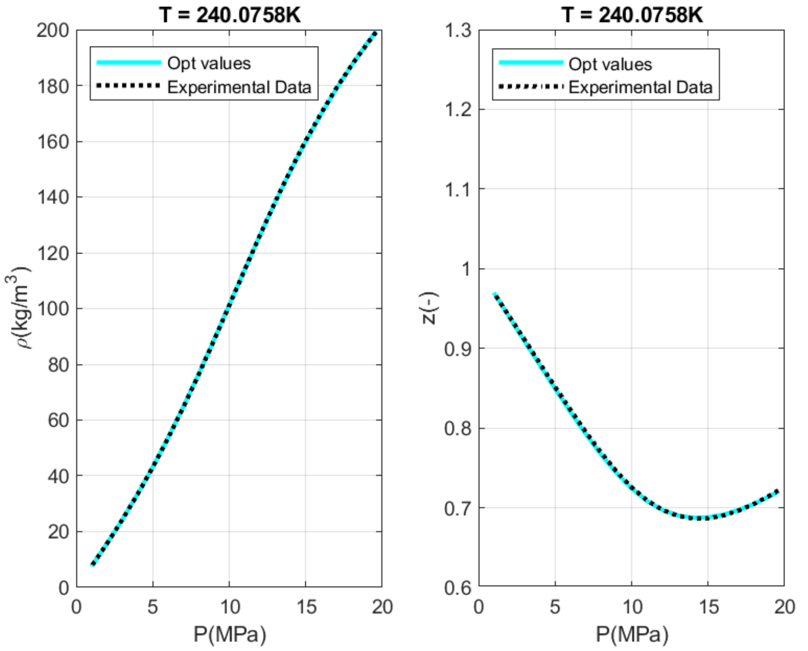

Figure 6.19: optimization results T1 – 90% CH_4 + 10% H_2, RKS.

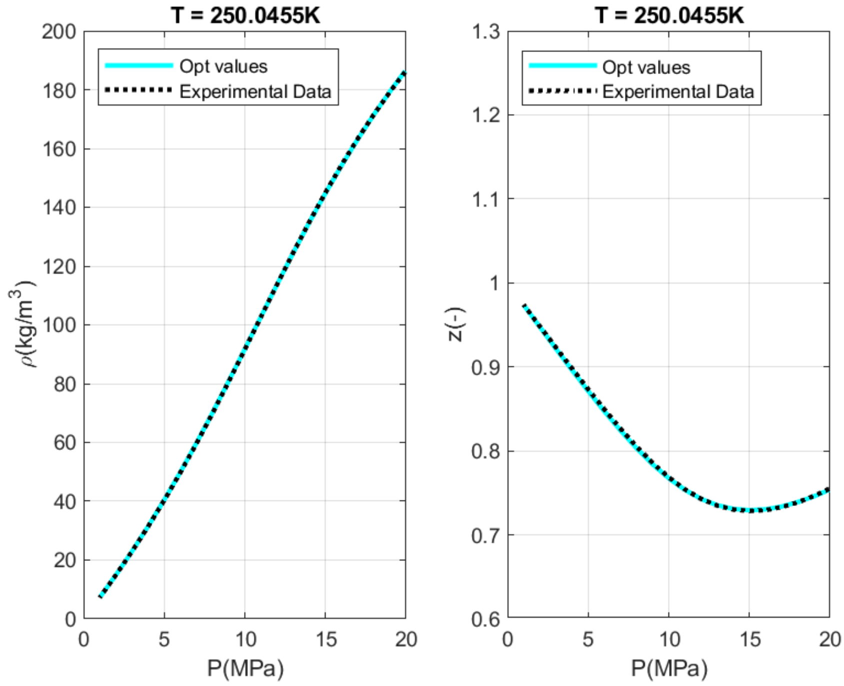

Figure 6.20: optimization results T2 – 90% CH_4 + 10% H_2, RKS.

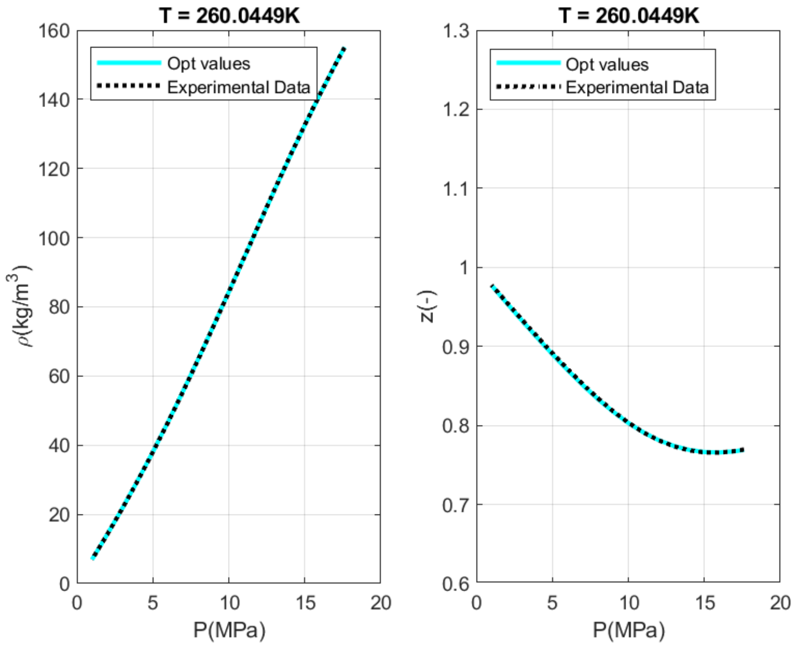

Figure 6.21: optimization results T3 – 90% CH_4 + 10% H_2, RKS.

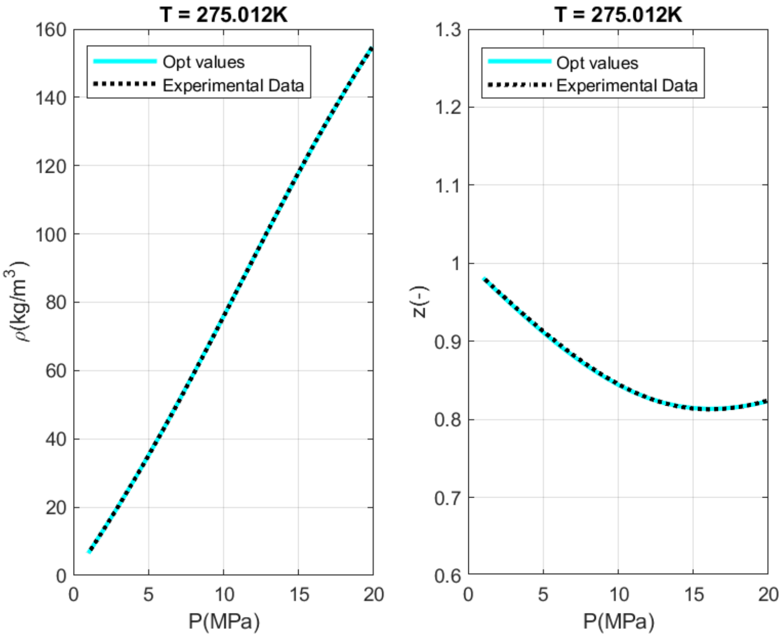

Figure 6.22: optimization results T4 – 90% CH_4 + 10% H_2, RKS.

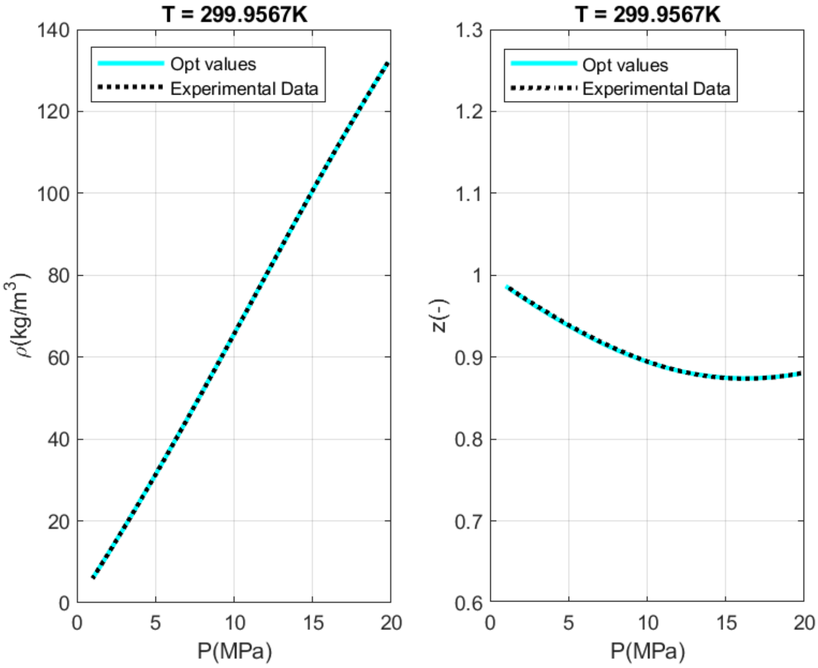

Figure 6.23: optimization results T5 – 90% CH_4 + 10% H_2, RKS.

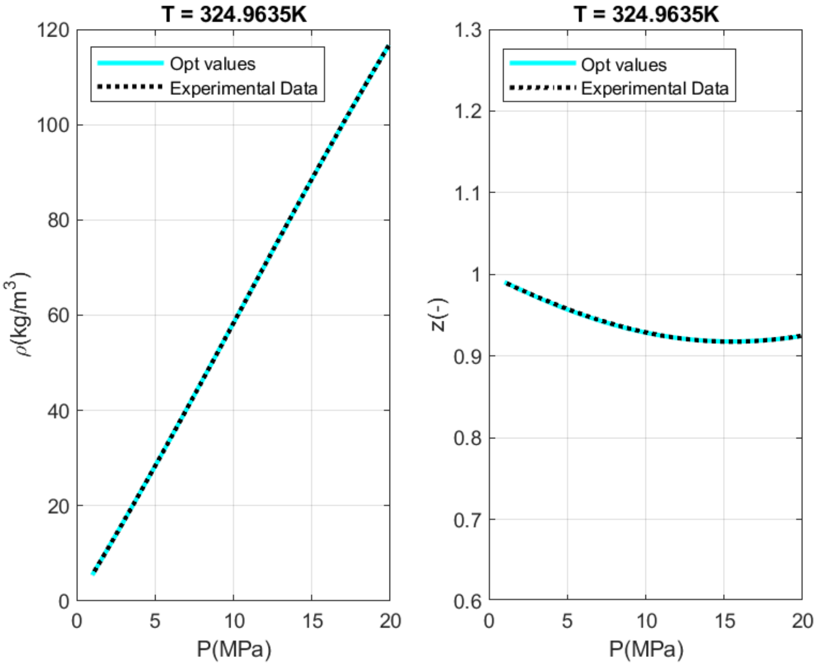

Figure 6.24: optimization results T6 – 90% CH_4 + 10% H_2, RKS.

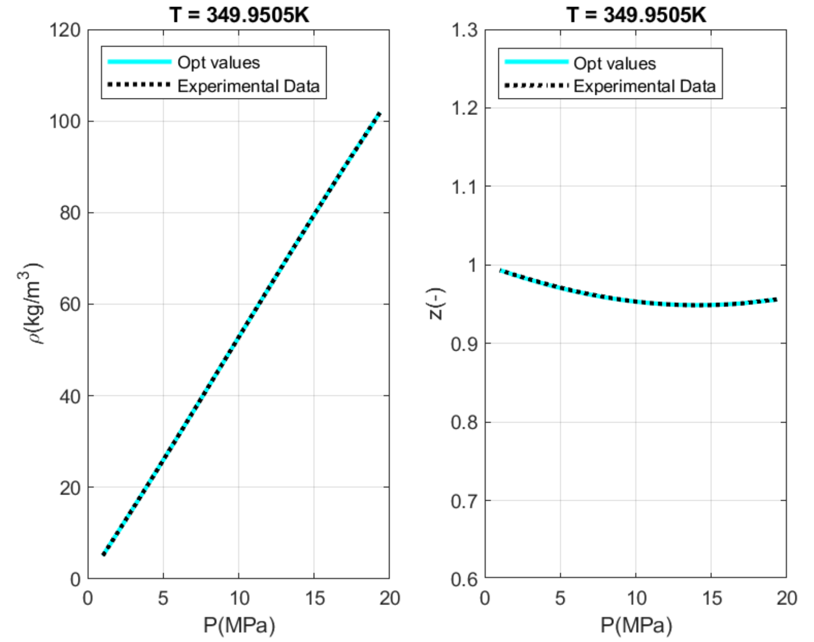

Figure 6.25: optimization results T7 – 90% CH_4 + 10% H_2, RKS.

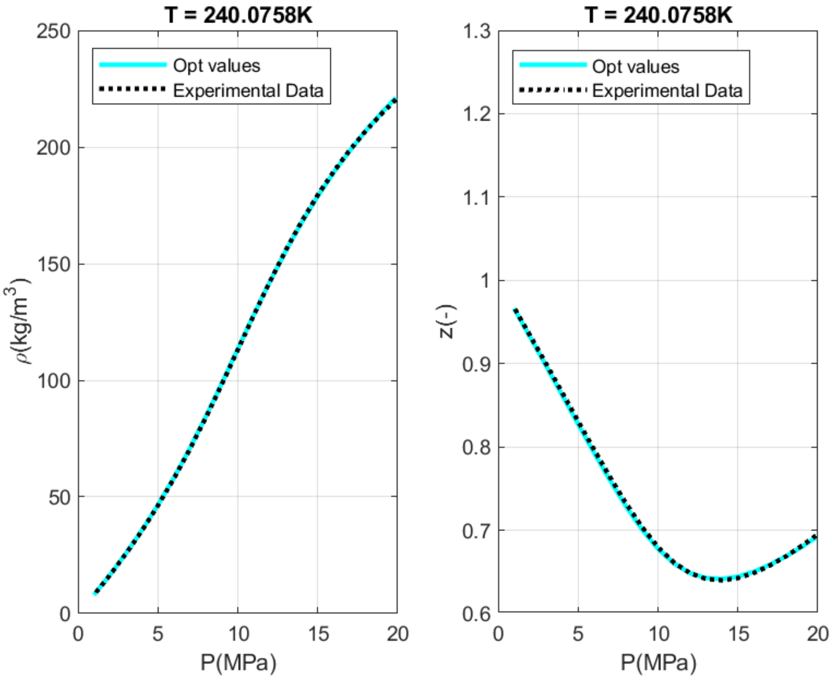

Figure 6.26: optimization results T1 – 95% CH_4 + 05% H_2, RKS.

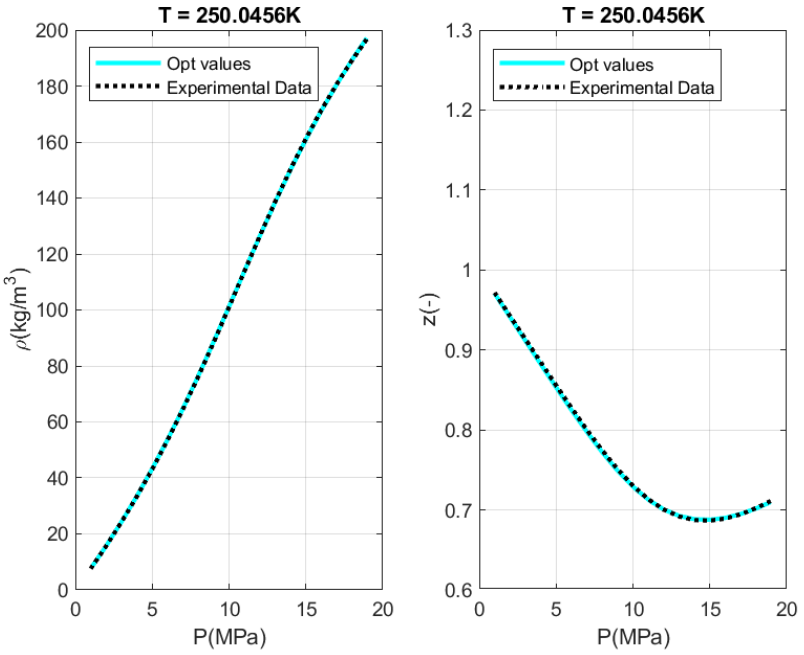

Figure 6.27: optimization results T2 – 95% CH_4 + 05% H_2, RKS.

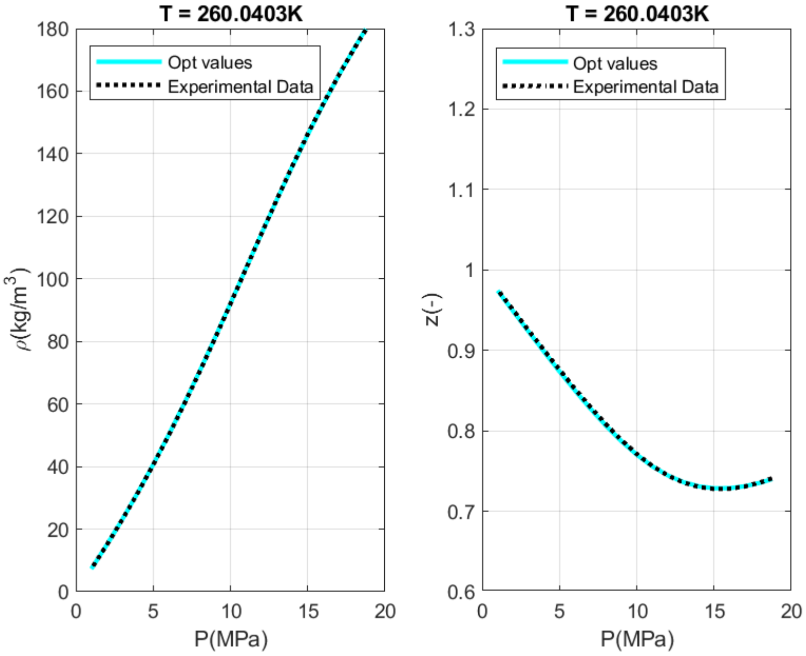

Figure 6.28: optimization results T3 – 95% CH_4 + 05% H_2, RKS.

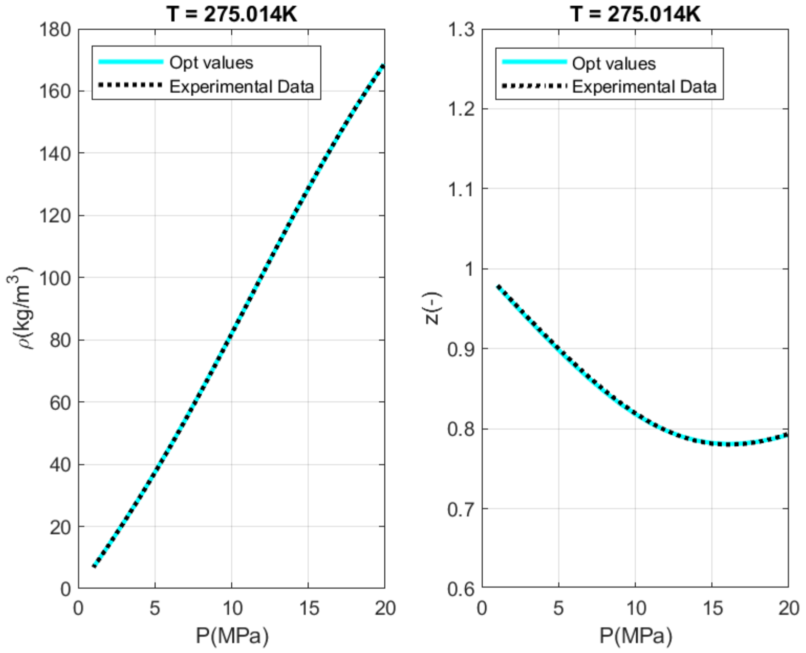

Figure 6.29: optimization results T4 – 95% CH_4 + 05% H_2, RKS.

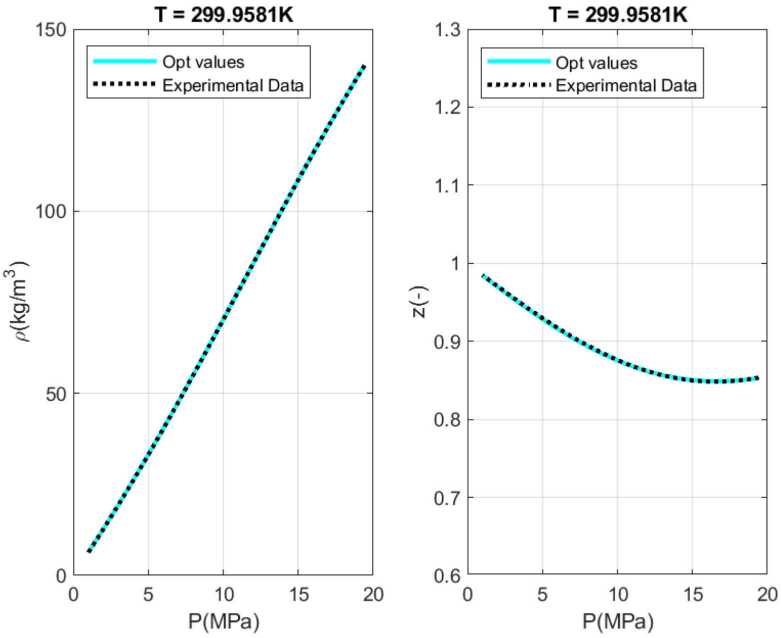

Figure 6.30: optimization results T5 – 95% CH_4 + 05% H_2, RKS.

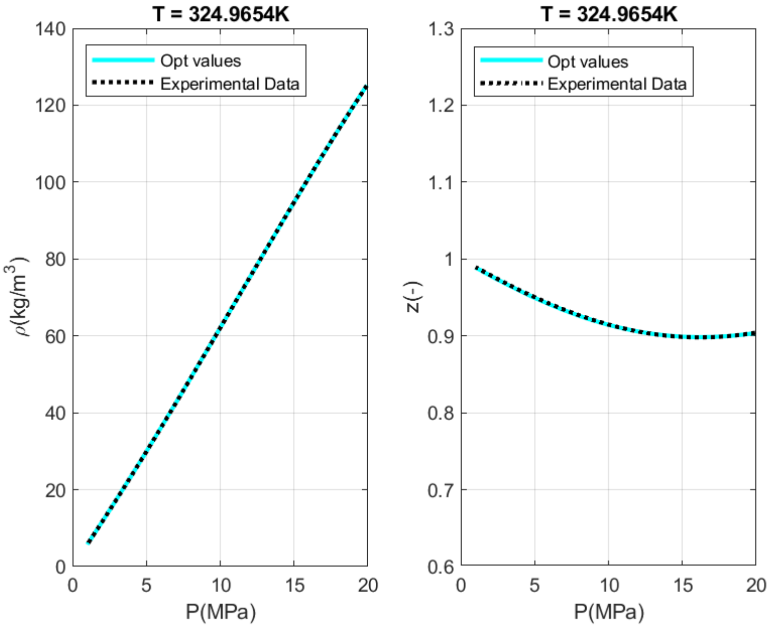

Figure 6.31: optimization results T6 – 95% CH_4 + 05% H_2, RKS.

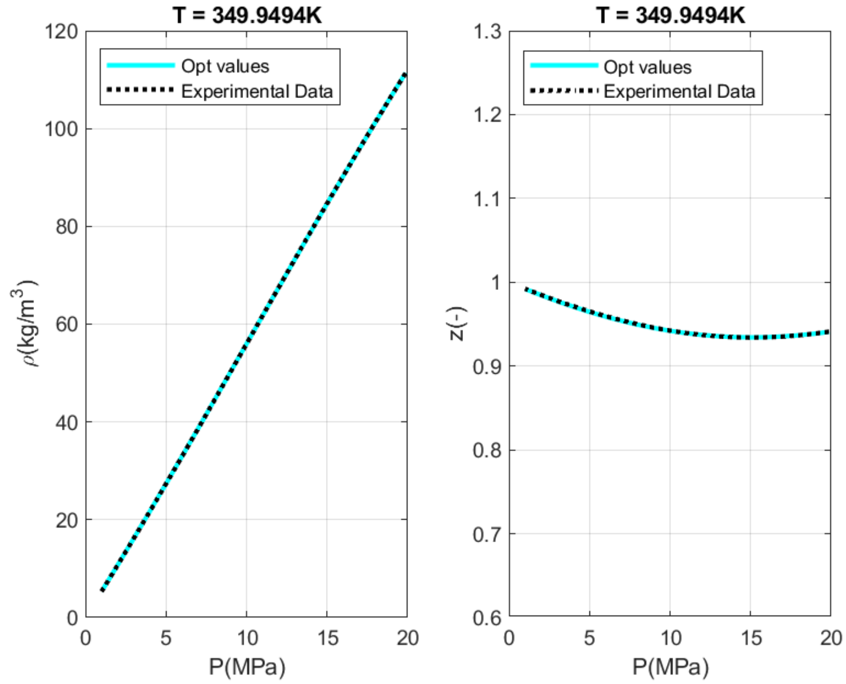

Figure 6.32: optimization results T7 – 95% CH_4 + 05% H_2, RKS.

Overall, from the plots, it can be seen that a good agreement has been obtained with the RKS EoS model for all the mixtures. The deviation for each curve remained around 0.075% both for the fitting of the density values and for the fitting of the compressibility values (overall, between 0.0072% and 0.26%).

The numerical results of the isotherm plots presented above are summarized in the tables below.

Table 6.2: Numerical results – 50% CH_4 + 50% H_2, RKS.

T(K)	**240.06945**	**250.036526**	**260.031368**	**275.004789**	**324.95925**	**349.94725**
$\boldsymbol{\Omega_a}$	0.56065391	0.56629414	0.57706326	0.59526469	0.59894783	0.5808579
$\boldsymbol{\Omega_b}$	0.08090345	0.08040996	0.08037343	0.080505	0.0814053	0.0824685
BIP	-0.1566383	-0.1559111	-0.1548533	-0.1535096	-0.1541032	-0.1567481
AAD($\boldsymbol{\rho}$) %	0.04164345	0.03635426	0.02689493	0.02087651	0.00722156	0.0125653
AAD(z) %	0.04162088	0.03633758	0.02688704	0.02087156	0.00722052	0.0125669

Table 6.3: Numerical results – 90% CH_4 + 10% H_2, RKS.

T(K)	**240.07575**	**250.0455**	**260.04489**	**275.012**	**299.95665**	**324.9635**	**349.9505**
$\boldsymbol{\Omega_a}$	0.4398949	0.44135676	0.4398157	0.4455105	0.4505373	0.4521802	0.454214
$\boldsymbol{\Omega_b}$	0.0819143	0.08177059	0.0809821	0.0814703	0.081398	0.0816183	0.0818622
BIP	-0.1500637	-0.1500596	-0.1500418	-0.1500379	-0.150003	-0.1500605	-0.1501276
AAD($\boldsymbol{\rho}$) %	0.1588674	0.13431152	0.0826178	0.0863342	0.0545113	0.0336005	0.0247728
AAD(z) %	0.1586165	0.13411718	0.0825375	0.0862501	0.0544767	0.0335884	0.0247653

Table 6.4: Numerical results – 50% CH_4 + 50% H_2, RKS.

T(K)	240.07575	250.0455	260.04489	275.012	299.95665	324.9635	349.9505
$\boldsymbol{\Omega_a}$	0.4320809	0.43160398	0.4322919	0.4356769	0.4391399	0.4424415	0.4468541
$\boldsymbol{\Omega_b}$	0.0820601	0.0816057	0.0813766	0.081527	0.081354	0.0815921	0.0820172
BIP	-0.1500111	-0.1500083	-0.1500078	-0.1500079	-0.1500007	-0.1500168	-0.150045
AAD($\boldsymbol{\rho}$) %	0.2625541	0.17465252	0.1393201	0.1182192	0.0632702	0.0488823	0.0302421
AAD(z) %	0.2619153	0.17434331	0.1391178	0.1180685	0.0632242	0.0488547	0.0302307

6.1.2 PR EoS Results

When using the PR EoS, the initial guesses for the parameters to be optimized are reported in table 6.5.

Table 6.5: Initial guesses for optimization when using PR EoS.

$\boldsymbol{\Omega_a}$	$\boldsymbol{\Omega_b}$	**BIP**
0.45724	0.0778	-0.15

The results for the mixture 50% CH_4 + 50% H_2 are shown in the Figures 6.33 to 6.38; the results for the mixture 90% CH_4 + 10% H_2 are shown in the Figures 6.39 to 6.45; the results for the mixture 95% CH_4 + 05% H_2 are shown in the Figures 6.46 to 6.52. the fitting of the density is reported in the first plot (the one on the left) and the fitting of the compressibility factor is reported in the second plot (the one on the right).

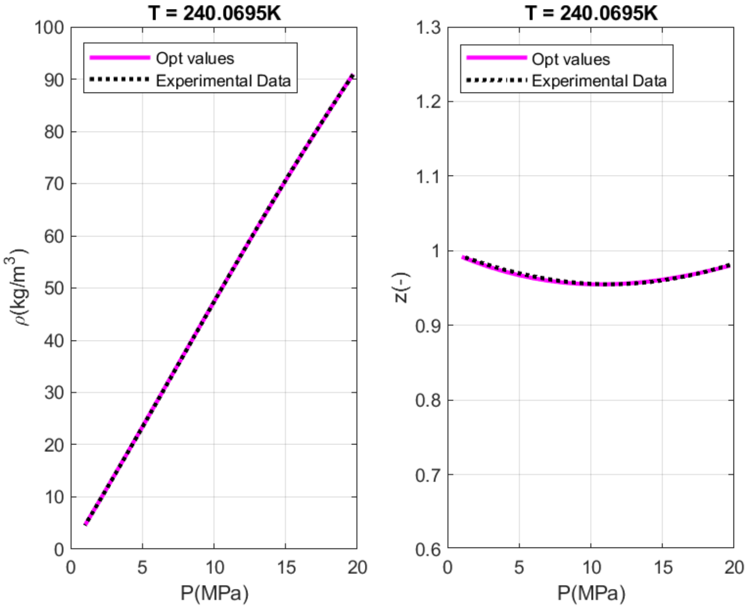

Figure 6.33: optimization results T1 – 50% CH_4 + 50% H_2, PR.

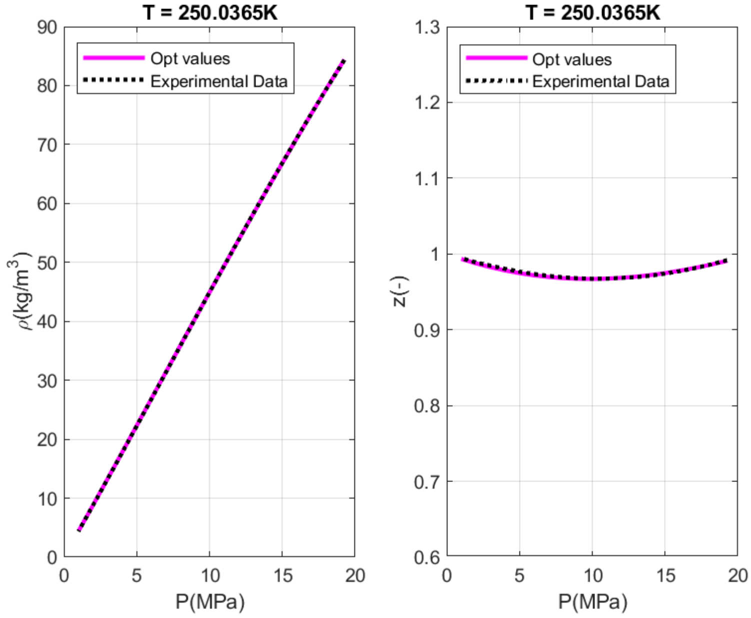

Figure 6.34: optimization results T2 – 50% CH_4 + 50% H_2, PR.

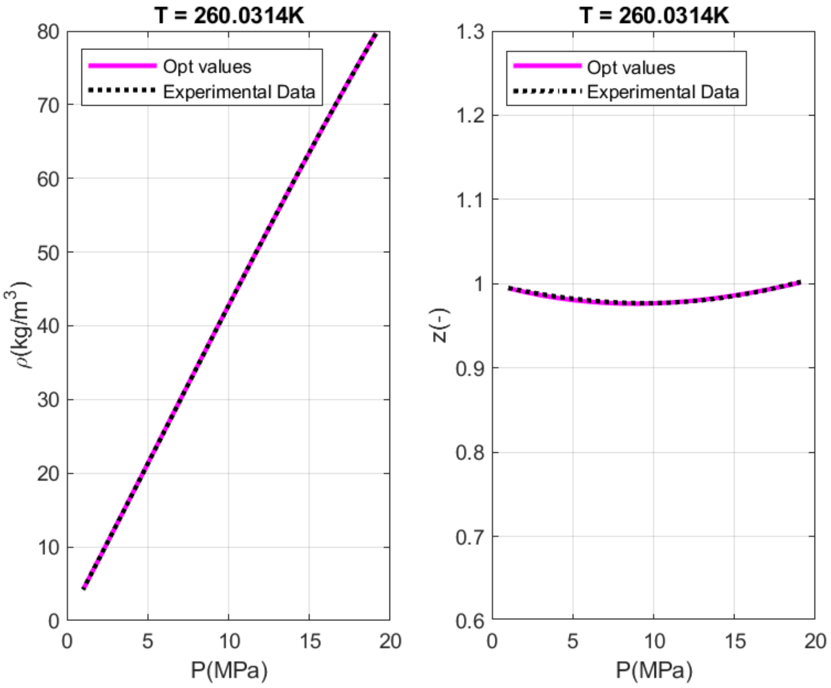

Figure 6.35: optimization results T3 – 50% CH_4 + 50% H_2, PR.

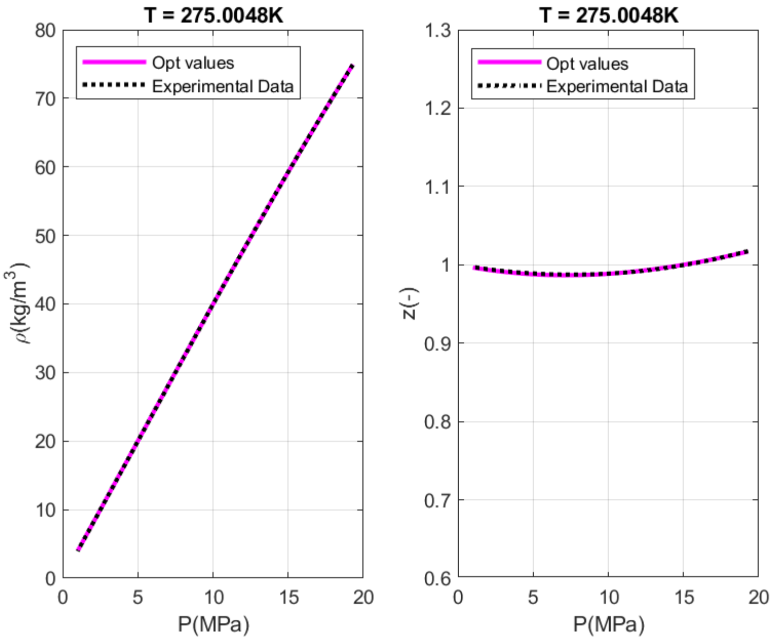

Figure 6.36: optimization results T4 – 50% CH_4 + 50% H_2, PR.

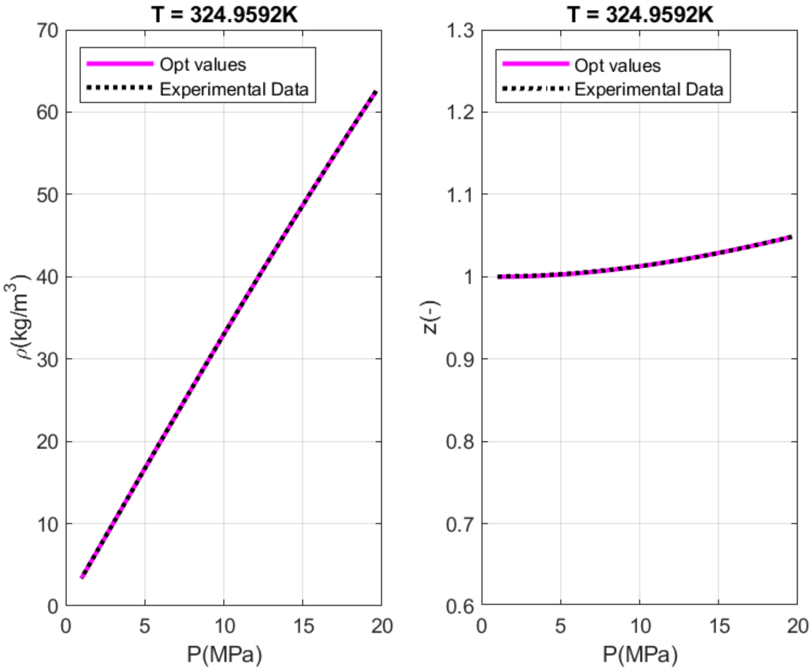

Figure 6.37: optimization results T5 – 50% CH_4 + 50% H_2, PR.

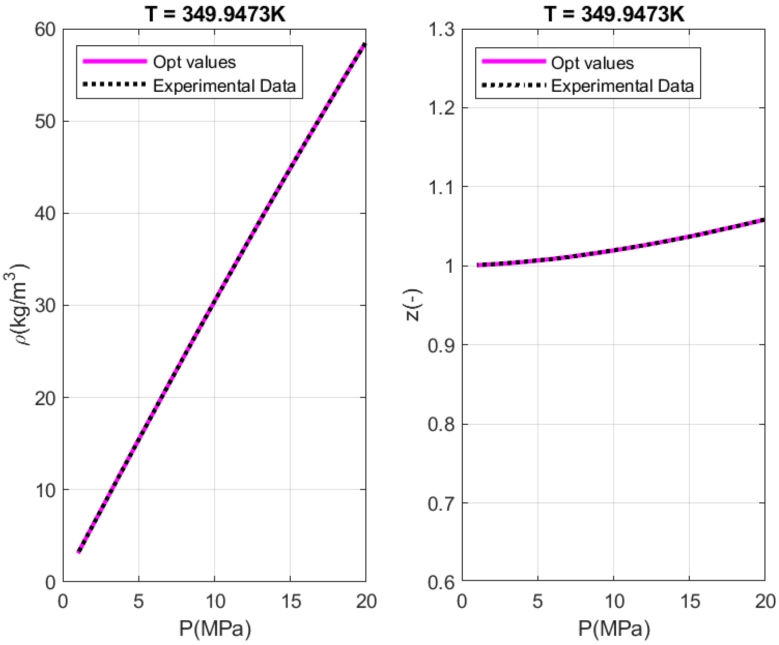

Figure 6.38: optimization results T6 – 50% CH_4 + 50% H_2, PR.

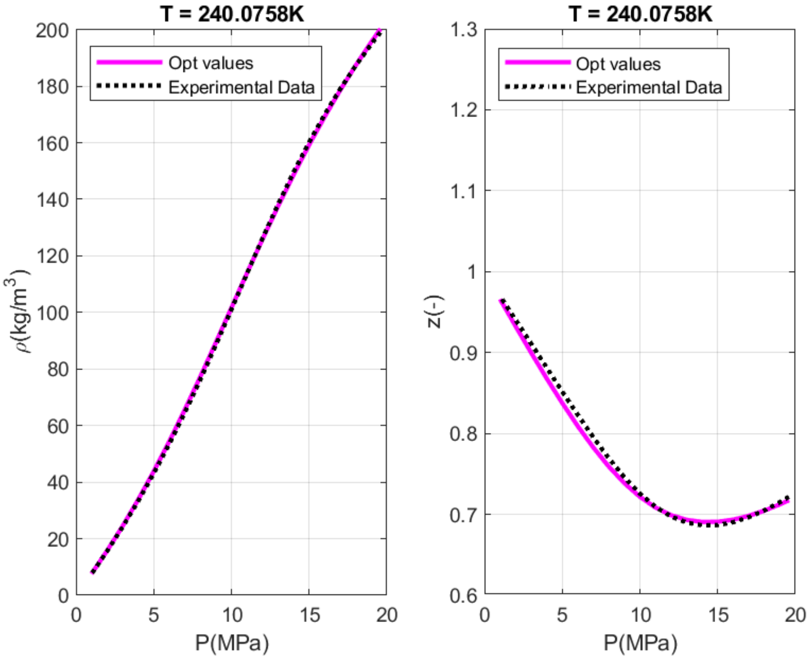

Figure 6.39: optimization results T1 – 90% CH_4 + 10% H_2, PR.

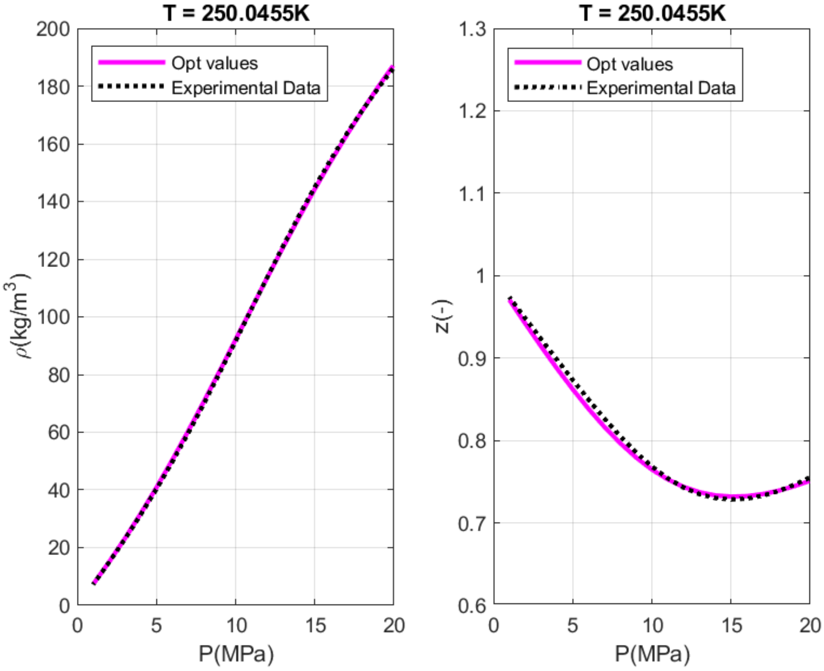

Figure 6.40: optimization results T2 – 90% CH_4 + 10% H_2, PR.

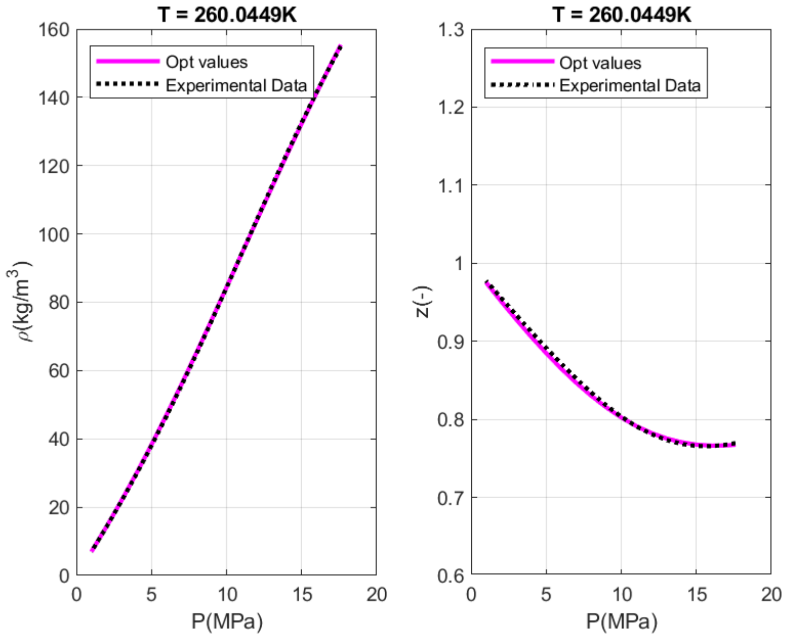

Figure 6.41: optimization results T3 – 90% CH_4 + 10% H_2, PR.

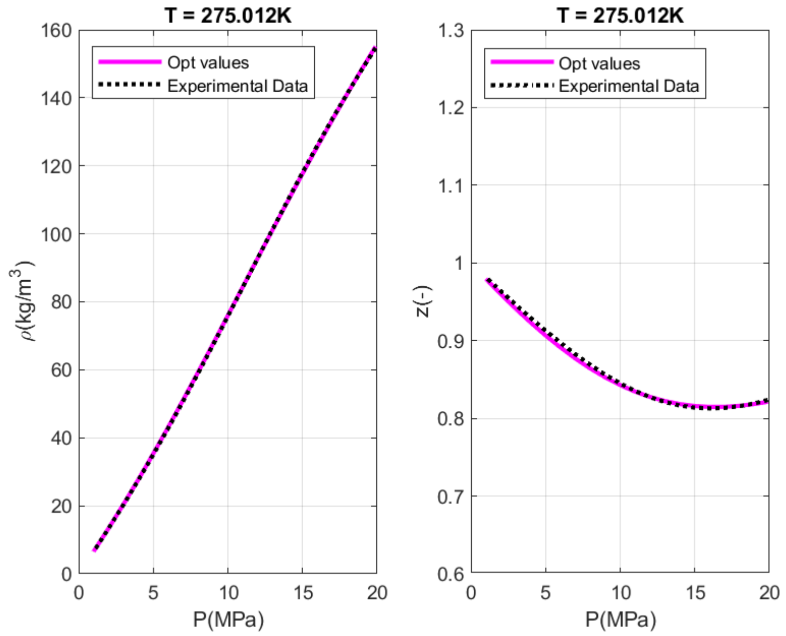

Figure 6.42: optimization results T4 – 90% CH_4 + 10% H_2, PR.

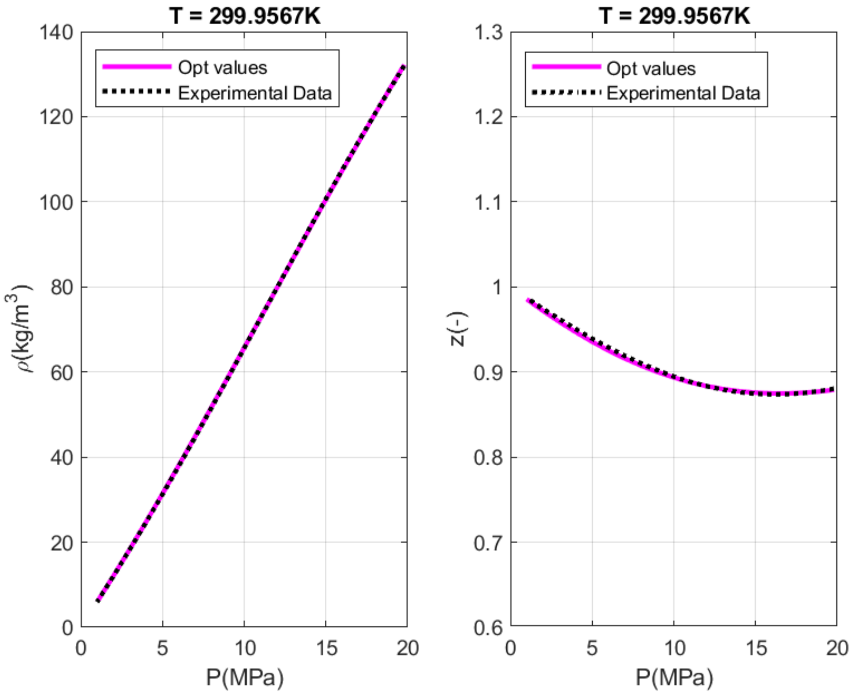

Figure 6.43: optimization results T5 – 90% CH_4 + 10% H_2, PR.

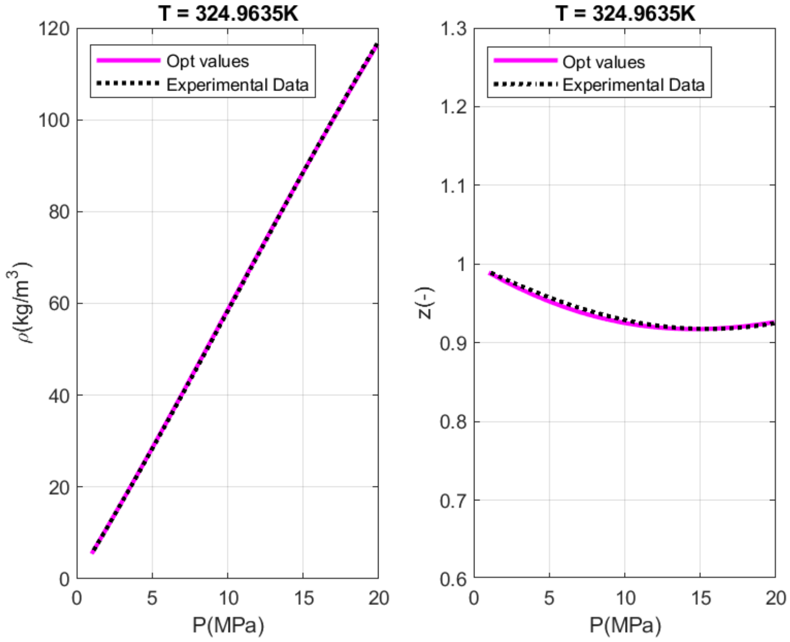

Figure 6.44: optimization results T6 – 90% CH_4 + 10% H_2, PR.

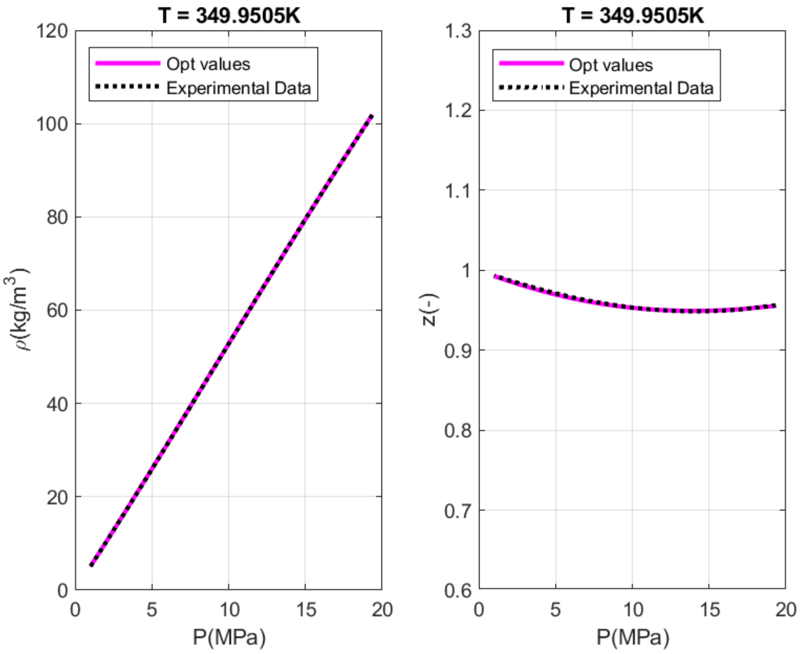

Figure 6.45: optimization results T7 – 90% CH_4 + 10% H_2, PR.

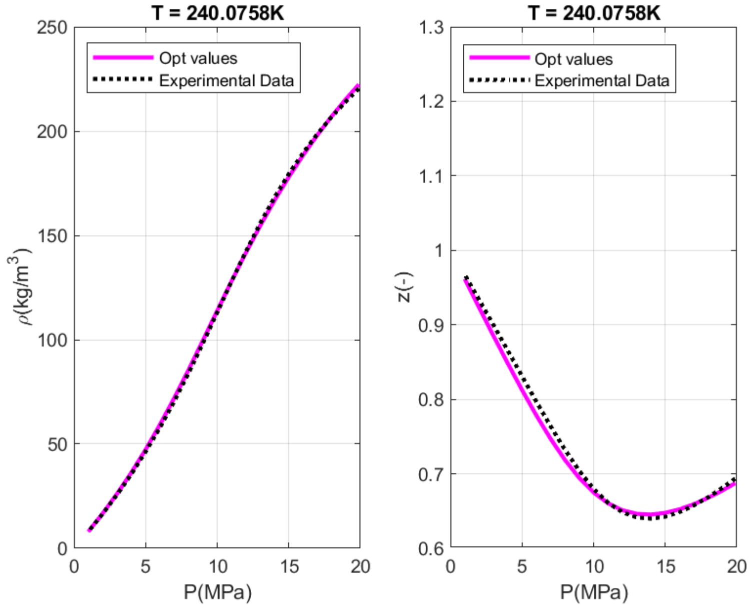

Figure 6.46: optimization results T1 – 95% CH_4 + 05% H_2, PR.

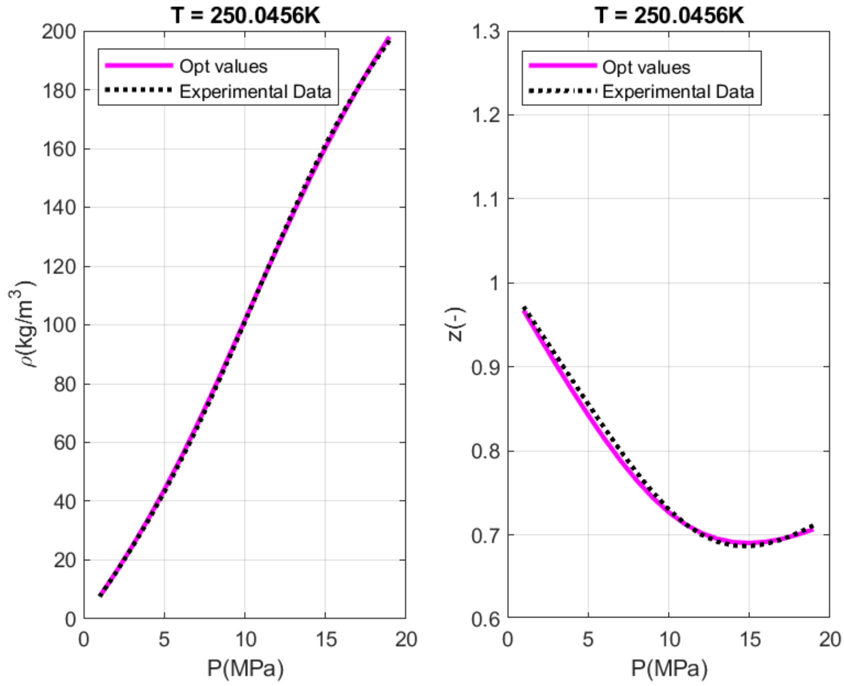

Figure 6.47: optimization results T2 – 95% CH_4 + 05% H_2, PR.

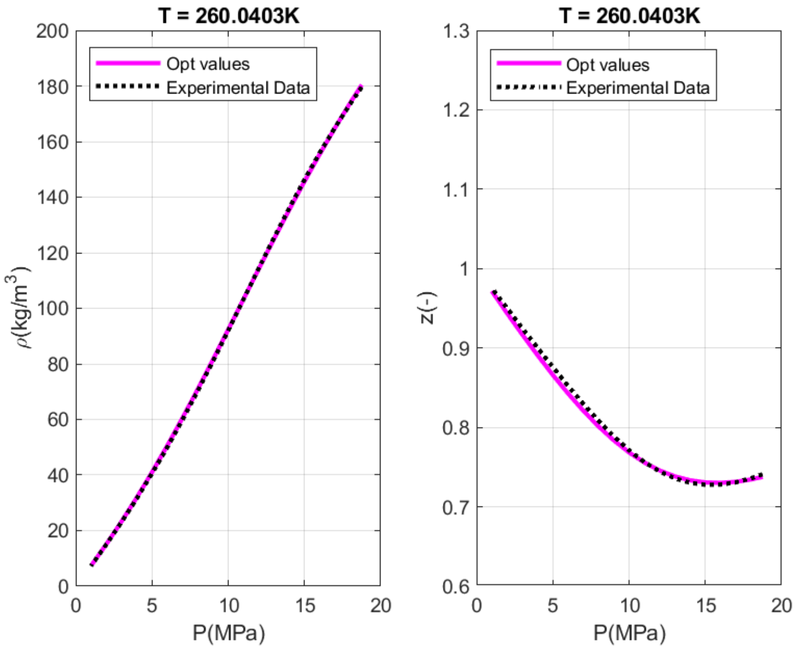

Figure 6.48: optimization results T3 – 95% CH_4 + 05% H_2, PR.

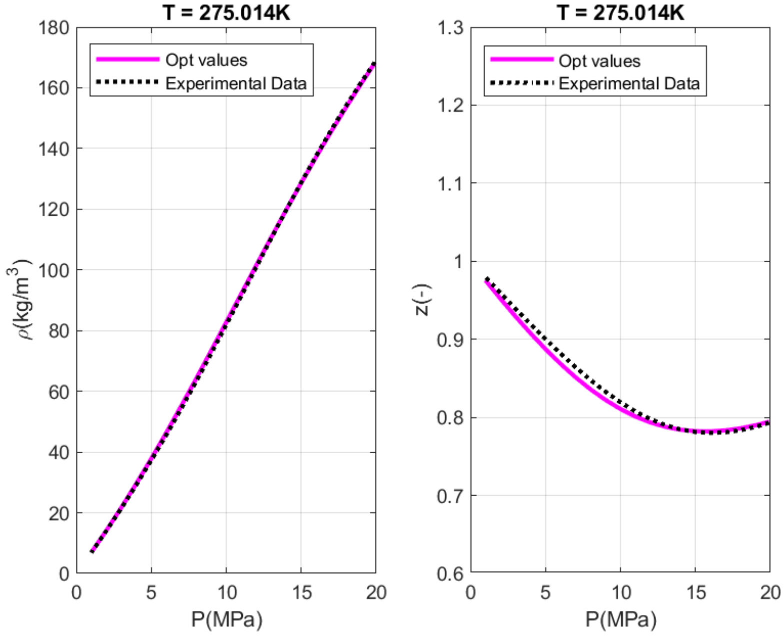

Figure 6.49: optimization results T4 – 95% CH_4 + 05% H_2, PR.

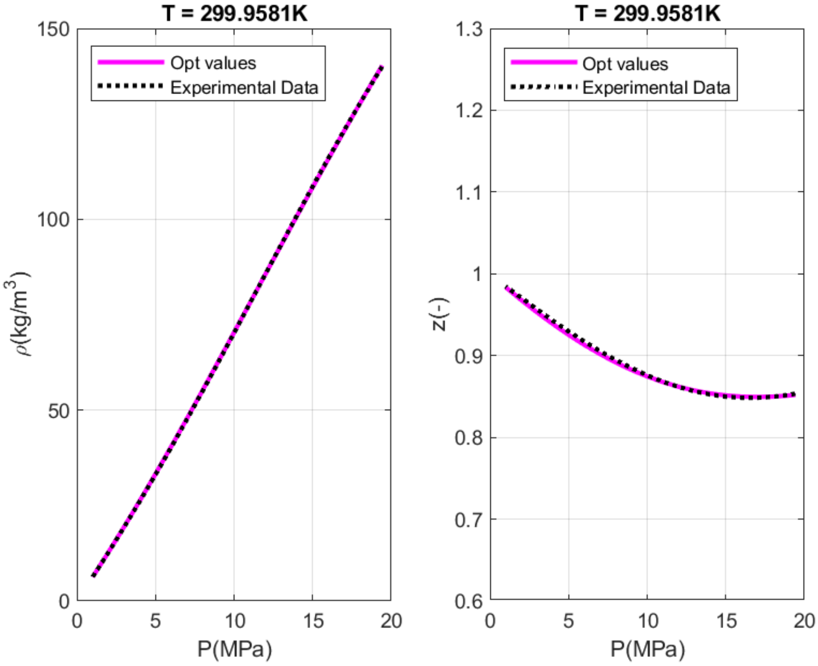

Figure 6.50: optimization results T5 – 95% CH_4 + 05% H_2, PR.

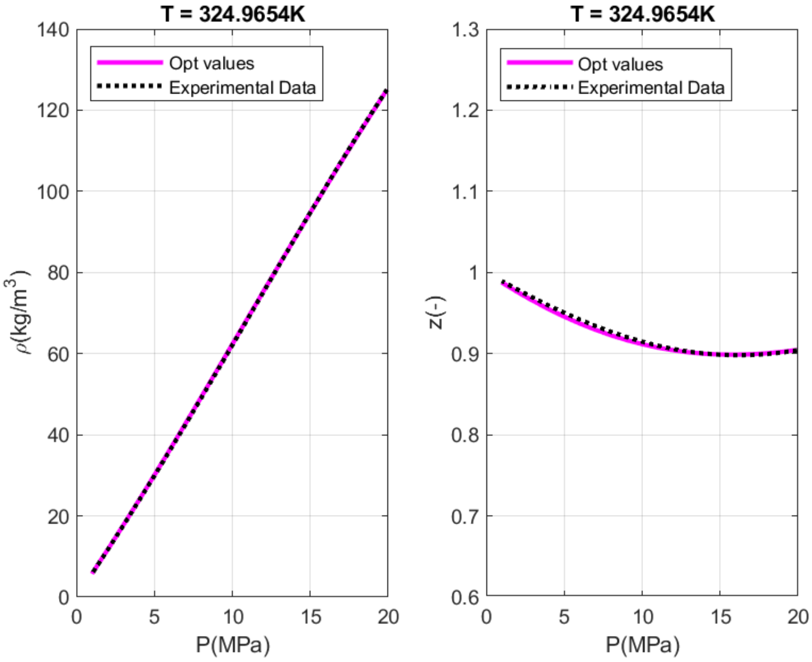

Figure 6.51: optimization results T6 – 95% CH_4 + 05% H_2, PR.

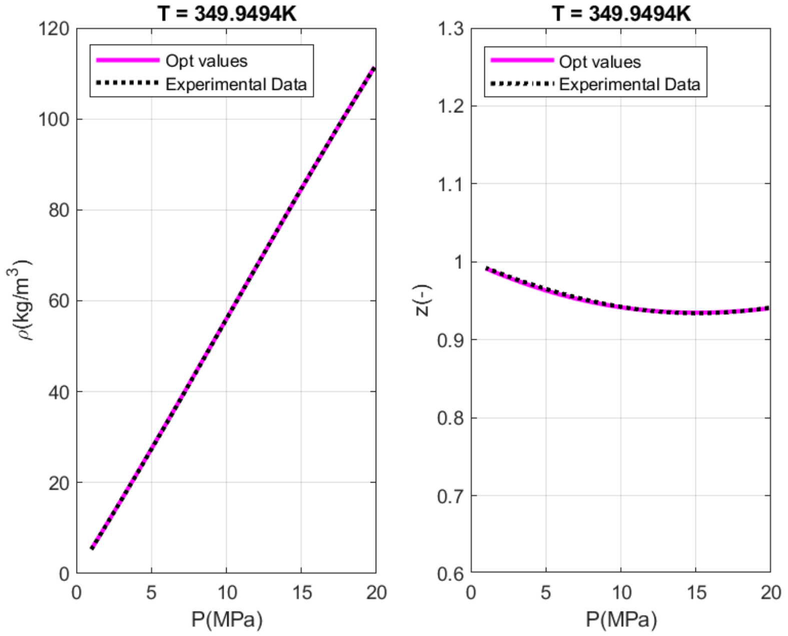

Figure 6.52: optimization results T7 – 95% CH_4 + 05% H_2, PR.

Also applying the PR EoS model the reproduction of the data is accurate since the deviation for each curve remained around 0.32%.

Furthermore, in this case it can be noted that the accuracy in the prediction of the properties decreases as the temperature decreases and as the quantities of CH_4 in the mixture increases; in fact, the highest AAD (about 1.1%) is obtained for the mixture whose composition is 95% CH_4 + 05% H_2 at a temperature equal to 240.07575 K.

The numerical results of the isotherm plots presented above are summarized in the tables below.

Table 6.6: Numerical results – 50% CH_4 + 50% H_2, PR.

T(K)	**240.06945**	**250.036526**	**260.031368**	**275.004789**	**324.95925**	**349.94725**
$\boldsymbol{\Omega_a}$	0.32810684	0.3175688	0.31151468	0.30231116	0.28731422	0.28439773
$\boldsymbol{\Omega_b}$	0.0730118	0.07217937	0.07208865	0.07234202	0.07394094	0.0753583
BIP	-0.1311617	-0.1299394	-0.1291725	-0.1470941	-0.125805	-0.1252995
AAD($\boldsymbol{\rho}$) %	0.12132905	0.09419504	0.07225183	0.05851647	0.02364271	0.01610412
AAD(z) %	0.12114217	0.09407788	0.07218586	0.05847548	0.02363421	0.01610257

Table 6.7: Numerical results – 90% CH_4 + 10% H_2, PR.

T (K)	**240.07575**	**250.0455**	**260.04489**	**275.012**	**299.95665**	**324.9635**	**349.9505**
$\boldsymbol{\Omega_a}$	0.4307505	0.42246395	0.4034672	0.4033544	0.3890934	0.4071238	0.3700024
$\boldsymbol{\Omega_b}$	0.0766939	0.07567053	0.0724408	0.0734227	0.0721942	0.0768826	0.0717181
BIP	-0.1491518	-0.1489043	-0.1483617	-0.1483463	-0.1478417	-0.1483567	-0.1472715
AAD($\boldsymbol{\rho}$) %	0.7874682	0.61863785	0.3689812	0.3323574	0.1900719	0.2963156	0.0779468
AAD(z) %	0.7798261	0.61394249	0.367354	0.3310215	0.1896352	0.2951719	0.0778729

Table 6.8: Numerical results – 95% CH_4 + 05% H_2, PR.

T(K)	240.07575	250.0455	260.04489	275.012	299.95665	324.9635	349.9505
$\boldsymbol{\Omega_a}$	0.4443178	0.43085571	0.4213159	0.4364410	0.3989005	0.4063489	0.382428
$\boldsymbol{\Omega_b}$	0.0776963	0.07564759	0.0743119	0.0776656	0.0721891	0.0749082	0.0720372
BIP	-0.1497866	-0.1495844	-0.1494427	-0.1496629	-0.1490767	-0.1491747	-0.1488272
AAD($\boldsymbol{\rho}$) %	1.0769858	0.75533963	0.564772	0.7418993	0.2238514	0.2570063	0.0956039
AAD(z) %	1.0627959	0.74845443	0.5609915	0.7342011	0.223248	0.2560745	0.0954916

6.1.3 Comparison between RKS and PR EoSs

Finally, the results obtained using the two EoSs have been compared (Figure 6.53 to 6.72).

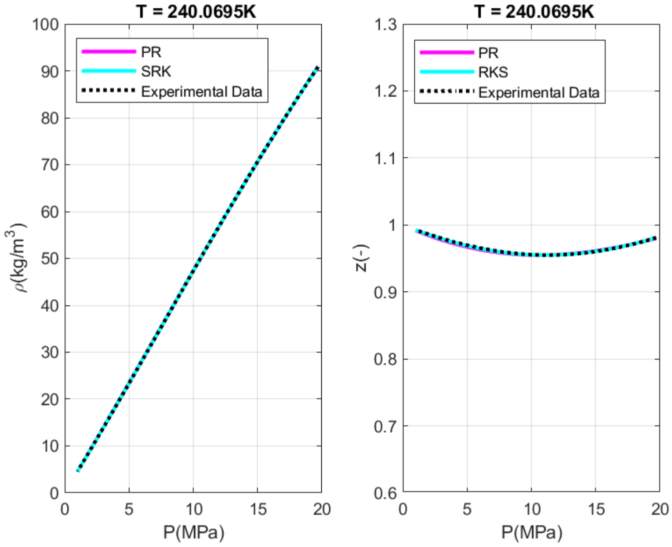

Figure 6.53: optimization results T1 – 50% CH_4 + 50% H_2.

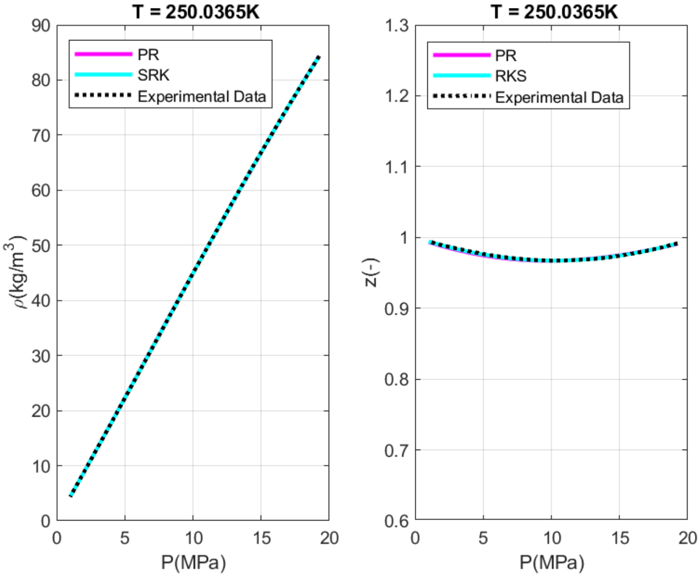

Figure 6.54: optimization results T2 – 50% CH_4 + 50% H_2.

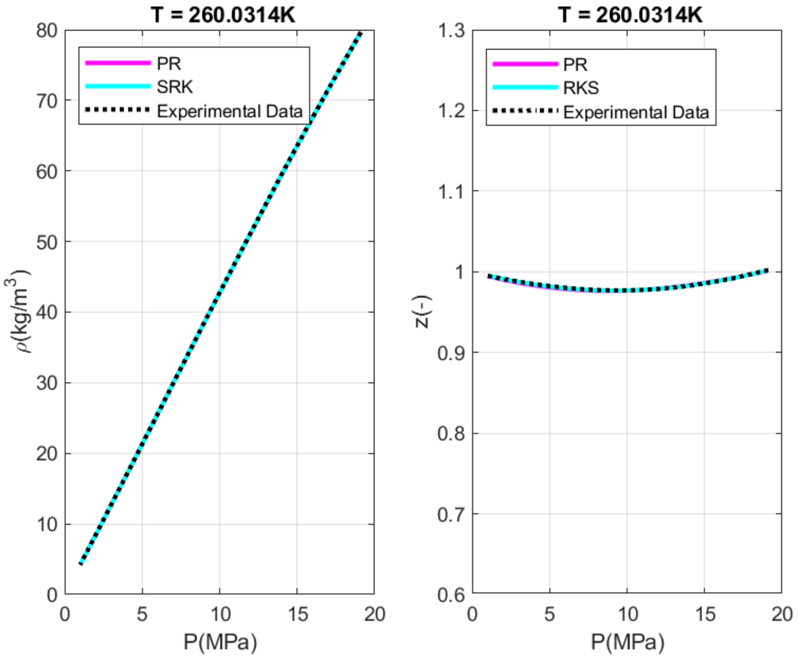

Figure 6.55: optimization results T3 – 50% CH_4 + 50% H_2.

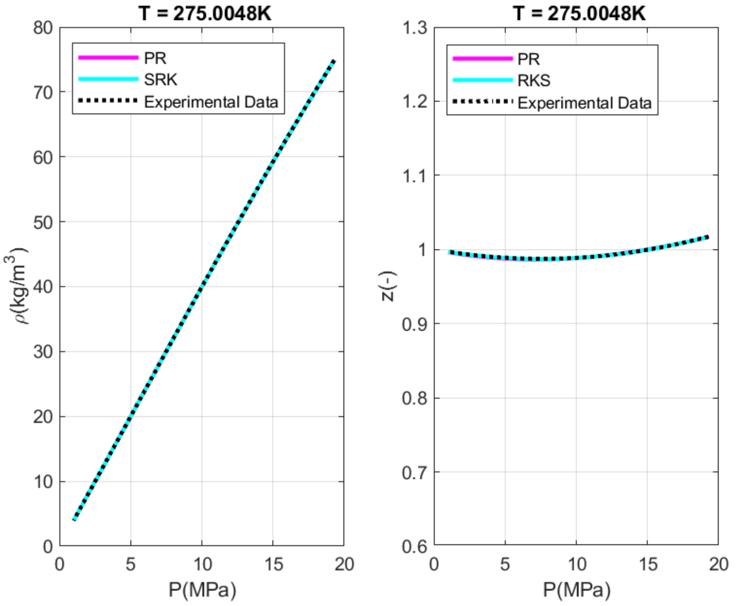

Figure 6.56: optimization results T4 – 50% CH_4 + 50% H_2.

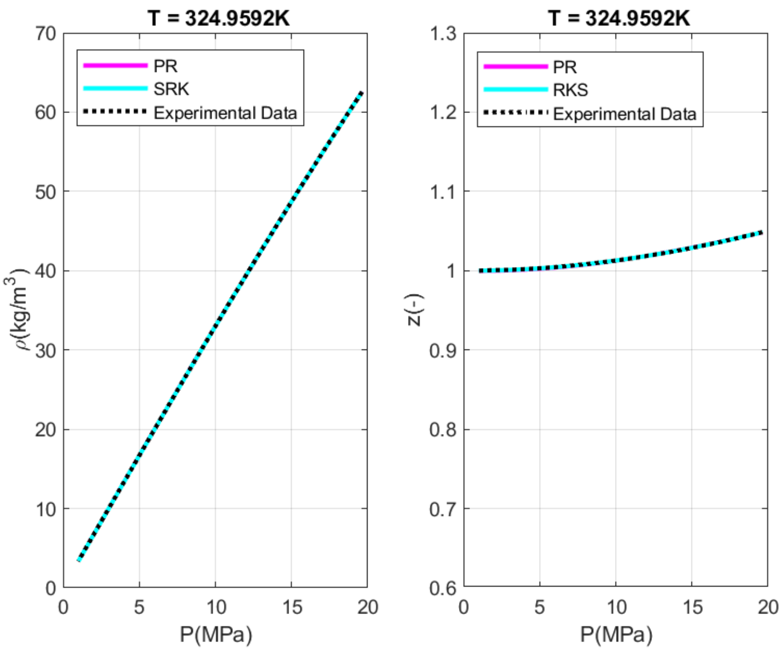

Figure 6.57: optimization results T5 – 50% CH_4 + 50% H_2.

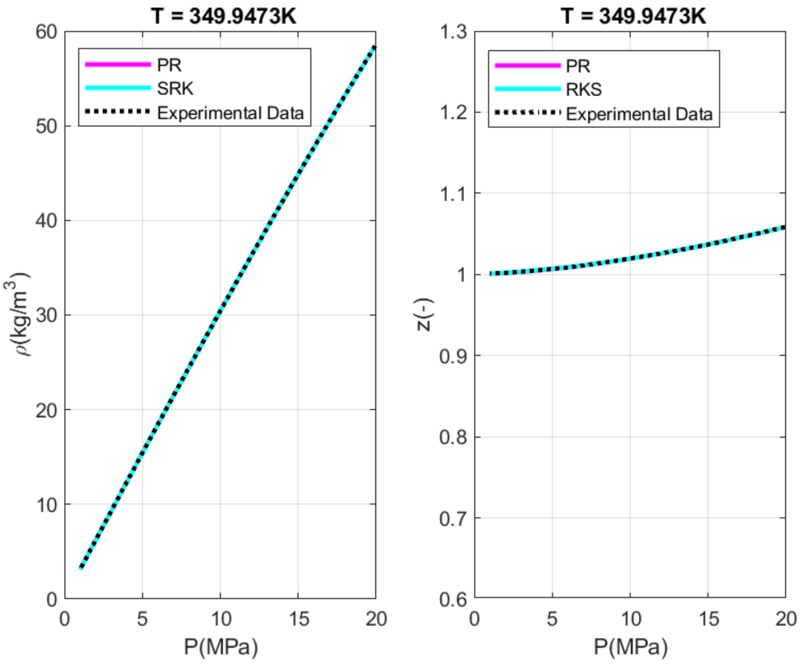

Figure 6.58: optimization results T6 – 50% CH_4 + 50% H_2.

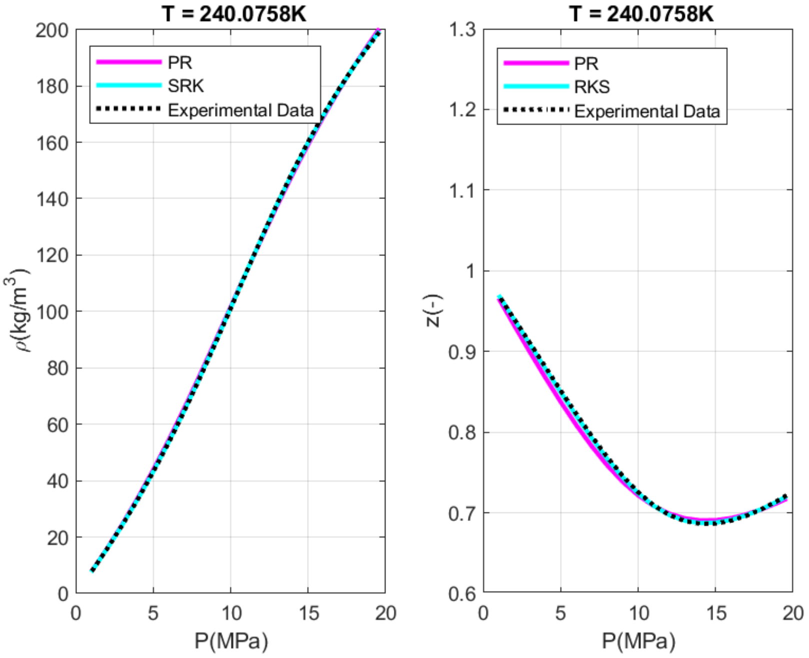

Figure 6.59: optimization results T1 – 90% CH_4 + 10% H_2.

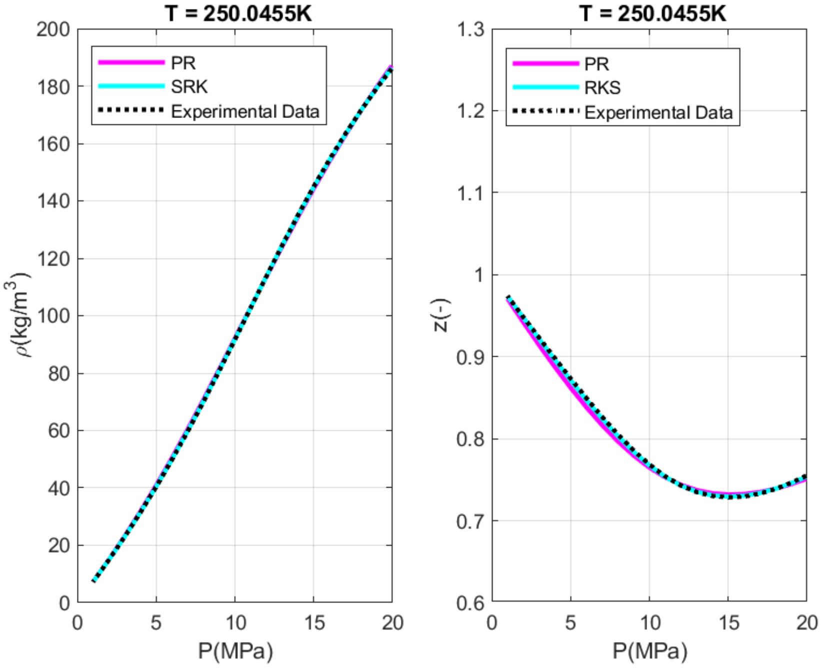

Figure 6.60: optimization results T2 – 90% CH_4 + 10% H_2.

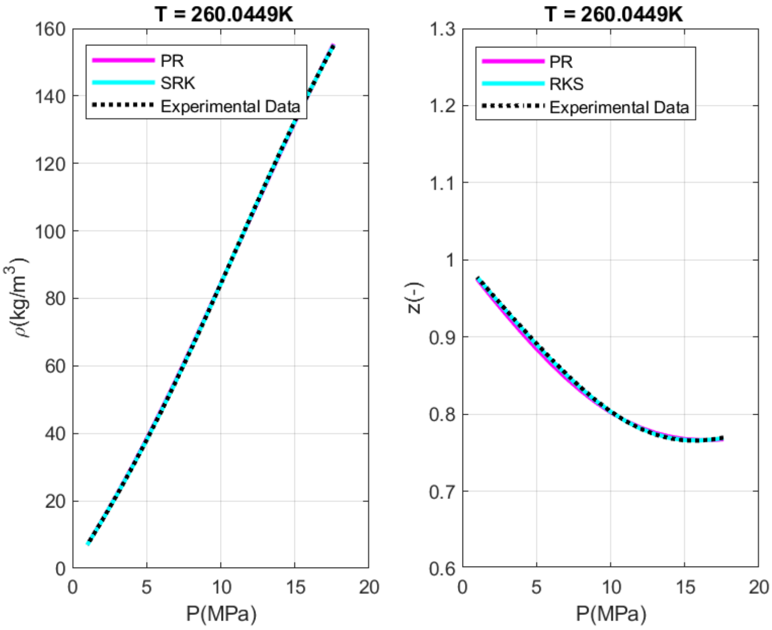

Figure 6.61: optimization results T3 – 90% CH_4 + 10% H_2.

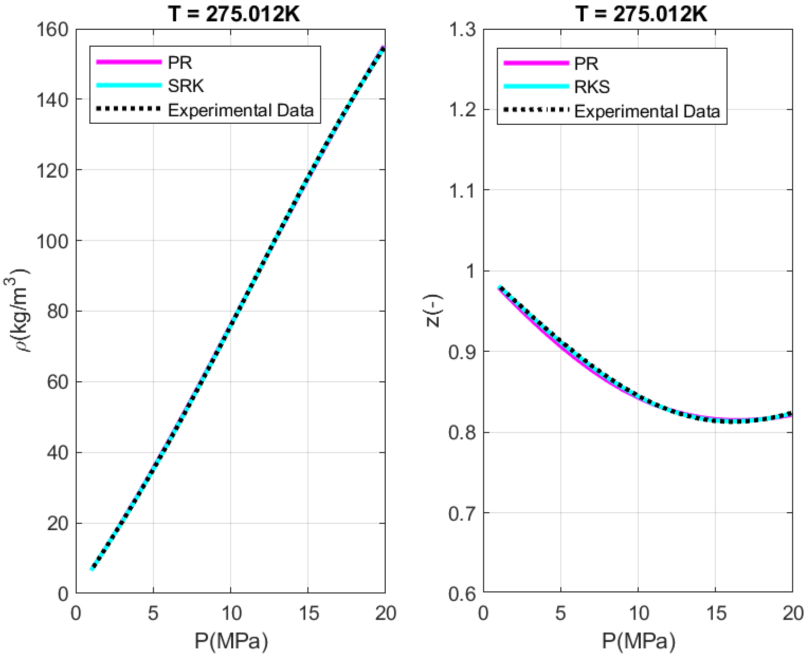

Figure 6.62: optimization results T4 – 90% CH_4 + 10% H_2.

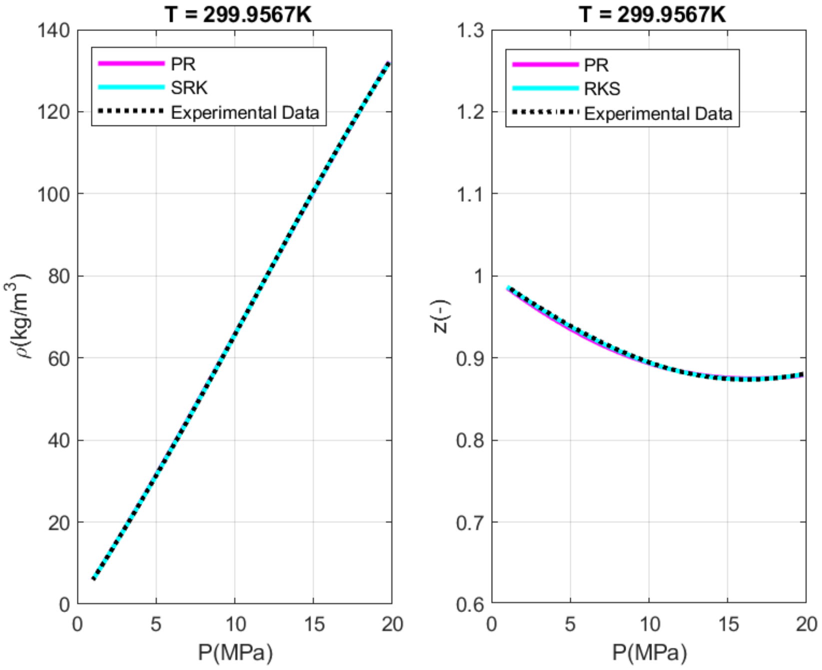

Figure 6.63: optimization results T5 – 90% CH_4 + 10% H_2.

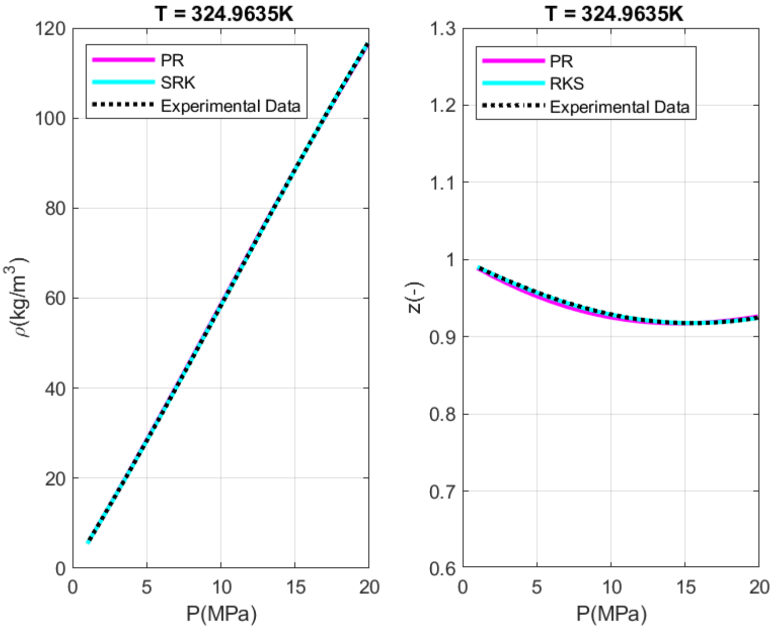

Figure 6.64: optimization results T6 – 90% CH_4 + 10% H_2.

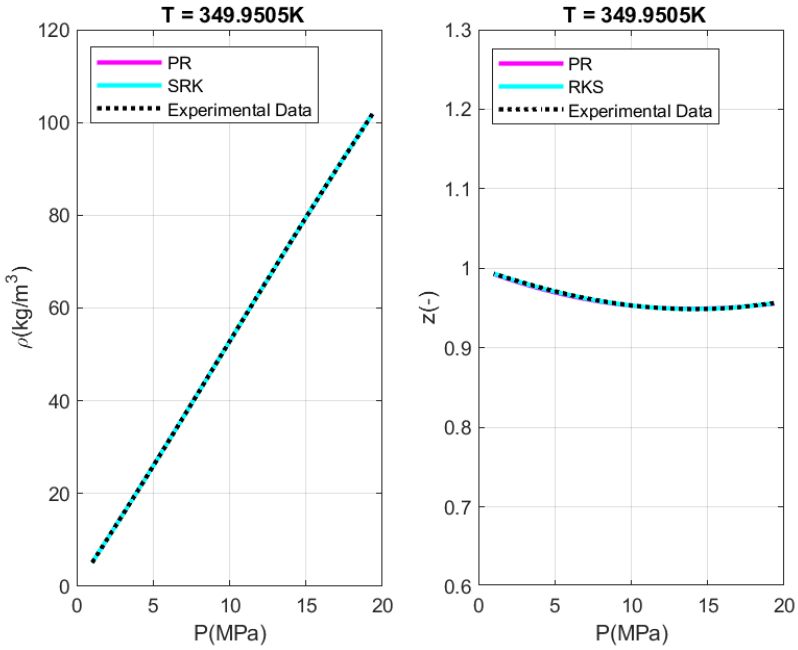

Figure 6.65: optimization results T7 – 90% CH_4 + 10% H_2.

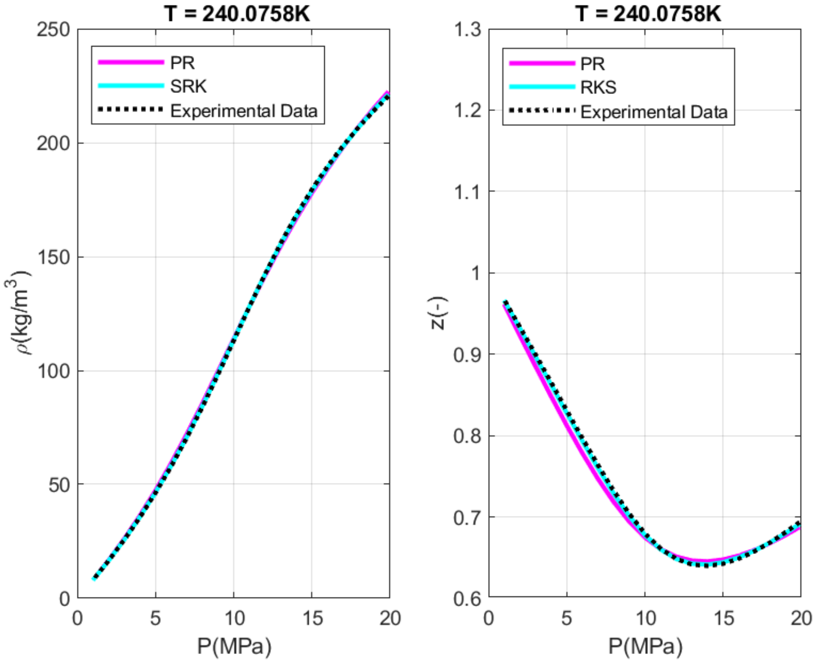

Figure 6.66: optimization results T1 – 95% CH_4 + 05% H_2.

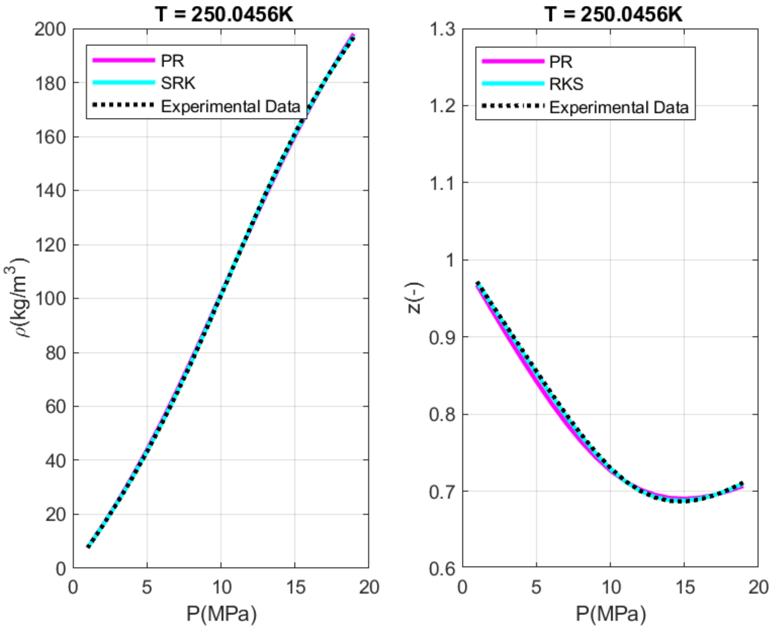

Figure 6.67: optimization results T2 – 95% CH_4 + 05% H_2.

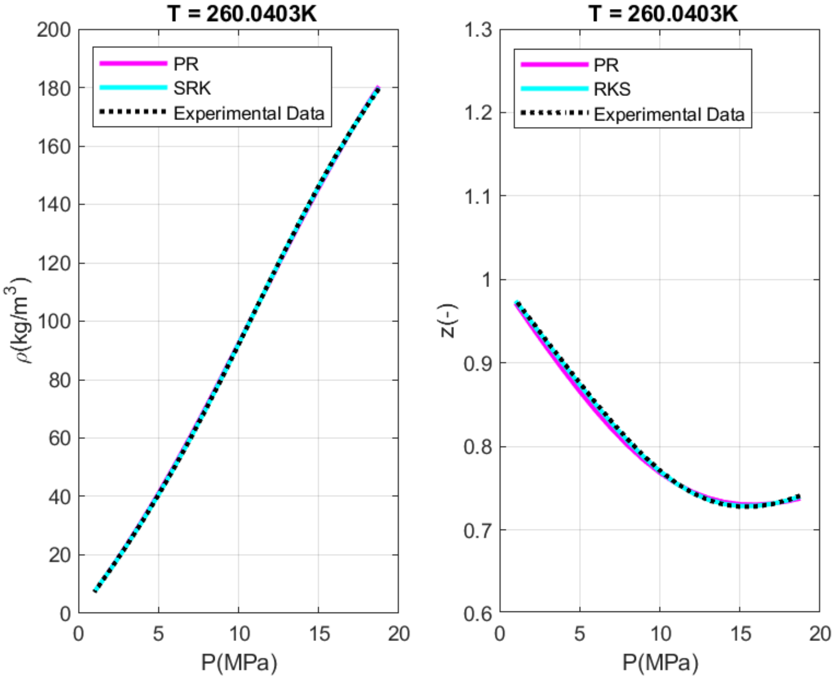

Figure 6.68: optimization results T3 – 95% CH_4 + 05% H_2.

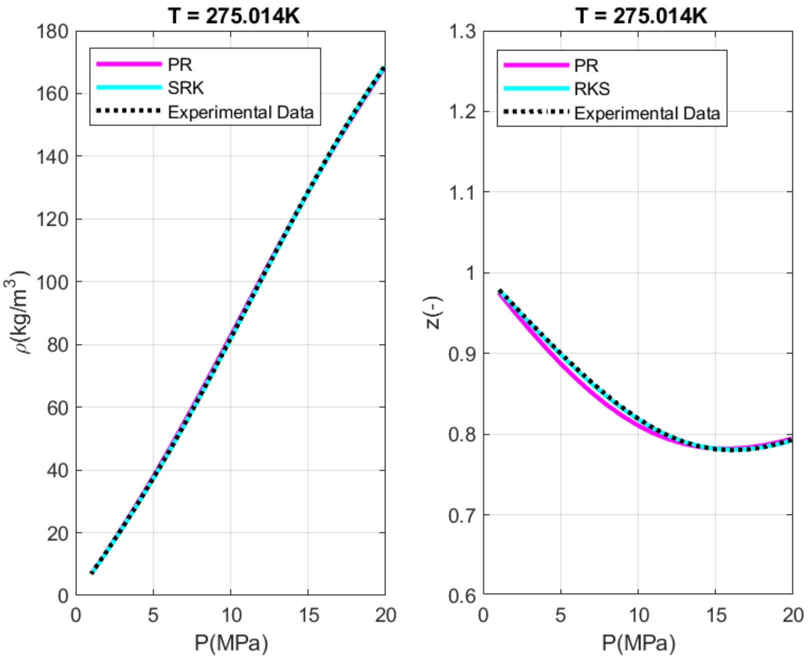

Figure 6.69: optimization results T4 – 95% CH_4 + 05% H_2.

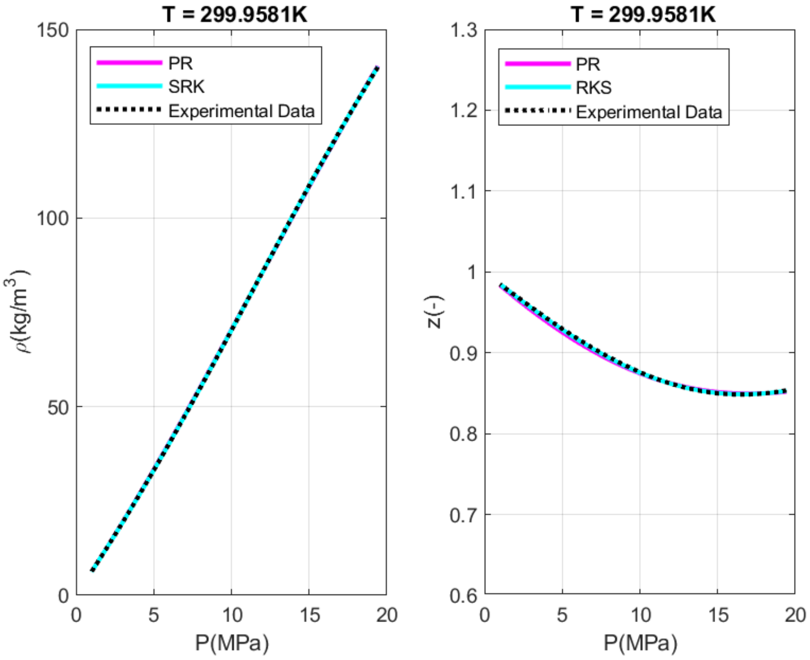

Figure 6.70: optimization results T5 – 95% CH_4 + 05% H_2.

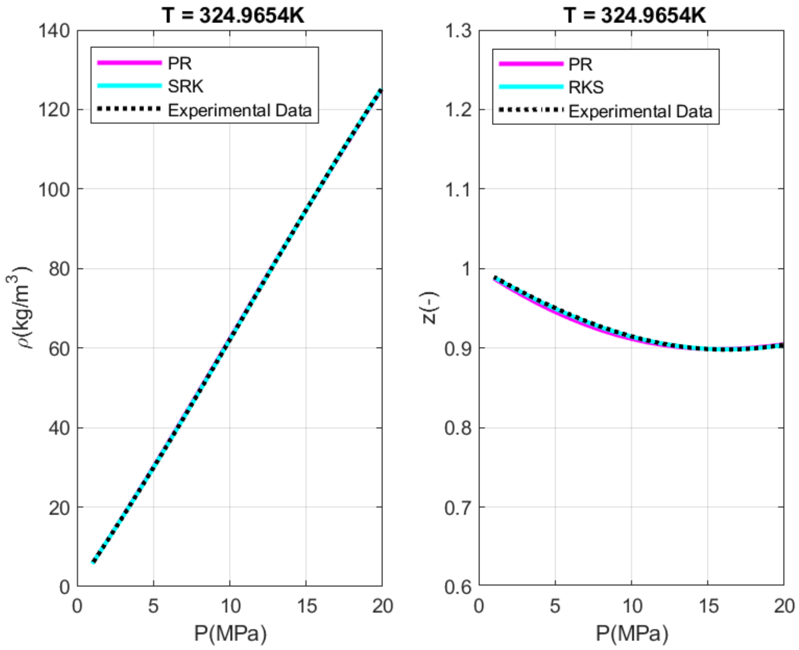

Figure 6.71: optimization results T6 – 95% CH_4 + 05% H_2.

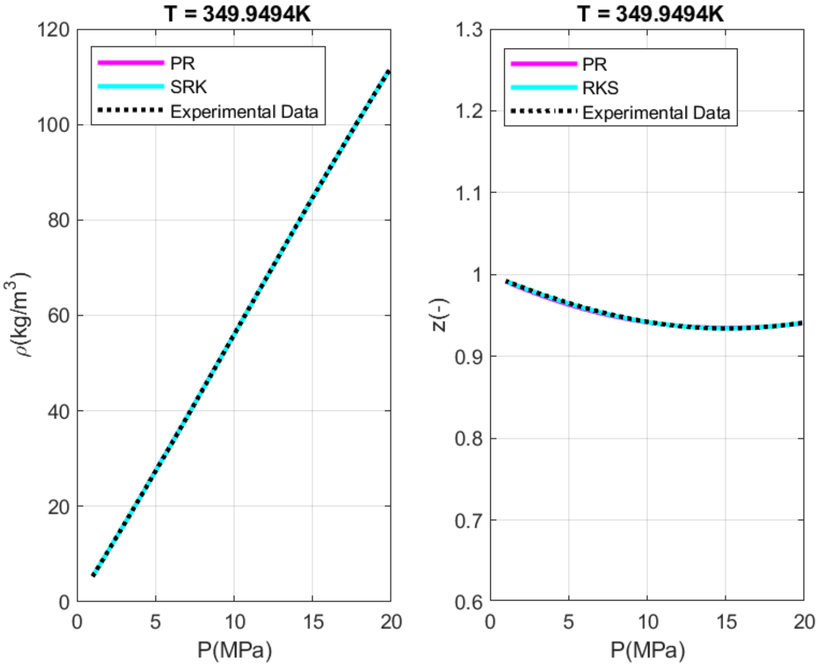

Figure 6.72: optimization results T7 – 95% CH_4 + 05% H_2.

As it can been from the overall plots, the RKS is the model which predicts the data in the most accurate way. In fact, apart from a visual observation, the values of AAD obtained using the RKS model are lower than the ones obtained using the PR EoS, as shown in the following tables.

Table 6.9: Comparison between AAD values between PR and RKS.

50% CH_4 + 50% H_2

T (K)	AAD(ρ)% PR	AAD(z)% PR	AAD(ρ)% RKS	AAD(z)% RKS
240.06945	0.121329051	0.12114217	0.04164345	0.04162088
250.036526	0.094195035	0.09407788	0.03635426	0.03633758
260.031368	0.072251829	0.07218586	0.02689493	0.02688704
275.004789	0.058516468	0.05847548	0.02087651	0.02087156
324.95925	0.02364271	0.02363421	0.00722156	0.00722052
349.94725	0.016104118	0.01610257	0.01256535	0.01256694

Table 6.10: Comparison between AAD values between PR and RKS.

90% CH_4 + 10% H_2

T (K)	AAD(ρ)% PR	AAD(z)% PR	AAD(ρ)% RKS	AAD(z)% RKS
240.07575	0.78746821	0.77982613	0.15886738	0.15861651
250.0455	0.61863785	0.61394249	0.13431152	0.13411718
260.044889	0.36898117	0.36735396	0.08261782	0.08253747
275.012	0.33235737	0.33102153	0.08633418	0.08625015
299.95665	0.19007193	0.18963525	0.05451134	0.05447672
324.9635	0.29631564	0.29517191	0.03360054	0.0335884
349.9505	0.07794682	0.07787294	0.02477281	0.02476533

Table 6.11: Comparison between AAD values between PR and RKS.

95% CH_4 + 05% H_2

T (K)	AAD(ρ)% PR	AAD(z)% PR	AAD(ρ)% RKS	AAD(z)% RKS
240.0758	1.07698582	1.06279589	0.26255412	0.26191533
250.045579	0.75533963	0.74845443	0.17465252	0.17434331
260.040263	0.56477196	0.56099152	0.13932013	0.13911783
275.01405	0.74189929	0.73420106	0.11821925	0.11806847
299.9581	0.22385136	0.22324795	0.06327025	0.06322423
324.9654	0.25700635	0.25607446	0.04888234	0.04885465
349.94945	0.09560388	0.09549158	0.03024213	0.03023071

From this comparison it is possible to appreciate that the RKS model is the one through which the better fitting with experimental data is obtained and so it is the one which better describes the behavior of H_2-CH_4 mixtures examined.

6.2 Robustness Analysis

For the results presented so far, the non-linear curve fitting was obtained with the following parameters:

Tolerance = 10^{-6}

Algorithm = Levemberg – Marquardt

Now, to understand the robustness of the results obtained, those parameters are varied and the change in the deviation is analyzed.

6.2.1 Tolerance

To analyze the impact of the tolerance in the optimization, the tolerance was varied between four values: 10^{-3}, 10^{-6}, 10^{-9} and 10^{-12} for the mixture with a composition of 50% H_2 + 50% CH_4. The resulting optimum Ω_a, Ω_b, the binary interaction parameter and AAD% were compared using the relative difference of the average values (RDA) of the Ω_a, Ω_b and the binary interaction parameter and AAD% for each tolerance, having the value 10^{-6} (the default used in the non-linear curve fitting Matlab code) as a reference.

The relative difference of average is calculated as:

$$RDA\% = \frac{avg\left(\Omega_{a_i}(tol_j)\right) - avg\left(\Omega_{a_i}(tol_{ref})\right)}{avg\left(\Omega_{a_i}(tol_{ref})\right)}. \tag{6.1}$$

In the same way the RDA for Ω_b, BIP and AAD are calculated.

The results are shown in the following table.

Table 6.12: Sensitivity analysis – Tolerance – RKS.

T(K)	240.06945	250.036526	260.031368	275.004789	324.95925	349.94725	**RDA (%)**
			Tol = 1e-3				
Ω_a	0.56049877	0.56565734	0.57706326	0.5952645	0.5989478	0.580858	-0.022776
Ω_b	0.08088542	0.08033715	0.08037343	0.08050499	0.0814053	0.082468	-0.018692
BIP	-0.1566324	-0.1558827	-0.1548533	-0.1535145	-0.1541032	-0.15675	-0.003039
AAD(ρ)%	0.04133638	0.03519148	0.02689493	0.02087642	0.0072216	0.012565	-1.009847
AAD(z)%	0.04131448	0.03517648	0.02688704	0.02087147	0.0072205	0.012567	-1.01
			Tol = 1e-6 (reference)				
Ω_a	0.56065391	0.56629414	0.57706326	0.59526469	0.5989478	0.580858	Ref.
Ω_b	0.08090345	0.08040996	0.08037343	0.080505	0.0814053	0.082468	Ref.
BIP	-0.1566383	-0.1559111	-0.1548533	-0.1535096	-0.1541032	-0.15675	Ref.
AAD(ρ)%	0.04164345	0.03635426	0.02689493	0.02087651	0.0072216	0.012565	Ref.
AAD(z)%	0.04162088	0.03633758	0.02688704	0.02087156	0.0072205	0.012567	Ref.
			Tol = 1e-9				
Ω_a	0.56065391	0.56629414	0.57706327	0.59526469	0.5989478	0.580858	0.0000003
Ω_b	0.08090345	0.08040996	0.08037343	0.080505	0.0814053	0.082468	0.00000004
BIP	-0.1566383	-0.1559111	-0.1548531	-0.1535096	-0.1541032	-0.15675	-0.000026
AAD(ρ)%	0.04164345	0.03635426	0.02689493	0.02087651	0.0072216	0.012565	0.000001
AAD(z)%	0.04162088	0.03633758	0.02688704	0.02087156	0.0072205	0.0125669	0.000001

	Tol = 1e-12						
Ω_a	0.56065394	0.56629414	0.57706327	0.59528349	0.5989478	0.580860	0.000601
Ω_b	0.08090345	0.08040996	0.08037343	0.080505	0.0814053	0.082468	0.00000015
BIP	-0.1566378	-0.1559111	-0.1548531	-0.15275	-0.1541032	-0.15671	-0.085929
AAD(ρ)%	0.04164345	0.03635426	0.02689493	0.02087651	0.0072216	0.012565	0.000006
AAD(z)%	0.04162089	0.03633758	0.02688704	0.02087156	0.0072205	0.012567	0.000006

Table 6.13: Sensitivity analysis – Tolerance – PR.

T(K)	240.06945	250.036526	260.031368	275.004789	324.95925	349.94725	**RDA (%)**
			Tol = 1e-3				
$\boldsymbol{\Omega_a}$	0.38929838	0.4277158	0.43444341	0.31753262	0.420186	0.43376394	32.313
$\boldsymbol{\Omega_b}$	0.08357494	0.09099939	0.09272976	0.07500057	0.0931877	0.09558786	20.997
BIP	-0.1390699	-0.1448379	-0.1459178	-0.1487983	-0.1434012	-0.1456494	10.045
AAD($\boldsymbol{\rho}$)%	0.58958464	0.84242844	0.79927533	0.11306229	0.4107127	0.35836992	-
AAD(z)%	0.58560617	0.8350703	0.79268115	0.11288668	0.4089991	0.35709663	-
			Tol = 1e-6 (reference)				
$\boldsymbol{\Omega_a}$	0.32810684	0.3175688	0.31151468	0.30231116	0.2873142	0.28439773	Ref.
$\boldsymbol{\Omega_b}$	0.0730118	0.07217937	0.07208865	0.07234202	0.0739409	0.0753583	Ref.
BIP	-0.1311617	-0.1299394	-0.1291725	-0.1470941	-0.125805	-0.1252995	Ref.
AAD($\boldsymbol{\rho}$)%	0.12132905	0.09419504	0.07225183	0.05851647	0.0236427	0.01610412	Ref.
AAD(z)%	0.12114217	0.09407788	0.07218586	0.05847548	0.0236342	0.01610257	Ref.
			Tol = 1e-9				
$\boldsymbol{\Omega_a}$	0.32810684	0.3175688	0.31151468	0.30231029	0.287315	0.28439773	-0.000004
$\boldsymbol{\Omega_b}$	0.0730118	0.07217937	0.07208865	0.07234202	0.0739409	0.0753583	0.0000003
BIP	-0.1311617	-0.1299394	-0.1291725	-0.147102	-0.1257976	-0.1252995	0.000078
AAD($\boldsymbol{\rho}$)%	0.12132905	0.09419504	0.07225183	0.05851646	0.0236427	0.01610412	0.000002
AAD(z)%	0.12114217	0.09407788	0.07218586	0.05847547	0.0236342	0.01610257	0.000002

Tol = 1e-12							
$\boldsymbol{\Omega_a}$	0.32810684	0.31755854	0.31151468	0.30231029	0.287315	0.28439773	-0.000564
$\boldsymbol{\Omega_b}$	0.0730118	0.07217937	0.07208865	0.07234202	0.0739409	0.0753583	0.000001
BIP	-0.1311617	-0.1300299	-0.1291725	-0.147102	-0.1257976	-0.1252995	0.011564
AAD($\boldsymbol{\rho}$)%	0.12132905	0.09419507	0.07225183	0.05851646	0.0236427	0.01610412	0.000010
AAD(z)%	0.12114217	0.09407791	0.07218586	0.05847547	0.0236342	0.01610257	0.000010

While using a tolerance equal to 10^{-3} decreases the effectiveness of the optimization process, decreasing the tolerance – from the default 10^{-6} as a reference – does not bring significant improvement in the prediction of the optimum values using the non – linear curve fitting algorithm. In fact, the value of RDA is always in between -1% to 1%, confirming that using a lower value of the tolerance does not improve the accuracy in the prediction of the properties but only increase the computational effort.

Therefore, we can conclude that the default value used by Matlab (equal to 10^{-6}) shows a good compromise between calculation time and precision.

6.2.2 Algorithm

The two algorithms compared are the trust-region and the Levemberg - Marquandt, because both are built-in components of the non-linear curve fitting in Matlab. For that simulation, the tolerance is be set to the default (10^{-6}).

Table 6.14: Sensitivity analysis – Algorithm – RKS. 50% CH_4 + 50% H_2

T(K)	240.06945	250.036526	260.031368	275.004789	324.95925	349.94725
			Levemberg - Marquandt			
Ω_a	0.56065391	0.56629414	0.57706326	0.59526469	0.59894783	0.5808579
Ω_b	0.08090345	0.08040996	0.08037343	0.080505	0.0814053	0.0824685
BIP	-0.1566383	-0.1559111	-0.1548533	-0.1535096	-0.1541032	-0.1567481
AAD(ρ)%	0.04164345	0.03635426	0.02689493	0.02087651	0.00722156	0.0125653
AAD(z)%	0.04162088	0.03633758	0.02688704	0.02087156	0.00722052	0.0125669
			Trust - Region			
Ω_a	0.54944613	0.55780344	0.56940561	0.589489507	0.59213165	0.5705435
Ω_b	0.08090345	0.08040997	0.08037345	0.080505	0.081405302	0.0824685
BIP	-0.36979806	-0.3435264	-0.3590787	-0.3891401	-0.39480122	-0.360207
AAD(ρ)%	0.04164346	0.03635443	0.02689507	0.020876504	0.007221564	0.0125653
AAD(z)%	0.04162089	0.03633775	0.02688719	0.020871555	0.007220522	0.0125669

Table 6.15: Sensitivity analysis – Algorithm – RKS. 90% CH_4 + 10% H_2

T(K)	240.07575	250.0455	260.044889	275.012	299.95665	324.9635	349.9505
			Levemberg - Marquandt				
Ω_a	0.43989485	0.44135676	0.43981574	0.44551048	0.45053727	0.4521802	0.454214
Ω_b	0.08191435	0.08177059	0.08098214	0.08147033	0.08139797	0.0816183	0.0818622
BIP	-0.1500637	-0.1500596	-0.1500418	-0.1500379	-0.150003	-0.1500605	-0.1501276
AAD(ρ)%	0.15886738	0.13431152	0.08261782	0.08633418	0.05451134	0.0336005	0.0247728
AAD(z)%	0.15861651	0.13411718	0.08253747	0.08625015	0.05447672	0.0335884	0.0247653
			Trust - Region				
Ω_a	0.43986968	0.44129203	0.43979945	0.4454696	0.45053416	0.4520968	0.4539495
Ω_b	0.08191436	0.08177059	0.08098213	0.08147033	0.08139796	0.0816183	0.0818622
BIP	-0.154908	-0.1649457	-0.1547359	-0.1690392	-0.1706444	-0.1830506	-0.2035915
AAD(ρ)%	0.15886799	0.13431152	0.08261738	0.08633393	0.05451128	0.0336005	0.0247727
AAD(z)%	0.15861712	0.13411719	0.08253703	0.0862499	0.05447667	0.0335884	0.0247652

Table 6.16: Sensitivity analysis – Algorithm – RKS. 95% CH_4 + 05% H_2

T(K)	240.07575	250.0455	260.044889	275.012	299.95665	324.9635	349.9505
Levemberg - Marquandt							
Ω_a	0.43208088	0.43160398	0.43229192	0.43567689	0.43913991	0.4424415	0.4468541
Ω_b	0.08206009	0.0816057	0.0813766	0.08152698	0.08135396	0.0815921	0.0820172
BIP	-0.1500111	-0.1500083	-0.1500078	-0.1500079	-0.1500007	-0.1500168	-0.150045
AAD(ρ)%	0.26255412	0.17465252	0.13932013	0.11821925	0.06327025	0.0488823	0.0302421
AAD(z)%	0.26191533	0.17434331	0.13911783	0.11806847	0.06322423	0.0488547	0.0302307
Trust - Region							
Ω_a	0.43198082	0.43165849	0.43227772	0.43567836	0.43913021	0.4424204	0.4467388
Ω_b	0.08206011	0.0816057	0.08137659	0.08152697	0.08135396	0.0815921	0.0820172
BIP	-0.1911055	-0.1231138	-0.1587577	-0.148507	-0.2893865	-0.1679477	-0.1997284
AAD(ρ)%	0.26255623	0.17465255	0.13931946	0.11821893	0.06327006	0.0488823	0.0302421
AAD(z)%	0.26191742	0.17434334	0.13911716	0.11806815	0.06322405	0.0488546	0.0302307

From Tables 6.14 to 6.16 it can be seen that the values of Ω_a and Ω_b are almost identical using the two algorithms and the same happens for the values of AAD. On the other hand, the optimal values of the binary interaction parameter change drastically. This can be a "hidden hint" to the fact that the value of the BIP does not influence the accuracy of the prediction.

Table 6.17: Sensitivity analysis – Algorithm – PR. 50% CH_4 + 50% H_2

T(K)	240.06945	250.036526	260.031368	275.004789	324.95925	349.94725
Levemberg - Marquandt						
$\boldsymbol{\Omega_a}$	0.32810684	0.3175688	0.31151468	0.30231116	0.28731422	0.2843977
$\boldsymbol{\Omega_b}$	0.0730118	0.07217937	0.07208865	0.07234202	0.07394094	0.0753583
BIP	-0.1311617	-0.1299394	-0.1291725	-0.1470941	-0.125805	-0.1252995
AAD($\boldsymbol{\rho}$)%	0.12132905	0.09419504	0.07225183	0.05851647	0.02364271	0.0161041
AAD(z)%	0.12114217	0.09407788	0.07218586	0.05847548	0.02363421	0.0161026
Trust - Region						
$\boldsymbol{\Omega_a}$	0.35645753	0.347611	0.34245243	0.336405673	0.324376213	0.3219167
$\boldsymbol{\Omega_b}$	0.07301177	0.07217932	0.0720886	0.072341983	0.073940979	0.0753583
BIP	0.0925951	0.11215117	0.12284802	0.135852181	0.185046505	0.1889917
AAD($\boldsymbol{\rho}$)%	0.12132828	0.09419411	0.0722513	0.058515921	0.023643035	0.016104
AAD(z)%	0.1211414	0.09407696	0.07218533	0.05847493	0.023634538	0.0161024

Table 6.18: Sensitivity analysis – Algorithm – PR. 90% CH_4 + 10% H_2

T(K)	240.07575	250.0455	260.044889	275.012	299.95665	324.9635	349.9505
			Levemberg - Marquandt				
Ω_a	0.43075052	0.42246395	0.40346723	0.40335436	0.38909345	0.4071238	0.3700024
Ω_b	0.0766939	0.07567053	0.07244082	0.07342271	0.07219417	0.0768826	0.0717181
BIP	-0.1491518	-0.1489043	-0.1483617	-0.1483463	-0.1478417	-0.1483567	-0.1472715
AAD(ρ)%	0.78746821	0.61863785	0.36898117	0.33235737	0.19007193	0.2963156	0.0779468
AAD(z)%	0.77982613	0.61394249	0.36735396	0.33102153	0.18963525	0.2951719	0.0778729
			Trust - Region				
Ω_a	0.43247811	0.42453576	0.40670423	0.4066388	0.3930695	0.3839695	0.37464
Ω_b	0.07669396	0.07567052	0.07244082	0.07342271	0.07219397	0.0719348	0.0717026
BIP	-0.0899485	-0.0770991	-0.0321282	-0.0316801	-0.0043139	0.0169411	0.0253307
AAD(ρ)%	0.78747372	0.618637	0.36898098	0.33235703	0.19006696	0.1142843	0.0776966
AAD(z)%	0.77983143	0.61394166	0.36735378	0.3310212	0.18963032	0.114124	0.0776234

Table 6.19: Sensitivity analysis – Algorithm – PR. 95% CH_4 + 05% H_2

T(K)	240.07575	250.0455	260.044889	275.012	299.95665	324.9635	349.9505
Levemberg - Marquandt							
Ω_a	0.44431776	0.43085571	0.42131594	0.43644104	0.39890053	0.4063489	0.382428
Ω_b	0.07769629	0.07564759	0.07431193	0.07766563	0.07218911	0.0749082	0.0720372
BIP	-0.1497866	-0.1495844	-0.1494427	-0.1496629	-0.1490767	-0.1491747	-0.1488272
AAD(ρ)%	1.07698582	0.75533963	0.56477196	0.74189929	0.22385136	0.2570063	0.0956039
AAD(z)%	1.06279589	0.74845443	0.56099152	0.73420106	0.22324795	0.2560745	0.0954916
Trust - Region							
Ω_a	0.44445502	0.43177359	0.42262719	0.41674468	0.40071408	0.3917397	0.3846502
Ω_b	0.07769628	0.07564766	0.07431165	0.07394623	0.07218905	0.0719064	0.0720372
BIP	-0.1405196	-0.0863588	-0.0577303	-0.0402193	-0.0194308	-0.0036854	0.0106346
AAD(ρ)%	1.07698412	0.75534643	0.5647527	0.43040575	0.22384964	0.150277	0.0956039
AAD(z)%	1.06279427	0.74846103	0.5609727	0.4281811	0.22324625	0.1500052	0.0954916

From Tables 6.17 to 6.19 the same conclusion can be achieved also when using the PR model: although in this case also the values of Ω_a obtained using the trust – region algorithm slightly differ from the ones obtained using the Levemberg – Marquandt one, the BIP values drastically change between the two algorithms but the AAD values remain the same, meaning that the accuracy in the fitting does not change.

In summary, from the results it is clear that for the mixtures tested the value of the BIP does not influence significantly the accuracy in the prediction of the properties.

6.3 Sensitivity analysis on Optimization results

In this section the optimization is performed for one parameter at time while the other two vary in a given range. The optimization procedure is the same as the one described in the Section 5.1, but in this case instead of optimizing the three parameters together they are optimized one at time. The aim of this study is to investigate the parameters that more influence the optimization results.

Furthermore, to retrieve the values of the parameters that allow the PR and RKS models to accurately predict the density and z – factor for the mixtures examined, the probability density function (PDF) is calculated for optimization result.

In probability theory and statistics, the PDF is a mathematical function that describes the probability distribution of a continuous random variable. It represents the relative likelihood of the random variable taking on different values or falling within specific intervals.

The PDF, denoted as $f(x)$, is a function that satisfies the following properties for a continuous random variable x:

- Non-negativity: $f(x) \geq 0$ for all x.
- Normalization: $\int (-\infty, \infty) f(x)\, dx = 1$, where the integral is taken over the entire range of x.

The PDF provides a way to quantify the relative likelihood or density of different outcomes occurring. More precisely, for a continuous random variable, the probability of X falling within a specific interval [a, b] can be computed as the integral of the PDF over that interval:

$$P(a \leq X \leq b) = \int [a, b] f(x) dx \tag{6.2}$$

In other words, the probability of X being in the interval [a, b] is equal to the area under the PDF curve between a and b.

The PDF describes the distribution of probabilities across the range of possible values of the random variable X. The height of the PDF at a particular value x represents the density of probabilities at that point. A higher value of $f(x)$ indicates a higher probability density.

The shape of the PDF depends on the specific probability distribution being modeled. For example, in the case we examine, as we will see, the distribution is normal and the PDF has a bell-shaped curve.

In summary, the PDF is a fundamental concept in probability theory and statistics that provides a mathematical description of the probability distribution for a continuous random variable. It enables us to analyze the likelihood of different values and calculate their probabilities.

The PDF is computed in the following lines of codes:

```
data_pr1 = matrixData1{i,1};
data_pr1 = reshape(data_pr1, [], 1);
    pd_cell1{i} = fitdist(data_pr1, 'normal');
    data_min1=min(data_pr1);
    data_max1=max(data_pr1);
    mu1=pd_cell1{i}.mu;
    sigma1=pd_cell1{i}.sigma;
    data_min1 = min(data_pr1);
    data_max1 = max(data_pr1);
    range_min1 = data_min1 - 3*sigma1;
    range_max1 = data_max1 + 3*sigma1;
    x_pdf1 = linspace(range_min1, range_max1, 1000);

    y_pdf1=pdf(pd_cell1{i},x_pdf1);
    y_max1=max(y_pdf1);
    [~, max_index1] = max(y_pdf1);
    x_max_prob1 = x_pdf(max_index1);
```

In this code, the optimized values are initially stored in the variable data_pr1. This variable is then reshaped into a column vector using reshape function, ensuring that it is a one-dimensional array since it could be also a matrix when two parameters vary and one is optimized.

The *fitdist* function in Matlab (https://it.mathworks.com/help/stats/fitdist.html) is used to estimate the parameters of a probability distribution that best fit a given dataset. It aims to find the distribution that provides the best statistical representation of the data.

The syntax for the *fitdist* function is as follows:

pd = fitdist(data, 'DistributionName', 'NameValuePairs')

Here, data is the input dataset for which the distribution parameters are estimated (in our case it is the variable called data_pr1, which contains the optimum values of the parameter). 'DistributionName' represents the name of the probability distribution to be fitted (in our case ‘Normal’), and 'NameValuePairs' is an optional set of additional parameter-value pairs that can be specified.

The fitdist function uses a maximum likelihood estimation (MLE) approach to fit the distribution. It searches for the parameter values that maximize the likelihood of observing the given data. In other words, it finds the parameters that make the observed data most probable under the assumed distribution.

The function returns an object (pd) of the ProbabilityDistribution class, which represents the fitted distribution. This object contains various properties that describe the estimated distribution, such as the parameter values, mean, standard deviation, etc. These properties can be accessed using dot notation (as shown in the code lines previously reported where the mean (‘mu=pd_cell{i}.mu’) and the standard deviation (‘sigma=pd_cell{i}.sigma’) are extrapolated).

Once the distribution is fitted using *fitdist*, you can further use the resulting probability distribution object (pd) to perform various operations, such as generating random numbers from the fitted distribution, calculating probabilities, computing quantiles, and more.

In summary, the *fitdist* function in Matlab is used to estimate the parameters of a probability distribution that best fits a given dataset. It employs maximum likelihood estimation to find the parameter values that maximize the likelihood of observing the data. The resulting probability distribution object allows for further analysis and calculations based on the fitted distribution.

In this case, the normal distribution is chosen by passing the 'normal' argument. The resulting fitted distribution is stored in pd_cell1{i}.

After fitting the distribution, the minimum and maximum values of the data are calculated using the min and max functions, respectively. These values are stored in data_min1 and data_max1.

The properties of the fitted distribution, such as the mean (mu1) and standard deviation (sigma1), are extracted from pd_cell1{i}.

Next, the code computes the range of x-values over which the PDF will be evaluated. To obtain a smoother curve when plotting the probability density function (PDF), the range is extended beyond the minimum and maximum values by adding and subtracting a certain multiple of the standard deviation (sigma1). In this case, the range is extended by 3 times the standard deviation.

Extending the range ensures that the entire distribution is captured and plotted, even if it extends beyond the observed minimum and maximum values. By extending the range, more data points are included in the plot, resulting in a denser set of points along the x-axis. This increased density helps in obtaining a smoother curve that better represents the shape of the probability density function.

Overall, extending the range by a multiple of the standard deviation helps to ensure that the full distribution is captured and represented in the plot, resulting in a more visually appealing and smoother curve for the probability density function.

The *linspace* function is used to generate 1000 equally spaced points within this range, resulting in the vector x_pdf1.

The *pdf* function is then applied to the fitted distribution (pd_cell1{i}) and the vector of x-values (x_pdf1).

The *pdf* function in Matlab (https://it.mathworks.com/help/stats/prob.normaldistribution.pdf.html) calculates the probability density function for a given probability distribution object at specified values.

The sintax is as follow:

y=pdf(pd,x)

Here, pd represents the probability distribution object for which the PDF is calculated (in our case pd_cell1{i}), and x is the input vector of values at which the PDF is evaluated (in our case x_pdf1).

The *pdf* function takes the probability distribution object (pd) obtained from *fitdist* as input. It calculates the probability density values corresponding to the specified x values.

The resulting y vector contains the probability density values at each element of x. The length of y is the same as the length of x, and it represents the density of probabilities associated with the corresponding values in x.

The *pdf* function uses the parameters of the probability distribution stored in the distribution object (pd) to calculate the PDF values. It applies the probability density function formula specific to the chosen distribution.

In the case of a normal distribution, the probability density function (PDF) can be represented by the following formula:

$$f(x) = \frac{1}{\left(\sigma * \sqrt{2\pi}\right)} * e^{(-\frac{(x-\mu)^2}{2\sigma^2})} \tag{6.3}$$

In this formula:

- $f(x)$ represents the probability density at a given value x.
- μ is the mean of the normal distribution.
- σ is the standard deviation of the normal distribution.
- π is a mathematical constant representing approximately 3.14159.

The PDF formula for a normal distribution describes a symmetric bell-shaped curve centered at the mean (μ). The spread of the curve is controlled by the standard deviation (σ). The constant factor $(1\ /\ (\sigma * \sqrt{}(2\pi)))$ ensures that the area under the curve integrates to 1, satisfying the normalization property of a PDF.

Therefore, the *pdf* function returns the corresponding probability density values, which are stored in y_pdf1.

Finally, the maximum value of the probability density is determined using the max function and stored in y_max1. Additionally, the index corresponding to the maximum is obtained using the max function with the output argument ~. The x-value associated with this maximum probability density is then extracted from x_pdf and stored in x_max_prob1.

Overall, this code fits a normal distribution to the data and calculates the probability density function (PDF) using the fitted distribution. It also identifies the maximum probability density and its corresponding x-value.

6.3.1 Optimization of Ω_a

The optimization is first performed only for Ω_a, whereas Ω_b varies between 0.01 and 0.1 and BIP between -1 and 1. When performing the optimization using the RKS model the starting point for Ω_a is 0.427447, whereas when using the PR model the initial guess of the parameter is 0.45724.

The following figures report the optimal value of Ω_a for every value of Ω_b and BIP tested, in particular Figures 6.73, 6.74 and 6.75 show the results when using RKS EoS and Figures 6.76, 6.77, 6.78 the ones obtained when applying the PR model.

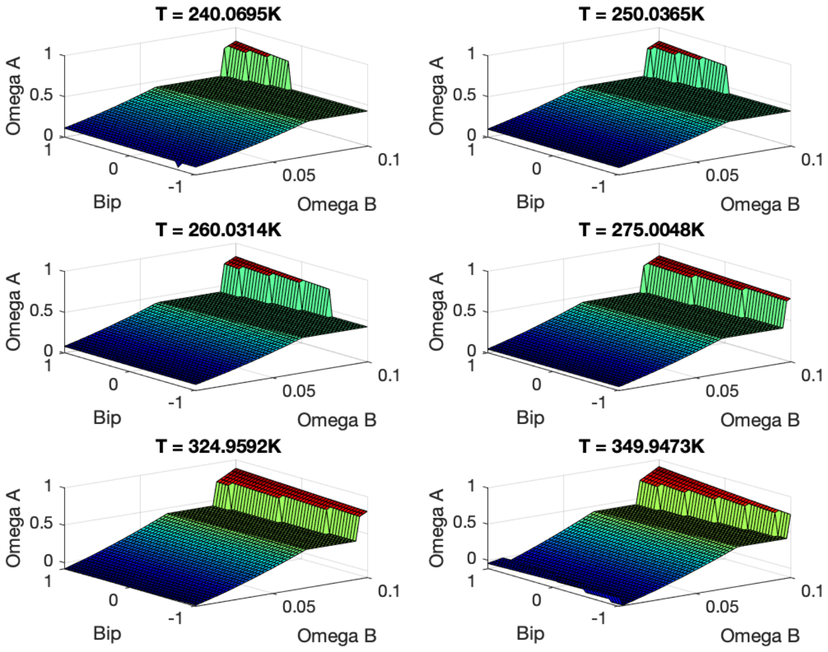

Figure 6.73: optimization of Ω_a – 50% CH_4 + 50% H_2, RKS.

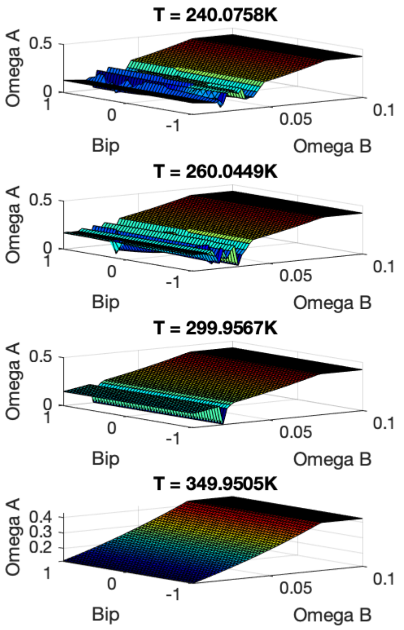

Figure 6.74: optimization of Ω_a – 90% CH_4 + 10% H_2, RKS.

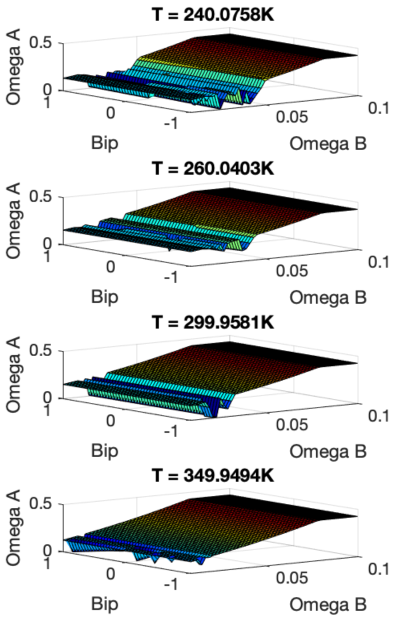

Figure 6.75: optimization of Ω_a – 95% CH_4 + 05% H_2, RKS.

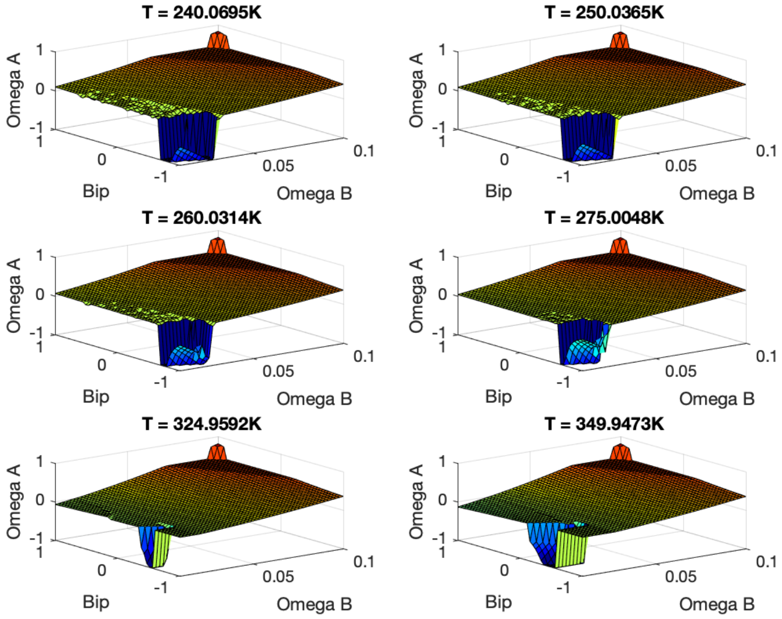

Figure 6.76: optimization of Ω_a – 50% CH_4 + 50% H_2, PR.

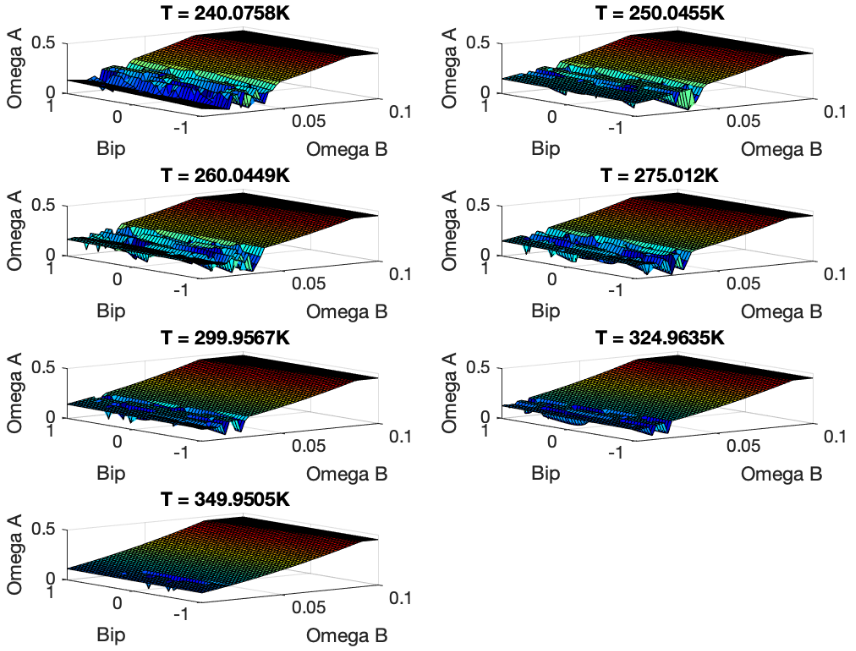

Figure 6.77: optimization of Ω_a – 90% CH_4 + 10% H_2, PR.

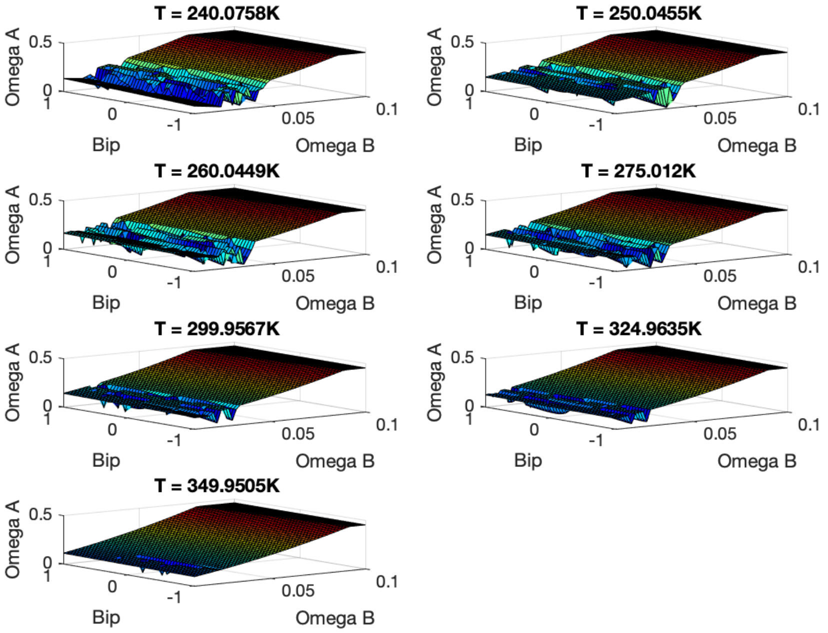

Figure 6.78: optimization of Ω_a – 95% CH_4 + 05% H_2, PR.

The overall plots show that varying Ω_b and BIP highly influence the result of the optimization since the value of Ω_a changes significantly according to the value of Ω_b and BIP which is used to perform the optimization.

In order to investigate which is the most frequent value of Ω_a resulting from the optimization the PDF is calculated for each optimal value of the parameter. The following figures report the PDF for every value of Ω_a, in particular Figures 6.79, 6.80 and 6.81 show the results when using RKS EoS and Figures 6.82, 6.83 and 6.94 the ones obtained when applying the PR model. The value of Ω_a with the highest PDF is displayed above each plot.

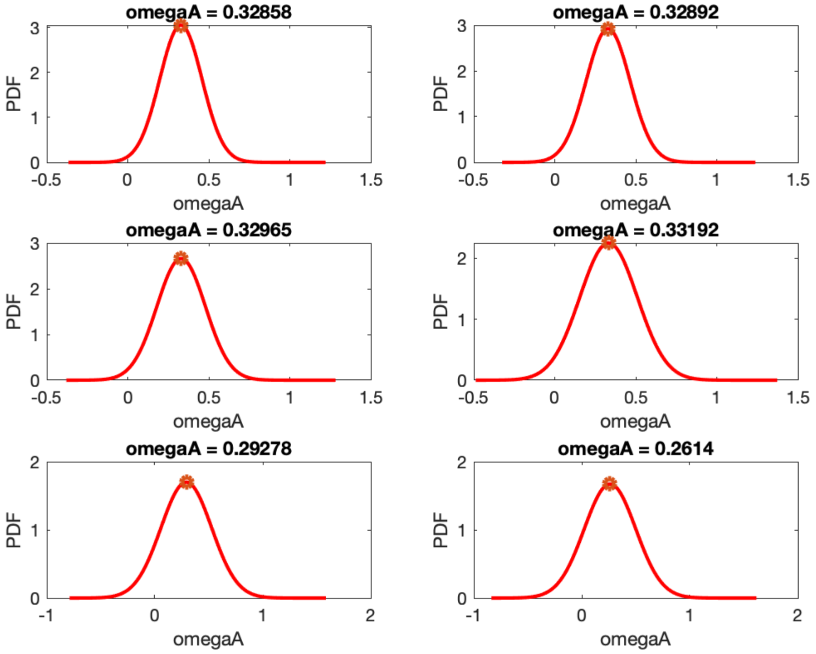

Figure 6.79: PDF vs Ω_a – 50% CH_4 + 50% H_2, RKS.

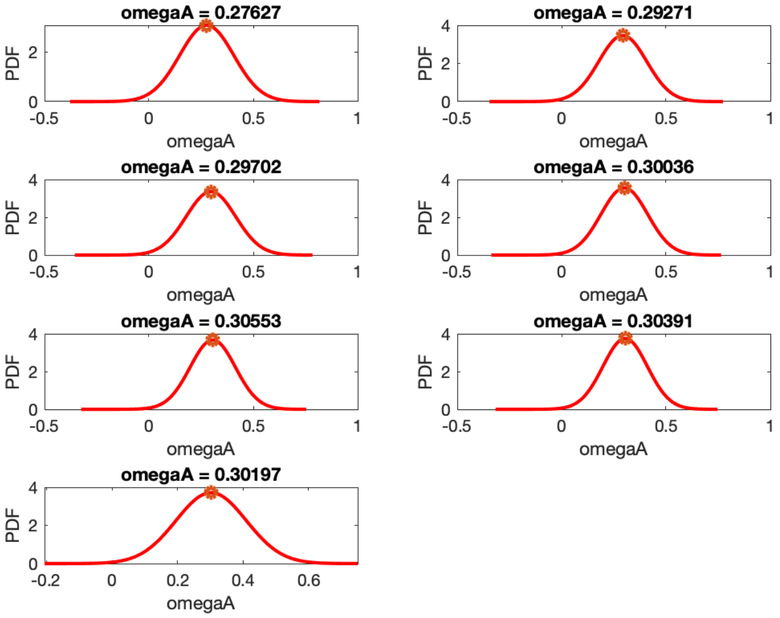

Figure 6.80: PDF vs Ω_a – 90% CH_4 + 10% H_2, RKS.

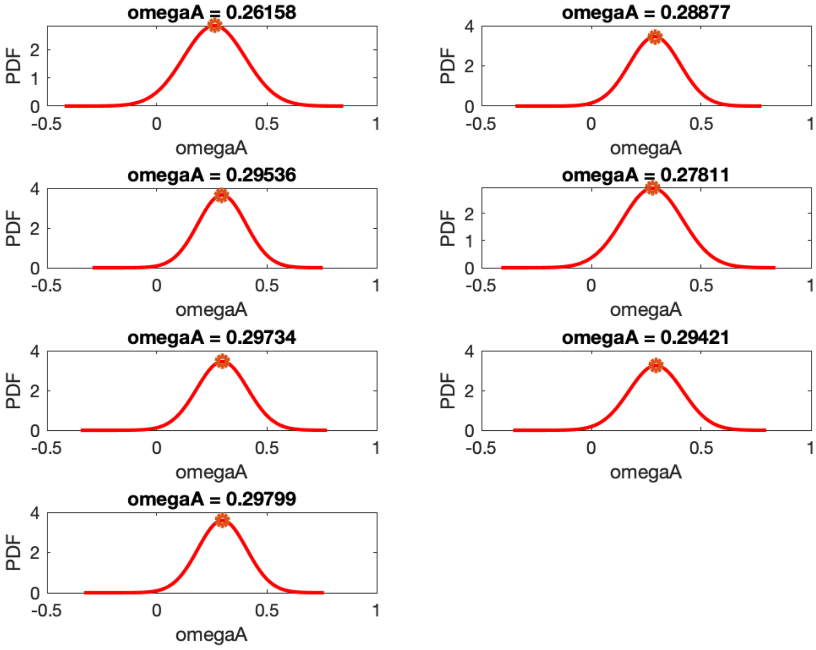

Figure 6.81: PDF vs Ω_a – 95% CH4 + 05% H_2, RKS.

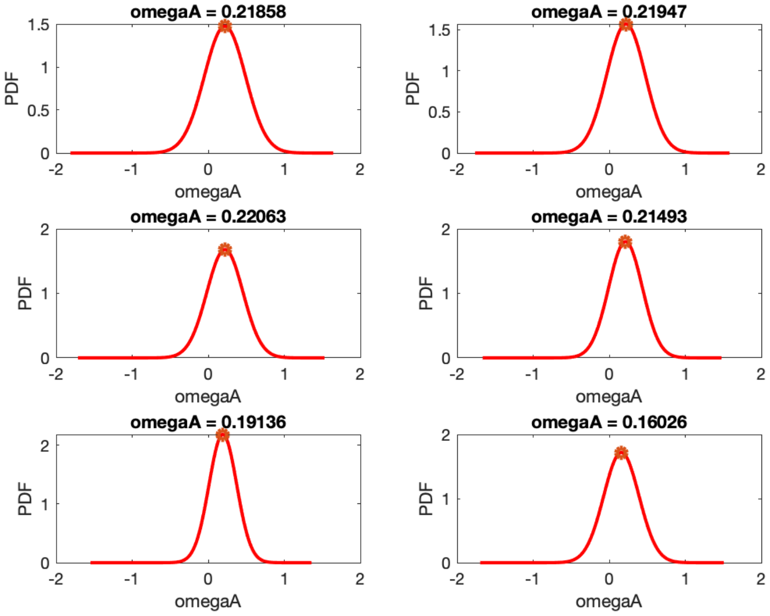

Figure 6.82: PDF vs Ω_a – 50% CH4 + 50% H_2, PR.

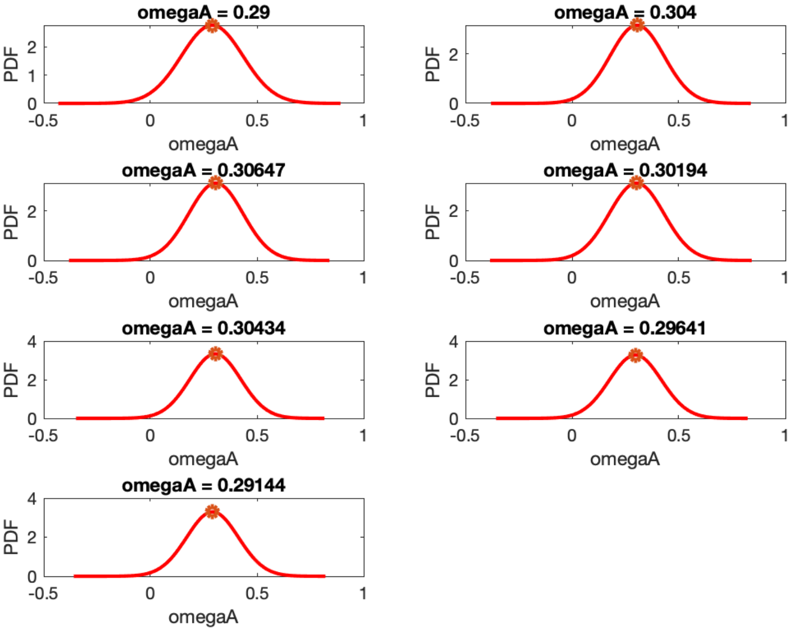

Figure 6.83: PDF vs Ω_a – 90% CH_4 + 10% H_2, PR.

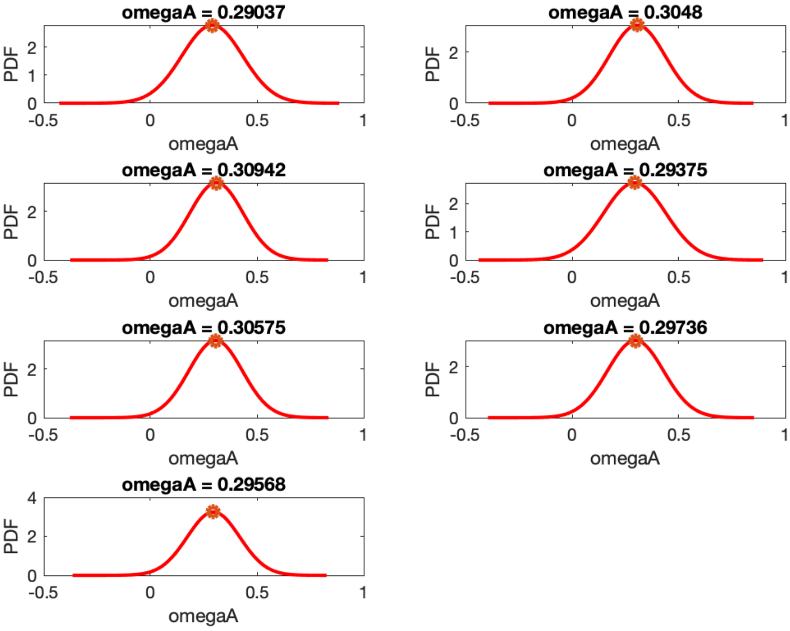

Figure 6.84: PDF vs Ω_a – 95% CH_4 + 05% H_2, PR.

6.3.2 Optimization of Ω_b

In this case the optimization is performed only for Ω_b, whereas Ω_a varies between 0.1 and 1 and BIP between -1 and 1. When performing the optimization using the RKS model the starting point for Ω_b is 0.08664, whereas when using the PR model the initial guess of the parameter is 0.0778.

The following figures report the optimal value of Ω_b for every value of Ω_a and BIP tested, in particular Figures 6.85, 6.86 and 6.87 show the results when using RKS EoS and Figures 6.88, 6.89 and 6.90 the ones obtained when applying the PR model.

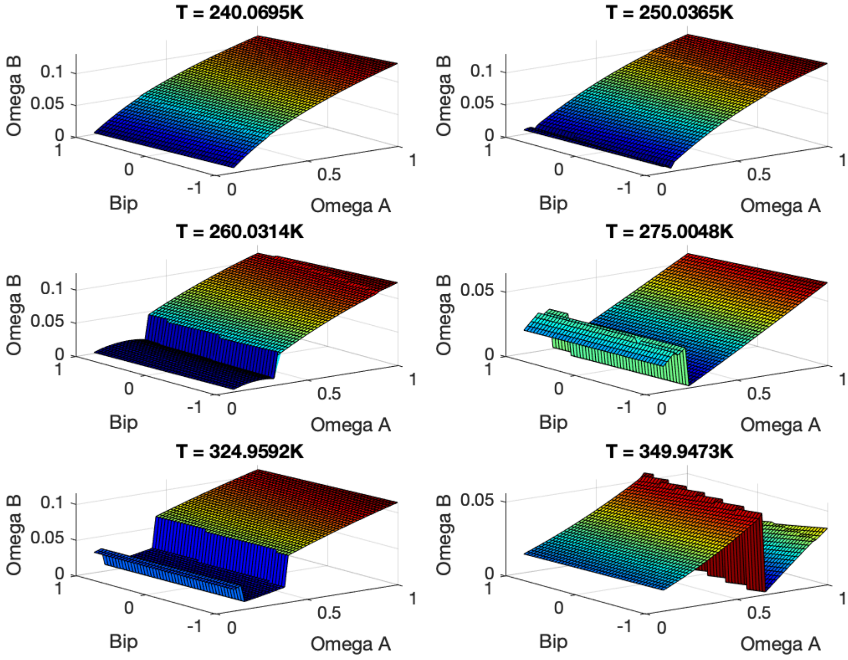

Figure 6.85: optimization of Ω_b – 50% CH_4 + 50% H_2, RKS.

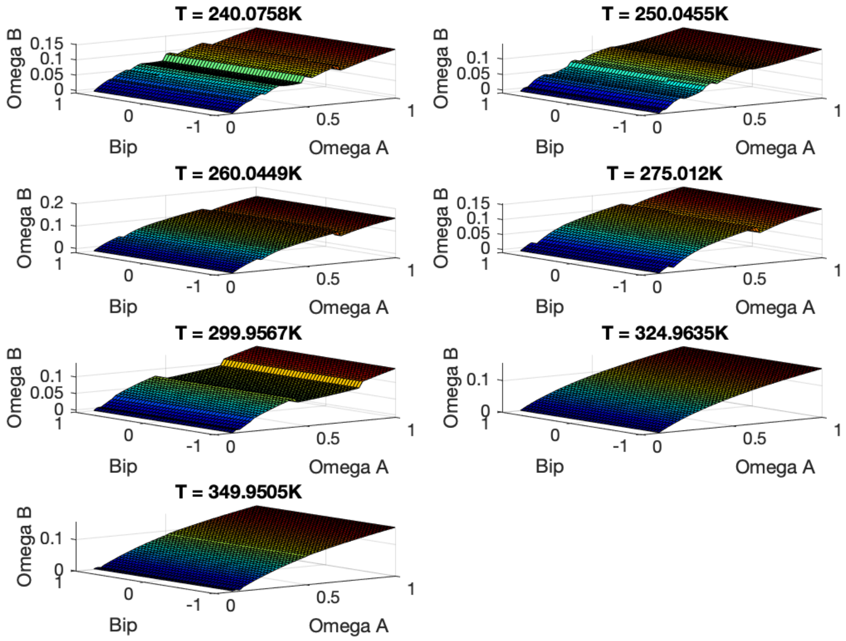

Figure 6.86: optimization of Ω_b – 90% CH_4 + 10% H_2, RKS.

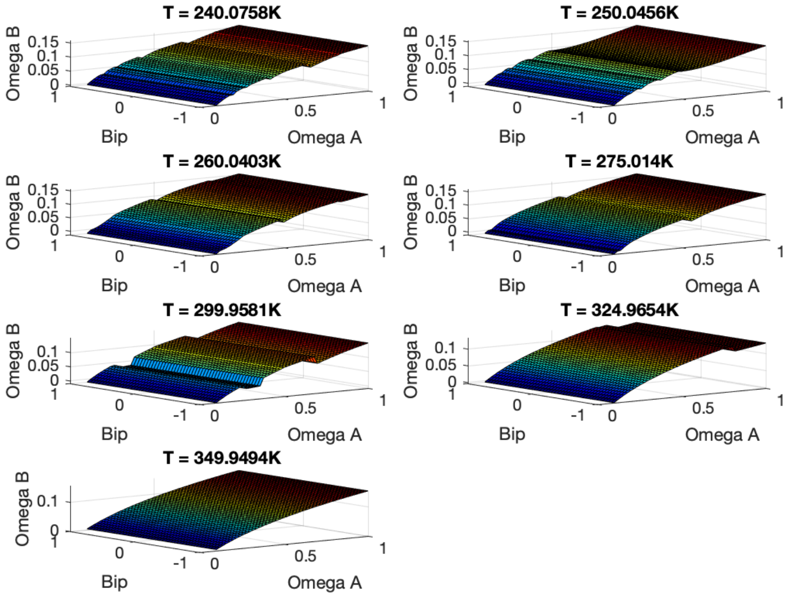

Figure 6.87: optimization of Ω_b – 95% CH_4 + 05% H_2, RKS.

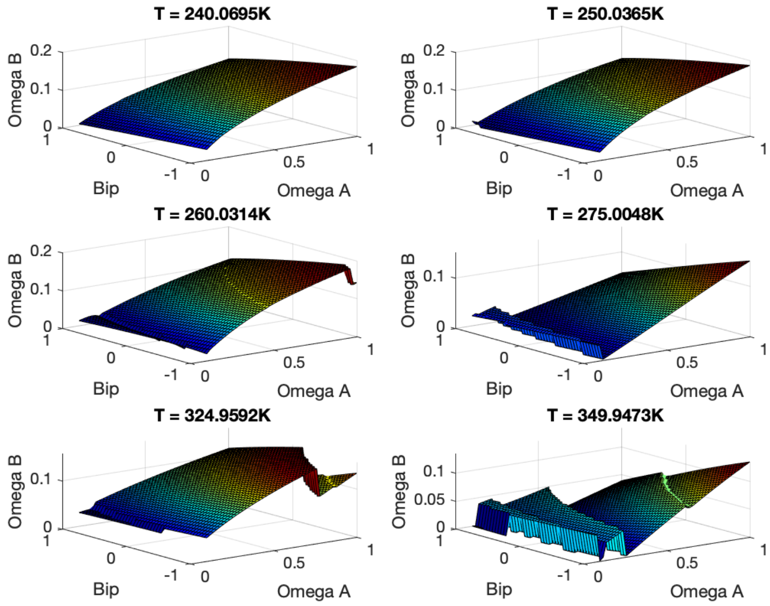

Figure 6.88: optimization of Ω_b – 50% CH_4 + 50% H_2, PR.

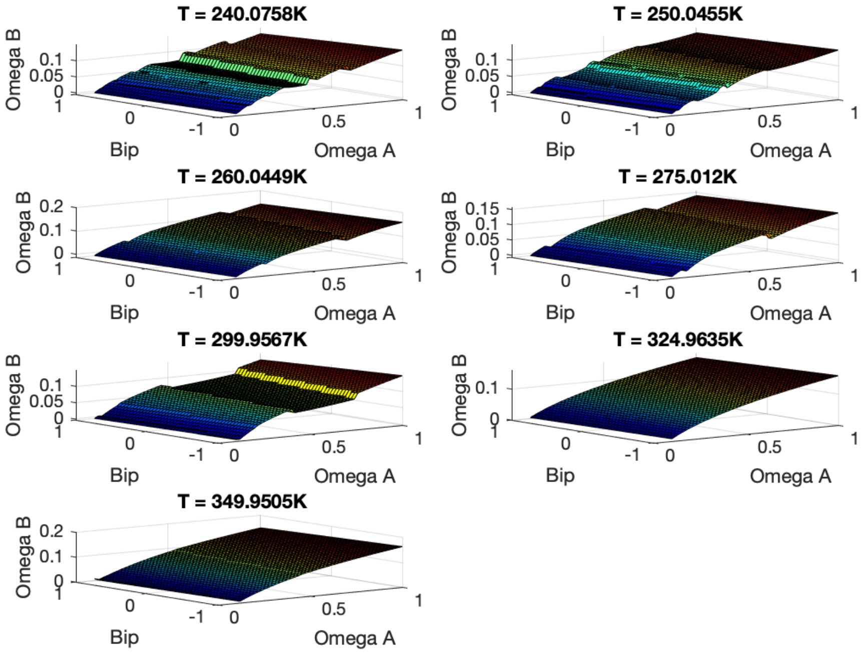

Figure 6.89: optimization of Ω_b – 90% CH_4 + 10% H_2, PR.

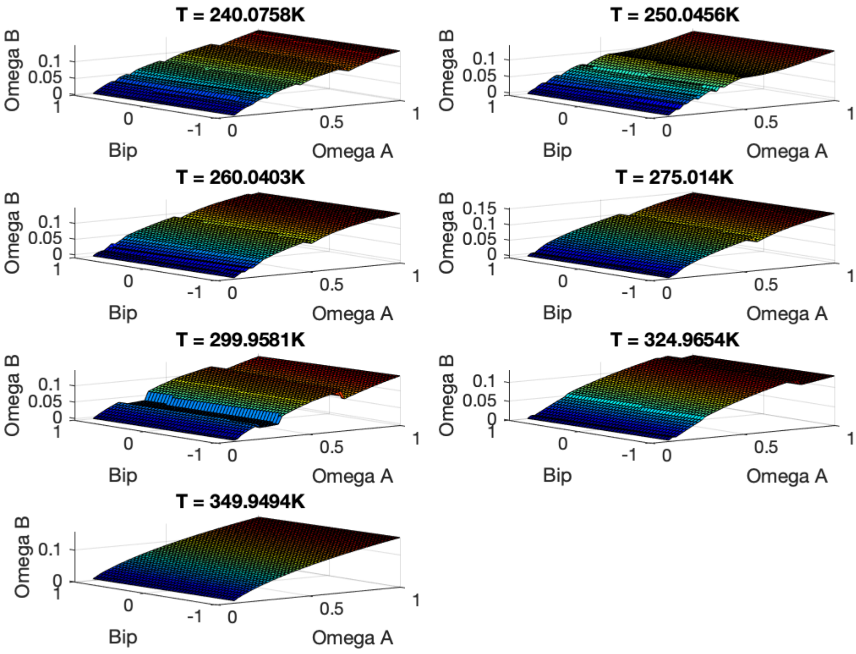

Figure 6.90: optimization of Ω_b – 95% CH_4 + 05% H_2, PR.

In this case, it can be noticed that the value of Ω_b and BIP highly affect the result of the optimization because Ω_b assumes different optimal values according to the value of Ω_a and BIP which is used to perform the optimization.

In order to investigate which is the most frequent optimal value of Ω_b the PDF is calculated. The following figures report the PDF for every value of Ω_a, in particular Figures 6.91, 6.92 and 6.93 show the results when using RKS EoS and Figures 6.94, 6.95 and 6.96 the ones obtained when applying the PR model. The value of Ω_b with the highest PDF is displayed above each plot.

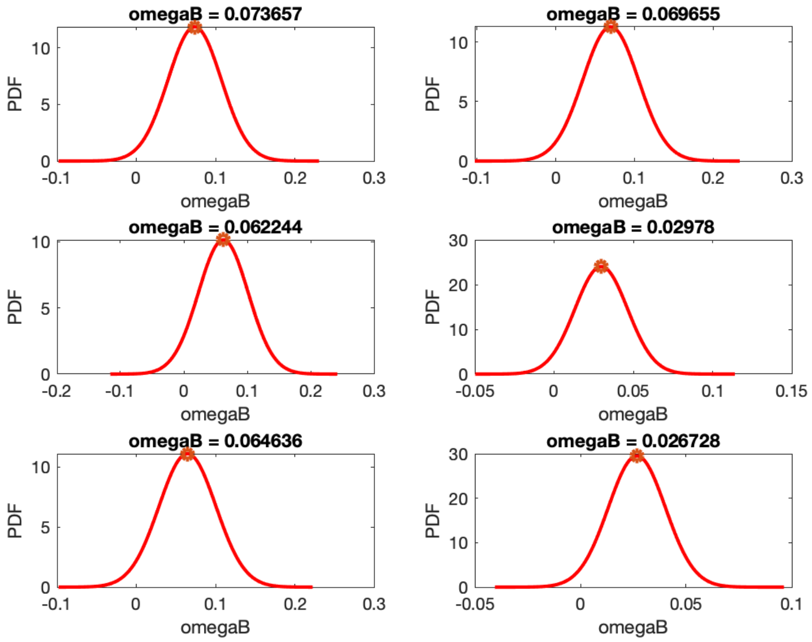

Figure 6.91: PDF vs Ω_b – 50% CH_4 + 50% H_2, RKS.

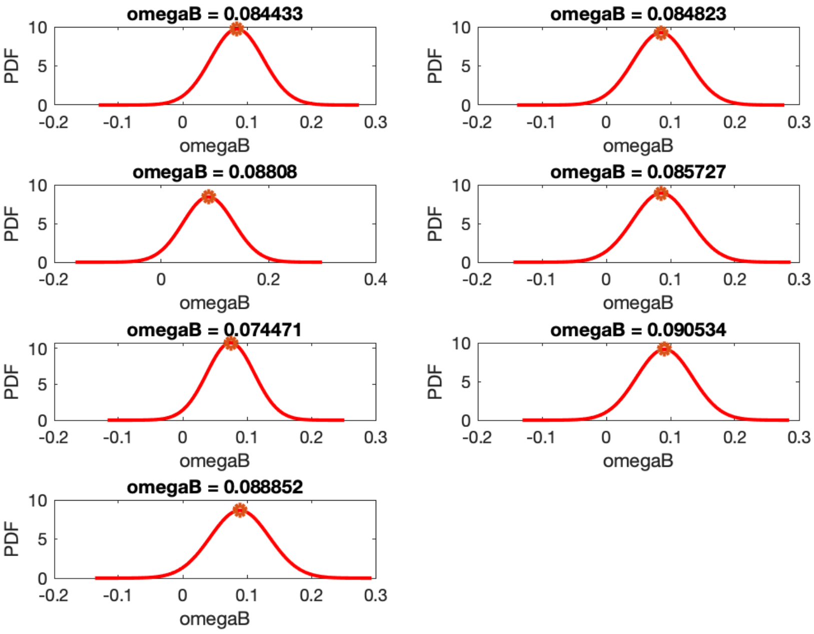

Figure 6.92: PDF vs Ω_b – 90% CH_4 + 10% H_2, RKS.

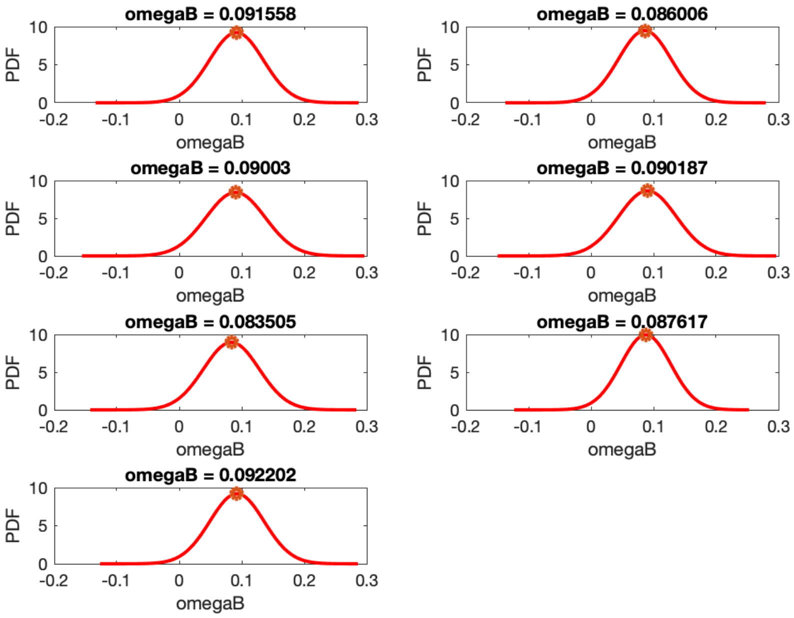

Figure 6.93: PDF vs Ω_b – 95% CH_4 + 05% H_2, RKS.

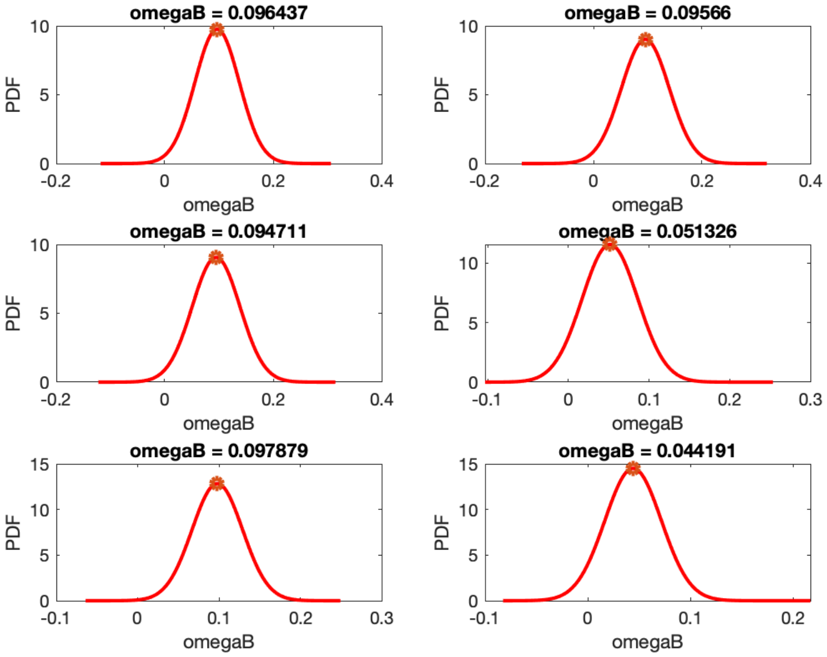

Figure 6.94: PDF vs Ω_b – 50% CH_4 + 50% H_2, PR.

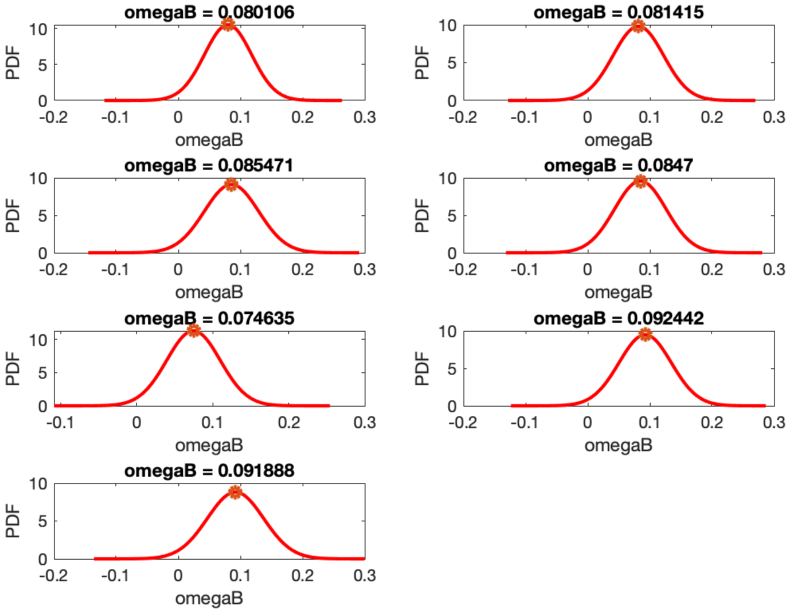

Figure 6.95: PDF vs Ω_b – 90% CH_4 + 10% H_2, PR.

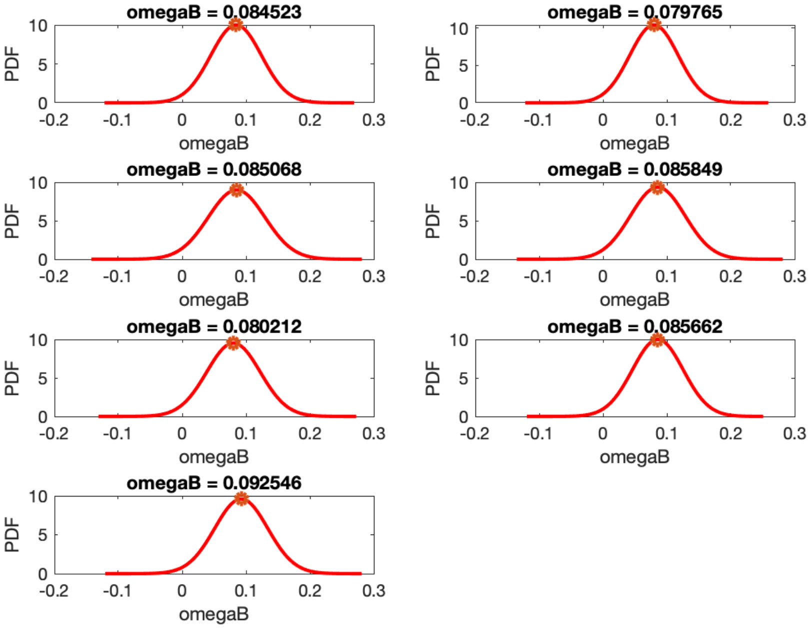

Figure 6.96: PDF vs Ω_b – 95% CH_4 + 05% H_2, PR.

6.3.3 Optimization of Ω_a and Ω_b

The optimization of Ω_a and Ω_b is performed whereas the BIP varies between -1 to 1. When performing the optimization using the RKS model the starting point for Ω_a is 0.427447 and for Ω_b is 0.08664, whereas when using the PR model the initial guesses of the parameters are 0.45724 and 0.0778, respectively.

The following figures report the optimal value of Ω_a for each BIP tested (Figures 6.97 to 6.99 and Figures 6.103 to 6.105) and the optimal values of Ω_b for each BIP tested (Figures 6.100 to 6.102 and Figures 6.106 to 6.108). In particular Figures 6.97 to 6.102 show the results when using RKS EoS and Figures 6.103 to 6.108 the ones obtained when applying the PR model.

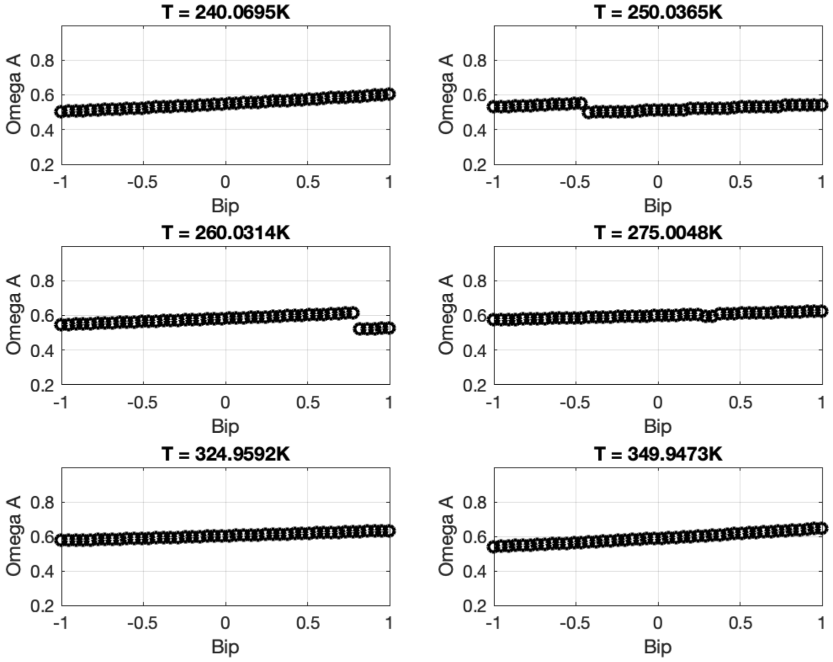

Figure 6.97: Ω_a vs BIP – 50% CH_4 + 50% H_2, RKS.

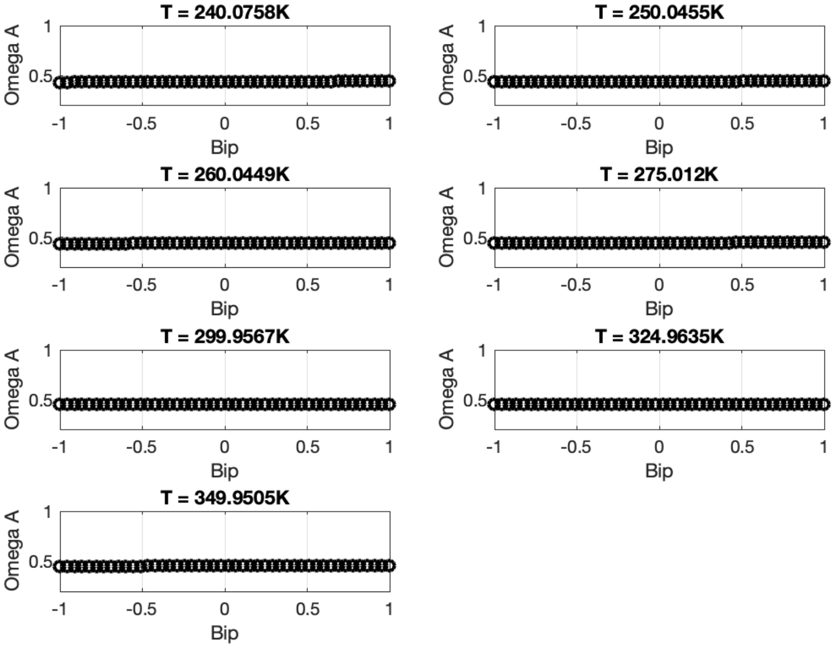

Figure 6.98: Ω_a vs BIP – 90% CH_4 + 10% H_2, RKS.

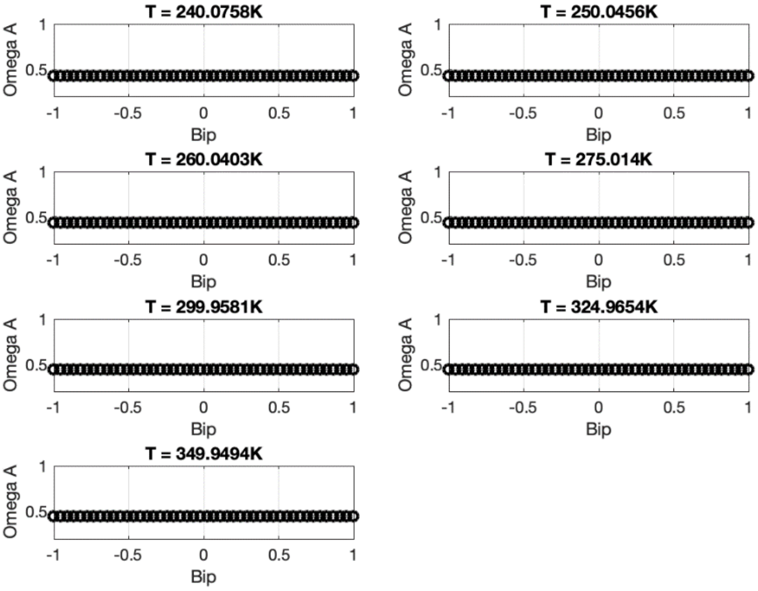

Figure 6.99: Ω_a vs BIP – 95% CH_4 + 05% H_2, RKS.

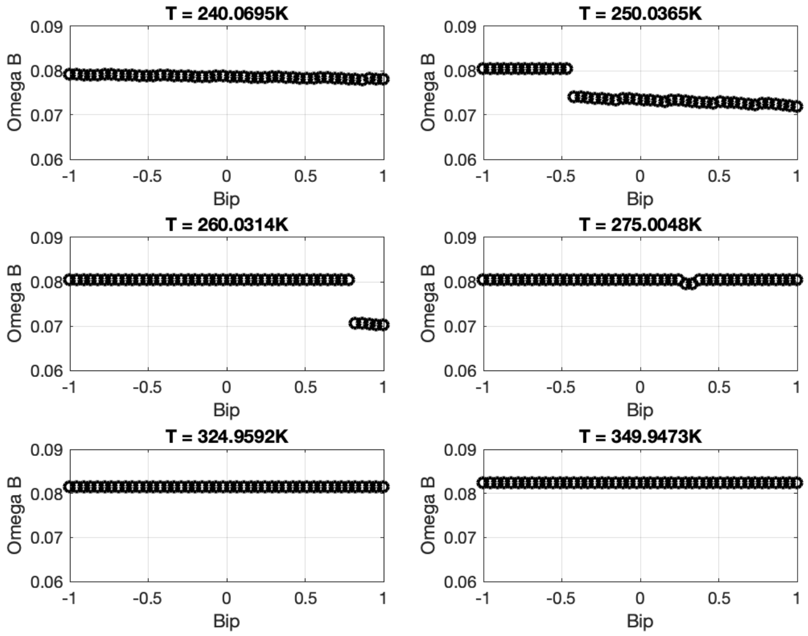

Figure 6.100: Ω_b vs BIP – 50% CH_4 + 50% H_2, RKS.

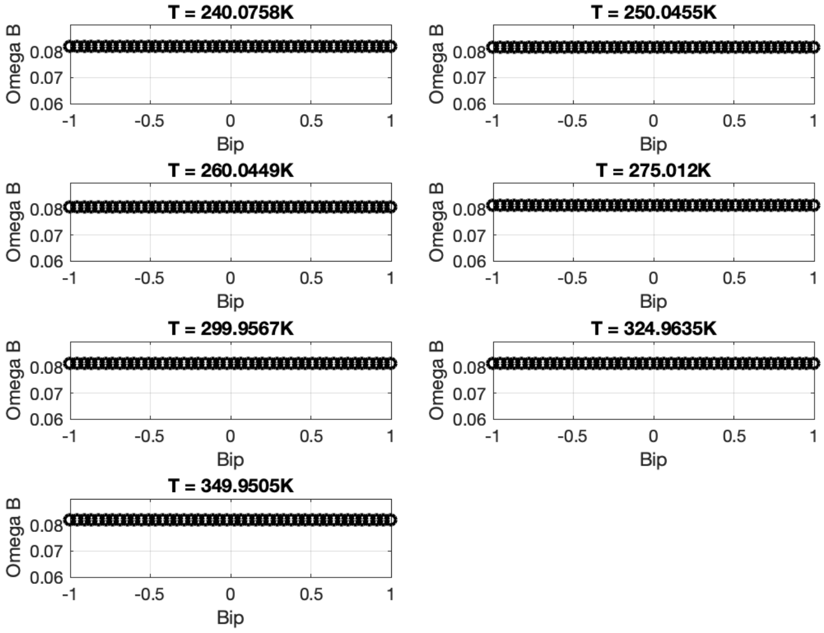

Figure 6.101: Ω_b vs BIP – 90% CH_4 + 10% H_2, RKS.

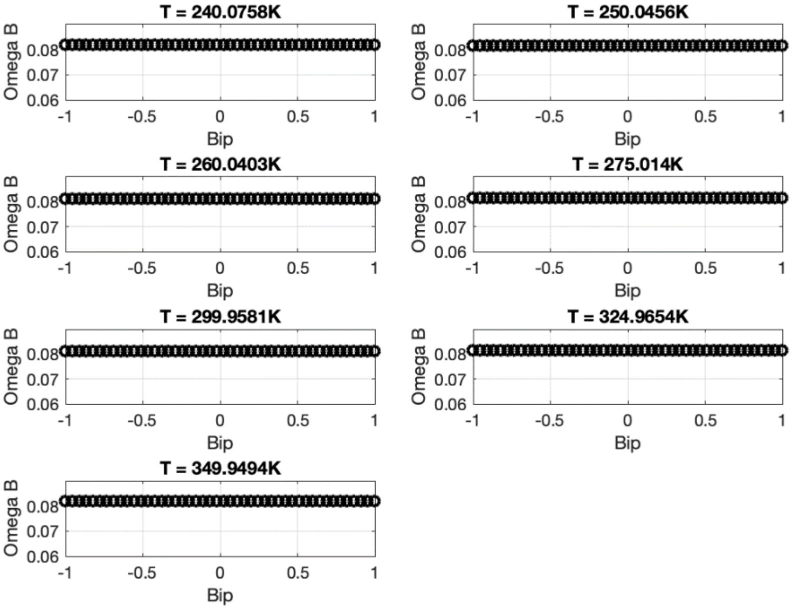

Figure 6.102: Ω_b vs BIP – 95% CH_4 + 05% H_2, RKS.

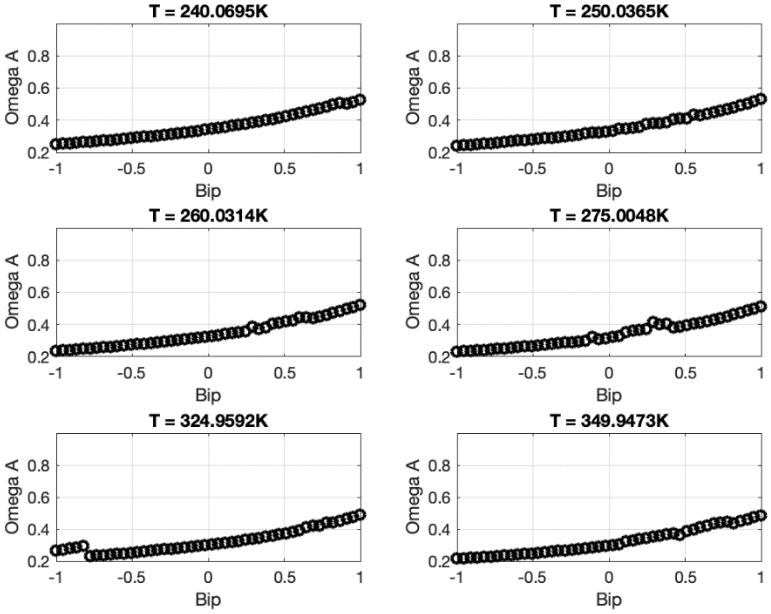

Figure 6.103: Ω_a vs BIP – 50% CH_4 + 50% H_2, PR.

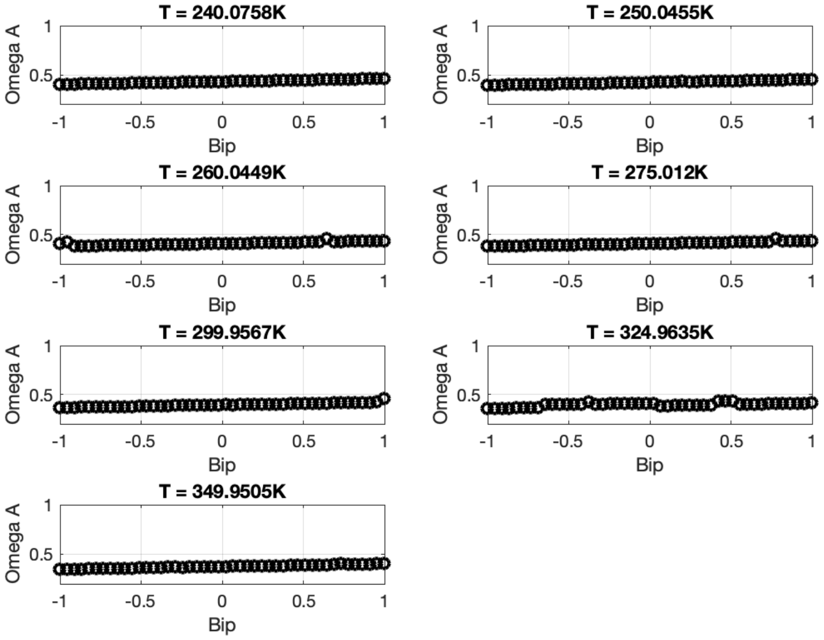

Figure 6.104: Ω_a vs BIP – 90% CH_4 + 10% H_2, PR.

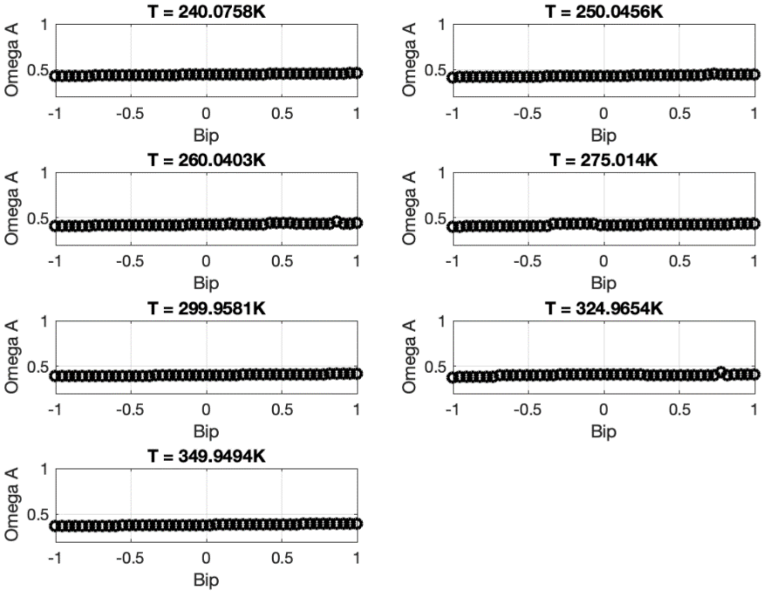

Figure 6.105: Ω_a vs BIP – 95% CH_4 + 05% H_2, PR.

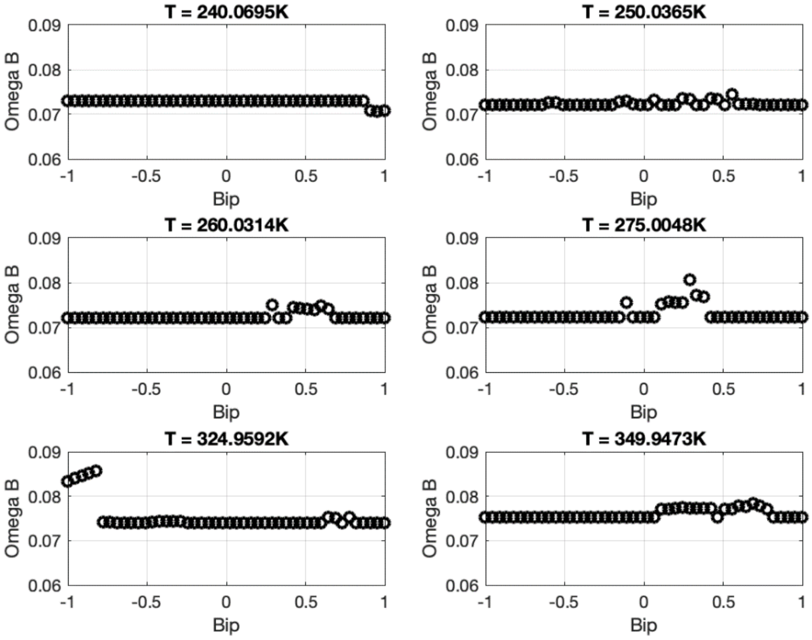

Figure 6.106: Ω_b vs BIP – 50% CH_4 + 50% H_2, PR.

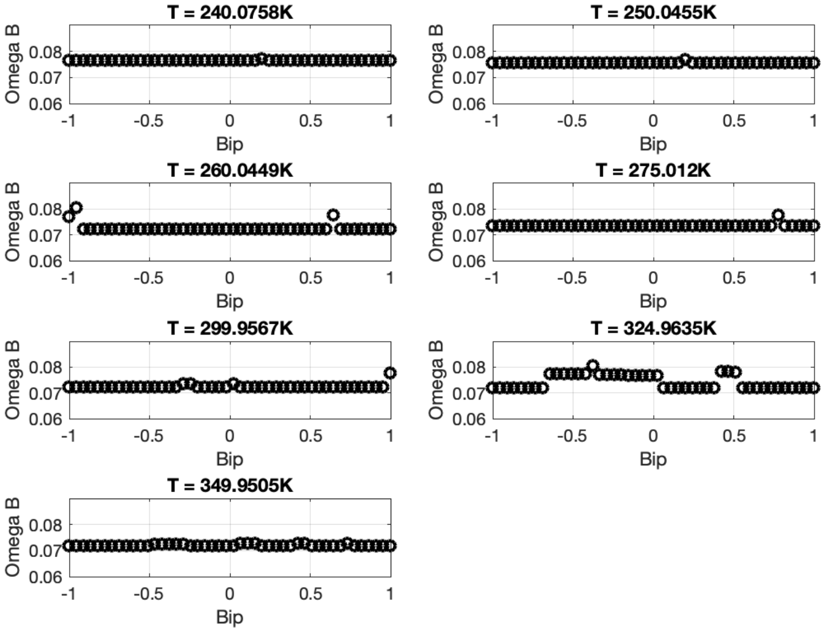

Figure 6.107: Ω_b vs BIP – 90% CH_4 + 10% H_2, PR.

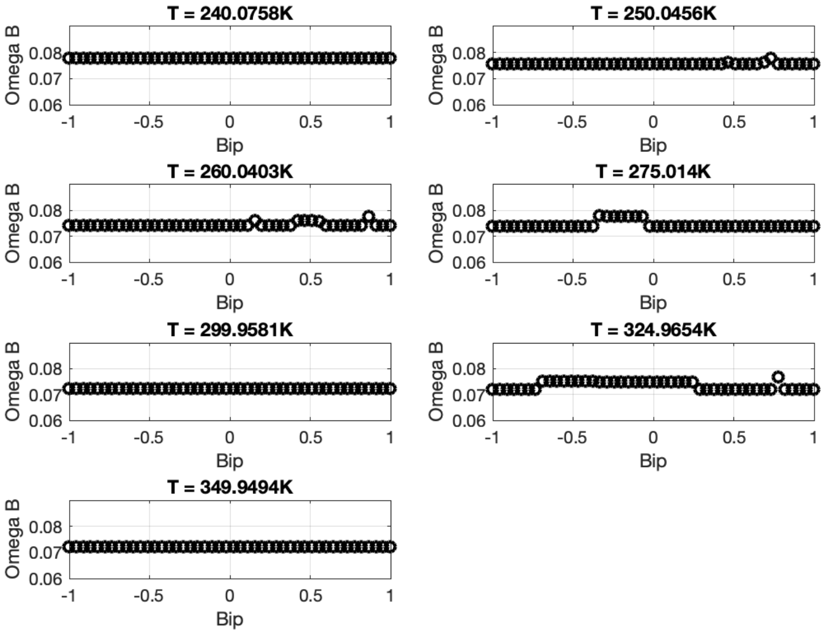

Figure 6.108: Ω_b vs BIP – 95% CH_4 + 05% H_2, PR.

The plots show that varying the value of BIP does not affect significantly the result of the optimization. In fact, the value of Ω_a and Ω_b vary in a very small range such that when plotting the optimal values of the two versus the different values of the BIP what comes out is almost an horizontal line. In particular the value of Ω_b hardly affected at all by BIP value both when applying the RKS model and the PR model; deviations from the horizontal line are observed only when the quantities of H_2 are higher (see Figures 6.100 and 6.106). In case the PR model is applied the influence of BIP on Ω_b is slightly higher (Figures 6.106, 6.107 and 6.108) in comparison to the result obtained by using RKS EoS (Figures 6.100, 6.101 and 6.102). On the other hand, the results show that Ω_a is more influenced by the value of BIP in comparison to Ω_b when the content of H_2 in the mixture is higher (see Figures 6.97 and 6.103), but when the quantities of CH_4 increase the BIP does not affect the results at all, in particular when using the RKS model.

This results further confirm that the accuracy of the models (i.e., RKS, PR) in predicting the density and the z – factor does not depend significantly on the value of BIP selected.

In order to investigate which is the most frequent optimal value of Ω_a and Ω_b the PDF is calculated. The following figures report the PDF for every value of Ω_a (Figures 6.109, 6.110, 6.111, 6.115, 6.116 and 6.117) and for every value of Ω_b (Figures 6.112, 6.113, 6.114, 6.118, 6.119 and 6.120), in particular Figures 6.109 to 6.114 show the results when using RKS EoS and Figures 6.115 to 6.120 the ones obtained when applying the PR model. The value of Ω_a and Ω_b with the highest PDF are displayed above each plot.

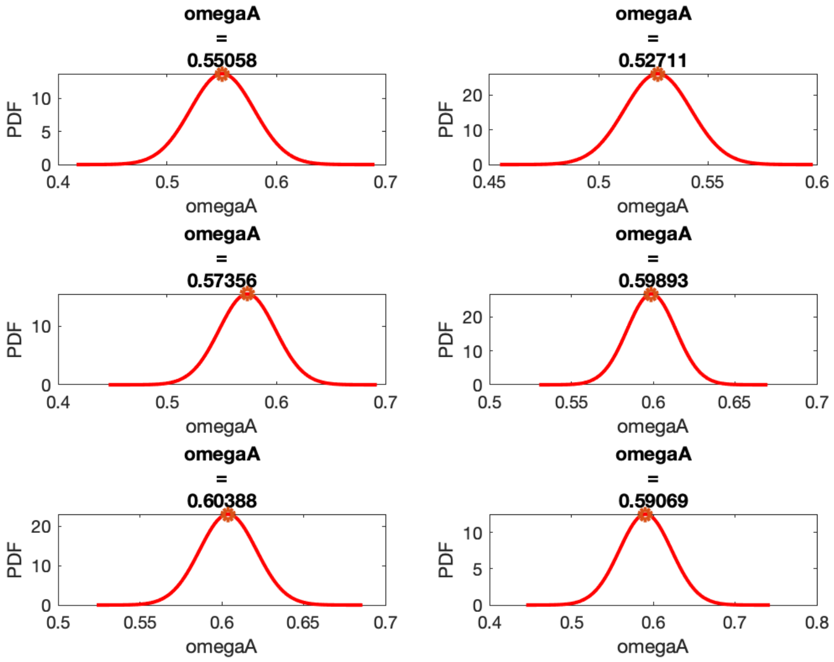

Figure 6.109: PDF vs Ω_a – 50% CH_4 + 50% H_2, RKS.

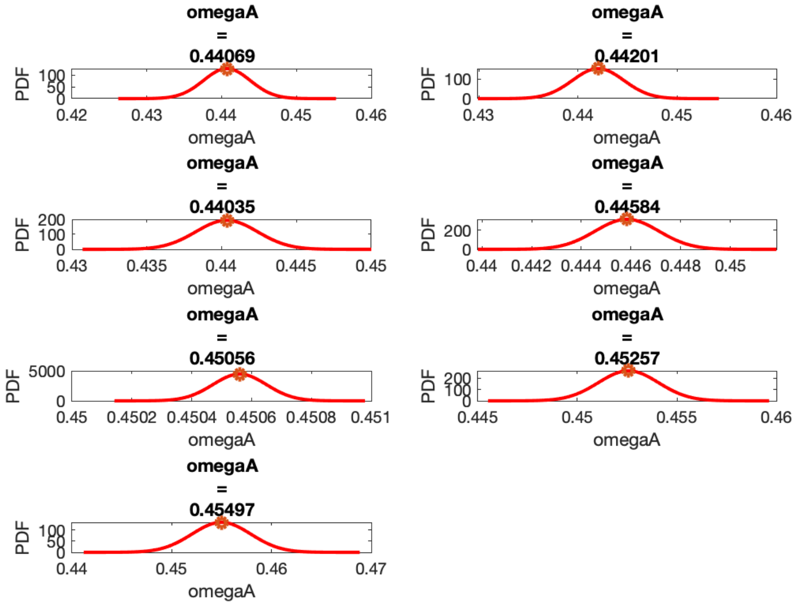

Figure 6.110: PDF vs Ω_a – 90% CH_4 + 10% H_2, RKS.

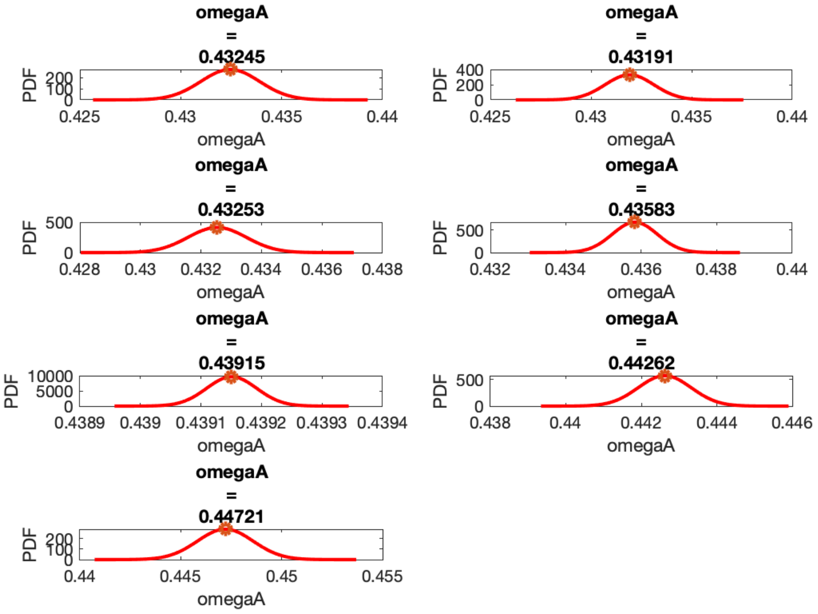

Figure 6.111: PDF vs Ω_a – 95% CH_4 + 05% H_2, RKS.

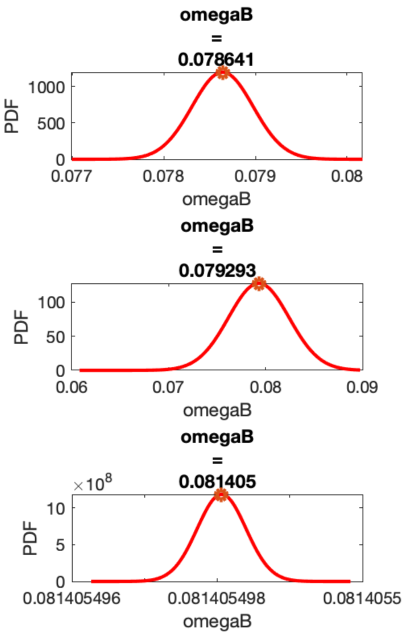

Figure 6.112: PDF vs Ω_b – 50% CH_4 + 50% H_2, RKS.

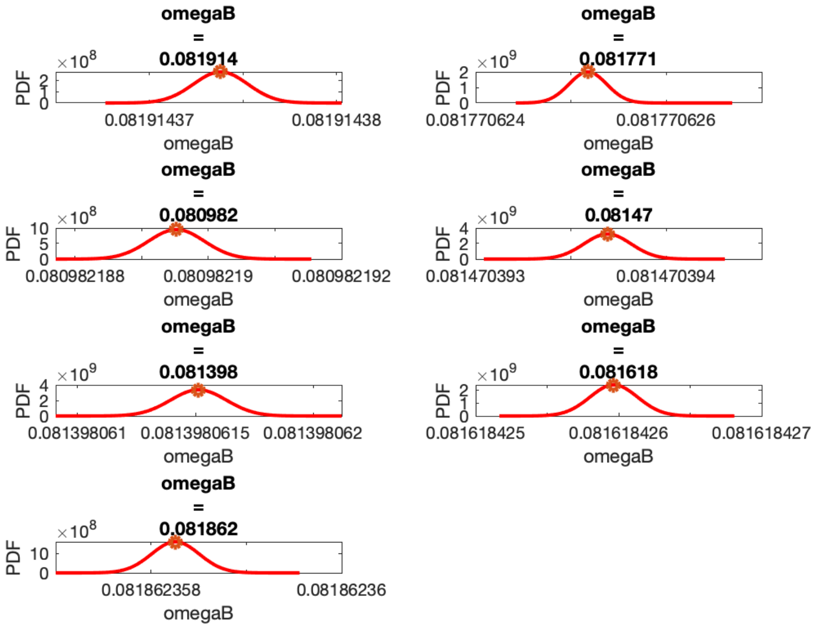

Figure 6.113: PDF vs Ω_b – 90% CH_4 + 10% H_2, RKS.

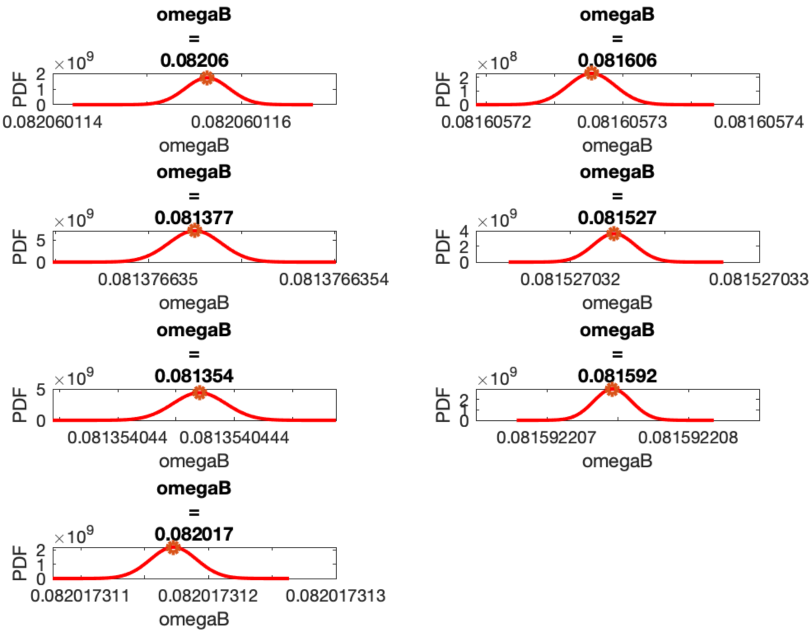

Figure 6.114: PDF vs Ω_b – 95% CH_4 + 05% H_2, RKS.

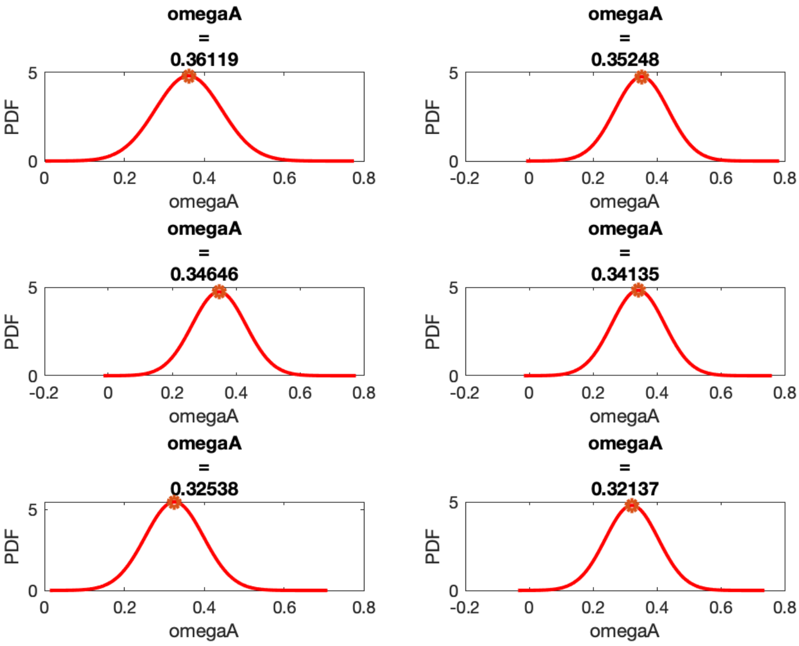

Figure 6.115: PDF vs Ω_a – 50% CH_4 + 50% H_2, PR.

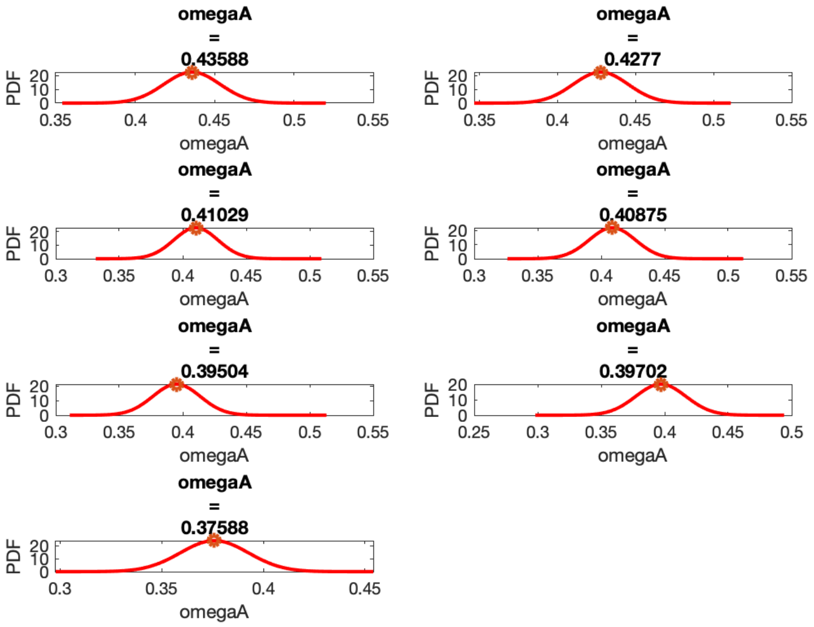

Figure 6.116: PDF vs Ω_a – 90% CH_4 + 10% H_2, PR.

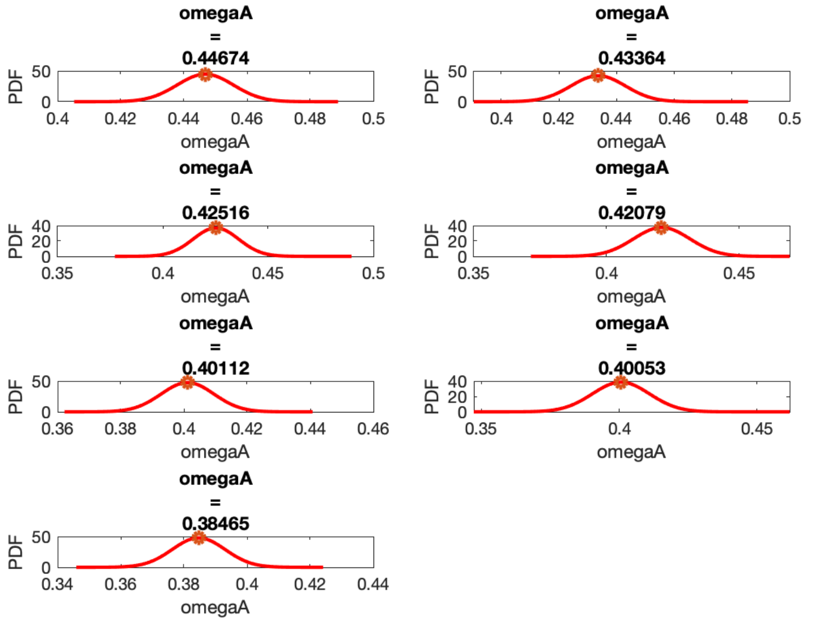

Figure 6.117: PDF vs Ω_a – 95% CH_4 + 05% H_2, PR.

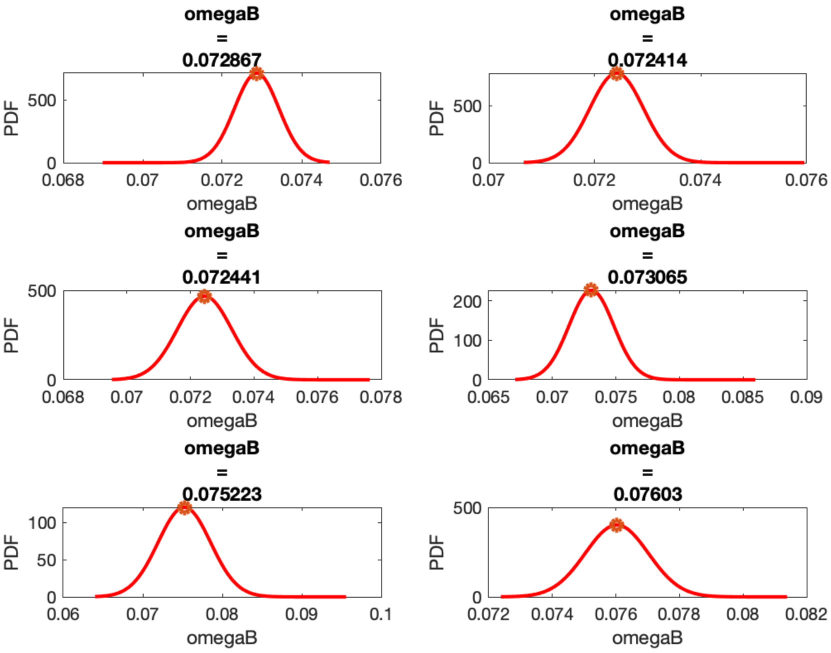

Figure 6.118: PDF vs Ω_b – 50% CH_4 + 50% H_2, PR.

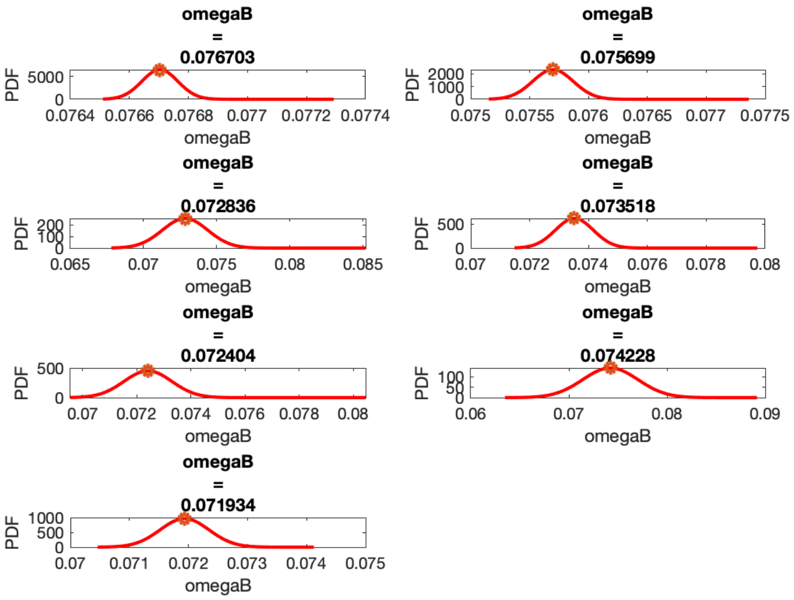

Figure 6.119: PDF vs Ω_b – 90% CH_4 + 10% H_2, PR.

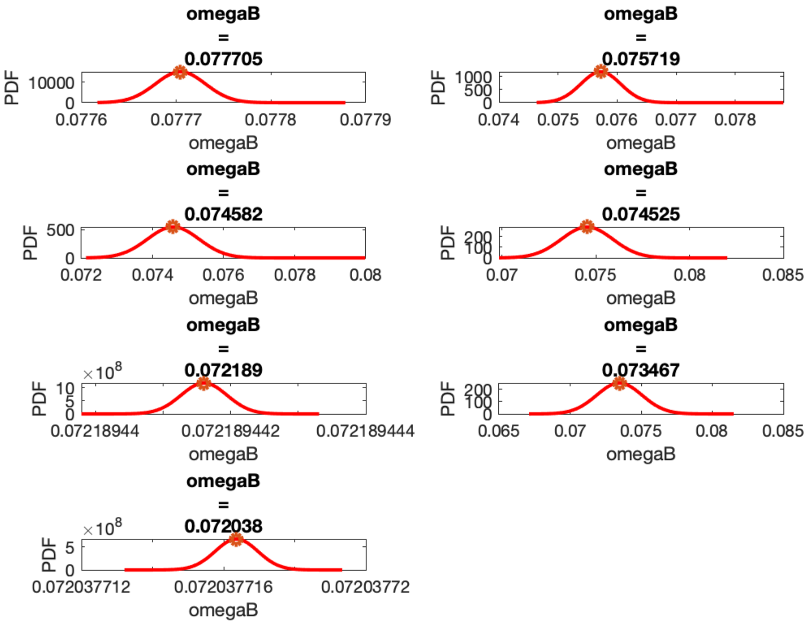

Figure 6.120: PDF vs Ω_b – 95% CH4 + 05% H2, PR.

6.3.4 Optimization of BIP

Finally, the optimization is performed only for BIP, whereas Ω_a varies between 0.1 and 1 and Ω_b between 0.01 and 0.1. The starting point for the BIP for both RKS and PR models is -0.15.

The following figures report the optimal value of BIP for every value of Ω_a and Ω_b tested, in particular Figures 6.121, 6.122 and 6.123 show the results when using RKS EoS and Figures 6.124, 6.125 and 6.126 the ones obtained when applying the PR model.

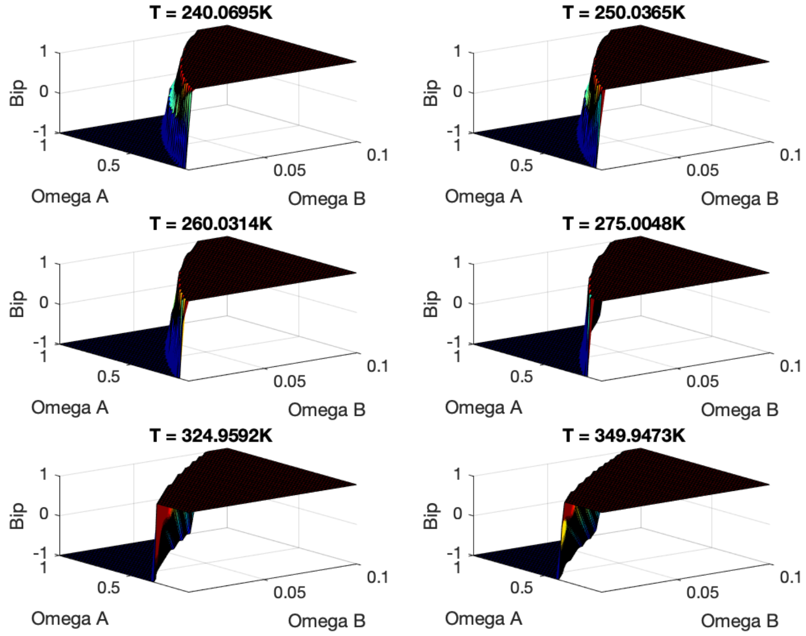

Figure 6.121: optimization of BIP – 50% CH_4 + 50% H_2, RKS.

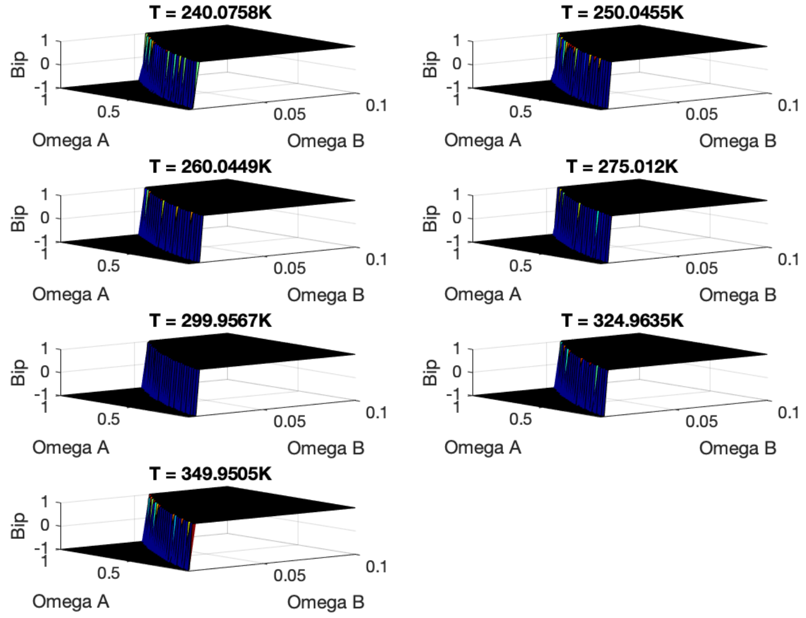

Figure 6.122: optimization of BIP – 90% CH_4 + 10% H_2, RKS.

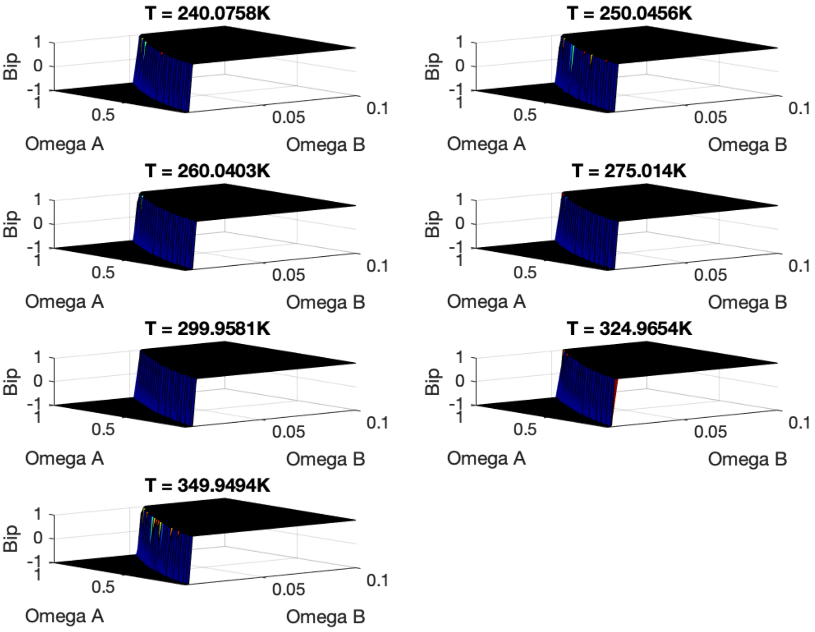

Figure 6.123: optimization of BIP – 95% CH_4 + 05% H_2, RKS.

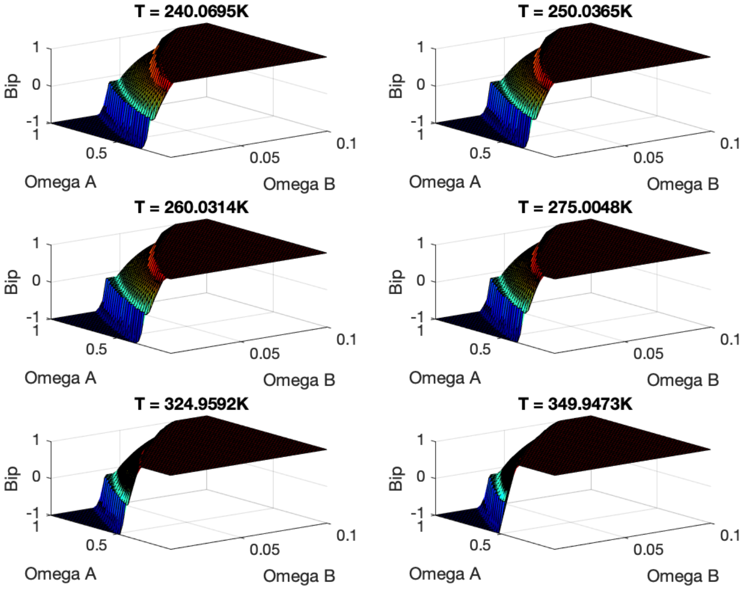

Figure 6.124: optimization of BIP – 50% CH_4 + 50% H_2, PR.

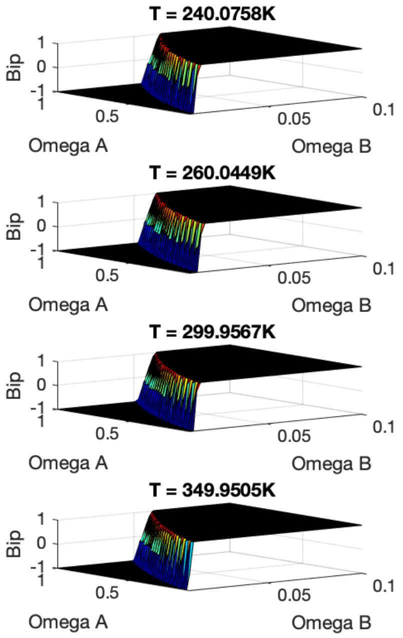

Figure 6.125: optimization of BIP – 90% CH_4 + 10% H_2, PR.

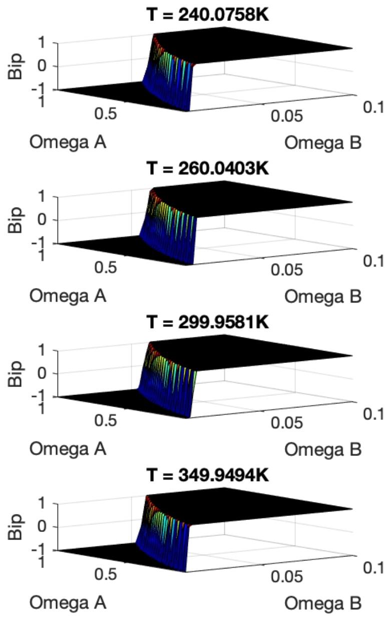

Figure 6.126: optimization of BIP – 95% CH_4 + 05% H_2, PR.

The overall plots show that varying Ω_a and Ω_b highly influence the result of the optimization.

In order to investigate which is the most frequent value of BIP that results from the optimization the PDF is calculated for each optimal value of the parameter. The following figures report the PDF for every value of BIP, in particular Figures 6.127, 6.128 and 6.129 show the results when using RKS EoS and Figures 6.130, 6.131 and 6.132 the ones obtained when applying the PR model. The value of BIP with the highest PDF is displayed above each plot.

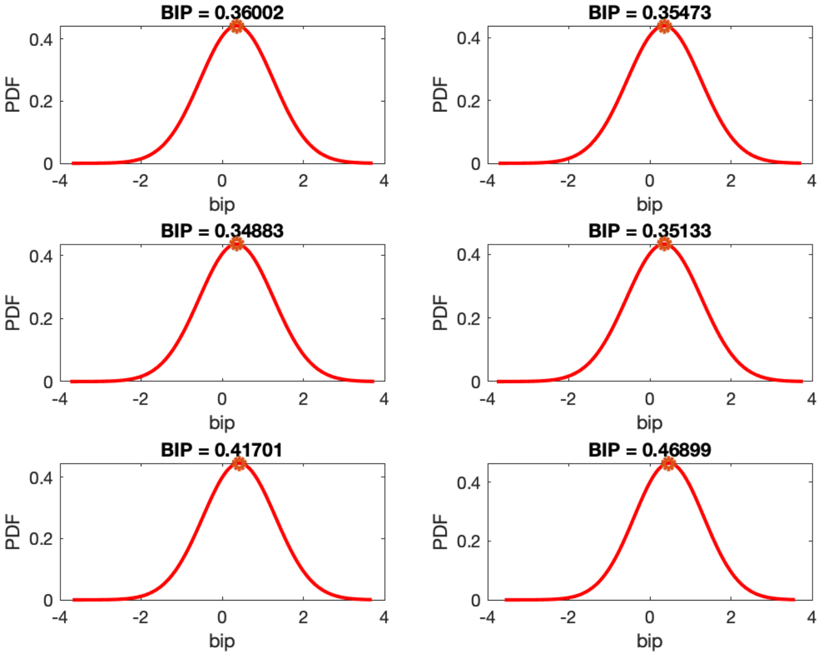

Figure 6.127: PDF vs BIP – 50% CH_4 + 50 % H_2, RKS.

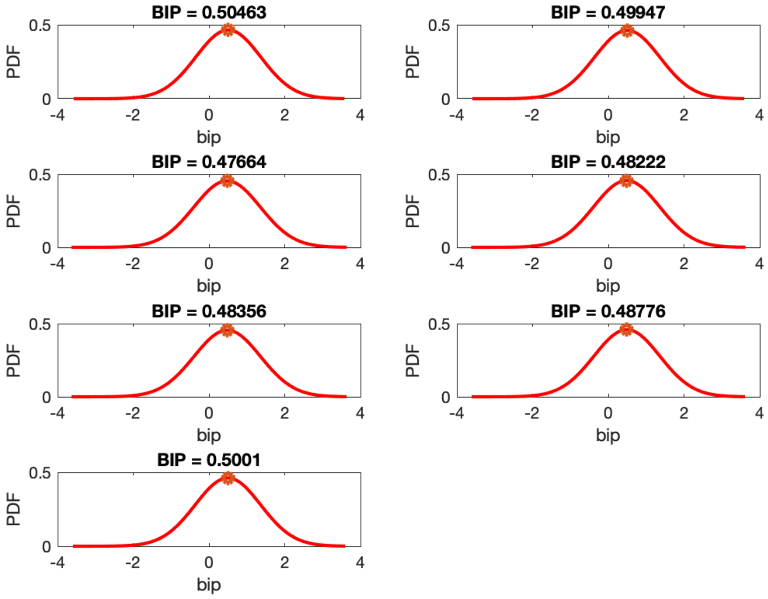

Figure 6.128: PDF vs BIP – 90% CH_4 + 10% H_2, RKS.

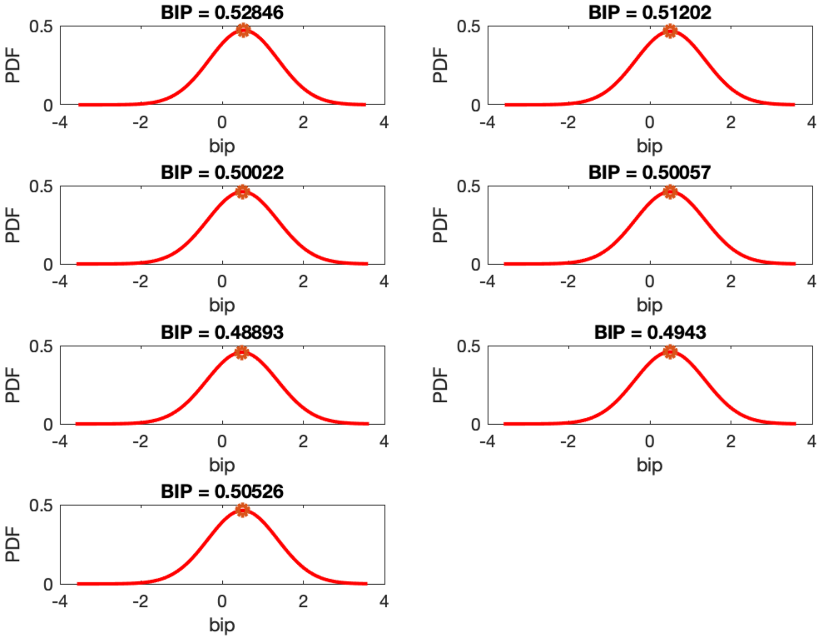

Figure 6.129: PDF vs BIP – 95% CH_4 + 05% H_2, RKS.

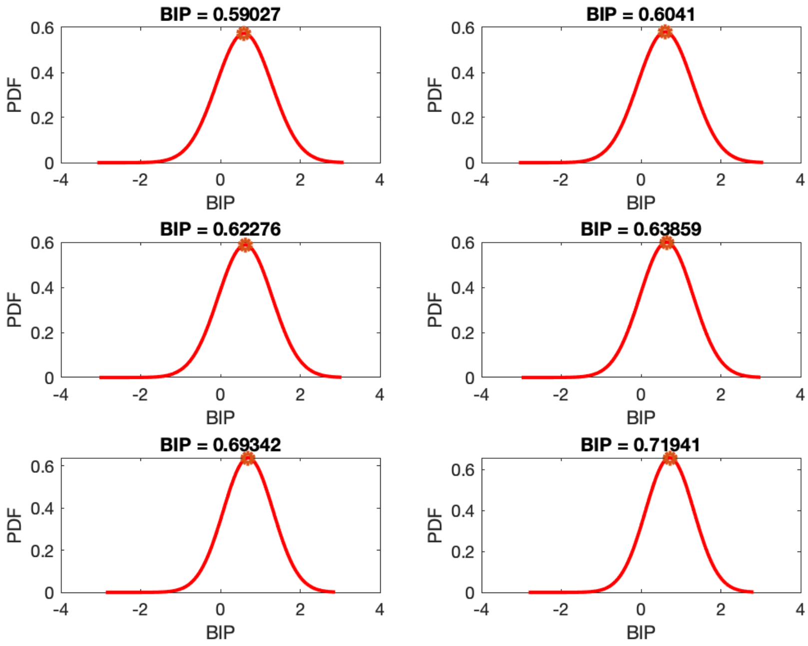

Figure 6.130: PDF vs BIP – 50% CH_4 + 50% H_2, PR.

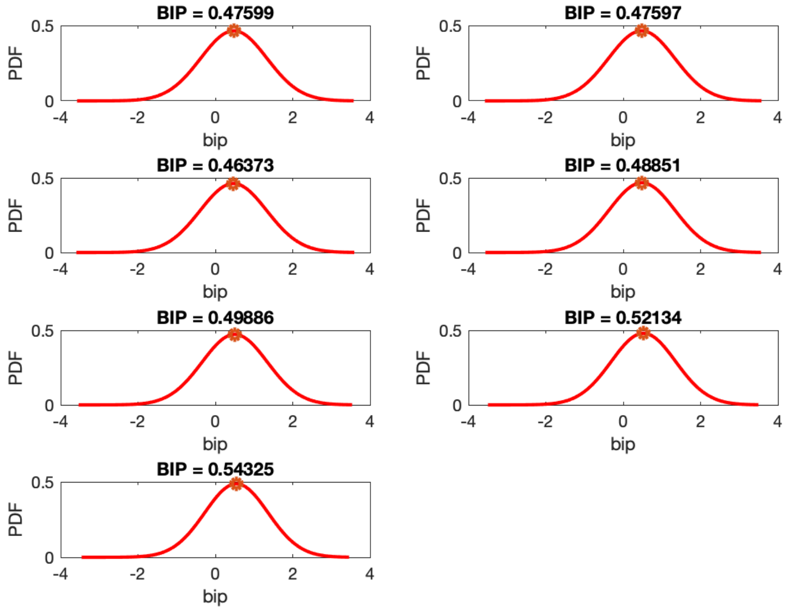

Figure 6.131: PDF vs BIP – 90% CH_4 + 10% H_2, PR.

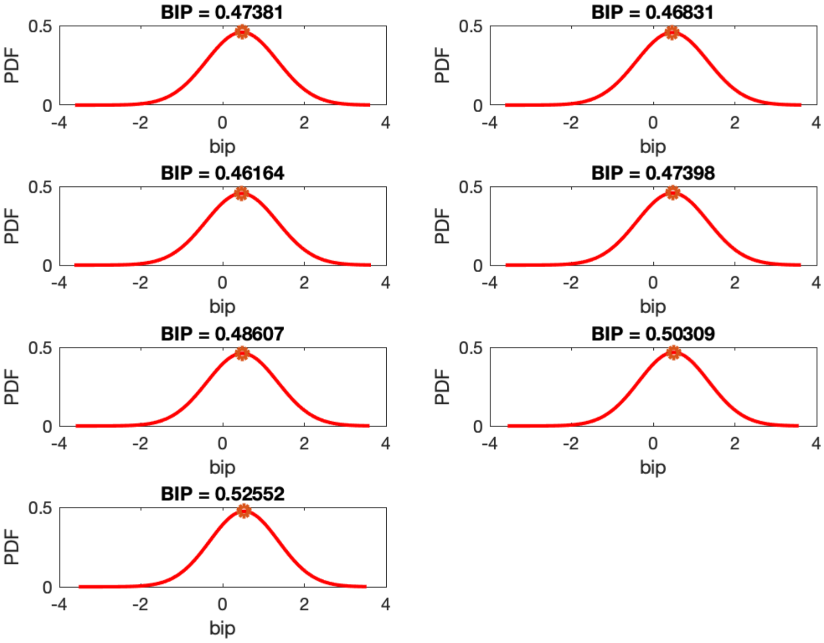

BIP = 0.47381

BIP = 0.46831

BIP = 0.46164

BIP = 0.47398

BIP = 0.48607

BIP = 0.50309

BIP = 0.52552

Figure 6.132: PDF vs BIP – 95% CH_4 + 05% H_2, PR.

Chapter 7

Conclusions

The presented study confirms that both Peng-Robinson EoS and Redlich – Kwong – Soave EoS can be applied to model the volumetric behavior of the H_2-CH_4 mixtures since in both cases the AAD is lower than 1%. Anyway, the model that better fits the data is the RKS one. The robustness analysis showed that increasing tolerance of the algorithm implemented may influence the results substantially, but decreasing the value does not result in an improvement of the accuracy of the algorithm in predicting the optimal values of the parameters. Therefore, the default value used by Matlab (equal to 10^{-6}) shows a good compromise between calculation time and precision . By changing the algorithm, it has been noted that the value of the BIP change drastically while the values of Ω_a and Ω_b are not significantly affected by the algorithm used for the optimization, although when applying PR model Ω_a slightly change. This has been a hint to further investigate how the BIP influence the accuracy of the fitting between the data obtained using the EoSs and the experimental data.

The results of sensitivity analysis carried out before performing the optimization already showed that when varying the BIP the density and the z – factor do not change significantly. In order to further confirm this thesis, the optimization has been performed for one parameter at time first and then for both Ω_a and Ω_b with the BIP varying in the range -1 to 1. The results of this study showed that, while changing Ω_a and Ω_b highly influence the results of the optimization, varying the BIP does not affect the resulting optimal values of Ω_a and Ω_b, in particular when the quantities of CH_4 in the mixtures are higher and when using the RKS model (since the results when using the PR model show a slightly higher dependency of the BIP value).

In the interest of further developments, other EoS and mixing rules may be analyzed. For the cubic EoS, the study of different mixing rules and EoS models would contribute to a better understanding of what is the most accurate analytical model available for the H_2-CH_4 mixtures studied and how the parameters of the EoS models influence the accuracy in the prediction of the data. Non-analytical EoSs are certainly more accurate, but they could be studied with the intention of optimizing their calculation to minimize the computational effort needed to calculate the solutions, since they are iterative.

References

Alanazi, A., et al. 2022. *Evaluation of cubic, PC-SAFT, and GERG2008 equations of state for accurate calculations of thermophysical properties of hydrogen-blend mixtures.* s.l. : Energy Reports 8, pp.13876-13899, 2022.

Alfriend, K.T., et al. 2010. *Chapter 3 - The Basics of Analytical Mechanics, Optimization, Control and Estimation.* s.l. : pp. 39-57, 2010.

Ali, M. 2018. *Effect of Organic Surface Concentration on CO_2-Wettability of Reservoir Rock.* Curtin University : s.n., 2018.

Ali, M., et al. 2021. *Hydrogen wettability of quartz substrates exposed to organic acids: Implications for hydrogen geo-storage in sandstone reservoirs.* s.l. : J. Pet. Sci. Eng. 207, pp. 109081, 2021.

Ali, M., et al. 2022. *Recent advances in carbon dioxide geological storage, experimental procedures, influencing parameters, and future outlook.* s.l. : Earth-Sci. Rev. 225, 2022.

Amid, A., Mignard, D. e Wilkinson, M. 2016. *Seasonal storage of hydrogen in a depleted natural gas reservoir.* s.l. : Int. J. Hydrogen Energy 41, pp. 5549–5558, 2016.

Aspen Tech. 2012. *Aspen physical property system.* 2012.

Aspen Technology Inc. 2015. *Aspen Plus ® User Guide.* s.l. : Aspen Technology, Inc, 2015.

Bai, M., et al. 2014. *An overview of hydrogen underground storage technology and prospects in China.* s.l. : Journal of Petroleum Science and Engineering 124, pp. 132–136, 2014.

Ball, M. e Wietschel, M. 2010. *The hydrogen economy: opportunities and challenges.* Cambridge, UK : Cambridge University Press, 2010.

Beckman, K.L., Determeyer, P.L. e Mowrey., E.H. 1995. *Natural gas storage: historical development and expected evolution.* Chicago : Gas Research Institute, 1995.

Beckmüller, R., et al. 2021. *New equations of state for binary hydrogen mixtures containing methane, nitrogen, carbon monoxide, and carbon dioxide.* s.l. : J. Phys. Chem. Ref. Data, 50, 2021.

Bejan, A. 2006. *Advanced Engineering Thermodynamics.* s.l. : Wiley, 2006.

Bendict, M., Webb, G. e Rubin, L.,. 1940. *An empirical equation for hydrocarbon thermodynamic properties of light hydrocarbons and their mixtures: methane, ethane, propane, and n-butane.* s.l. : Journal of Chemical Physics 8, pp. 334e345, 1940.

Bockris, Dr. John O'M., 1923-2013. 2013. s.l. : Infinite Energy Magazine, 2013.

Bonyadi, M. e Esmaeilzadeh, F. 2007. *Prediction of gas condensate properties by Esmaeilzadeh–Roshanfekr equation of state.* s.l. : Fluid Phase Equilibria, Volume 260, Issue 2, pp. 326-334, 2007.

Borthwick, W. 2006. *Overview of the hydrogen economy: perspectives from Europe. In proc. Int. Seminar on the Hydrogen Economy for Sustainable Development.* Reykjavik, Iceland : United Nations Department of Economic and Social Affairs, 2006.

Boston, J.F. e Mathias, P.M. 1980. *Phase equilibria in a third-generation process simulator.* s.l. : In: EFCE Publication Series (European Federation of Chemical Engineering), 1980.

Branch, M.A., Coleman, T.F. e Li, Y. 1999. *A SUBSPACE, INTERIOR, AND CONJUGATE GRADIENT METHOD FOR LARGE-SCALE BOUND CONSTRAINED MINIMIZATION PROBLEMS.* s.l. : SIAM J. SCI. COMPUT, Vol 21, No. 1, pp. 1–23, 1999.

Brandon, N.P. e Kurban, Z. 2017. *Clean energy and the hydrogen economy.* s.l. : Philos. Trans. Royal Soc. A 375, 20160400, 2017.

Bunton, D. 2002. Generic moves in PhD thesis introductions. [aut. libro] J. Flowerdew. *Academic discourse.* London : Pearson Education Limited, 2002, p. 57-75.

Buzek, F., et al. 1994. *Carbon isotope study of methane production in a town gas storage reservoir.* s.l. : Fuel 73, pp. 747–752, 1994.

Caglayan, D.G., et al. 2020. *Technical potential of salt caverns for hydrogen storage in Europe.* s.l. : International Journal of Hydrogen Energy 45, pp. 6793–6805, 2020.

Calsep, PVTSim Software. *2018.*

Chapman, W.G., et al. 1989. *SAFT: Equation-of-state solution model for associating fluids.* s.l. : Fluid Phase Equilib., 52, 1989.

Chueh, P.L. e Prausnitz, J.M. 1967. s.l. : Industrial & Engineering Chemistry Fundamentals, 6, 492, 1967.

Coleman, T.F. e Li., Y. 1994. *On the convergence of interior-reflective Newton methods for nonlinear minimization subject to bounds.* s.l. : Mathematical Programming 67, pp. 189-224, 1994.

Crotogino, F. 2016. *Chapter 20 – Larger Scale Hydrogen Storage, in: Letcher, T.M. (Ed.),.* s.l. : Storing Energy. Elsevier, Oxford, pp. 411-429., 2016.

Crotogino, F., et al. 2010. *Large-scale hydrogen underground storage for securing future energy supplies.* s.l. : In: 18th World Hydrogen Energy Conference 2010 WHEC 2010 Parallel Sessions Book 4: Storage Systems/Policy Perspectives, Initiatives and Co-Operations, vol. 78., 2010.

Danesh, A. 1998. *PVT and Phase Behavior of Petroleum Reservoir Fluids.* London : Elsevier Science B.V., 1998.

Daridon, J.L., et al. 1993. *A generalized process for phase equilibrium calculation with cubic equations of state.* s.l. : Int. J. Thermophys. 14, 1993.

Das, Debabrata e Vezirogly, T.Nejat. 2001. *Hydrogen production by biological processes: a survey of literature.* s.l. : International Journal of Hydrogen Energy, Volume 26, Issue 1, pp.13-28, ISSN 0360-3199, 2001.

Dawood, F., Anda, M. e Shafiullah, G.M. 2020. *Hydrogen production for energy: An overview.* s.l. : Int. J. Hydrogen Energy, 2020.

DOE. 2019. s.l. : Stanfor University, College of the Desert and Green Rconometrics Research, 2019.

Dunn, Seth. 2002. *Hydrogen futures: toward a sustainable energy system.* s.l. : International Journal of Hydrogen Energy, Volume 27, Issue 3, pp.235-264, ISSN 0360-3199, 2002.

Economou, I.G. 2010. *Chapter 4: Cubic and generalized van der waals equations of state.* s.l. : Appl. Thermodyn. Fluids pp. 53–83, 2010.

Economou, I.G. e Tsonopoulos, C. 1997. *Associating models and mixing rules in equations of state for water/hydrocarbon mixtures.* s.l. : Chemical Engineering Science 52 (4), pp. 511-525, 1997.

Egeland-Eriksen, Torbjorn, Hajizadeh, Amin e Sartori, Sabrina. 2021. *Hydrogen-based systems for integration of renewable energy in power systems: Achievements and perspectives.* s.l. : International Journal of Hydrogen Energy, Volume 46, Issue 63, pp. 31963-31983, ISSN 0360-3199, 2021.

EIA. 2021. *California's curtailments of solar electricity generation continue to increase.* 2021.

Energy Technologies Institute. 2015. *Hydrogen – The role of hydrogen storage in a clean responsive power system.* 2015.

Esmaeilzadeh, F. e Roshanfekr, M. 2006. *A new Cubic Equation of State for Reservoir Fluids.* s.l. : Fluid Phase Equilibria 239, 2006.

European Commission. 2003. *Hydrogen energy and fuel cells: a vision of our future.* 2003.

European Union. *Fuel Cell and Hydrogen Joint Undertaking (FCHJU).*

Evans, D., et al. 2021. *Salt Cavern Exergy Storage Capacity Potential of UK Massively Bedded Halites, Using Compressed Air Energy Storage (CAES).* s.l. : Applied Sciences 11, pp. 4728, 2021.

Falzolgher, F. e Altieri, G. 2005. *Underground storage of natural gas. Encyclopaedia of Hydrocarbons: Exploration, production and transport.* s.l. : I, Marchesi grafiche editoriali S.p.A., pp. 879–910, 2005.

Feldmann, F., et al. 2016. *Numerical simulation of hydrodynamic and gas mixing processes in underground hydrogen storages.* s.l. : Environ. Earth Sci. 75, 2016.

Firoozabadi, A. 1989. *Thermodynamics of Hydrocarbon Reservoirs.* s.l. : McGraw-Hill, 1989.

Flanigan, O. 1995. *Underground gas storage facilities: Design and implementation.* s.l. : Elsevier, 1995.

Fletcher, R. 1971. *A modified Marquardt subroutine for non-linear least squares.* 1971.

Foh, S. e Novil, M.: Rockar, E.: Randolph, P. 1979. *Underground Hydrogen Storage. Final Report.* New York : Brookhaven National Lab., 1979.

Gallo, A.B., et al. 2016. *Energy storage in the energy transition context: A technology review.* s.l. : Renew. Sustain. Energy Rev., 2016.

Global CSS Institute. 2022. *Global Status of CCS.* 2022.

Götz, Manuel, et al. 2016. *Renewable Power-to-Gas: A technological and economic review.* s.l. : Renewable Energy, Volume 85, pp. 1371 - 1390, ISSN 0960-1481, 2016.

Gross, J. e Sadowski, G. 2001. *Perturbed-chain SAFT: An equation of state based on a perturbation theory for chain molecules.* s.l. : Ind. Eng. Chem. Res. 40, pp. 1244–1260, 2001.

H2USA. 2013. 2013.

Haddenhorst, H.G. e Tek, M.R. 1989. *Underground storage of natural gas.* 1989.

Hassanpouryouzband, A., et al. 2020. *Thermodynamic and transport properties of hydrogen containing streams.* s.l. : Sci. Data 7, 2020.

Heinemann, N., et al. 2021. *Enabling large-scale hydrogen storage in porous media—The scientific challenges.* s.l. : Energy Environ. Sci. 14, pp. 853-864, 2021.

Hernández-Gómez, R., et al. 2018. *Accurate Experimental (p, ρ, and T) Data for the Introduction of Hydrogen into the Natural Gas Grid (II): Thermodynamic Characterization of the Methane–Hydrogen Binary System from 240 to 350 K and Prssures up to 20 MPa.* s.l. : J. Chem. Eng. Data 63, pp. 1613-1630, 2018.

Hirschfelder, J.O., et al. 1954. *Molecular Theory of Gases and Liquids.* New York : Wiley, 1954.

Hosseini, M., et al. 2022. *Hydrogen wettability of carbonate formations: Implications for hydrogen geo-storage.* s.l. : J. Colloid Interface Sci. 614, pp. 256–266, 2022.

Huang, S.H. e Radosz, M. 1991. *Equation of state for small, large, polydisperse, and associating molecules: Extension to fluid mixtures.* s.l. : Ind. Eng. Chem. Res., 30, 1991.

Huron, M.-J. e Vidal, J. 1979. *New mixing rules in simple equations of state for representing vapour-liquid equilibria of strongly non-ideal mixtures.* s.l. : Fluid Phase Equilibria 3 (4), pp. 255-271, 1979.

IEA, Internationa Energy Agency. 2018. *Energy efficiency, 2018. Analysis and outlooks to 2040.* Paris : International Energy Agency, 2018.

IEA, Internationa Energy Agency. 2019. *Renewables 2020 gloval status report, 2019. World Energy Outlook 2019 - Analysis.* Paris : Internationa Energy Agency, 2019.

IEA, Internationa Energy Agency. 2023. *Statista 2023.* Paris : Internationa Energy Agency, 2023.

IEA, Internationa Energy Agency. 2019. *World Energy Outlook.* Paris : International Energy Agency, 2019.

IEA, Internationa Energy Agency. 2021. *World Energy Outlook 2021.* Paris : Internationa Energy Agency, 2021.

IEA, International Energy Agency. 2014. *Energy Technology Perspectives 2014.* Paris : International Energy Agency, 2014.

Iglauer, S., Ali, M. e Keshavarz, A. 2021. *Hydrogen wettability of sandstone reservoirs: Implications for hydrogen geo-storage.* s.l. : Geophys. Res. Lett. 48, e2020GL090814, 2021.

IGU. 2018. *Global Natural Gas Insights.* s.l. : International Gas Union, 2018.

Institute of Chemical Engineering. *Combination of power-to-gas with biogas plant.* Vienna, Austria : Institute of Chemical Engineering.

Iordache, I., et al. 2014. *Hydrogen underground storage in Romania, potential directions of development, stakeholders and general aspects.* s.l. : International Journal of Hydrogen Energy 39, pp. 11071-11081, 2014.

IPCC. 2014. *Fifth Assessment Report of the IPCC.* Geneva, Switzerland : IPCC, 2014.

ISO 6142-1. 2015. *Gas Analysis - Preparation of calibration gas mixtures - Part 1: Gravimetric method for Class I mixtures.* Geneva : International Organization for Standardization, 2015.

Jackson, G., Chapman, W.G. e Gubbins, K.E. 1988. *Phase equilibria of associating fluids spherical molecules with multiple bonding sites.* s.l. : Mol. Phys., 65, pp. 1-31, 1988.

Krejbjerg, K. e Pedersen, K.S. 2006. s.l. : in Canadian International Petroleum Conference. OnePetro, 2006.

Kruck, O. e Crotogino, F. 2013. *Assessment of the potential, the actors and relevant business cases for large scale and seasonal storage of renewable electricity by hydrogen underground storage in Europe: Benchmarking of Selected Storage Options.* s.l. : HyUnder Deliverable No 3.3, 2013.

Kundu, G., Upadhyay, R. e Kumar, A. 2023. *Reliable Binary Interaction Parameters for SRK EOS for Modeling CO_2 and H_2 Storage in Depleted Oil and Gas Reservoirs.* s.l. : Research Square, 2023.

Kunz, O. e Wagner, W. 2012. *The GERG-2008 wide-range equation of state for natural gases and other mixtures: An expansion of GERG-2004.* s.l. : J. Chem. Eng. Data 57, 2012.

Kunz, O., et al. 2007. *The GERG-2004 wide-range equation of state for natural gases and other mixtures.* s.l. : GERG TM15, 2007; Fortschr.-Ber. VDI, Reihe 6, Nr. 557, VDI Verlag: Düsseldorf. Also available as GERG Technical Monograph 15, 2007, 2007.

Kwak, T. e Mansoori, G. 1986. *Van der Waals mixing rules for cubic equations of state. Applications for supercritical fluid extraction modelling.* s.l. : Chemical Engineering Science 41 (5), pp. 1303-1309, 1986.

Le Duigou, A., et al. 2017. *Relevance and costs of large scale underground hydrogen storage in France.* s.l. : International Journal of Hydrogen Energy 42, pp. 22987 – 23003, 2017.

Leachman, J. W., et al. *2009.* s.l. : J. Phys. Chem. Ref. Data 38, 721.

Lemieux, A., Sharp, K. e Shkarupin, A. 2019. *Preliminary assessment of underground hydrogen storage sites in Ontario, Canada.* s.l. : Int. J. Hydrog. Energy 44, pp. 15193–15204., 2019.

Lemieux, A., Shkarupin, A. e Sharp, K. 2020. *Geologic feasibility of underground hydrogen storage in Canada.* s.l. : International Journal of Hydrogen Energy 45, pp. 32243–32259, 2020.

Lemmon, E.W.,. 2007. *REFPROP: Reference Fluid Thermo-dynamic and Transport Properties.* s.l. : NIST Standard Database, Version8.0., 2007.

Levenberg, K. 1944. *A Method for the Solution of Certain Nonlinear Problems in Least Squares.* s.l. : Quarterly of Applied Mathematics, vol. 2, no. 2, pp. 164-168, 1944.

Li, J., et al. 2019. *Modeling the construction of energy storage salt caverns in bedded salt.* s.l. : Applied Energy 255, pp. 113866, 2019.

Liu, W., et al. 2020. *Feasibility evaluation of large-scale underground hydrogen storage in bedded salt rocks of China: A case study in Jiangsu province.* s.l. : Energy 198, pp. 117348, 2020.

Lord, A.S. 2009. *Overview of geologic storage of natural gas with an emphasis on assessing the feasibility of storing hydrogen.* United States : s.n., 2009.

Lux, K.-H. 2009. *Design of salt caverns for the storage of natural gas, crude oil and compressed air: Geomechanical aspects of construction, operation and abandonment.* s.l. : Geological Society, London, Special Publications 313, pp. 93-128, 2009.

Ma, J., et al. 2019. *Hydromechanical Response and Impact of Gas Mixing Behavior in Subsurface CH_4 Storage with CO_2-Based Cushion Gas.* s.l. : Energy & Fuels 33, pp. 6527–6541, 2019.

Mahlia, T.M.I., et al. 2014. *A review of available methods and development on energy storage; technology update.* s.l. : Renew. Sustain. Energy Rev., 2014.

Mangold, F., et al. 2019. *Equation of state and thermodynamic properties for mixtures of H2O, O2, N2, and CO2 from ambient up to 1000 K and 280 MPa.* s.l. : J. Supercrit. Fluids 153, 2019.

Marquardt, D.W. 1963. *An Algorithm for Least-Squares Estimation of Nonlinear Parameters.* s.l. : Journal of the Society for Industrial and Applied Mathematics, vol. 11, no. 2, pp. 431-441, 1963.

Mason, E.A. e Spurling, T.H. 1969. *The Virial Equation of State.* s.l. : Pergamon, 1969.

Mathias, P.M. 1983. *A versatile phase equilibrium equation of state.* s.l. : Ind. Eng. Chem. Process Des. Dev. 22, 1983.

Mathias, P.M., e Copeman, T.W. 1983. *Extension of the peng-robinson equation of state to complex mixtures: Evaluation of the various forms of the local composition concept.* s.l. : Fluid Phase Equilib., 13, 1983.

Mathias, P.M., Klotz, H.C. e Prausnitz, J.M. 1991. *Equation-of-state mixing rules for multicomponent mixtures: The problem of invariance.* s.l. : Fluid Phase Equilib., 67, 1991.

Michalski, J., et al. 2017. *Hydrogen generation by electrolysis and storage in salt caverns: potentials, economics and systems aspects with regard to the German energy.* s.l. : Int. J. Hydrog. Energy 42, pp. 13427 - 13443, 2017.

Michels, A. e Goudeket, M. 1941. *Compressibilities of hydrogen between 0 ◦C and 150 ◦C up to 3000 atmospheres.* s.l. : Physica 8, 1941.

Ministry of Economy, Trade and Industry. 2016. *Compilation of the revised version of the strategic roadmap for hydrogen and fuel cells.* Tokyo, Japan : Ministry of Economy, Trade and Industry, 2016.

Misra, B.R., et al. 1988. *The use of inert base gas in underground natural gas storage.* s.l. : In SPE Gas Technology Symposium (Society of Petroleum Engineers), 1988.

Mohanty, U.S., et al. 2021. *Current advances in syngas (CO+H_2) production through bi-reforming of methane using various catalysts: A review.* s.l. : Int.J.HYdrogen Energy 46, pp.32809-32845, 2021, 2021.

Moustakas, K., et al. 2020. *A review of recent developments in renewable and sustainable energy systems: Key challenges and future perspective.* s.l. : Renew. Sustain. Energy Rev., 2020.

Muhammed, N.S., et al. 2022. *A review on underground hydrogen storage: Insight into geological sites, influencing factors and future outlook.* s.l. : Energy Reports, Volume 8, pp. 461-499, ISSN 2352-4847, 2022.

Nelson, L.C. e Obert, E.F. 1954. *Generalizedp-v-T properties of Gases.* s.l. : Trans. A.S.M.E., Vol. 76 p. 1057, 1954.

Nielsen, Markus Hays, et al. 2023. *Fluid Modeling of Underground Hydrogen Storage in a Depleted Natural Gas.* Vienna : SPE EuropEC - Europe Energy Conference featured at the 84th EAGE Annual Conference & Exhibition, 2023.

Nikolaidis, I.K., et al. 2021. *Assessment of the perturbed chain-statistical associating fluid theory equation of state against a benchmark database of high-quality binary-system data.* s.l. : Ind. Eng. Chem. Res., 60, pp. 8935-8946, 2021.

Nishiumi, H. 1980. *An improved generalized BWR equation of state with three polar parameters applicable to polar substances.* s.l. : Journal of Chemical Engineering of Japan 13 (3), pp. 178-183, 1980.

Nishiumi, H. e Saito, S. 1975. *An improved generalized BWR equation of state applicable to low reduced temperatures.* s.l. : Journal of Chemical Engineering of Japan 8 (5), pp. 356-360, 1975.

Nishiumi, H., Kura, S. e Yokoyama, T. 1991. *Extended BWR equation of state for fluorocarbons, chloroform and carbon tetrachloride.* s.l. : Fluid Phase Equilibria 69, pp. 141e153, 1991.

Nocedal, J. e Wright, S. J. 2006. *Numerical Optimization.* s.l. : Springer, Second Edition, 2006.

Northern Gas Networks, Amec Foster Wheeler e Kiwa Gastec. 2016. *H21 Leeds City Gate report.* s.l. : Northen Gas Networks; Kiwa Gastec; Amec Foster Wheeler, 2016.

Oellrich, L., et al. 1981. United States : Int. Chem. Eng, 21, 1981.

Oldenburg, C. M. 2003. *Carbon dioxide as cushion gas for natural gas storage.* s.l. : Energy & Fuels 17, pp. 240–246, 2003.

Oldenburg, C. M. e Pan, L. 2013. *Utilization of CO2 as cushion gas for porous media compressed air energy storage.* s.l. : Greenh. Gases Sci. Technol. 3, pp. 124–135, 2013.

Onnes, H.K. 1901. *Expression of the equation of state of gases and liquids by means of series.* s.l. : In: KNAW, Proceedings, 1901.

Ozarslan, A. 2012. *Large-scale hydrogen energy storage in salt caverns.* s.l. : International Journal of Hydrogen Energy, HYFUSEN 37, pp.14265–14277, 2012.

Panfilov, M. 2016. *4 – Underground and pipeline hydrogen storage, in: Gupta, R.B., Basile, A., Veziroglu, T.N. (Eds.), Compendium of Hydrogen Energy, Woodhead Publishing Series in Energy.* s.l. : Woodhead Publishing, pp. 91-115, 2016.

Panfilov, M. 2010. *Underground storage of hydrogen: In situ self-organisation and methane generation.* s.l. : Transp. Porous Media 85, 2010.

Patel, N.C. e Teja, A.S. 1982. *A new cubic equation of state for fluids and fluid mixtures.* s.l. : Chemical Engineering Science 37 (3), pp. 463-473, 1982.

Peneloux, A., Rauzy, E. e Freze, R. 1982. *A Consistent Correction for Redlich-Kwong-Soave Volumes.* s.l. : Fluid Phase Equilibria 8, 1982.

Peng, D.-Y. e Robinson, D.B. 1976. *A new two-constant equation of state.* s.l. : Industrial & Engineering Chemistry Fundamentals 15 (1), pp. 59e64, 1976.

Pfeiffer, W.T. e Bauer, S. 2015. *Subsurface porous media hydrogen storage–scenario development and simulation.* s.l. : EnergyProcedia76, pp. 565–572, 2015.

Pfeiffer, W.T., Beyer, C. e Bauer, S. 2017. *Hydrogen storage in a heterogeneous sandstone formation: Dimensioning and induced hydraulic effects.* s.l. : Pet. Geosci. 23, 2017.

Pitzer, K. S. 1955. *The volumetric and thermodynamic properties of fluids, I: Theoretical basis and viral coefficients.* s.l. : J. Am. Chem. Society, Vol. 77, pp. 3427-3433, 1955.

Poling, B. E., Prausnitz, J. M. e O'Connell, J. P. 2001. *The properties of gases and liquids, 5th edition.* s.l. : McGrall-Hill, 2001.

Prausnitz, J.M., Lichtenthaler, R.N. e de Azevedo, E.G. 1998. *Molecular Thermodynamics of Fluid-phase Equilibria.* s.l. : Pearson Education, 1998.

Precedence Research. 2022. *Hydrogen Energy Storage Market Size, Growth, Report 2022-2030.* 2022.

Press, W. H., et al. 2007. *Numerical Recipes: The Art of Scientific Computing, 3rd Edition.* s.l. : Cambridge University Press, 2007.

PVTsim Nova - Calsep. 2020. 2020.

Rahbari, A., et al. 2019. *Solubility of water in hydrogen at high pressuress: A molecular simulation study.* s.l. : J.Chem.Eng.Data 64, pp.4103-4115, 2019.

Redlich, O. e Kwong, J.N. 1949. *On the thermodynamics of solutions. V. An equation of state. Fugacities of gaseous solutions.* s.l. : Chemical Reviews 44 (1), pp. 233-244, 1949.

Riazi, M. 2005. *Characterization and Properties of Petroleum Fractions.* s.l. : ASTM, 2005.

Rifkin, J. 2004. *The hydrogen economy.* New York, NY : Tarcher/Penguin, 2004.

Robinson, D.B. e Peng, D.Y. 1978. *The characterization of the heptanes and heavier fractions for.* s.l. : Gas processors association, 1978.

Sadus, R.J. 1992. *Influence of quantum effects on the high-pressure phase behavior of binary mixtures containing hydrogen.* s.l. : J. Phys. Chem. 96, 1992.

Saidi, K. e Omri, A. 2020. *The impact of renewable energy on carbon emissions and economic growth in 15 major renewable energy-consuming countries.* s.l. : Environ.Res.186, 2020.

Schmidt, G. e Wenzel, H. 1980. *A modified van der Waals type equation of state.* s.l. : Chemical Engineering Science 35 (7), pp. 1503-1512, 1980.

Schwartzentruber, J. e Renon, H. 1989. *Extension of UNIFAC to high pressures and temperatures by the use of a cubic equation of state.* s.l. : Ind. Eng. Chem. Res. 28, 1989.

Seo, S.-K., Yun, D.-Y. e Lee, C.-J. 2020. *Design and optimization of a hydrogen supply chain using a centralized storage model.* s.l. : Applied Energy, Volume 262, pp.114452, ISSN 0306-2619, 2020.

Seward, T.M. e Franck, E.U. 1981. *System hydrogen - water up to 440 ◦C and 2500 bar pressure.* s.l. : Ber. Bunsenges. Phys. Chem. Chem. Phys. 85, 1981.

Soave, G. 1995. *A noncubic equation of state for the treatment of hydrocarbon fluids at reservoir conditions.* s.l. : Industrial & Engineering Chemistry Research 34 (11), pp. 3981-3994, 1995.

Soave, G. 1972. *Equilibrium constants from a modified Redlich-Kwong equation of state.* s.l. : Chem. Eng. Sci., Vol. 27, pp. 1197-1203, 1972.

Starling, K. 1966. *A new approach for determining equation-of-state parameters using phase equilibria data.* s.l. : Society of Petroleum Engineers Journal 6 (04), pp. 363e371, 1966.

Starling, K.E. 1973. *Fluid Thermodynamic Properties for Light Petroleum Systems.* s.l. : Gulf Pub. Co, 1973.

Stryjek, R. e Vera, J. 1986c. *PRSV: an improved Peng-Robinson equation of state for pure compounds and mixtures.* s.l. : The Canadian Journal of Chemical Engineering 64 (2), pp. 323-333, 1986c.

Stryjek, R. e Vera, J. 1986b. *PRSV: an improved Peng-Robinson equation of state with new mixing rules for strongly nonideal mixtures.* s.l. : The Canadian Journal of Chemical Engineering 64 (2), pp. 334-340, 1986b.

Stryjek, R. e Vera, J. 1986a. *PRSV2: a cubic equation of state for accurate vapor liquid equilibria calculations.* s.l. : The Canadian Journal of Chemical Engineering 64 (5), pp. 820-826., 1986a.

Tarkowski, R. e Czapowski, G. 2018. *Salt domes in Poland – Potential sites for hydrogen storage in caverns.* s.l. : International Journal of Hydrogen Energy 43, pp. 21414-21427, 2018.

Tarkowski, R. 2019. *Underground hydrogen storage: Characteristics and prospects.* s.l. : Renewable and Sustainable Energy Reviews 105, pp. 86-94, 2019.

Tassios, G., Kontogeorgis, F. e Sandler, W. 2002. *Parameter Estimation for Equations of State.* s.l. : in Modeling in Transport Phenomena, Elsevier, 2002.

Taylor, J.B., et al. 1986. *Technical and economic assessment of methods for the storage of large quantities of hydrogen.* s.l. : Int. J. Hydrogen Energy 11, 1986.

The White House. 2003. *Hydrogen economy fact sheet.* 2003.

Tumakaka, F., Gross, J. e Sadowski, G. 2005. *Thermodynamic modeling of complex systems using PC-SAFT.* s.l. : Fluid Phase Equilib., 228–229, pp. 89-98, 2005.

Twu, C.H., et al. 1991. *A cubic equation of state with a new alpha function and a new mixing rule.* s.l. : Fluid Phase Equilib., 69, 1991.

U.S. Department of Agriculture, U.S. Environmental Protection Agency e U.S. Department of Energy. 2014. *Biogas opportunities roadmap.* 2014.

United Nations. 2016. *Framework Convention on Climate Change (COP21) Paris Agreement.* 2016.

United Nations. 2016. *World population projected to reach 9.7 billion by 2050.* s.l. : Department of Economic and Social Affairs, 2016.

Valderrama e J.O. 2003. *The state of the cubic equations of state.* s.l. : Ind. Eng. Chem. Res., 42 (2003), pp. 1603-1618, 2003.

van der Roest, Els, Snip, Laura e Fens, Theo, van Wijk. 2020. *Introducing Power-to-H3: Combining renewable electricity with heat, water and hydrogen production and storage in a neighbourhood.* s.l. : Applied Energy, Volume 257, 114024, ISSN 0306-2619, 2020.

van der Waals, J. D. 1913. *The law of corresponding states for different substances.* s.l. : KNAW, Proceedings, Vol. XV, 1913.

Verga, F 2022. *Reservoir Engineering course material for the M.Sc. in Petroleum and Mining Engineering* . Politecnico di Torino : Unpublished Material, 2022.

Wang, S., Xiang, H. e Han, B. 2001. *The modification and generalization of BWR equation.* s.l. : Fluid Phase Equilibria 181 (1), pp. 71-82, 2001.

Wang, Z., et al. 2012. *Comparison of thermochemical, electrolytic, photoelectrolytic and photochemical solar-to-hydrogen production technologies.* s.l. : International Journal of Hydrogen Energy, Volume 37, Issue 21, pp. 16287-16301, ISSN 0360-3199, 2012.

Wertheim, M.S. 1984b. *Fluids with highly directional attractive forces, I. Statistical thermodynamics.* s.l. : J. Stat. Phys., 35, pp. 19-34, 1984b.

Wertheim, M.S. 1984a. *Fluids with highly directional attractive forces, II. Thermodynamic perturbation theory and integral equations.* s.l. : J. Stat. Phys., 35, pp. 35-47, 1984a.

Wertheim, M.S. 1986. *Fluids with highly directional attractive forces, IV. Equilibrium polymerization.* s.l. : J. Stat. Phys., 42 (3), pp. 477-492, 1986.

World Energy Scenario. 2013. *Composing energy futures to 2050.* London, UK : World Energy Council, 2013.

Zivar, D., Kumar, S. e Foroozesh, J. 2021. *Underground hydrogen storage: a comprehensive review.* s.l. : Int. J. Hydrog. Energy 46, pp. 23436–23462., 2021.